Effective interactions in liquid-liquid phase separated protein solutions induced by multivalent ions

Dissertation

der Mathematisch-Naturwissenschaftlichen Fakultät

der Eberhard Karls Universität Tübingen

zur Erlangung des Grades eines

Doktors der Naturwissenschaften

(Dr. rer. nat.)

vorgelegt von

Marcell Wolf

aus Kirn

Tübingen

2014

Gedruckt mit Genehmigung der Mathematisch-Naturwissenschaftlichen Fakultät der Eberhard Karls Universität Tübingen

Tag der mündlichen Qualifikation:	21.11.2014
Dekan:	Prof. Dr. Wolfgang Rosenstiel
1. Berichterstatter:	Prof. Dr. Frank Schreiber
2. Berichterstatter:	Prof. Dr. Roland Roth

Contents

List of Figures

List of Tables

Glossary

abbreviation	description
B_2	second virial coefficient
$E_{1cm}^{1\%}$	percent solution extinction coefficient
F	Helmholtz free energy
I_0	incident intensity
$I_e(q)$	scattered energy
$I_{solvent}(q)$	solvent scattering intensity
$I_{std,abs}$	absolute scattering intensity of the standard
I_{std}	standard scattering intensity
$I_s(q)$	solution scattering intensity
L_2	sample detector distance
M	molarity
N	number of particles
N_A	avogadro number
P	porod exponent
$P(q)$	form factor
PDI	polydispersity index
R	gas constant
S	entropy
$S(\bar{q})$	interparticle structure factor
$S(q)$	structure factor
$S(q)_{eff}$	effective structure factor
SLD	scattering length density
T_C	critical temperature
T_M	total measurement time
U	internal energy
V	volume
Δ	width of the interaction potential
ΔG	difference in Gibbs free energy
Δt	time interval
Π	osmotic pressure
β	setup dependent coherence term
ϵ	molar extinction coefficient
η	viscosity
η_c	critical packing fraction
λ	wave length

abbreviation	**description**
Φ_{D_2O}	volume fraction of heavy water
μ	chemical potential
π	osmotic pressure
$\rho(r)$	radial density
σ	hard sphere diameter
τ_d	delay time
θ	scattering angle
γ	interfacial free energy
ρ	number density
ζ	zeta potential
c	concentration
$c(r)$	direct correlations
c_p	protein concentration
c_s	salt concentration
$d\sigma/d\Omega$	differential cross-section
$g(r)$	pair correlation function
$h(r)$	total correlation
i	dimensionless van't Hoff factor
k	modulus of a wave
n	refraction index
$n_{solvent}$	solvent refraction index
n_s	solution refraction index
p	pressure
r_G	radius of gyration
r_a	minor axis of the ellipsoid (rotation axis)
r_b	major axis of the ellipsoid
$u(r)$	interaction potential
u_0	depth of the attractive well
$AlCl_3$	aluminium chloride
BLG	β-lactoglobulin
CD	circular dichroism
CNT	classical nucleation theory
Cys	cystine
D_2O	heavy water
DLS	dynamic light scattering
$FeCl_3$	iron chloride
FTIR	fourier transformed infra-red

abbreviation	**description**
$GdCl_3$	gadolinium chloride
H_2O	normal water
$HfCl_4$	hafnium chloride
$LaCl_3$	lanthanum chloride
LCST	lower critical solution temperature
LLPS	liquid-liquid phase separation
LYZ	lysozyme
OVA	ovalbumin
PEG	polyethylene glycol
Phe	phenylalanine
RC	reentrant condensation
RPM	revolutions per minute
SANS	small angle neutron scattering
SAS	small angle scattering
SAXS	small angle X-ray scattering
SD	sample-to-detector distance
SLS	static light scattering
$SpeCl_4$	spermidine chloride
Trp	tryptophan
Tyr	tyrosin
UCST	upper critical solution temperature
WAS	wide angle scattering
Y^{3+}	yttriumion
$YbCl_3$	ytterbium chloride
YCl_3	yttrium chloride

1 Deutsche Zusammenfassung

1.1 Motivation

Proteine sind kleine molekulare Biopolymere, welche essentiell für alle Prozesse des Lebens sind [1]. Jedes Protein hat eine spezielle Funktion, die auf dem jeweiligen Aufbau und der Dynamik des Proteins beruht. Die Struktur jedes Proteins kann unterteilt werden in die primäre, sekundäre, tertiäre und quartäre Struktur. Die primäre Struktur ist durch die einzigartige strangartige Anordnung Aminosäuren, derer es insgesamt 20 unterschiediche gibt, gegeben. Durch die unterschiedlichen Eigenschaften der einzelnen Aminosäuren (hydrophil, hydrophob, geladene und ungeladene Seitengruppen etc.) faltet sich die primäre Struktur in eine einzigartige 3-dimensionale Struktur, welche in α-Helix, β-Faltblätter und willkürliche Windungen unterteilt ist. Mehrere sekundäre Strukturen bilden die tertiäre Struktur, welche bei einigen Proteinen zur Ausbildung einer quartäre Struktur führt. Um die Funktion eines Proteins zu bestimmen ist es unumgänglich dessen Struktur zu kennen [2]. Für kleine Proteine kann dies mithilfe von magnetischer Kernresonanz (NMR, nuclear magnetic resonance) geschehen. Die am meisten verwendete Methode für die Strukturbestimmung ist die Beugung von elektromagnetischer Strahlung am dem Protein-Kristallgitter. Diese Methode hat keine Beschränkung in der Proteingröße, allerdings werden für die Messung Kristalle von hoher Qualität benötigt, welche gerade für Proteine nur schwer herzustellen sind.

Computer-Simulationen an globulären Proteinen zeigen eine Absenkung der für die Kristallisation benötigten Energie, falls sich in einer Proteinlösung vor dem Kristallisationsprozess eine proteinreiche Phase ausbildet [3]. Diese Simulationen werden von vielen experimentellen Studien bestätigt, welche eine Flüssig-Flüssig-Phasentrennung (LLPS, liquid-liquid phase separation) beobachten, bevor die ersten Kristalle sichtbar sind [4–7]. Eine LLPS kann nur für kurzreichweitige Wechselwirkungen auftreten [8], bei denen die Stärke der Wechselwirkungen in einem bestimmten Bereich liegen muss [9]. Eine Möglichkeit um die Stärke der Wechselwirkung richtig einzustellen besteht darin, Salze zur Proteinlösung hinzuzugeben. Durch die Hinzugabe von Salzen kann der Abschirmeffekt von Ladungen verstärkt oder direkte Protein-Salz Wechselwirkungen induziert werden.

Unsere Arbeitsgruppe hat herausgefunden, dass durch die Zugabe von dreiwertigen Salzen ein sogenanntes „reentrant condensation“-Phasenverhalten auftreten kann [10]. Bei diesem Phasenübergang trübt eine Lösung mit negative geladenen Proteinen bei Zugabe von dreiwertigen Salzen ein und wieder aufklart bei weiterer Zugabe. Unter speziellen Bedingungen kann innerhalb der getrübten Lösung die Bildung von flüssigen proteinreicher Phase beobachtet werden.

In dieser Arbeit zeigen wir, dass durch die Zugabe des dreiwertigen Salzes Yttriumchlorid (YCl_3) zu einer Serumalbumin-Lösung eine LLPS innerhalb des getrübten Bereichs des dazugehörigen Phasendiagrammes induziert werden kann. Die jeweiligen Konzentrationen der sich dabei gebildeten proteinarmen und proteinreichen Phase werden gemessen und die Wechselwirkungsstärke zwischen Proteinen und Salzen wird anhand des Konzentrationsverhältnisses zwischen armer und reicher Phase bestimmt. Wir zeigen, dass die Stärke der Protein-Protein-Wechselwirkung durch die Konzentration der dreiwertigen Salze eingestellt werden kann. Des Weiteren betrachten wir den Einfluss der Temperatur und des Lösungsmittels auf das Phasenverhalten. Der Struktur der proteinreichen Phase wird untersucht, wodurch deren optischen Eigenschaften bestimmt werden. Die Metastabilität der LLPS wird anhand der Bildung von Proteinkristallen aus der proteinarmen und -reichen Phase beobachtet.

Als letzter Punkt dieser Arbeit wird die Entwicklung eines neuen Probenhalters für die simultane Messung von Neutronstreu- und Lichtspektroskopieexperimente beschrieben. Die einzelnen Schritte der Entwicklung werden vorgeführt und erklärt.

1.2 Ergebnisse

Das Phasendiagramm von Serumalbumin (Serumalbumin des Menschen, *human*, HSA, und des Rindes, *bovine*, BSA) bei Zugabe von Yttriumchlorid zeigt mehrere Besonderheiten, wie z.B. reentrant condensation, LLPS, Kristallisation, Aggregation und Gelation. Diese Phänomene können dadurch beeinflusst werden, dass ein oder mehrere Parameter des Systems verändert werden.

In den ersten beiden Abschnitten dieser Arbeit (Sekt. 4.1 und Sekt. 4.2) diskutieren wir, wie das Phasendiagramm gemessen und interpretiert werden kann. Aufgrund des Phasenverhaltens können Rückschlüsse bezüglich der effektiven Wechselwirkungen des Systems gezogen werden. Diese effektiven Wechselwirkungen werden daraufhin experimentell bestimmt. Die Änderung der effektiven Wechselwirkungen mit der Temperatur wird im dritten Abschnitt (Sekt. 4.3) dargestellt. Im darauf folgenden Abschnitt (Sekt, 4.4) werden die Struktur der proteinreichen Phase und die hier auftretenden effektiven Wechselwirkungen diskutiert. Anschließend betrachten wir den Einfluss des Lösungsmittels auf das Phasenverhalten und auf die effektiven Wechselwirkungen in Sekt. 4.5. Im darauf folgenden Abschnitt (Sekt. 4.6) wird das Langzeitverhalten der proteinarmen und -reichen Phase untersucht, bevor im letzten Abschnitt (Sekt. 4.7) die Entwicklung eines neuen Probenhalters beschrieben wird.

1.2.1 Flüssig-Flüssig-Phasentrennung und reentrant condensation in einem Serumalbumin-Phasendiagramm

Als erster Schritt wurde die Zusammensetzung der beiden verwendeten Protein in Lösung betrachtet. Dabei wurde festgestellt, dass in BSA-Lösungen ein nicht zu vernachlässigbarer Dimer-Anteil vorhanden ist. Dies wurde schon in unterschiedlichen Publikationen

beobachtet [11, 12]. Mit Hilfe von Lichtmikroskopie kann gezeigt werden, dass sich innerhalb einer bestimmten Region des getrübten Bereichs des reentrant Phasendiagrammes flüssige Tropfen bilden, die auf eine LLPS hinweisen. Die Proteinkonzentration in den zu beobachtenden flüssigen Tropfen (proteinreiche Phase) ist gegenüber der umgebenden proteinarmen Lösung erhöht. Mit Hilfe von Zentrifugation kann die proteinreiche von der proteinarmen Lösung getrennt werden. Die Protein- und Salzkonzentration in der resultierenden proteinarmen und -reichen Phase wird mit Hilfe von UV-Vis Spektroskopie und Röntgenabsorption bestimmt. Dadurch, dass in der proteinreichen Phase eine erhöhte Protein- und Salzkonzentration festgestellt wurde, kann man auf attraktive Protein-Yttrium-Wechselwirkungen schließen.

Die effektiven Wechselwirkungen in den unterschiedlichen Regionen des Phasendiagrammes werden durch statische Lichtstreuexperimente bestimmt. Da Lichtstreuexperimente nur an klaren oder leicht trüben Lösungen möglich sind, wurden für diese Experimente nur niedrige Proteinkonzentrationen verwendet, bei denen keine LLPS auftritt. Die dadurch erhaltenen effektiven Wechselwirkungen zeigen ein repulsives Verhalten innerhalb des ersten und dritten Regimes des reentrant Phasendiagramms. Innerhalb des zweiten Regimes kann ein Wechsel zu attraktiven Wechselwirkungen beobachtet werden. Durch Kleinwinkelröntgenstreuung (small angle X-ray scattering, SAXS) können die effektiven Wechselwirkungen bei höheren Proteinkonzentration, vor allem innerhalb der LLPS-Region, beobachtet werden. Die Ergebnisse dieser Experimente zeigen, dass die attraktiven Wechselwirkungen an den LLPS-Grenzen am geringsten sind. Je weiter innerhalb die Probe in der LLPS Region lokalisiert ist, desto stärker werden die attraktiven Wechselwirkungen im System.

Die Erhöhung der Temperatur einer proteinarmen Phase nach einer LLPS führt zu einer weiteren LLPS. Gleichzeitige SAXS Messungen zeigen, dass mit zunehmender Temperatur die attraktiven Wechselwirkungen stärker werden, bis das Maximum an dem Punkt der zweiten LLPS erreicht ist. Eine weitere Erhöhung der Temperatur führt zu einer Reduktion der attraktiven Wechselwirkungen innerhalb des Systems. Dieses Verhalten kann dadurch erklärt werden, dass die Kompressibilität des Systems am Punkt der LLPS, welche nahe an der Spinodalen liegt, zunimmt. Dies führt auch zu einer Zunahme des Strukturfaktors und der Streuintensität führt.

1.2.2 Morphologie und Phasenverhalten der proteinreichen Phase

Aufgrund Ihrer hohen Proteinkonzentration weist die proteinreiche Phase eine sehr hohe Viskosität auf. Diese entsteht aufgrund der hohen Proteinkonzentration. Werden die optischen Eigenschaften der proteinreichen Phase betrachtet, fällt auf, dass diese bei niedrigen Temperatur eine gelbliche klare Lösung darstellt. Wird die Temperatur dieser Phase über eine kritische Temperatur hinaus erhöht, trübt die Phase stark ein. Die gelbliche Färbung der Lösung kann auf die Eigenfarbe des Proteins zurückgeführt werden. Betrachtet man die Unterschiede zwischen den beiden Serumalbuminen, so fällt auf, dass im Falle von HSA bei niedrigen Temperaturen eine leichte Trübung zu beobachten ist. Mit Hilfe von optischer Mikroskopie können in einer proteinreichen HSA-Lösung bei niedriger Temperatur runde Strukturen beobachtet werden, während für eine BSA-Lösung

nur eine klare Flüssigkeit sichtbar ist. Für Temperaturen oberhalb der kritischen Temperatur kann in beiden Serumalbuminlösungen eine starke Trübung beobachtet werden. Dabei bleiben die runden Strukturen, welche in HSA-Lösungen auftauchen, erhalten.

Aufgrund der starken Trübung der Probe konnten keine Lichtstreuexperimente durchgeführt werden. Die Verwendung von Röntgen- und Neutronenstrahlung ist dafür geeigneter. Röntgenstrahlung hat allerdings den Nachteil, dass bei den verwendeten hohen Proteinkonzentrationen mit Strahlschäden gerechnet werden muss, welche die Streukurve vor allem für kleine Streuvektoren q beeinflussen. Daher wurde die proteinreiche Phase im weiteren Verlauf mit Neutronstreuexperimenten charakterisiert. Die Streukurven für niedrige Temperaturen zeigen im Fall von BSA keine Bildung von großen Aggregaten, wodurch sich die klaren Proben erklären lassen. Wird HSA verwendet, zeigt die Streukurve einen Anstieg bei niedrigen q-Werten, was auf die Bildung von größeren Strukturen schließen lässt. Bei Erwärmung zeigt sich bei beiden verwendeten Proteinlösung ein starker Anstieg der Streuintensitä bei niedrigen q-Werten, was auch hier auf die Bildung von größeren Strukturen hinweist. Die Proben werden im sichtbaren Licht als trüb wahrgenommen. Um die Streukurven bei niedrigen q-Werten besser zu charakterisieren, wurde Ultra-Kleinwinkelstreuung (ultra small angle neutron scattering, USANS) verwendet. Die verschieden Streukurven werden mit Hilfe von verschiedenen Fitmethoden für unterschiedlichen q-Bereiche analysiert. Es zeigt sich, dass sich die Proteinmonomere zu kleinen Clustern zusammenschließen. Im Falle von BSA wachsen diese Cluster mit der Erwärmung der Probe, bis die kritische Temperatur erreicht ist. Eine weitere Erwärmung führt zum Schrumpfen der vorhandenen Clustern und zur Bildung von größeren Strukturen. Daraus kann man schließen, dass sich die großen Strukturen aus den kleinen bilden. Da im Falle von HSA auch schon bei niedrigen Temperaturen große Strukturen beobachtet werden, kann das Anwachsen der kleinen Cluster hier nicht beobachtet werden, sondern nur deren Schrumpfen. Mit Hilfe eines Beaucagefits wird für die großen Strukturen ein einen Gyrationsradius, r_G, von 1.75 µm ermittelt. Dabei zeigen die große Strukturen eine diffuse Oberfläche auf, welche aus dem Porodexponent von P=4.1 sichtbar wird. Erste Rheologieexperimente an BSA-Lösungen zeigen, dass die proteinreiche BSA Lösung durch Erwärmung ihren Zustand von einer Flüssigkeit zu einem Gel wechselt. Mit dieser Information können wir den Gyrationsradius der großen Strukturen zu den Abständen innerhalb des Gelnetzwerkes zuordnen. Da die Streukurven von HSA-Lösungen zumindest bei hohen Temperaturen vergleichbar mit denen von BSA sind, gehen wir davon aus, dass in HSA-Lösungen schon bei niedrigen Temperaturen gelartige Eigenschaften aufweisen. Möglicherweise könnte bei niedrigeren Temperaturen auch für HSA eine klare Lösung erreicht werden, was aber zu Problemen in der technischen Ausführung führt.

Durch die Verwendung eines „sticky hard sphere“Potentials lassen sich auch hier die effektiven Wechselwirkungen zwischen den Proteinmolekühlen abschätzen. Dadurch erhalten wir B_2/B_2^{HS}-Werte, welche über dem kritischen Wert einer LLPS von -1.5 liegen. Momentan suchen wir noch nach einer Erklärung für dieses Phänomen. Allerdings muss man hierbei beachten, dass die Virialentwicklung streng genommen nur für niedrige Konzentrationen gilt, was für die proteinreiche Phase nicht mehr der Fall ist. Dies kann zu Abweichungen von den realen B_2/B_2^{HS}-Werten führen. Generell kann man jedoch be-

obachten, dass die Stärke der effektiven Wechselwirkungen mit steigender Temperatur abnimmt. Dabei wurde eine Korrelation zwischen den B_2/B_2^{HS}-Werten und der Salzkonzentration für die klaren BSA-Proben festgestellt. Diese Korrelation geht verloren, sobald die Probe den Gelzustand erreicht.

In diesem Abschnitt haben wir den Aufbau der proteinreichen Phase für die verwendeten Proteine charakterisiert und haben herausgefunden, dass die Proben eine Gelation unterlaufen, sobald eine kritische Temperatur überschritten wird. Die effektiven Wechselwirkungen konnten aufgrund der hohen Proteinkonzentrationen nicht korrekt bestimmt werden.

1.2.3 Einfluss von schwerem Wasser auf das Flüssig-Flüssig-Phasenverhalten

Unteren kritische Flüssigkeitstemperatur (lower critcal solution temperature, LCST) wurden in der Literatur bis jetzt nur bei Systemen erwähnt, welche einen starken Einfluss von Hydrationseffekten aufweisen. Um diesen Einfluss zu untersuchen, wurde innerhalb dieser Arbeit das Lösungsmittel Wasser (H_2O) durch schweres Wasser (D_2O) ersetzt. Mit bloßem Auge kann bei der Verwendung von D_2O eine verstärkte Aggregationsbildung beobachtet werden. Ferner wird lichtmikroskopisch keine LLPS mehr festgestellt. Die Phasendiagramme für jeweils eine feste BSA- und HSA-Konzentration unter Variation der Salzkonzentration und des Anteils an schweren Wassers wurden aufgenommen. Es wird sichtbar, dass mit steigendem D_2O-Anteil die LLPS-Region kleiner wird, bis sie ab einem Anteil von 80 % nicht mehr beobachtet werden kann. Für die unteren kritischen Grenzen des „reentrant"Phasenverhaltens (c^*) lässt sich eine kaum wahrnehmbare Variation nachweisen. Im Gegensatz dazu verschiebt sich die c^{**}-Grenze deutlich stärker zu höheren Salzkonzentration mit steigendem D_2O-Anteil.

Durch den Vergleich von verschieden Streukurven bei verschiedenen Positionen im Phasendiagramm zeigt sich, dass im ersten Regime nur geringe Veränderungen beobachtet werden können. Im dritten Regime sind die größten Variationen zu beobachten, welche aber durch die unterschiedlichen Abstände der Messpunkte zu c^{**} erklärt werden können. Die interessantesten Variationen lassen sich im zweiten Regime für die Proben, welche bei der Verwendung von H_2O LLPS aufzeigen, beobachten. Der Vergleich der Streukurven bei fester Salzkonzentration für verschiedene Anteile von schwerem Wasser zeigt, dass schweres Wasser die Bildung von kleineren Clustern gegenüber der Bildung von mittelgroßen Clustern bevorzugt. Da optische Mikroskopie mit steigendem D_2O-Anteil eine Zunahme von Clustern zeigt, gehen wir davon aus, dass diese beobachteten großen Cluster, welche aber außerhalb des beobachteten q-Bereichs der SAXS-Experimente liegen, durch die kleineren Cluster gebildet werden. Eine weitere Ursache für die Variation der Streuintensität ist auch die Änderung der effektiven Protein-Protein Wechselwirkungen, welche für verschiedene Anteile von schwerem Wasser über die Bestimmung von B_2/B_2^{HS} ermittelt werden können. Es zeigt sich, dass die Stärke der Wechselwirkungen mit zunehmendem D_2O-Anteil leicht abnimmt. Allerdings sinkt die Stärke für keine beobachtete Probe unterhalb den für das Auftreten von LLPS kritischen

Wert. Da aber für hohe D_2O-Anteile kein makroskopisches LLPS zu beobachten ist, gehen wir davon aus, dass die Absenkung der Proteinkonzentration in der proteinarmen Phase dafür verantwortlich ist. UV-Vis Messungen an der proteinarmen Phase zeigen eine Verschiebung der Proteinkonzentration zu niedrigeren Konzentration, welche sogar unterhalb der unteren Grenze der LLPS-Regionen für normales Wasser liegen. Dies zeigt, dass in den Proben, bei denen keine LLPS beobachtet wird, die Proteinkonzentration zu gering ist, um eine Flüssig-Flüssig-Phasentrennung auszulösen.

1.2.4 Langzeitstabilität der proteinarmen und -reichen Phasen

Die Metastabiliät der LLPS ist am einfachsten daran zu erkennen, dass in den phasengetrennten Proben nach einiger Zeit Kristalle beobachtet werden können. In der proteinarmen Phase kann Kristallisation bei niedrigen Salzkonzentrationen innerhalb von 3-4 Tagen beobachtet werden. In der proteinreichen Phase dauert es über einen Monat, bis die ersten Kristalle beobachtet werden können. Während sich in der proteinarme Phase innerhalb eines Salzkonzentrationsbereichs bei Raumtemperatur immer Kristalle bilden, wird Kristallisation in der proteinreichen Phase nur selten beobachtet. Dies könnte aber auch daran liegen, dass wir aufgrund der starken Trübung der Probe immer nur kleine Bereiche aus der Probe beobachten konnten. Daher besteht die Möglichkeit, dass Kristallisation in einem nicht beobachteten Bereich der Probe stattgefunden hat.

Die Kristallstruktur von HSA mit YCl_3 (noch nicht publiziert) wurde mit Hilfe von Röntgenbeugung von unseren Kooperationspartnern aus der Biochemie (AG Stehle, IFIB, Tübingen) bestimmt. Aus SAXS-Messungen geht hervor, dass alle untersuchten Kristalle (aus der proteinarmen Phase) die selbe Kristallstruktur aufweisen. Kleinwinkelneutronenstreuung-Messungen (small angle neutron scattering, SANS) an Kristallen aus der proteinreichen Phase zeigen einen sichtbaren Bragg-Peak, welcher mit dem ersten Bragg-Peak für die bekannte Kristallstruktur übereinstimmt. Es wurden keine weiteren Bragg-Peaks detektiert. Aufgrund der ungenauen Bestimmung der Wellenlänge im Neutronenexperimenten „verschmieren“die Peaks. Durch das Verschmieren werden die Bragg-Peaks nicht mehr bei einem definierten q-Wert, sondern bei mehreren q-Werten gemessen, wodurch sich die Halbwertsbreite des Peaks vergrößert. Dies führt dazu, dass die maximale Streuintensität bei einem gemessen q-Wert absinkt. Dadurch kann es vorkommen, dass durch die erhöhte Untergrundintensität von H_2O keine weiteren Bragg-Peaks sichtbar sind. Daher können wir nur vermuten, dass auch die Kristallstruktur der proteinreichen Phase mit der bekannten Struktur übereinstimmt. Eine experimentelle Bestätigung durch Röntgenbeugung steht noch aus.

1.2.5 Entwicklung eines Probenhalters für simultane Lichtspektroskopie- und Neutronenstreuexperimente

Ein weiteres Projekt, über welches in dieser Arbeit berichtet wird, dient der Entwicklung eines neuen Probenhalters. Dieser soll für kombinierte Licht- und Neutronenstreumessungen eingesetzt werden. Diese Arbeit steigt in dieses Projekt nach dem ersten

erfolglosen Test ein. Während des ersten Tests wurde kein stabiles optisches Signal gemessen. In dieser Arbeit wurde der Aufbau daher auf das Wesentliche reduziert und nur ein einfacher Diodenlaser als Lichtquelle und eine Photodiode als Detektor verwendet. Bei den ersten Versuchen in diesem Aufbau wurde der Laserstrahl noch über einen Spiegel auf die Photodiode gelenkt. Dieser Aufbau blieb über mehrere Stunden stabil, solange die Temperatur konstant gehalten wurde. Sobald die Temperatur der Probe, und damit auch die Temperatur des Probehalters um 10°C erhöht wurden, ging das Messsignal verloren. Dies kann darauf zurückgeführt werden, dass sich durch die Materialausdehnung, für welche kein Spielraum in der Konstruktion vorgesehen ist, die Orientierung des Spiegels verändert hat. Um dieses Problem zu lösen, wurde der Spiegel durch eine einfache Glasplatte ersetzt, unter welcher die Photodiode platziert wurde. Damit konnte man die Trübung einer Lösung bei unterschiedlichen Temperaturen erfolgreich aufzeichnen. Im nächsten Schritt wurde dann der Laser am oberen Ende des Probenstabs montiert. Allerdings wurde dabei eine leichte Krümmung des Probenstabes festgestellt, wodurch der Laserstrahl nicht unreflektiert durch den hohlen Stab wandern konnte. Durch Erwärmung wurde der Punkt der Reflektion auf dem Probenstab durch die Materialausdehnung verschoben, wodurch sich auch die Position des reflektierten Strahls auf der Photodiode änderte. Darauf wurde ein Entwurf erstellt, bei welchem der Laser direkt über dem Probentopf montiert wird und die Photodiode noch weiter an den Laser geschoben wird. Aktuell ist dieser Aufbau noch unter Konstruktion und die ersten experimentellen Messungen stehen noch aus.

1.3 Schlussfolgerungen

Der Schwerpunkt dieser Arbeit liegt auf der Charakterisierung der Flüssig-Flüssig-Phasentrennung (LLPS) und der daraus entstehenden proteinarmen und -reichen Phase. Das Auftreten einer LLPS wird mit Hilfe von optischer Mikroskopie bestätigt. Durch die Aufnahme eines Phasendiagramms kann die attraktive Wechselwirkung zwischen den verschiedenen Serumalbuminen und der Yttrium-Kationen visualisiert werden. Die Stärke dieser Wechselwirkung wurde durch die sogenannten „Tie-lines“charakterisiert. Die effektiven Protein-Protein-Wechselwirkungen in den proteinreichen und -armen Phasen der LLPS und in den verschiedenen Bereichen des Phasendiagramms wurde durch Röntgen- und Neutronenkleinwinkelstreuung und Lichtstreuexperimente bestimmt. Es zeigt sich, dass innerhalb der proteinarmen Phase die effektive Stärke der Wechselwirkungen oberhalb der benötigten kritischen Wechselwirkung für eine LLPS liegt, wodurch sich das Auftreten einer LLPS erklären lässt. Dies trifft für die proteinreiche Phase nicht zu. Die genaue Erklärung dafür fehlt leider noch, wobei man dabei auch berücksichtigen muss, dass die benutzte Virialentwicklung nur für geringe Proteinkonzentrationen gilt.

Für Temperaturen oberhalb einer kritischen Temperatur weist die proteinreiche Phase großer Strukturen auf. Diese werden dem Gelationsprozess, welcher bei hohen Temperaturen in der proteinreichen Phase stattfindet, zugeschrieben. Des Weiteren zeigt sich eine diffuse Oberfläche für die Gelstrukturen in den Streudaten. Dabei zeigt sich, dass der Gelationsprozess vollständig reversibel ist, sobald die Probe unterhalb die kritische

Temperatur abgekühlt wird.

Der Einfluss des Lösungsmittels wird anhand des partiellen Austausches von normalem zu schwerem Wasser demonstriert. Der Einfluss auf das Phasenverhalten der Proteinlösungen wurde aufgezeichnet und für hohe Anteile von D_2O wurde ein Verschwinden der LLPS beobachtet. Die effektiven Wechselwirkungen können die Abwesenheit einer LLPS-Region nicht erklären, da erstere zwar schwächer, aber immer noch oberhalb des kritischen Wertes liegen. Daher wird das Verschwinden der LLPS durch die Reduktion der Proteinkonzentration der proteinarmen Phase, welche auf starke Aggregation zurückgeführt wird, erklärt. Durch das Absinken der Proteinkonzentration fällt die Proteinlösung aus dem Bereich einer LLPS heraus.

Mit der Zeit können sich in den phasenseparierten Proben Kristalle bilden. Röntgenkleinwinkelstreuungsdaten an verschiedenen Kristallen aus der proteinarmen Phase stimmen mit einer bisher nicht veröffentlichten Kristallstruktur überein. Für Kristalle aus der proteinreichen Phase konnte bis jetzt nur der erste Bragg-Peak beobachtet werden, welcher mit der bekannten Kristallstruktur übereinstimmt, weshalb wir davon ausgehen, dass sich die Kristallstruktur zwischen der proteinarmen und -reichen Phase nicht ändert.

Mit dieser Arbeit konnte gezeigt werden, dass das Phasenverhalten einer Serumalbumin-Lösung mit der Zugabe von YCl_3 beeinflusst werden kann. Die gewünschte Stärke der effektiven Wechselwirkungen kann durch die richtige Wahl der YCl_3-Konzentration eingestellt werden und das gewünschte Phasenverhalten somit induziert werden.

2 Introduction

In nature aqueous solutions of globular proteins are ubiquitous. In general such protein solutions represents a complex system which shows a rich phase behavior. This rich phase behavior can be influenced by various environmental parameters such as temperature, pH and concentration and type of the salt used. Controlling the phase behavior of such solutions is an essential cornerstone for bio related applications and for the description of cellular processes [2]. In literature the temperature is used as the first control parameter. Adding salt into the protein solutions induces protein-salt interactions influencing the protein-protein interaction, which controls the phase behavior of the protein solution. This introduction gives an overview of the topics under investigation and embeds this thesis into the scientific literature.

2.1 Proteins as biological soft matter

Proteins plays an important role in nature because all biological processes depends on proteins [2]. A particular function can be related to each protein which is defined by the individual structure and dynamic of each protein. The structure of proteins shows a hierarchical organization which is the key for the variation of the structure and function in the different protein domains. A protein is build up by amino acids which are aligned in a linear chain. This alignment of the amino acids in the chain is called primary structure and is unique for each protein. By hydrogen bridges and hydrophobic interactions the linear chain form α-helix, β-sheets and random coils which are included into the secondary structure. The tertiary structure is described by the assembling of the secondary structure into a compact domain. And the tertiary structure can finally contribute to the quaternary structure of the protein. The unique primary structure and their alignment into the secondary, tertiary and quaternary structure is the reason that a protein system can be used as a monodisperse model system. In the case of globular proteins they form a natural model system for colloids. The phase behavior and the diffusional dynamic of globular protein system can be at least qualitatively described in terms of colloidal physics. Another feature of proteins is that water-mediated effects influences the structure and dynamics of the protein. In the case of molecular recognition the protein association depends the hydrophobic and hydrophilic surface pattern which are embedded into cellular structures such as biomembranes.

From this it is obvious that proteins represent an interesting research topic, especially if the focus is on medical applications. The condensation of proteins are related to several human and animal diseases. The condensation of γ-crystallins is responsible for the formation of cataracts [2, 13, 14]. The formation of sickle hemoglobin into fibers is the

reason for sickle cell anemia [2] and amyloid β is related to Alzheimer's disease [15–17]. An overview of the different diseases which are related to protein or peptide aggregation is given by Chiti [18].

Another important feature of proteins is the non-spherical, rough, porous and flexible shape and inhomogeneous surface pattern of charge and hydrophobicity which makes them very complex systems. In such complex system several interactions play a crucial role such as Coulomb repulsion, van der Waals interaction and the solvent-mediated influence of depletion and hydrophobic interaction. This is the reason why theoretical results for colloidal systems can only be applied to protein systems with care.

2.2 Protein-ion interaction

In this study we added trivalent metal ions, in the form of salts, to the solution to tune the phase behavior of the protein solution. In order to understand the influence of the salt on the protein-protein interaction the interaction between the protein and the used ions must be understood beforehand. In this section we give a short overview of different type of protein-ion interactions. We begin with the unspecific interaction, described by the Poisson-Boltzmann theory, Sec. 2.2.1. Afterwards, 3 deviations from this theory, the Hofmeister series (Sec. 2.2.2), counterions condensation (Sec. 2.2.3) and binding of protein ions on the surface (Sec. 2.2.4) are discussed.

2.2.1 Poisson-Boltzmann and DLVO theory

The Poisson-Boltzmann theory can be used to describe the charge distribution around a charged object in a solution with ions. This theory combines the exact Poisson equation with a mean field relation between the electrostatic potential and the potential of mean force on ions [19–21]. An electrostatic double-layer, resulting from the charge distribution, forms around the charged object. This electrostatic double layer causes a screening effect in electrolyte solutions. In general, the nonlinear Poisson-Boltzmann equation cannot be solved analytically. In this case the linearized version of the Poisson-Boltzmann equation, the Debye-Hückel theory [22], is used. Both theories are useful for the better understanding of electrostatic phenomena in soft matter.

Another theory to describe the interaction in the system is the DLVO theory, named after Derjaguin and Landau (1941), [23], and Verwey and Overbeek (1948) [24]. In this theory the screened Coulomb interaction and the van der Waals attraction are combined to describe the charge stabilization in a charged solution.

The Poisson-Boltzmann and DLVO theories are based on several important assumptions. Complex interactions, such as the ion-ion correlation, excluded volume, polarization and hydration effects are ignored or not included into these theories. Therefore it is quite reasonable that in experiments a deviation from these theories can be observed [21, 25, 26]. Surprisingly, these theories still provide a good description of many systems, especially when a full description of the system is not possible.

2.2.2 The Hofmeister series

That salt can induce different phase behavior in protein solutions is known for more than a century. The first observations were done by Hofmeister [27] by using a series of different salts, known as Hofmeister series. In colloidal solutions different salt can sorted by their behavior to stabilize (salting-in) or their ability to induce precipitation (salting-out) [28, 29]. For proteins two competitive abilities of the Hofmeister series are important, the salting-out of nonpolar functional groups and the salting-in of the polar peptide groups [30]. The variations of the phase behavior shows that the different ions have an specific effect which is not included into the Poisson-Boltzmann theory and so the DLVO theory cannot explain the observed behavior. Usually the ion-specific effects are visible at relatively high salt concentration above 100 mM.

In literature different ways to explain the molecular origin of the Hofmeister effect can be found. One way follows the idea of Collins [31, 32] is that the strength of the ion-water interactions changes by varying the type of ions in a salt. For strongly interacting ions, kosmotropes, the surrounding water aligned relatively to the ions which leads to the formation of an additional structure. For weakly interacting ions, chaotropes, the structuring of water is not observed. Another way is that the ions may influence the dielectric constant at the protein-water interface. This would allow the non-localized absorption of polarizable ions at non-polar, hydrophobic areas at the surface [33–35]. This absorption leads to another possible mechanism for the Hofmeister effect explained by dispersion forces [36–38].

2.2.3 Condensation of counterions

A deviation of the observed charge distribution from the mean-field Poisson-Boltzmann approach can be observed in systems where the counterions have a high charge density. As long as the charge density is higher than a critical value, which depends on the counterion valency and the surface geometry, condensation of counterions on the surface can be observed [39].

This phenomenon is described by ion-ion correlations which are due to strong Coulomb coupling. For such a system with a strongly charged surface as well as ion distributions that depend on the valency and size of the counterions the condensation of counterions are found [21, 40–43]. This can lead to a charge inversion of the surface [42, 44–46].

Compared to the specific surface-ion interaction the ion-ion interaction is expected to be small, in general [45]. It was also found experimentally that the specific surface-ion interaction appears to be more relevant [47].

2.2.4 Ion binding at the protein surface by functional groups

The protonation state of the functional surface groups, the basic and acidic amino acid side chains (Arg, His, Lys, Asp and Glu) and the protein carboxy and amino terminus depends on the pH of the solution [48, 49]. In solution these side chains are exposed to the solvent and a charge regulation of the protein surface occurs.

If some ions are added to the solution not only the water molecules can interact with the side chains of the proteins. Especially multivalent ions can bind to the protein side chains. This binding to specialized functional surface groups explains the storage and transport function of proteins for metal ions [50–54]. It is found that transition metals, such as iron (Fe), Yttrium (Y) and Lanthanum (La), bind to amino acids with carboxylate (Aspartic acid, Glutamic acid), thiol (Cysteine), thioether (Methionine) and imidazole groups (Histidine) [55, 56]. Another important influence is the hydrophobicity of the surrounding area of the binding side. The binding of a metal ion to a hydrophilic binding side is enhanced when the binding side is surrounded by a hydrophobic area [57]. Such surface groups can be found on all proteins which suggests that the binding of salt counterions to inversely charged side groups at the protein surface is the most important pathway of protein-ion interaction [33, 58, 59].

2.3 Rich phase behavior in protein solutions

The phase diagram of an aqueous salt solution with charged particles shows a rich phase behavior, such as a mixture of a gas and solid phase, crystallization, aggregation (clusters and fibers), liquid-liquid phase separation (LLPS) as well as the formation of an arrested state (gelation, glass state) [8, 60, 61]. The here mentioned gas phase is clearly not a real gas because we have an one-component liquid but it can be compared with the one-component gas phase. This comparison between the one-component liquid and gas show that in the gas phase the sample is completely mixed and in the liquid-gas phase a further liquid can be observed in the „gas"-liquid. A special behavior, reentrant condensation, can occur by adding a multivalent salt into solutions of charged particles [10, 62]. An overview of the most important type of phase behavior, which play a role in this thesis, is given in this section. We will specialize the overview on the phase behavior of a protein solution but if it is necessary the relation to other biological systems is discussed.

2.3.1 Liquid-liquid phase separation

The phase separation from a one-solution system into a two-solution system was observed the first time in a protein system from the calf, rat and human eye lenses by Tanaka et al.[63, 64]. In this system the phase separation was induced by varying the temperature. Starting at a temperature where the solution shows no phase separation and then cooling down the system leads to a critical temperature where the solution starts to become turbid and a second phase appears. Such phase behavior upon temperature decrease is observed for most protein solutions, which undergoes a liquid-liquid phase separation (LLPS). The phase separation at lower T is called an upper critical solution temperature (UCST) behavior. For system where the sample shows a phase separation with increasing temperature the critical point is located at a low temperature and higher temperatures lead to a phase separated sample. This is referred to a lower critical solution temperature (LCST) behavior. The temperature where the phase separation starts is known as the cloud-point temperature and can be measured by cloud-point experiments. At such a

phase separation the solution splits up into two coexisting liquids, which is the reason for the name liquid-liquid phase separation (LLPS). The concentration of both phase separated liquids can be connected by a so called coexistence curve, or binodal line, which connects all the temperature dependent concentrations of both liquids. Waiting some time or centrifugation of the sample leads to a sharp meniscus between both liquids.

The influence of different parameters such as ionic strength, nature of the salt and pH on the LLPS of Lysozyme, LYZ, in an aqueous solution has been intensively studied [65–69]. The already mentioned protein from the eye lens, the γ-crystallin family, was in detail studied by Benedek and co-workers [13, 70–75]. A ternary mixture with two kinds of γ-crystallin proteins in water was investigated to get a deeper understanding into the crystallization process [76]. LLPS has been also observed in hemoglobin, which is related in literature to the diseases of sickle cell anemia [77–79] and other solutions such as BPTI [80], urate oxidase [81], glucose isomerase [82] and immunoglobulins, Ig, or antibodies [83–87]. Up to now less than 20 protein systems are known which can undergo an LLPS. Annunziata et al. assume that this is due the limited temperature window (from ≈ -10°C up to 40°C) in which proteins can be investigated before the solution freezes or the proteins denatures [5].

One way to shift the critical temperature of the LLPS is by adding nonabsorbing polymers, such es polyethylene glycol (PEG) to the protein solution. in This way an increase of the critical temperature is observed which depends on the molecular weight [88] and the concentration of the polymer [5]. By this method, the critical temperature of γS-crystallin was successfully shifted from -28°C into the experimental window, thus allowing the observation of LLPS [88]. The attraction between the proteins can be significantly enhanced through depletion forces by adding PEG [89]. If the size of the added PEG becomes larger than the protein the PEG concentration fluctuations strongly affect the protein-protein interaction [90]. Wang et al. demonstrated that the addition of HSA to an immunoglobulin-water mixture decreases the critical temperature of LLPS [87]. This feature can be related to the IgG-HSA attractive interaction as opposed to the repulsive protein-PEG depletion interaction. It was experimentally shown that by adding the correct interaction agent it is possible to tune the critical temperature into the desired direction [87, 88]. Therefore we can expect that in the future more proteins with an LLPS behavior will be observed.

Experimental observations suggest that the LLPS is metastable and decays over time to aggregates, gels or crystals [67, 69, 79]. Bio-macromolecular crystallographers have long known that the appearance of a LLPS plays a crucial role for crystallization. LLPS has been often observed before the appearance of the first crystals or to directly participate in the crystallization process [91]. Ten Wolde and Frenkel simulated that the appearance of a denser fluid in advance of visible crystallization reduces the energy barrier for the formation of a crystal [3].

The phase diagrams of different proteins in the (T,Φ) plane such as LYZ and γ-crystallins, show a similar behavior in spite of the different size, structure and biological function of these proteins [67, 69, 71, 73, 74, 92]. The typical features of these phase diagrams are the appearance of a metastable liquid-liquid coexistence curve below the solubility line and the absence of a triplet point, where three phases (gas, liquid and

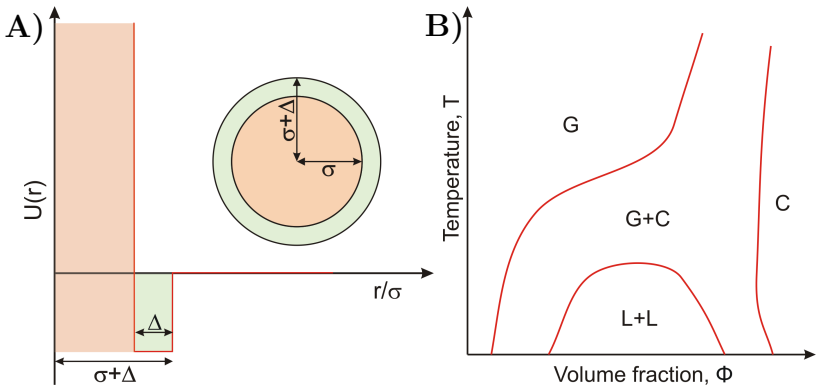

Figure 2.1: A) Sketch of a square well potential as a function of the ratio between the distance from the particle centre and the particle diameter r/σ. When the attractive well-width, Δ, is significantly smaller than the diameter of the particle, σ, ($\Delta/\sigma < 0.25$), the phase behavior results in the phase diagram in B). An important feature of the phase diagram is a metastable liquid-liquid coexistence ($L + L$) below the gas crystal line ($G + C$).

solid) of the substance coexist in thermodynamic equilibrium. This phase behavior can be reproduced by a system of spheres interacting via a short-range interaction potential, where the attractive well-width, Δ, is significantly smaller than the diameter of the particle, σ, ($\Delta/\sigma < 0.25$), as shown in Fig. 2.1a) with the corresponding phase diagram in Fig. 2.1b). How this phase diagram differs from a long-range and a pure hard sphere system is reported in [8].

Another possibility to describe the appearance of an LLPS is the model of patchy particles [59, 93–96]. In such a model a predefined number of attractive sticky sites, patches, decorate the surface of the particle. Only if the patches bounced to each other this patches becomes active and both patches sticking together. An interesting result of a patchy particle system is the shift of the critical concentration to lower volume fraction by decreasing the number of patches on the particle surface. If the amount of patches on the particle is sufficiently low, critical volume fractions below the limits of a spherical short-range and long-range attractive system [87] can be achieved [94]. By reducing the number of patches on a particle less of them can interact with each other through the patches, leading to a saturation of the patches at lower volume fractions.

2.3.2 Cluster formation

In solution different proteins can form different kinds of clusters. One possible kind of a cluster is the so called equilibrium cluster. The formation of equilibrium clusters can be predicted for charged particles by simple argumentation [97, 98]. If particles exhibits short-range attraction and a long-range (Coulombic) repulsion the monomers starts to attach to each other due to the attraction. Through this clustering the charge of the cluster increases with an increasing amount of monomers and also the strength

of the repulsive interaction increases until the repulsion of the whole cluster becomes sufficiently strong to destabilize further attachment of further attraction. At this point a further attachment of a monomer to the cluster leads to a detachment of another monomer from the cluster into solution. This argument was confirmed by simulations of particles with competing interactions [98–103].

Studies from Stradner et al. [104, 105] claim the existence of equilibrium clusters in lysozyme solutions which triggered an extensive discussion about the nature of the observed clusters. Within this discussion further experiments, combining different techniques such as small angle X-ray and neutron scattering (SAXS and SANS), nuclear magnet resonance (NMR), neutron spin echo (NSE) and dynamic light scattering (DLS), suggest that the observed protein clusters are rather dynamic or transient nature instead of static and irreversible [106–111]. The difference of those cluster compared to equilibrium clusters is their lifetime. For transient clusters the lifetime is so short that the constituent proteins move almost independently. In contrast to the transient cluster it is also possible that the same structure is formed by proteins which are moved together, similar to permanent clusters but after a short time the monomers escape from the cluster [108]. An example for transient clusters is given by Piazza and Iacopini, who observed the spontaneous formation of transient clusters in a BLG solution [112]. Light scattering and Brownian microscopy experiments on hemoglobin, lysozyme and lumazine synthase reveals the formation of large metastable clusters [110, 113–116].

Controlling the cluster formation is of practical interest, especially for aggregation dependent diseases or for drug delivering. Especially reversible aggregation is a promising why for drug delivering [117]. The drug can be build into the aggregate and by bringing the aggregate into the body the aggregate dissolves over time and release the drug. In this way a time dependent drug delivery into the body can be achieved. It was also observed that the presence of clusters might affect the pathway of protein crystallization [118].

2.3.3 Crystallization

Until now the growth of high-quality protein crystals is the bottleneck for protein structure determination. Predictions for the best crystallization conditions mainly apply for a few special systems. In order to achieve a general understanding, a lot of studies on the connection of phase behavior and crystal nucleation are performed which have the goal to find the optimum protein crystallization conditions. To achieve an optimal crystallization conditions the strength of the protein interactions must be located in the so-called crystallization slot. Performing light scattering experiments on the crystallization of different proteins George and Wilson [119] found that the measured second virial coefficient, B_2, is located in a certain slot. When the attraction between the proteins is to weak, the nucleation process needs a too long time and for an interaction which is too strong, multiple nucleation processes take place which leads to irregular and arrested assembly of proteins. Not only the correct interaction strength but also the location of the sample plays an important role. Vliegenthart and Lekkerkerker [9] suggested that crystallization takes place in two different regions of the phase diagram: First, close to

the critical point of the metastable LLPS. Simulations at this point found that critical fluctuations lead to an enhanced nucleation rate [3]. Second, close to the LLPS binodal, small dense droplets act as regions with increased nucleation rates [6, 120, 121]. The enhanced nucleation in the two mentioned areas of the phase diagram was experimentally observed [68, 122, 123].

In both described conditions, a two-step crystallization process takes place where in a first step a dense precursor is formed in the solution which then reorders in to a structured crystal nucleus [124]. The classical nucleation theory, CNT, describes the so called one-step crystallisation process. In this theory, the two order parameters structure and density are coupled and the (Gibbs) free energy cost, ΔG, for the formation of a nucleus with radius r can be described as:

$$\Delta G = \frac{4}{3}\pi\rho\Delta\mu r^3 + 4\pi\gamma r^2 \tag{2.1}$$

where ρ is the number density of the crystal, γ is the crystal-liquid interfacial free energy, and $\Delta\mu = \mu_c - \mu_l$ is the difference in chemical potential of the crystal and the liquid. From the first term it is visible that the crystal phase is more stable compared to the liquid phase because of the negative sign of $\Delta\mu$. The second term plays against the formation of a crystal because of the positive sign which shows that the formation of a crystal-liquid interface costs free energy [8, 125]. Applying the CNT to more complex systems, such as protein systems, has proven to be defective [125–127]. In more complex systems, often a two-step crystallization process can be observed which can be described by the separation of both order parameters. It was observed that not only the dense liquid after a LLPS acts as precursor for the crystallization, but also protein clusters might represent precursor structures [128]. It should be mentioned that the two-step process was not only observed in protein and colloidal systems, but also in systems of small molecules [127, 129–131].

2.3.4 Arrested phases: gels and amorphous aggregates

The observed phase behavior of a system depends not only on the equilibrium properties but also on the kinetic pathways. Because of the differing kinetics of phase transitions, a metastable LLPS with respect to the solid phase can be observed. Additional to the LLPS, a kinetical arrested state, such as gels and glasses, also occurs in colloidal systems with short-range attractions [98, 132, 133]. Within the liquid-gel phase transition the subunits of the systems form a macroscopical network in which the liquid is trapped. Through this network formation the system becomes viscoelastic which means that the systems shows the material characteristics of a solid but with a non-zero shear modulus [134]. In a glass transition the system is still a liquid but with very slow dynamics. Normally the formation of this phase is possible for high densities and low temperatures [135]. For systems with a strong attractive interactions each proteins bind to fast to his neighbours to undergo an ordering process. In this case the proteins sticks together in an unordered structure which leads to amorphous aggregates. Gibaud and Schurtenberger found that gelation in a protein system takes place due to an arrested metastable

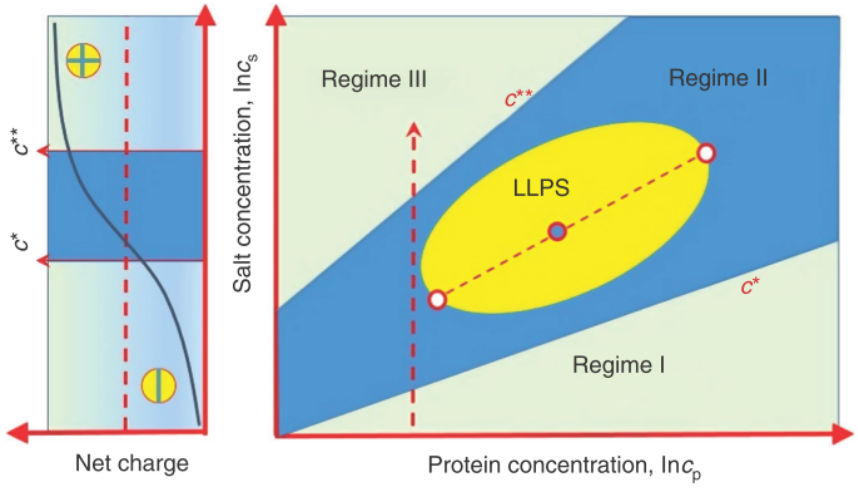

Figure 2.2: Scheme for the phase behavior of protein solutions in the presence of trivalent ions. The different regimes of the RC phase behavior are separated by the two critical salt concentrations c^* and c^{**}. Inside of regime II an LLPS occurs in a closed area shown by the yellow ellipsoid. A pair of phase separated solution is connected by the so called "tie-line" (dashed line). In the left panel, the charge state of the protein along the dashed arrow is shown. From this panel it is visible that the protein undergoes a charge inversion. The figure was taken from Ref. [62]

.

LLPS [60]. Another way for the gelation due to the formation of cluster was found by several other studies [109, 136, 137]. The appearance of an arrested metastable LLPS might represent the reason that crystals cannot form at high attraction strength [138].

2.3.5 Reentrant condensation by multivalent salts

A protein solution with no or a small amount of trivalent salt looks clear. At this stage the sample is located in regime I. Increasing the salt concentration over time leads to a first critical point, c^* where the solution becomes turbid and enters the regime II or "condensed regime", shown in Fig. 2.2. A further increase of the salt concentration leads to a second critical point, c^{**}, where the solution becomes clear again and the solutions enter the "reentrant regime". This phase behavior is already known for multicomponent liquid mixture systems [139]. Typical examples for a RC are systems of polyelectrolytes and DNA in the presence of multivalent counterions [42, 44, 46, 140–153]. For a protein system, this effect was discovered the first time in a BSA solution by adding YCl_3 by Zhang et al. [10].

The physical reason behind the RC phase behavior is the charge inversion of the proteins [10, 47, 62]. For a solution of negatively charged protein at neutral pH (pI < 7) without any salt, a Coulombic repulsion dominates the system. By adding salt into the solution the cation can condensate to the surface groups of the protein, mainly to the aspartic and glutamic acids. Through this condensation, the surface charge of the

protein becomes first less negative and the Coulombic repulsion becomes less important. At the c^* boundary the short-range attraction interaction (van der Waals) and short-ranged Coulombic attraction becomes dominating and the proteins start to aggregate. Through this aggregation the solution becomes turbid. A further increase of the salt concentration leads first to a zero net charge of the protein before the charges inverted to a positive net charge, the charge inversion. When the positive net charge becomes large enough the Coulombic repulsion starts to dominate again the interactions through which the clusters start to dissolve and the solution becomes clear again, which shows that the solution enters the "reentrant regime" . The behavior of the net charge is shown in the left panel of Fig. 2.2.

In principle it is possible that by binding of trivalent ions to the protein surface the native structure of the protein changes. A change of the native protein structure can also explain the aggregation, which is responsible for the turbid solution in the condensed regime. Spectroscopic experiments, fourier transformed infra-red (FTIR) and circular dichroism (CD), shows no change of the amide I and amide II band in the case of FTIR and no change in the range of 200 nm - 250 nm in the CD spectra. These two techniques show that the secondary structure of the protein is preserved in the presence of multivalent metal ions, indicating that the native structure of the protein is not changed [47, 154].

It should be mentioned that the RC behavior is not only restricted to BSA in the presence of YCl_3. The RC behavior is also observed for other negatively charged proteins at neutral pH such as HSA, β-lactoglobulin (BLG) and ovalbumin (OVA). It is also possible to use other trivalent salts such as lanthanum chloride ($LaCl_3$), iron chloride ($FeCl_3$) and aluminium chloride ($AlCl_3$) to induce the RC behavior [47]. For the used salts with a higher valency no RC is observed. For spermidine chloride ($SpeCl_4$), which is quite successful to introduce RC to DNA solutions, no RC in protein solutions can be observed. Zhang et al. [47] argues that the charge density of the spermidine is quite small and that for this reason spermidine acts as a monovalent salt for proteins. For another salt with higher valency hafnium chloride ($HfCl_4$), the influence on the pH in a solution is strong. For such salts only very small amount of salt is enough to bring the pH of the solution below the isoelectric point.

2.3.6 Phase behavior induced by multivalent salt

In principal all of the presented phase behavior can be induced by multivalent ions. As already shown the reentrant condensation of globular proteins was found by Zhang [10]. Further studies shown that the formation of clusters starts close to the c^* boundary. Inside the second regime the cluster sizes becomes big enough to scatter light and to observe these clusters by optical microscopy. Inside the reentrant regime the cluster size decreases again but the clusters are not dissolved again [155]. The formation of an LLPS in a human serum albumin solution is described theoretical by a patchy model [59]. The formation of liquid droplets and clusters and their role in the crystallization process of BLG is also investigated by Zhang [118]. As far as we know the formation of an arrested protein state by multivalent ion is not observed until now but as presented in

Sec. 2.3.4 the formation of an arrested state in a protein solution is possible. From the observation of the discussed phase behaviors in protein solutions induced by multivalent ions arises the following questions which will be discussed in this thesis? Can we observe all mentioned phase behavior in a serum albumin system with yttrium chloride? What is the difference in effective interactions between the different phases? How can the structure of the dense protein phase after phase separation can be described? Is it possible to influence the phase behavior by varying the solvent? Is the LLPS metastable against the mixed stated or the crystal state? What kind of crystallization process occurs in the system?

2.4 Theoretical background of phase transitions

Almost all phase transitions include a transition from a more ordered phase into a more disordered phase. A phase transition reflects the change of an order parameter, such as the density ρ. The change of this order parameter depends on the change of the entropy and energy inside the phase transition. Assuming a constant volume of the sample the entropy is connected to the energy via the Helmholtz free energy F defined by [134]:

$$F = U - TS \tag{2.2}$$

where U is the internal energy and S the entropy.

The goal of this section is to introduce simple models which describe a phase separation. The first model describes the ideal case of an one component system, which is in the most cases not fulfilled, Sec. 2.4.1. The theoretical calculations of a phase separation in a multicomponent system is shown in Sec. 2.4.2 where the simplest case of a binary system is presented. For system with more than 2 types of molecules the same calculations can in principle be performed but it becomes more complicated.

2.4.1 Single component system

Three macroscopic thermodynamic properties describes the physical state of a phase, pressure p, volume V and temperature T. For an ideal gas the equation of state is given by [156]:

$$pV = cN_A k_b T = \rho RT \tag{2.3}$$

where c is the number of moles of particles of the concentration, N_A is the avogadro number, k_b the Boltzmann constant and R the gas constant. According to Eq. 2.3 the ideal gas can never undergo a phase transition. Undergoing a phase transition means a lost of entropy for the system which has to be compensated by the gain in interaction energy, shown in Eq. 2.2. For an ideal system with non-interacting parameter this gain of interaction energy is not possible.

In order to describe the condensation of a liquid the van der Waals gas is introduced by adding two non-idealities: a volume which a particle occupies and an inter-particle

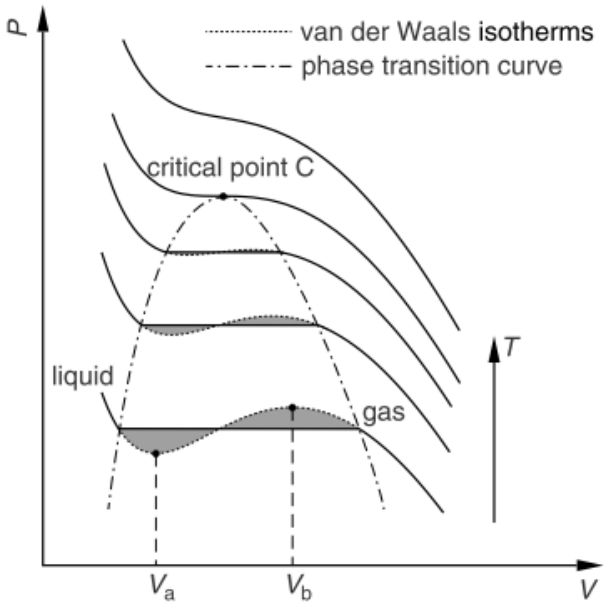

Figure 2.3: Set of van der Waals isotherms at different T in a p-V plot in the region near the critical point (C). The integration of the van der Waals isotherm over the volume with in the phase transition curve (dashed dotted line) must be equal to zero, since the areas above and below the horizontal lines are equal with opposite signs. The phase transition curve is given by the horizontal line which goes through the inflection point and their edge are located on the van der Waals isothermal. The figure was taken from Ref. [156].

interaction term. With this expansion Eq. 2.3 can be written [156]:

$$\left[p + \left(\frac{N}{V}\right)^2 a\right](V - Nb) = cN_A k_b T \tag{2.4}$$

where the inter-particle interaction is generated by an internal pressure expressed as $(N/V)^2 a$ where a is a proportionality constant. For a small interaction part this equations is close to the ideal gas. For a non negligible inter-particle interaction a phase separation can occur. Plotting Eq. 2.4 at constant T leads to isotherms shown in Fig. 2.3 for different T.

For isotherms with a temperature above the critical temperature no phase separation takes place. Decreasing T to the critical temperature, T_C, leads to an isotherm where a singularity appears. At this singularity the first and second derivatives of p with respect to V at constant T are equal to 0 [156]:

$$\left(\frac{\partial p}{\partial V}\right)_T = 0 \text{ and } \left(\frac{\partial^2 p}{\partial V^2}\right)_T = 0. \tag{2.5}$$

For $T < T_C$ the isotherm shows a local minimum and maximum, with the volume V_a

and V_b (dashed lines in Fig. 2.3). Between these two dashed line $(\partial p/\partial V)_t$ becomes positive. The compressibility, χ_T, is defined as $\chi_T = -(\partial V/\partial p)_T/V$ and becomes negative within this region. Therefore, the van der Waals equation, Eq. 2.4, predicts that with increasing V, p also increases, which is unphysical and the system is unstable. Within this unstable region a small fluctuation is enough to achieve a phase separation. Within this phase separation the system separates into a gas, low concentration, and a liquid, high concentration, phase. The concentrations of both phases are determined by the Maxwell construction which is given by a horizontal lines which connects the gas and liquid phase on the isotherm. The horizontal line is given by the fact that the integral of the isothermal with respect to the horizontal line becomes 0. The volume of the gas and liquid phases for different $T$are shown by the dashed dotted line in Fig. 2.3, which is also called "binodal" line. Connecting all points of the minima and maxima leads to also to a curve with a similar shape as the binodal line and is called the "spinodal" line. The spinodal line indicate the unstable region.

The van der Waals equation was the first attempt to describe a phase separation with a mean-field approach. The van der Waals gas is an easy way to describe a phase separation but the reality is much more complicated.

For an ideal solution the Morse equation instead of the van der Waals equation must be used [157]:

$$\Pi = iMRT, \tag{2.6}$$

where Π ist the osmotic pressure, i the dimensionless van't Hoff factor, and M the molarity. Comparing the Morse equation with the van der Waals equation reveal the similar behavior of both equations. Both equation show that a pressure is equal to a system constant times RT. With this similarity a solution can also be discussed in the sense of a gas. For a protein-salt mixture it is often possible to focus on the behavior of the largest particle, the protein, in the system. This can be done in a rigorous way by mapping the Hamilton of the mixture onto that of an effective one-component system [158–160] by integrating out the degree of freedom of the background. The interactions in this system are changed from the bare interaction between all possible species combinations, i.e. protein-water, protein-ion, etc., to effective interactions between the protein. A spherical symmetric interaction potential is assumed.

As already shown, the system loses entropy by undergoing a LLPS into a low density fluid phase and a high density fluid phase. This loses in entropy must be compensated by the gain of interaction energy which is only possible if a sufficiently strong attractive tail in addition to the repulsion at very short distances exist in the system. The effective second virial coefficient B_2 is a conventional way to measure the strength of attraction in the system.. For the assumed spherical interaction potential B_2 is defined by

$$B_2(T) = 2\pi \int_0^\infty r^2 \left[1 - \exp\left(-\beta V_{eff}(r)\right)\right] dr. \tag{2.7}$$

Positive values indicate a repulsive effective interaction and negative values an attractive effective interaction. Collecting different experimental results Vliegenthart and

Lekkerkerker found that the B_2 for the critical point for different system seem universal [9]:

$$\frac{B_2}{B_2^{HS}} \approx -1.5, \tag{2.8}$$

where $B_2^{HS} = 16\pi r_{HS}^3/3$ is the second virial coefficient of a hard sphere with radius r_{HS}. Noro and Frenkel confirmed this observation [161] and it was tested for hard-sphere mixtures [162] using the depletion potential [159].

In order to understand the origin of the observation by Vliegenthart and Lekkerkerker we have a closer look onto the phase coexistence between the low density gas (ρ_I) and the high density liquid (ρ_{II}) phase. The two phases can coexistence at the same T if they are in mechanical and chemical equilibrium, i.e.

$$p(\rho_I) = p(\rho_{II}) \text{ and } \mu(\rho_I) = \mu(\rho_{II}) \tag{2.9}$$

where p is the pressure and μ the chemical potential of the system under consideration. The pressure in a low density phase is low and to achieve a mechanical equilibrium between the phases the pressure in the high density phase must be equal to the low density phase. At coexistence the pressure can be expand into a virial series with only few terms. The most prominent contribution in this virial series is the the second virial coefficient [160]:

$$\beta p(\rho) \approx \rho + B_2\rho^2 + B_3\rho^3 + ... \tag{2.10}$$

The pressure of a high density phase can only be equally low to the low density phase if the attraction is sufficiently strong.

The location of the critical point ρ_c and T_c, which is the onset of a fluid-fluid phase separation which is reflected by the onset of a van der Waals loop in the pressure, follows from [160]

$$\left.\frac{\partial p(\rho)}{\partial \rho}\right|_{\rho=\rho_c} = 0 = \left.\frac{\partial^2 p(\rho)}{\partial \rho^2}\right|_{\rho=\rho_c}. \tag{2.11}$$

The vanishing of the first derivative of p w.r.t. to ρ expresses also the vanishing of the inverse compressibility or the bulk modulus. For $q \to 0$ the structure factor $S(q \to 0 = k_b T \rho \chi_T)$ is proportional to the compressibility, χ_T and with a vanishing inverse compressibility $S(q)$ diverges for $q \to 0$ at the critical point or the spinodal line. In the condition of coexisting phases, i.e. on the binodal line, the system is close to the spinodal line, which implies that the compressibility and hence $S(q \to 0)$ is large, but do not diverge. Close to the critical point the binodal the location of the binodal is closer to the spinodal as far away of the critical point. Therefore also $S(q \to 0)$ increases if the system comes close to the critical point. The result of B_2 at the critical point can be calculated by combining Eqs. 2.10 and 2.11. One finds that

$$\frac{B_2}{B_2^{HS}} \approx -\frac{1}{4\eta_c} \approx -2.06 \tag{2.12}$$

where the value of the critical packing fraction, η_c, due to Baxter [163] (Eq. 4.5), which is introduced in Sec. 3.5.3.3, was inserted. Clearly their is no perfect agreement between the results of Eqs. 2.8 and 2.12, this simple argument, based on the mechanical stability, helps to rationalize the origin of the B_2 criterion. Note that the B_2 at the critical point changes for other estimations of the critical packing fraction η_c.

2.4.2 Two component system

In contrast to a single component system, where all molecules are chemical identical and all inter molecular interaction are equal, the interactions in a multi-component system arise from the different types of molecules, which are also chemical different. The theoretical considerations of such a two component system is based on [134]. Assume a binary system of two liquids which are miscible in all proportions at high T. Lowering T can lead to a separation into two distinct phases. Using this system with the help of a model called "regular solution model", which is based on mean field assumptions, our aim is to predict the free energy of mixing. In the assumed system we have two liquids, A and B, with the corresponding volume fractions of Φ_A and $\Phi_B = 1 - \Phi_A$ in the unmixed phase. The free energy for the unmixed phase can be written as $F = F_A + F_B$. When both phases are mixed together the free energy for the mixed phase is given as $F = F_{A+B}$. If we mixed both liquids the system can stay in the phase separated or mixed state and the free energy of this mixture system can be written as [134]:

$$F_{mix} = F_{A+B} - (F_A + F_B)\,. \tag{2.13}$$

This equation shows that the mixed and phase separated states are in competition to each other. If the free energy of the phase separated state is higher the mixture phase separates, otherwise the system stays in the mixed state.

As we know from Eq. 2.2 the free energy of the mixed state is given by the entropy, S_{mix}, and the change of energy on the mixed state, U_{mix}. Imagine a lattice on which the different molecules A and B are arranged, with the knowledge that in a liquid the lattice is not a regular crystalline one. On this lattice each molecule has z other molecules as nearest neighbors. The composition of the molecules inside the mixture can be expressed by Φ_A or Φ_B, with the simplification that $\Phi_A + \Phi_B = 1$ is the total volume and that the volume of a single molecule A is equal to volume of a single molecule B. Clearly we cannot say if a specific side of a molecule is occupied by molecule A or B. With this uncertainty we can use the Boltzmann formula to write down the entropy of the mixture for a binary system as [134]

$$S_{mix} = -k_B \left(\Phi_A \ln \Phi_A + \Phi_B \ln \Phi_B\right), \tag{2.14}$$

where the probability that a specific side is occupied by a molecule A or B is given by their volume fractions. For this we assumed that if a side is occupied by a molecule B it is more or less likely that a neighboring side is similarly occupied. If Φ_A or Φ_B is one, S_{mix} becomes zero, as expected for a pure liquid. To get the internal energy of the mixture, U_{mix}, we assume that each molecule interacts only with its direct neigh-

bors in a way that is pairwise additive. For the interaction energies we assume that the interaction between two neighboring A molecules given as ϵ_{AA}, between two neighboring B molecules ϵ_{BB} and between a A molecule and a neighboring B molecules ϵ_{AB}. We use the mean field assumption that a given side has $z\Phi_A$ A neighbors and $z\Phi_B$ B neighbors. With this assumption the interaction energy per site can be written as [134] $(z/2)\left(\Phi_A^2\epsilon_{AA} + \Phi_B^2\epsilon_{BB} + 2\Phi_A\Phi_B\epsilon_{AB}\right)$. Subtracting the energy of the unmixed state, $(z/2)\left(\Phi_A\epsilon_{AA} + \Phi_B\epsilon_{BB}\right)$, leads to the energy of the mixing [134]:

$$U_{mix} = \frac{z}{2}\left[\left(\Phi_A^2 - \Phi_A\right)\epsilon_{AA} + \left(\Phi_B^2 - \Phi_B\right)\epsilon_{BB} + 2\Phi_A\Phi_B\epsilon_{AB}\right]. \tag{2.15}$$

Assuming an incompressible sample, $\Phi_A + \Phi_B = 1$, the strength of the interaction between A and B relative to their self-interactions can be described by a dimensionless parameter χ, which can be written as [134]:

$$\chi = \frac{z}{2k_BT}\left(2\epsilon_{AB} - \epsilon_{AA} - \epsilon_{BB}\right). \tag{2.16}$$

Thus χ is the energy change when a molecule A is taken away from a pure A environment and placed into an environment of pure B. With this, Eq. 2.15 can be simplified to [134]:

$$U_{mix} = \chi\Phi_A\Phi_B. \tag{2.17}$$

Using Eq. 2.2 with Eq. 2.13, Eq. 2.14 and Eq. 2.17 leads to [134]:

$$\frac{F_{mix}}{k_BT} = \Phi_A \ln\Phi_A + \Phi_B \ln\Phi_B + \chi\Phi_A\Phi_B. \tag{2.18}$$

The behavior of this equation for the free energy of the mixing is presented in Fig. 2.4. For $\chi < 2$ a single minimum occurs at $\Phi_A = \Phi_B = 0.5$. The resulting curves show a concave shape from which it is visible that each phase separation into two pairs of volume fractions leads to an increased free energy compared to the starting position, so the mixture is stable.

Two minima and a single local maximum located at $\Phi_A = \Phi_B = 0.5$ appear for values of $\chi > 2$. In this case a part of the free energy curve shows a convex behavior, around the single maximum. For such a convex behavior it is possible to find a starting point of phase separation which shows an higher free energy compared to the phase separated one, so the mixture is unstable and will phase separate. If the phase separated volume fractions are not located in the two minima each separated phase falls down the free energy curve until a local minima is reached. The minima are shown by the black boxes in Fig. 2.4. An increase of the attractive strength, higher χ-values, leads to a shift of the coexisting volume fractions of the phase separation away from the local maximum. The coexistence curve or the binodal connects the volume fractions of the separated phases at different interaction strengths and is plotted as a violet short dashed dotted line in Fig. 2.4.

The curvature of the free energy curve, $\partial^2 F/\partial\Phi^2$, can be positive of negative. For negative values the free energy of the system is decreasing by small fluctuation which

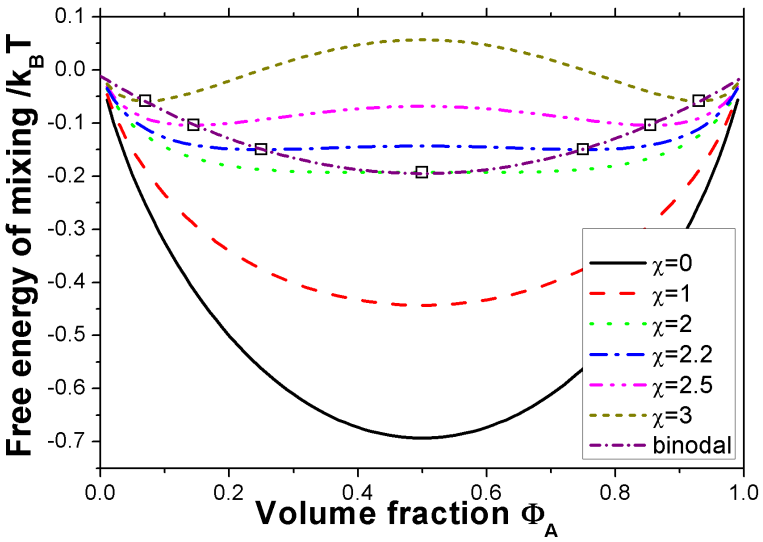

Figure 2.4: The free energy of mixing per side divided by k_BT as a function of composition is plotted for different interaction parameters χ. For the volume fraction it was assumed that the solutions are incompressible, $\Phi_A + \Phi_B = 1$

leads to a phase separation. A positive value of the curvature means that through a small fluctuation of the system the free energy of the system would be increased. This means that this new free energy is unstable compared to the starting point and the system returns to the starting point. In this case the system is at least locally stable. If the system is locally stable a bigger fluctuation can overcome an energy barrier and the system can reach another local minimum with a reduced free energy or the global minimum and the system phase separates. For a curvature value of 0 the system reaches the limit of local stability and the locus of these points is known as the spinodal. The critical point of the system is defined by $\partial^3 F/\partial\Phi^3 = 0$ additional to a curvature of 0, and it is the point where the binodal and spinodal of a system meet. In total we can summarize the behavior to:

$$f(x) = \begin{cases} \dfrac{\partial^2 F}{\partial \Phi^2} > 0 & \text{locally stable} \\ \dfrac{\partial^2 F}{\partial \Phi^2} = 0 & \text{spinodal} \\ \dfrac{\partial^2 F}{\partial \Phi^2} < 0 & \text{phase separation} \\ \dfrac{\partial^2 F}{\partial \Phi^2} = 0 \text{ and } \dfrac{\partial^3 F}{\partial \Phi^3} = 0 & \text{critical point} \end{cases} \tag{2.19}$$

The phase diagram of a mixture can now be calculated with the knowledge of the relationship between the shape of the free energy of mixing curve as a function of composition and Eq. 2.18. A very useful simplification comes from the symmetric behavior of the system around $\Phi = 0.5$; in this case the coexistence curve is given by $dF/d\Phi = 0$

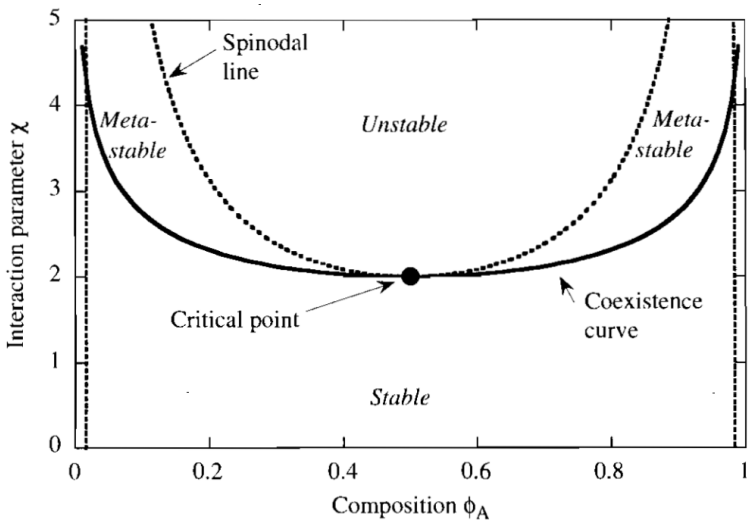

Figure 2.5: Phase diagram of a liquid mixture whose free energy of mixing is described by the regular solution model. The figure is taken from Ref. [134]

which is not in general true, because the coexistence curve is defined by the condition of equal chemical potentials. The resulting phase diagram is plotted in Fig. 2.5.

In the simplest model of the interaction parameter the interactions, ϵ_{AA}, ϵ_{AB} and ϵ_{BB}, were regarded as being purely energetic. In this case the interactions are independent from T and the interaction parameter must vary with $1/T$. In this simple model an UCST behavior is found and the system phase separates at low T and stays in a mixture at higher T. Including specific interactions, such as hydrogen bonds and van der Waals forces, χ becomes much more complicated and cannot be explained by purely energetic interaction alone. In this case also entropic components must be included. In these cases the T dependent behavior of χ becomes much more complicated.

In this section we show two different ways to describe our system. The picture of the effective one-component system is used in literature for the description of B_2 and for applying colloidal models for protein systems. In this thesis we used the effective one-component system for the calculation of the second virial coefficient. In contrast to the one-component system the model of the two-component component system is used for polymer models in literature. We used this two-component model for the calculation of the attractive interaction between the protein and the yttrium ion from the tie-lines, shown in Sec. 4.2.3.3.

2.5 Outline

The focus of this thesis is placed on several scientific questions. Where in the phase diagram an LLPS can be occur? What we can learn from the resulting phase diagram on the protein-cation interaction? A part of the focus is placed on the effective interaction

in the LLPS region and how it can be influenced in order to achieve a deeper understanding of the system. The dense protein phase show an interesting optical behavior with varying temperature. How can this behavior described by the structural variations of the dense protein phase an the resulting effective interactions? Changing the solvent leads to the vanishing of the LLPS region. How can this vanishing of the LLPS region can be described? From literature it is known that more high quality crystals can be observed when an LLPS occurs before or inside the crystallization process. Can we induce crystallization of the used proteins by adding a trivalent salt? Is their a change in the crystal structure when the crystals grows from different regions in the phase diagram? The in this thesis presented experiments and discussions are based on these scientific questions.

In the following an outline of the structure of this thesis is given. In Ch. 3 the used materials, experimental techniques and the analysing procedure of experimental data is introduced. The experimental results are presented in Ch. 4. The result chapter is divided into five sections where each describes another aspect of this thesis.

In the first two sections (Sec. 4.1 and Sec. 4.2) the phase behavior of a serum albumin solution is investigated and related to the effective interaction in the second regime, determined by the second virial coefficient. In the first step the monodispersity of the protein solution is investigated by different experimental methods, from which we found that a part of the BSA monomers forms dimers in solution as opposed to HSA is always a monomer in solution. The LLPS phase boundaries are investigated using optical microscopy and with the help of UV-Vis and X-ray absorption the protein and salt concentrations at the binodal line are determined. The partitioning into a dilute and dense protein phase is shown by the so called tie-lines from which the attraction strength between the protein and the multivalent metal ion is calculated. The effective interaction strength between the proteins is measured by the second virial coefficient inside and outside of the LLPS region and the influence of the temperature is monitored.

The temperature-dependent morphology and phase behavior of the dense protein phase is the main focus of the second section, Sec. 4.4. In a first step the morphology of the denser protein phase is determined by eye and by microscopy. The temperature-dependent structure of the dense protein phase is measured by small angle scattering techniques and the effective attractive potential is estimated by fitting the scattering curves.

The importance of the solvent is shown by the stepwise change of normal water to heavy water in Sec. 4.5. The phase diagram for different volume fractions of D_2O is determined by eye and by optical microscopy. Interestingly no LLPS is observed for solutions with a high D_2O volume fraction. The structural changes by varying the water volume fraction are recorded by small angle scattering experiments from which the effective potential between the proteins is calculated by fitting the scattering data.

The time dependent stability and the crystallization of the protein solution is analyzed in Sec. 4.6. The growth of crystals is confirmed by optical microscopy. These microscopy observations only reveal the formation of HSA crystals, while until now no BSA crystals could be seen. Structure analysis of the small angle scattering data with an unpublished HSA crystal structure explains the observed Bragg peaks.

Finally the development of a sample holder in order to combine light spectroscopic and neutron scattering experiments is discussed in the fifth section, Sec. 4.7. The ideas behind the several development steps and the results obtained from first test measurements are explained.

After presenting the result part of this thesis a general conclusion is shown Ch. 5. An outlook for further work is given in Ch. 6. An appendix, Ch. 7 is following the outlook chapter where several tabular and blue prints from the result part, Ch. 4 can be found.

3 Materials and methods

3.1 Serum albumins and yttrium chloride

This thesis is based on experiments performed with two proteins, bovine (BSA) and human (HSA) serum albumin. Serum albumins are components of mammal blood. The serum albumins are synthesized in the liver of the corresponding mammal. In the case of humans the typical concentration of serum albumin in the blood is 50 g/l [164]. Serum albumins have the advantage that they are easily commercially available and the purification is not difficult. Another advantage of serum albumins is that they do not affect the properties of enzymes. This is the reason that especially BSA is used as a standard protein to investigate protein systems [10, 165–173]. The serum albumins carry out several functions in the organism, such the transport of drugs, metabolites and hormones, the binding of calcium and maintaining oncotic pressure and pH. As all proteins, serum albumins are built up from 20 different types of amino acids. The alignment of these amino acids is called its primary structure. The 3 dimensional orientation of the primary structure is known as the secondary structure. It has been found that the secondary structure of BSA is mainly helical [11, 12]. The secondary structures of the used serum albumins, BSA [12] and HSA [174], are shown in Fig. 3.1. Both used serum albumins, BSA and HSA are quite similar. The molecular weights of both proteins are similar, 65.752 kDa (BSA) to 66.472 kDa (HSA). The numbers of amino acids are nearly identical too, with 583 residues (BSA) and 585 resdiues (HSA). The pI value shows at which pH the surface charge of the protein is neutral. Both proteins have a pI of 4.6 [47].

In order to change the surface charge of the protein, yttrium chloride (YCl_3) is used in this study. Using this salt has several advantages for the used system. The surface charge of the protein can be inverted by adding enough multivalent salt into the solution. Normally such a multivalent salt shows a strong effect onto the pH of the solution. To avoid the influence of varying pH onto the sample buffers can be used. These buffers contain salts which lead to additional interactions between the proteins and the salt from the buffer [175]. The biggest advantage of YCl_3 is that the pH remains almost constant over a broad range of yttrium concentration in the solution. This effect leads to the advantage that no buffer need to be used in the system and a tertiary system of protein, salt and water can be achieved.

Both proteins, BSA (with the product number A3059) and HSA (A9511), and YCl_3 (451963) were purchased from Sigma-Aldrich, St. Louis, USA. The protein and YCl_3 powders are dissolved in deionized (18.2 MΩ) and degassed Milli-Q water to prepare stock solutions. Removing the CO_2 content from the Milli-Q water by degassing leads to a neutral pH of the used water. Each sample is prepared by diluting the protein

stock solution with water until the desired protein concentration is reached. The desired amount of salt is then added to the diluted protein solution.

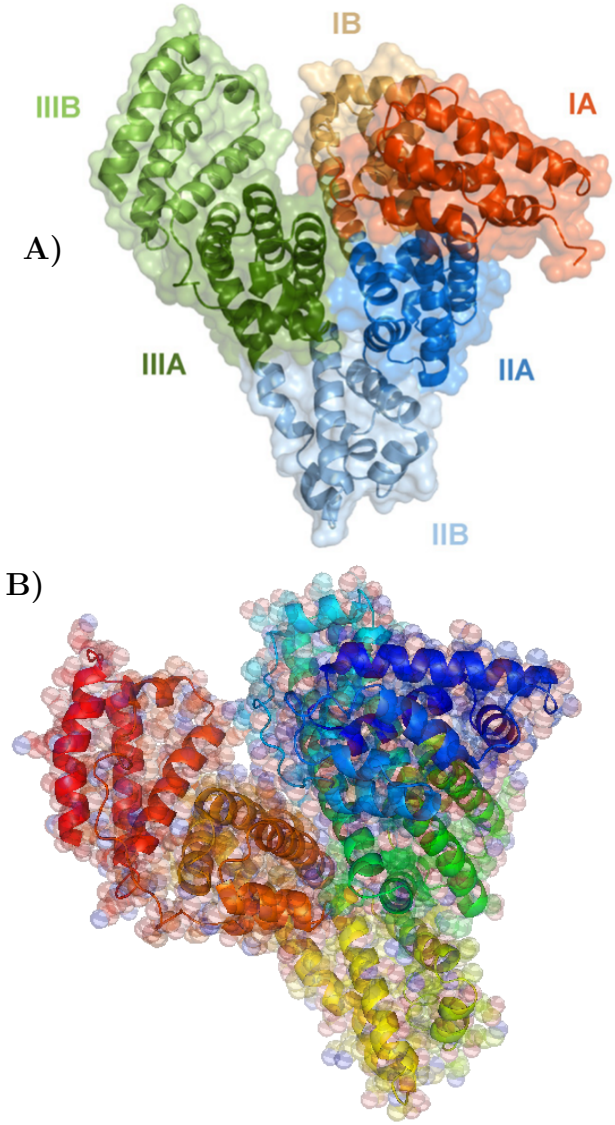

Figure 3.1: Published crystal structures of BSA and HSA. A) The BSA crystal structure (PDB code 3V03) is shown. In B) the HSA crystal structure with the PDB code 1AO6 is shown. The picture of the HSA crystal structure is modified by changing the color code of the different subparts from the secondary structure and by adding spheres for the different size chains of the amino acids compared to the original publication.

3.2 UV-Vis absorption

UV-Vis absorption is used in this thesis to obtain the protein concentration of the stock solutions and the phase separated samples. The absorption of a sample is connected to the intensity of the light beam before (I_0) and after it passed the sample (I) by the Lambert-Beer law [176]:

$$A = -log_{10}\left(\frac{I}{I_0}\right) = \epsilon\, c\, l \tag{3.1}$$

where ϵ is the molar extinction coefficient with the units [$\mathrm{L\,mol^{-1}\,cm^{-1}}$], c is the molar concentration and l is the pathlength in cm.

Amino acids with aromatic side chains exhibit strong UV light absorption. Three different amino acids with such an aromatic side chain are known, tryptophan (Trp) with $\epsilon_{Trp,280} = 5500$ at a wavelength of $\lambda = 280\,\mathrm{nm}$, tyrosine (Tyr) with $\epsilon_{Tyr,280} = 1490$ and phenylalanine (Phe) which absorbs only at wavelengths lower than $\lambda = 280\,\mathrm{nm}$. The disulfide bounds in cystine (Cys) also contribute slightly to the absorbance with an $\epsilon_{Cys,280} = 125$. From this ϵ at a wavelength of $\lambda = 280\,\mathrm{nm}$ can be calculated as [177]:

$$\epsilon_{280} = n_{Trp} \cdot \epsilon_{Trp} + n_{Tyr} \cdot \epsilon_{Tyr} + n_{Cys} \cdot \epsilon_{Cys} \tag{3.2}$$

where n is the number of each residue. In reality deviations from this theoretical ϵ can be observed. For a real system the best absorption coefficient is the empirically determined one. To determine ϵ empirically the absorption of a sample with a well defined protein concentration is measured and ϵ is calculated from the absorption value. Alternatively, the ϵ of many proteins can be found in standard biochemistry and biological handbooks, such as the Handbook of Biochemistry [178] or other publications. Known absolute values have the advantage that no standard is needed.

In literature, two kind of absorption coefficients are found. The first is the already mentioned molar extinction coefficient ϵ_{molar} and the other is the so called percent solution extinction coefficient, which describes the absorption of a solution containing 1 % of protein pathway of 1 cm for the light beam, $E^{1\%}_{1cm}$. The unit for the $E^{1\%}_{1cm}$ is [$\mathrm{g\,dl^{-1}\,cm^{-1}}$]. To get the extinction coefficient in units of [mg/ml], which are normally used in protein solutions, the value $E^{1\%}_{1cm}$ must be multiplied by the constant factor of 10. With this the relationship between ϵ_{molar} and $E^{1\%}_{1cm}$ is given by:

$$\epsilon_{molar} \cdot 10 = E^{1\%}_{1cm} \cdot M_W \tag{3.3}$$

In this thesis the absorbance of the sample is measured with a Varian Cary 50 UV-Vis spectrometer (Agilent Technologies Inc., Santa Clara, California, USA) In order to calculate the protein concentration an $E^{1\%}_{1cm}$ value of 6.67 [178], in the case of BSA, and 5.1 [164], in the case of HSA, is used to calculate the protein concentration, c_p of the sample at a wavelength of $\lambda = 280\,\mathrm{nm}$. The absorbance of the sample cell and the solvent is subtracted from the total absorbance of the sample to extract the absorbance caused by the proteins.

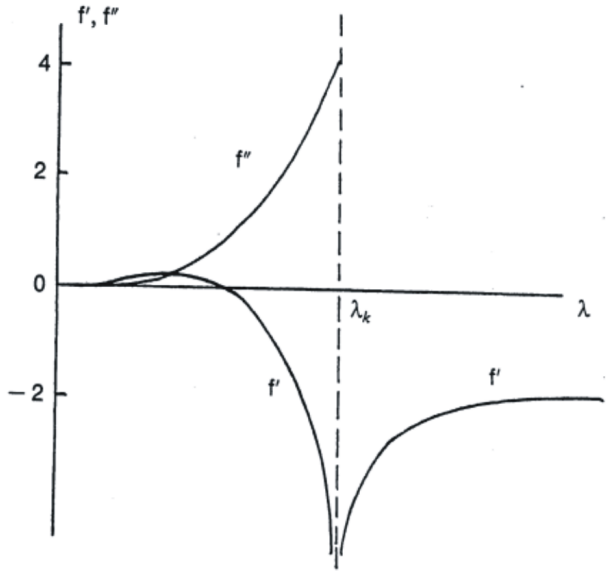

Figure 3.2: Real and imaginary parts of X-ray anomalous scattering factors f' and f'' as a function of the wavelength λ (corresponding to the K_α absorption edge with the wavelength λ_k). The figure was taken from Ref. [179].

3.3 X-ray absorption

Two phenomena contribute to the total absorption of X-rays: the photoelectric absorption and scattering. In the photoelectric absorption process electrons become exited into higher quantum levels. After a short time the excited electron falls back to the ground state. A photoelectron with an energy corresponding to the difference in energy between the ground and exited state is emitted. This process leads to a flat fluorescence background in the scattering curve. With the wavelength of X-rays scattering and for low molecular mass elements the photoelectric absorption dominates the total absorption of the sample. For photon energies far away from the absorption edges of the irradiated materials the fluorescence intensity is wavelength independent. If the energy of the incident radiation is close to the absorption edge this changes and the absorption depends strongly on the wavelength. In general the X-ray scattering factor can be written as a complex function [180]:

$$f(\lambda) = f_0 + f'(\lambda) + if''(\lambda) \tag{3.4}$$

at small scattering wavelengths $f_0 = Z$, whereas the corrections $f'(\lambda)$ and $f''(\lambda)$ become significant close to the absorption edge. The real and imaginary part of the X-ray scattering factors f' and f'' are plotted in Fig. 3.2 as a function of λ. The figure corresponds to the K_α absorption edge. In the case of Y^{3+} ions the K_{alpha}-absorption edge is around 17.038 keV [181]. In principle also the different L-absorption edges of heavier atoms can be used for this technique. This is also the principle of anomalous small angle X-ray scattering, where structural information of the salt ions can be determined.

In this study the energy dependent absorption is used for the measurement of the real salt concentration in the sample. To follow the wavelength dependent fluorescence the fluorescence at high-q-values is determined at three different energies, far away from (16.038 keV), close to (17.032 keV) and at the absorption edge (17.038 keV). The real energies for the absorption edge deviates through a small instrumental shift in energy from the literature value. For this reason the correct energy for the absorption edge has to be measured before the experiment. The fluorescence level is determined by subtracting the different fluorescence intensities at different energies. This level is calibrated at different energies to pure salt solutions at different concentration. A linear behavior of the fluorescence level at different energies with increasing salt concentration is found. By comparison of the fluorescence level from the sample with the level of the calibration the real salt concentration in the sample is observed.

3.4 Size exclusion chromatography

This section is based on the book "Principles of Biochemistry" by Nelson & Cox [182]. SEC is a powerful technique to separate particles of different sizes, or molecular weights. This is used in the purification process of proteins. SEC can also be used to identify the sizes of particles in solution and their corresponding molecular weight. The column is filled with porous beads of a particular material with engineered cavities of a certain size (stationary phase) and a buffer (the mobile phase), which percolates through the beads. The protein solution is loaded onto the top of the column. Bigger proteins will travel through the column faster than the smaller ones. This counterintuitive behavior can be explained by the fact that the bigger proteins cannot enter the cavities and so take a shorter part through the column. At the bottom of the column the buffer and the proteins are separated into different fractions, depending on the time they need to travel through the column. The amount of protein in this fractions is monitored by UV absorption ($\lambda = 280\,\mathrm{nm}$).

3.5 Scattering

In this thesis different kind of scattering techniques are used. In the beginning of this section (Sec. 3.5.1) an overview of the principal small angle scattering concept is given. The principal concepts can also be used for other scattering techniques but the notation is based on the small angle technique. After the introduction of the principal concept the scattering differences between different radiation sources is explained in Sec. 3.5.2. In Sec. 3.5.3 different methods for the analysis of the scattering data are shown. In the next step the small angle scattering protocol is introduced in Sec. 3.5.4 before the experimental setup for the different small angle scattering experiments is presented (Sec. 3.5.5). In the last part of this section (Sec. 3.5.6 different light scattering techniques are introduced.

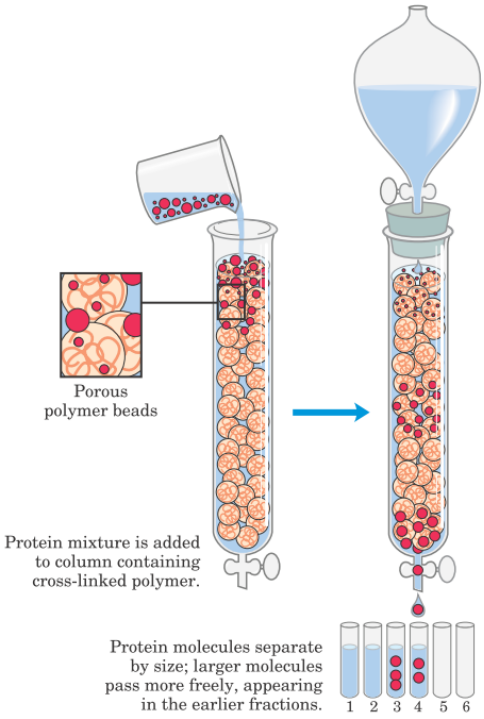

Figure 3.3: Size-exclusion chromatography, also called gel filtration, separates proteins according to size. The column matrix is a cross-linked polymer with pores of selected size. Larger proteins migrate faster than smaller ones, because they are too large to enter the pores in the beads and hence take a more direct route through the column. The smaller proteins enter the pores and are slowed by their more labyrinthine path through the column. The figure was taken from Ref. [182].

3.5.1 Principal concept of small angle scattering

If a sample is illuminated with monochromatic plane electro-magnetic waves, such as visible light, X-rays and neutrons, with a wavevector with modulus $k = |\mathbf{k}| = \mathbf{2}\pi/\lambda$, where λ is the wave length, the atoms inside the sample interact with the incident radiation. Each atom inside the illuminated volume becomes excited and radiates spherical waves. In this study only the special case of elastic scattering is considered. This means that the modulus of the scattered wave is the same as from the incident beam, $k' = |\mathbf{k}'| = \mathbf{k}$. This is only the case when no energy transfer takes place in the scattering process. The momentum transfer between the incident and the scattered beam is given by the scattering vector q

$$q = k' - k = \frac{4\pi n}{\lambda} sin\frac{2\theta}{2} \tag{3.5}$$

with n being the refraction index and θ being the scattering angle. For X-ray and neutron scattering the refraction index, $n \approx 1$, is neglected in standard textbooks of

X-ray and neutron scattering, such as [179, 180, 183, 184]. The scattering vector q is shown in a sketch in Fig. 3.4.

For a dilute system, in an ideal case only one particle, the positions of the different particles are not correlated. For the special case of a monodisperse system, only one unique kind of particles is present in the system, in general of inhomogeneous particle density $\rho(r)$, and for a given orientation of the particle the normalized scattering amplitude can be written as [183]:

$$f(q) = \int_{V_{part}} \rho(r) e^{-iqr} dr \tag{3.6}$$

with the volume of a particle V_{part}. Thus the scattering intensity from a particle can be expressed as

$$I_{part} = f(q) f^*(q) = V^2 P(q) \tag{3.7}$$

with

$$P(q) = \frac{1}{V_{part}} \int_{V_{part}} \rho(u) e^{-iqu} du \tag{3.8}$$

being the form factor of the particle. For a real solution, which contains more than one particle, the intensity can be expressed by:

$$I(q) = \Phi \cdot V_{part}^2 P(q) \tag{3.9}$$

with the volume fraction $\Phi = N/V$ and N denoting the number of particles inside the volume V.

Up to this point no description of the scattering strength, or in other words, how strongly a sample scatters, is given. This description is given by the differential cross-section $d\sigma/d\Omega$. $d\sigma/d\Omega$ is defined as the ratio between the scattered energy, $I_e(q)$ [1/unit solid angle · s], and the incident energy which corresponds to the incident intensity, I_0 [1/unit area · s]. The dimension of this ratio corresponds to an area, which is shown in Fig. 3.5. The measured intensity in the detector, $I_{meas}(q)$, is not equal to the scattered intensity because $I_e(q)$ is scattered onto a small area, which grows with increasing distance between the sample and the detector L_2. $I_{meas}(q)$ can be described by the following equation [180]:

$$I_{meas}(q) = \frac{I_e}{L_2^2} = \frac{I_0}{L_2^2} \frac{d\sigma}{d\Omega}(q) \tag{3.10}$$

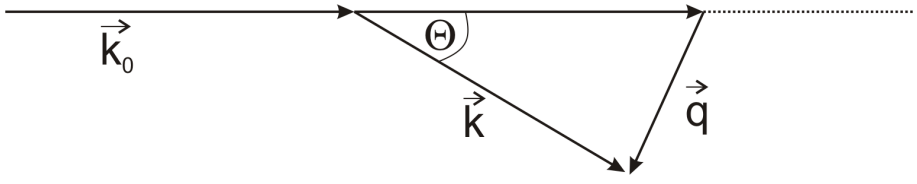

Figure 3.4: Sketch defining scattering vector q.

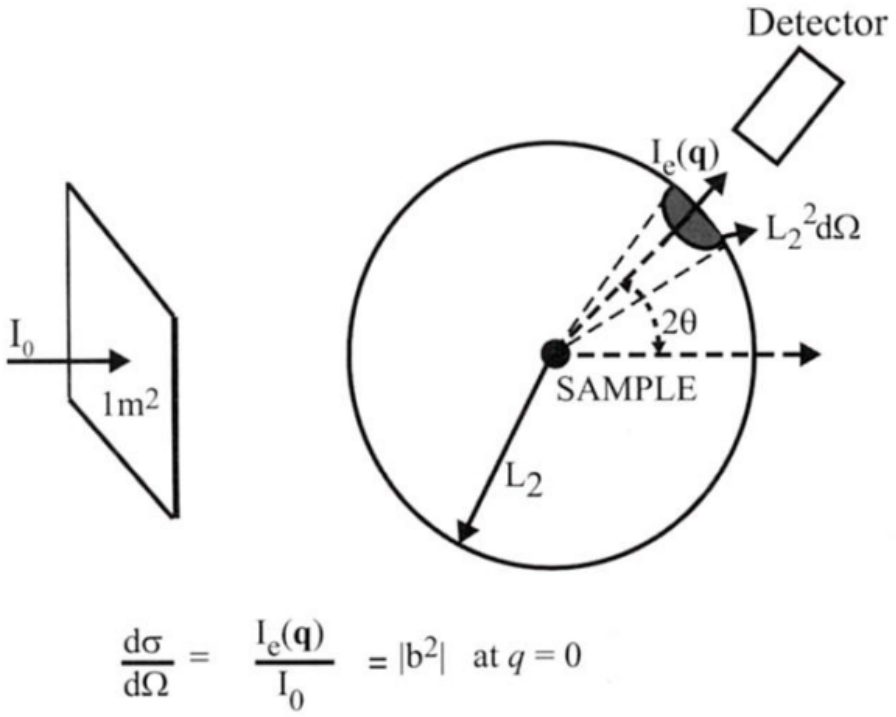

Figure 3.5: Definition of the scattering cross section. $I_e(q)$ is the energy scattered in the direction of 2θ, where I_0 is the incident beam. The ratio of these two quantities has the dimension of an area. L_2 is the sample-detector distance. The figure and the caption were taken from Ref. [180].

The counted number of photons/neutrons in a detector pixel of area A during the time Δt is therefore

$$N_{meas}(q) = I_0 \frac{A}{L_2^2} \frac{d\sigma}{d\Omega}(q) \Delta t. \tag{3.11}$$

In the following we refer to the scattering cross-section as the scattering intensity. However, this is not fully accurate because I_{meas} and $\frac{d\sigma}{d\Omega}$ are proportional to each other.

In the discussion above it is assumed that the particles in the solutions do not interact with each other and that all particles are oriented in the same direction. Considering a monodisperse system, the total scattering depends on their distribution in the sample. In this case the scattering amplitude, Eq. 3.6, will be a convolution of the particle density distribution $\Delta\rho(r)$ and the function which describes the position and orientation of the particles in the volume, $d(r)$: $\Delta\rho_{total} = \Delta\rho(r) \cdot d(r)$. This will expand Eq. 3.9 to

$$I(q) = \Phi \cdot V_{part}^2 P(q) \cdot S(q) + B \tag{3.12}$$

where $S(q)$ is the structure factor and B is the incoherent background, which plays mainly a role for neutron scattering and can be neglected for X-ray scattering. The convolution can be described as follows: the form factor $P(q)$ carries the scattering

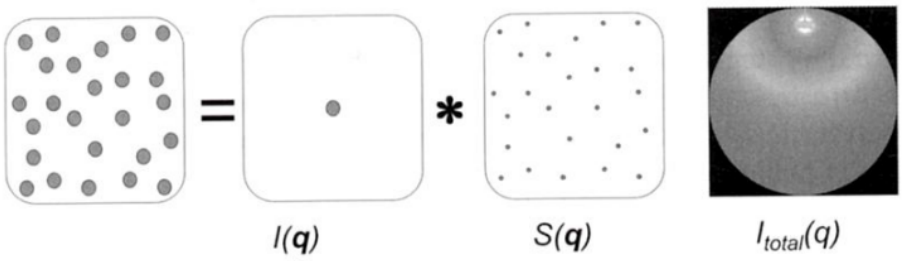

Figure 3.6: The right panel shows a typical experimental pattern from a solution. In the left panel the particle distribution is shown. The two panels in the middle show the scattering information of one particle, $P(q)$, referred to $I(q)$ in the used reference, and the information of the particle distribution in the sample, $S(q)$. The figure was taken from Ref. [180].

information of a single particle and $S(q)$ the information about the distributions of single points in the sample. This principle is shown in Fig. 3.6. The structure factor also contains information about the effective interaction potential in the sample. The interactions between all particles describe the structure of the solution [135, 180, 183]:

$$S(q) = 1 + \frac{N}{V}\int_0^{\inf}(g(r)-1)\frac{\sin(qr)}{qr}4\pi r^2 dr. \tag{3.13}$$

where $g(r)$ is the pair correlation function, which depends on the interaction potential $u(r)$ between the particles.

The scattering strength also depends on the composition of the sample and so $d\sigma/d\Omega$ is a material dependent constant. The nature of the individual scatterer can be described by $d\sigma/d\Omega = |b^2|$, where b is the scattering length. To obtain a scattering difference between the the sample and the matrix of the system, i.e. the solvent, both must have a different scattering length. The difference between these two scattering cross-sections is called scattering contrast $\Delta\rho$. The contrast does not only depend on the difference between the scattering cross-section; the nature of the incident beam also plays a role. X-rays are scattered by the electrons in the system, where the electron density is important, and neutrons interact with the nucleus and their spin. In spite of the different nature of the different radiations, they can be described by the same theory. Including the scattering contrast to Eq. 3.12 leads to

$$I(q) = \Phi \cdot (\Delta\rho)^2 \cdot V_{part}^2 P(q) \cdot S(q) \tag{3.14}$$

In general the system is polydisperse and the orientation of the non-spherical particles is not fixed. For such a system it can be shown that the effect of the polydispersity and

orientational average is given by [167, 168, 185]

$$\frac{d\sigma}{d\Omega} = \rho_p^2 P(\bar{q}) S'(\bar{q}) \tag{3.15}$$

defining the terms

$$S'(\bar{q}) = 1 + \beta(\bar{q})[S'(\bar{q}) - 1], \tag{3.16}$$

$$\beta(\bar{q}) = |\langle f(\bar{q})\rangle|^2 / \left\langle |f(\bar{q})|^2 \right\rangle, \tag{3.17}$$

where $P(\bar{q}) \equiv \langle |f(\bar{q})|2\rangle$. $P(\bar{q})$ is the averaged form factor over all different particle shapes in the solution. ρ_p is the averaged number density of particles in the solution. $S'(\bar{q})$ acts as an apparent interparticle structure factor. β is a q-dependent factor between zero and one that suppresses the oscillation of the true structure factor $S(\bar{q})$, which is the interparticle structure factor. This equation can be rewritten in order to bring it into the form of Eq. 3.12

$$I(q) = \Phi \cdot V_{part}^2 P(\bar{q}) \cdot S_{eff}(\bar{q}). \tag{3.18}$$

In the case of a monodisperse solution $P(\bar{q})$ becomes $P(q)$ and including the contrast term the equation can be rewritten to

$$I(q) = \Phi \cdot V_{part}^2 \rho_p^2 P(q) \cdot S_{eff}(\bar{q}). \tag{3.19}$$

In the special case of monodisperse spheres, where the orientation plays no role, β equals 1 and $S_{eff}(q) = S(q)$.

3.5.2 Peculiarities of scattering with different particles

In this thesis three different radiation sources, X-ray, neutron, and visible light, for the scattering experiments are used. The different radiation sources shows differences in several important scattering features. The first of the differences is related to the radiated wave length of the beam. The typical wavelength for a X-ray source is around 1 Å. For neutrons the wavelength can vary over several length magnitudes depending on the temperature of the neutrons. In this thesis cold neutrons with a wavelength between 4 and 12 Å are used. The longest wavelength can be observed by light scattering which is in the range of several hundred nanometer or in this study for the used HeNe laser of 632.8 nm. The variation of the wavelength is connected to a variation of the scattering vector q by the Eq. 3.5. From this equation it is visible that an increase in the wavelength leads to a decrease of q which means that longer length scales can be observed. This is the reason that light scattering is used for the observation of longer lengthscale.

Another important difference is the physical reason for the scattering which is expressed by the scattering contrast. For X-rays the scattering is related to the electron density of the sample which is in contrast to the scattering contrast of neutrons, which comes from the nuclei. The important feature of the neutron scattering contrast is that the scattering depends on the different isotopes in the nuclei. In this case the neutron scattering is sensitive to isotopes. For neutrons the scattering contrast can also be influ-

enced by polarizing the incident neutron beam. With this polarizing effect the scattering can be triggered by different nucleus. In contrast to X-rays and neutrons the refractive index of the sample is responsible for the scattering of light. With these differences in the scattering contrast with varying types of radiation it is possible to choose the radiation source by the feature which should be observed by the scattering experiment.

A disadvantage of neutron scattering is the so called smearing effect. In contrast to X-rays and light sources the wavelength for SANS experiments is selected by velocity selectors which leads to a spread of the used wavelength which is normally given by a $\Delta\lambda/\lambda$ value. Due to this wavelength spread the full width half maximum of an observable peak becomes broader and the maximum intensity of the peak decreases because the area below the peak must stay constant. Another effect which is also responsible for the smearing effect is the use of a non point like source. Normally no point like incident beam is used for neutron scattering techniques because of the low flux of the incident beam. This leads to a deviation in the scattering angle which has the same smearing effect.

The different detectors for the different radiations plays also a role. For light and X-ray beam small and very efficient detectors with a high pixel number are available in contrast to neutron detectors. The efficiency of the neutron detectors is lower as for the other types of radiations. The effective detection material for neutrons is ^{3}He which is filled in gas detectors. These detectors have the disadvantage of the small amount of available pixels per area. This limits the resolution of the detector. The resolution can be improved by using other detection materials which leads to a reduced efficiency of the detector and longer measuring times.

3.5.3 Modelling of scattering data

For the data analysis of the scattering curves several methods are available. They can be divided into non-software based analysis and software-based analysis. For the software based analysis different kinds of software are freely available. These can be divided into two kinds of software. The first kind is designed to fit the form factor of a sample. In this case it is necessary to have a crystal structure of the protein of interest. Based on this crystal structure the form factor is fitted to the scattering curve. These softwares are designed to extract an exact form factor of the measured protein. The disadvantage is that they cannot calculate a structure factor and so a diluted non-interacting sample is necessary to use these softwares. The other kind of software can fit a structure factor to the scattering curve with the disadvantage that no complex form factor can be considered. Normally the form factor of a protein is very complex. In order to get a structure factor for the used protein sample the form factor of the protein must be simplified. For this purpose it is assumed that simple geometric structures, such as spheres, rods, plates and ellipsoids can approximate the real form factor of the used protein. In this section several non-software and software based methods for the analysis of scattering curves are discussed.

3.5.3.1 Model independent analysis

For this study two methods are used to extract the radius of gyration, r_G, and the Porod asymptotic behavior, which is described by the Porod exponent P, of the sample.

Long wavelength limit: Guinier analysis

It can be shown that the scattering intensity for long wavelengths, small q, can be approximated to [180, 183, 184, 186]:

$$I(q) \approx I(0) \exp\left(-\frac{q^2 r_G^2}{3}\right) \tag{3.20}$$

As already mentioned this approximation holds only for small q-values, in the range of about $0 < q < 1/r_G$. Plotting the scattering curve in a $\ln I - q^2$ plot shows a linear behavior in the valid q-range and from the slope r_G and from the y interception $I(0)$ can be determined. Cluster formation can lead to a non-linear behavior in the valid range of a protein monomer. In such a case this analysis may not work.

Short wavelength limit: Porod analysis

In the short-range limit, $q \cdot r >> 1$, but still large compared to inter-atomic spacing, the scattering intensity for a spherical particle with a sharp interface can be written as [180, 183, 184, 186]:

$$I(q) = \frac{2\pi\Delta\rho^2}{q^P}\frac{S_{int}}{V} \tag{3.21}$$

where S_{int} is the sum of internal scattering surfaces. A deviation from this equation can be observed for rough surfaces, fractal systems and the influence of curvature in some symmetric bodies. In such cases the Porod exponent, P differs from the value in Eq. 4.22 of 4. Using a log-log plot of the scattering curve a linear behavior in the valid q region is observable and P can be determined from the slope of this linear relation. For a spherical object with a sharp interface P becomes 4, 2 or 1 in a 3-D, 2-D or 1-D system, respectively [183, 184, 186]. Depending on this Porod exponent the kinds of fractals can be observed. Generally, for surface fractals $3 < P < 4$, $P < 3$ for mass fractals and $P > 4$ for a diffusive interface [183, 187, 188]. A value of $P = 2$ can also be a feature of a Gaussian polymer [187]. Several other values can be also found in literature for fractal systems.

For the two introduced methods no special model describing the form factor and interactions in the system is used. This will change in the following methods where the form of the particles and the interaction potentials inside the solution ia described.

3.5.3.2 Form factor

In this thesis two different models for the form factor are used. The first one, the ellipsoid of revolution, describes the protein monomer and the second one, the Beaucage model, is used to describe the low-q part of the dense protein phase data.

Ellipsoid of revolution

In literature several form factors for BSA are mentioned. One kind of these form factors is an equilateral, triangular prismatic shell with a side length of 84 Å and a thickness of 31.5 Å [189]. The other models are based on an ellipsoid form. A prolate ellipsoid form with a radius of $a \,\mathrm{x}\, b \,\mathrm{x}\, b = 70 \,\mathrm{x}\, 20 \,\mathrm{x}\, 20$ Å^3 is mentioned [166, 168]. Zhang et al. described an oblate ellipsoid form with radii $a \,\mathrm{x}\, b \,\mathrm{x}\, b = 17 \,\mathrm{x}\, 42 \,\mathrm{x}9\, 42$ Å^3 [172]. We found that this model can successfully fit our scattering data for the dilute and dense protein phase. The used ellipsoid form factor can be described by [172]:

$$P(q) \equiv \left\langle |F(q)|^2 \right\rangle = \int_0^1 \left| \frac{3(\sin u - u \cos u)}{u^2} \right|^2 \text{ with} \qquad u = qb \left[(a/b)^2 x^2 + (1-x)^2 \right]^{1/2} \tag{3.22}$$

Power-law model

The power-law model is used to fit the increasing part of the curve when an increase of the scattering intensity at low-q is observed. This increase in intensity stems from bigger particles which can be observed at lower q-values. In the measured q-range the scattering part of these bigger particles only shows a linear increase in a log-log plot. The fit function can be written as:

$$I(q) = Aq^{-P} + b \tag{3.23}$$

where A is a coefficient to scale the scattering intensity and b is the isotropic background. It is clear that one can also derive the Porod exponent from this model. Therefore we can also use this model to obtain information about the fractal dimension of the bigger particle. Comparing to the Beaucage model only a small q region is used for fitting of P, which leads to a higher error in P. For this reason we used the P from the Beaucage model for the discussion. The different values for P are listed in Tab. A4. In this table the values from the power-law model are mentioned as Porod fit.

Beaucage model

This model is based on a publication by Beaucage [187] where the two models for the long wavelength limit and short wavelength limit are combined into a unified model:

$$I(q) = G \exp(-q^2 r_G^2/3) + B(1/q^*)^P \tag{3.24}$$

where $q^* = q/[erf(kqr_G/6^{1/2})]^3$, G is the Guinier prefactor, B is a prefactor specific for power-law scattering and P ist the Porod exponent.

The polydispersity index, PDI, of the system can be calculated by [190]:

$$PDI = Br_G^4/G \tag{3.25}$$

and the normalized polydispersity index by:

$$PDI_n = Br_G^4/1.62G \tag{3.26}$$

For particles with an inhomogeneous density profile, where $P > 4$, PDI can be rewritten as [188]:

$$PDI = Br_G^{4+2\beta}/GPDI_n = Br_G^{4+2\beta}/[t(\beta)G] \tag{3.27}$$

where

$$\begin{aligned} t(\beta) &= \frac{1}{8}[(\beta+1)(\beta+2)(\beta+3)\Gamma(\beta+1)]^2 \left[\frac{12}{(\beta+4)(\beta+5)}\right]^{2+\beta} \\ &\simeq 1.62 + 1.78\beta + 0.88\beta^2. \end{aligned} \tag{3.28}$$

where β is assumed to be small and Γ is the Γ-function.

3.5.3.3 Structure factor

As shown in Eq. 3.13 the structure factor depends on the pair correlation function $g(r)$. In principal $g(r)$ can be calculated using liquid state theory. g_r can be related to thermodynamic properties of the sample such as pressure and compressibility. The calculation of the form and structure factor is easily done for a monodisperse spherical system and the scattering intensity can be modeled by this calculation. For polydisperse systems of non-spherical particles this calculation can no longer be easily performed. $S(q)$ can be calculated from the equilibrium arrangement of particles, $g(r)$, which is determined by the interparticle potential. For a homogenous isotopic fluid of spheres, the Ornstein-Zernicke (OZ) equation can be used to calculate $S(q)$ [183]:

$$h(r) = g(r) - 1 = c(r) + n \int c(|\vec{r} - \vec{x}|)h(x)d\vec{x} \tag{3.29}$$

where $h(r)$ is the total correlation between two particles, which is the sum of the direct correlations, $c(r)$ and the sum of all other correlations which are felt indirectly by all other particles. It is obvious that $S(q)$ depends directly on $c(r)$. Usually both correlations, $h(r)$ and $c(r)$, are unknown and the OZ equation can only be solved with another relation, the so-called closure relation. The simplest of these relations is the Percus-Yevick closure relation, which relates the interaction potential to the direct correlation by [183]:

$$c(r) = g(r)[1 - \exp\{\beta u(r)\}] \tag{3.30}$$

This relation provides a good approximation for short-range interaction potentials. Such a short-range interaction potential, the sticky hard sphere (SHS) potential, is used in this thesis.

Sticky hard sphere potential

The sticky hard sphere potential, SHS, describes short-range attractive potentials. This model is normally used to describe an LLPS behavior in protein systems, because the LLPS behavior is related to a short-range attraction. It can also be used to perform

simplified calculations of a patchy particle system. This model, also known as Baxter model, was introduced by Baxter [163]:

$$U_{SHS}(r) = \begin{cases} \infty, & \text{for } 0 < r < \sigma \\ -u_0 & \text{for } \sigma < r < \sigma + \Delta \\ 0 & \text{for } \sigma + \Delta < r \end{cases} \tag{3.31}$$

where σ is the hard sphere diameter, u_0 and Δ are depth and width of the attractive well, respectively. The perturbation parameter, $\iota = \Delta/(\sigma + \Delta)$, must be smaller than 0.1. Within the SHS potential the strength of the attraction can be described by [191]

$$\tau = \frac{1}{12\iota} \exp u_o/k_B T \tag{3.32}$$

With this equation the depth of the interaction potential, u_0, can be calculated in orders of $k_B T$:

$$u_0 = -\ln 12 \cdot \iota \cdot \tau \tag{3.33}$$

and the reduced second virial coefficient, B_2/B_2^{HS} can be described by:

$$\lim_{\Delta \to 0} \frac{B_2}{B_2^{HS}} = 1 - \frac{1}{4\tau} \tag{3.34}$$

Within the Percus-Yevick closure relation Baxter found that the critical point of the system of interest is given by [160, 163]:

$$\tau_c = \frac{2 - \sqrt{2}}{6} \approx 0.0976, \quad \text{and} \quad \eta_c = \frac{3\sqrt{2} - 4}{2} \approx 0.1213, \tag{3.35}$$

with a critical B_2/B_2^{HS} value of

$$\frac{B_2(\tau = \tau_c)}{B_2^{HS}} = 1 - \frac{1}{4\tau_c} \approx -1.56. \tag{3.36}$$

This value was used in this thesis as the lowest limit for an LLPS in the discussion of the second virial coefficient results. From this calculation of the critical B_2/B_2^{HS} we can conclude that a B_2/B_2^{HS} should be strong enough to drive the system into an LLPS.

3.5.4 Experimental protocol

In this study aqueous solutions of proteins are used. The solvent, being a H_2O-salt mixture also scatters. Therefore, scattering events from both the sample and the solvent are detected. To get the signal of the sample scattering the solvent scattering must be subtracted. The scattering data is not only influenced by the solvent scattering, but also by other phenomena which are contribute to the signal of the detector, such as electronic noise, X-ray, neutron and light noise from the environment, scattering from apertures and collimators, scattering from the sample holder as well as absorption and

transmission. Sec. 3.5.4.1 shows how the data can be corrected for these effects is shown in . In some cases it is also necessary to calibrate the scattering intensities to a standard intensity. This is called absolute calibration and is discussed in Sec. 3.5.4.2

3.5.4.1 Data reduction

Nowadays the scattering intensities are detected by the use of two-dimensional detectors. The observed diffraction pattern shows a spherical symmetry with respect to the center of the unscattered beam, because the molecules/proteins may take all possible orientations in solution. Only nonisotropic samples, such as single crystals and fibres or filaments, which orient when injected into a capillary, show an azimuthal dependence of the scattering. For isotropic scatterers the only dependence of the scattered intensity is on the radial position corresponding to the scattering angle (2θ) between the unscattered and the scattered beam. By radial averaging over the different scattering vectors the 2D data can be reduced to 1D data. To get rid of disturbing influences onto the scattering intensities, the following measurements should be done:

- Measurement without a beam to detect the electronic noise of the detector (dark count). This value is normally very weak and can usually be neglected.

- To record the environmental noise the beam is blocked after the sample by a suitable absorber. The difference to the dark count measurement is that with this method the scattering from other radiation sources and from scattering outside of the designed pathway for the beam can be observed.

- The radiation can also be reflected or scattered by the collimation system or the sample aperture. This contribution is determined by a measurement without the sample and the sample container. This is called the measurement of the empty beam.

- Normally the sample is placed into a sample container, which also scatters the incident beam. For this reason the empty cell without a solution is measured.

- The solvent shows the biggest contribution to the total scattering intensity. To quantify this influence the solvent without the sample is measured.

- For the absolute calibration the recorded scattering intensity must be corrected by the transmission of the sample. The transmission is determined by measuring the intensity of the unscattered beam once with and once without the sample inside the beam. In most cases the direct, without sample, and the unscattered beam, with sample, is attenuated. This is necessary because in most cases the intensity of the incident beam is too strong to be correctly recorded from the detector, far outside of the linear region of the detector, or even destroy the detector.

After these different measurements have been performed the corrected scattering intensity I_s is obtained by [180]:

$$\begin{aligned} I_s(q) &= \tilde{I}_s(q) - \tilde{I}_{noise}(q) - \frac{T_{s/ec}}{\tilde{I}_{ec}(q) - \tilde{I}_{noise}(q)} \\ &= \tilde{I}_s(q) - T_{s/ec}\tilde{I}_e c(q) - (1 - T_{s/ec})\tilde{I}_{noise}(q) \end{aligned} \tag{3.37}$$

and the solvent scattering $I_{solvent}(q)$ is similarly given by

$$I_{solvent}(q) = \tilde{I}_{solvent}(q) - T_{solvent/ec}\tilde{I}_{ec}(q) - (1 - T_{solvent/ec})\tilde{I}_{noise}(q) \tag{3.38}$$

where the tildes (˜) indicate measured quantities, s denotes 'solution', and ec denotes 'empty cell'. In the case that the buffer/salt composition in the solution and solvent are exactly matched, the scattering intensity of the protein or macromolecule is given as:

$$I_{solute}(q) = I_s(q) - I_{solvent}(q) \tag{3.39}$$

For the absolute calibration this intensity must be normalized to unit concentration and sample transmission.

3.5.4.2 Absolute intensity calibration

As shown in Eq. 3.11 the measured intensity or amount of neutrons/photons depends on the experimental setup of the device. For this reason I_{meas} is only valid for the used beamline or lab source. To get information about the form factor this device dependant intensity is no problem, because the scattering intensity of the form factor is scaled by a constant in the available fitting routines. To achieve knowledge about the compressibility, the specific surface of the porous medium, the molecular mass M_W of the particles and for the measurement of the incoherent scattering cross sections, the scattering intensity has to be normalized to absolute scales. This absolute calibration also has the advantage that the scattering results from different experimental setups can be compared to each other.

Absolute intensity calibration for neutrons

In neutron experiments the absolute calibaration can ideally be done using H_2O, because of the strong incoherent scattering from light water. According to [180, 192], the scattering from an incoherent scatterer can be estimated as

$$I_{inc}(q) = \frac{(1 - T_{inc})I_0 S \Delta\Omega}{4\pi}[neutrons * s^{-1}] \tag{3.40}$$

where T_{inc} is the transmission through the sample after incoherent scattering took place, S is the cross sectional area between the incident beam and the sample and Ω is a geometrical term, which takes into account the angular aperture of the incident beam and the solid angle of detection. In this equation it is assumed that the non transmitted neutrons are scattered isotropically. This is not true in the case of light water, since

the scattering is inelastic. For this reason a correction factor f is introduced, which takes into account the non-isotropic nature of the scattering. The change of λ during the inelastic scattering process can also lead to a change in the detection probability of the scattered neutron, which is also included in f. With the sensitivity of the detector, η, the equation of the scattered intensity of light water can be written as [180]

$$I_{H_2O} = \frac{(1 - T_{H_2O}) I_0 \eta S \Delta\Omega}{4\pi f} [neutrons * s^{-1}]. \tag{3.41}$$

If the water and sample scattering are measured under identical conditions the intensity in forward direction $I(0)$ is given by [180]

$$I(0) = \frac{I_s(0)}{I_{H_2O}(0)} \frac{(1 - T_{H_2O})}{4\pi f} \frac{T_{ap}}{DT_s} [sr^{-1} cm^{-1}] \tag{3.42}$$

where T_s and T_{ap} are the transmission of the sample and aperture with respect to the empty cell. This method for absolute calibration has the disadvantage that f depends on the used wavelength and instrument/detector. If f is known for a given instrument it is not necessary to determine the intensity of the direct beam.

Absolute intensity calibration for X-rays

For neutrons the measurement of water is an ideal way for the absolute intensity calibration because of the high incoherent background. For X-rays the such a preferable tool does not exist, because of the negligible incoherent scattering.

Water can also be used for the absolute calibration in X-ray experiments. The scattering differential cross-section of water can be calculated theoretically, which can be used for the calibration. Another possibility for the absolute calibration for X-rays is the use of a secondary standard such as Lupolen (low-density polyethylene), which provides a strong peak corresponding to a spacing of 15 nm [193].

3.5.5 Small angle scattering experimental setup

Historically two major classes of scattering experiments defined by the recorded scattering angles, for wide angles, WAS, and for small angles, SAS. A scattering experiment is defined by the angle of the scattered beam. For a WAS experiment the measured scattering angle, θ_{meas} is greater than 10°, $\theta_{meas} = 2\theta \geq 10°$. The scattering is called SAS for all scattering angles between $0.1° \leq \theta_{meas} \leq 10°$.

A sketch of the typical realization of a SAXS or SANS experiment is plotted in Fig. 3.7. Usually the radiation source emits a polychromatic beam, except for small angle light scattering, where a laser is used as the radiation source. To achieve a monochromatic beam different monochromators are used. In the case of X-rays single silicon crystals or multilayer optics can be used. For such crystals only X-rays with the correct wavelength, corresponding to the lattice spacing, can be selected by using Bragg's law of diffraction $2d \sin\Theta = n\lambda$ and $\lambda = 12.4/E$, where d is the lattice space in Å, Θ is the glancing angle, n is a natural number and E is the energy of the incident beam in keV. By using

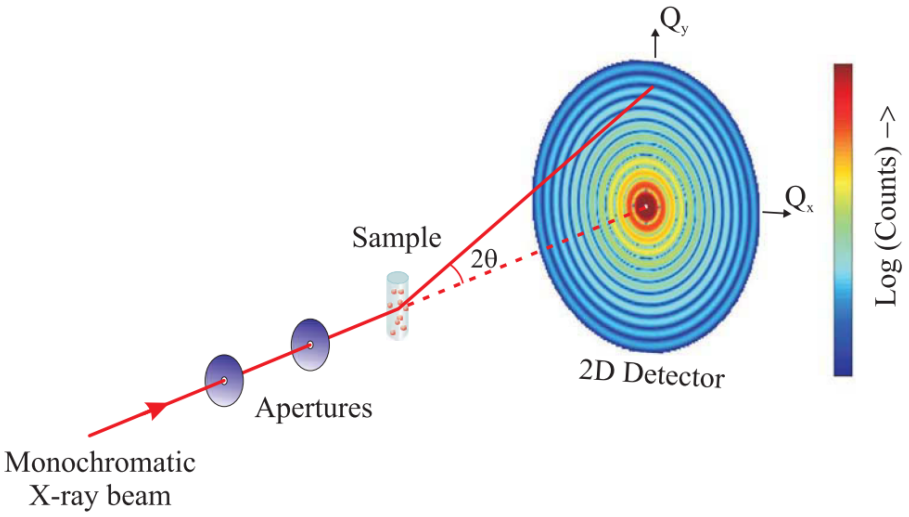

Figure 3.7: A sketch of a small angle scattering setup is shown. The incident beam is focussed over the apertures system onto the sample. The scattered beam is recorded under the angle of 2θ on a 2 dimensional detector. The figure was taken from Ref. [186].

different materials of single crystals or by varying the incident angle onto the crystal the desired wavelength can be selected. In the case of neutrons single crystals can also be used. This is normally done for inelastic experiments, where a monochromatic beam is important, but the flux of the incident beam is reduced significantly. In the most cases a velocity selector is used in SANS experiments to get the desire wavelength with a well defined spread of wavelengths between 1 % and 20 %. The advantage of using such velocity selectors is the gain of flux of the incident beam. The disadvantage is appearance of a wavelength smearing effect. This smearing effect must be considered in the analysis of the scattering data.

New instrumental developments led to new camera setup, which make it possible to go to much lower scattering angles. These new instruments are called USAS, ultra small angle scattering, or VSAS, very small angle scattering. To detect such small scattering angles several techniques are used. Bonse-Hart double crystal cameras [194, 195] can be used in for X-rays and neutrons. This technique suffer from very low count rates. Another way to very small scattering angles is described by [196], where they used a focusing-mirror for neutrons. Such an instrument, KWS-3 [197] is realized at the Maier-Leibniz Zentrum in Munich. This instrument is used for the studies of Sec. 4.4. Also different other techniques are known to perform USANS or VSANS experiments. A short overview about these different techniques is shown in [180].

In this section the principle concept of SAS experiments is explained, without saying anything about special properties for the different radiation sources. In the following two subsections these special features for the different radiations will be discussed. In Sec. 3.5.5.1 the developing of the X-ray contrast and the special feature of radiation

damage is shown. The nature of the contrast for neutron scattering and the feature of contrast matching is discussed in Sec. 3.5.5.2.

3.5.5.1 Small angle X-ray scattering

As shown in Eq. 3.14 the scattering intensity depends on the difference of scattering contrast between the particles and the solvent. In the case of a X-ray radiation the incident beam is scattered by electrons. In this case the scattering contrast is given by the difference in electron density between the sample and the solvent. The electron density of a sample increases with the atomic number of the atoms composing the sample. For this reason X-ray scattering is sensitive to heavier elements. This can leads to big changes in the electron density of salt solution, especially in the case of trivalent ions of ^{26}Fe, ^{39}Y, ^{57}La and^{13}Al. Following [10], these salt can induce a RC behavior in a solution of negatively charged proteins. In comparison to most atoms inside the proteins, the metal ions have higher atomic numbers.

The electron density for pure H_2O is $334\,\mathrm{e\,nm^{-3}}$ [180]. In contrast to this value the electron density of Proteins is around $420\,\mathrm{e\,nm^{-3}}$. Adding salt into the solvent the electron density of the solvent increases and the contrast between the protein and the solvent will decrease with increasing salt. Knowing the electron densities or the SLD of the salts the amount of salt can be calculated, at which the electron densities of the protein and the salt water mixture is the same. In this case a matched system occurs and no scattering from the protein will be observed. Another way to match the solvent SLD and the protein SLD would be to add sucrose ($\approx 65\,\%$) or PEG to the solution. The disadvantage for the different contrast matching methods in X-ray scattering is that in the most cases adding salts, PEG or sucrose will induce some interactions, such as screening effects, depletion and others, between the proteins. This makes these methods not suitable for use in biological systems.

Another important feature is the X-ray radiation-induced damage of the sample. X-ray interact with matter through absorption and scattering. For an example with an incident beam of 12 keV light atoms in biological sample will absorb 90 % of the radiation, which is absorbed or scattered. This absorption leads to a photoelectric effect followed by Auger emission, shake-up excitations and secondary electron cascades [180]. This phenomena can damage the sample. Another effect is the creating of hydroxyl or hydroperoxyl radicals by the interaction of X-rays with water molecules. The proteins becomes activated by the radicals and tend to be cross-linked with other proteins by covalent and/or non-covalent bonds [198]. This cross-linking leads to cluster formation inside the sample, which can be observed by an increase of I at low-q. A third mechanism of radiation damage can be explained by the energy deposition in the absorption process. This energy deposition leads to a local increase of T, which can locally induce a phase transition. This takes places for sample, which are prepared closed to a phase transition boundary and an increase of Twould induce this phase transition. We observed this phenomena several times for our samples close to critical concentrations. Switching on the beam leads to a locally turbid solution and by switching off the X-ray beam the sample becomes clear again.

Beam damage can be avoided by following methods. An energy increase of the incident beam leads to a higher scattering part compared to the absorption part. This is the reason why we usually perform our X-ray measurements at the ESRF at around 17 keV. To choose the correct energy for an experiment other effects, such as absorption from absorption edges, as described in Sec. 3.3, are to be considered. Another factor of the used energy is the wavelength λ of the beam, which is directly related to the observed scattering vector q. The desired q-range of the experiment is normally fixed by the used system and is fixed by the features of the system, which should be observed. λ is related to the energy by $E = hc/\lambda$ [180]. The energy is normally given in keV. Also a reduction of the exposure time reduces the effect of beam damage. This would lead to an decreased quality of the scattering curves. To compensate this reduced exposure time a flow cell can be used. For such a cell a series of X-ray pictures with short exposure times can be performed. Between each picture the sample is replaced by a fresh sample. This is done by a continuous or step-wise flow of the sample through the flow cell. Calculating the sum of all recorded X-ray pictures delivers the averaged X-ray picture. With this a total longer exposure time can be used for recording the X-ray image without recording the effect of beam damage. The correct exposure time must be measured at the beginning of the beam time.

The feature of beam damage is only observed at synchrotron source, because of their high brilliance of the incident beam. At lab sources this effect is negligible. Also for neutrons this effect is not seen, because of the smaller used energies.

All SAXS experiments from this study are performed at the ESRF, Grenoble, France at the beamline ID02 at an X-ray energy of 16.038 keV, which corresponds to a wavelength of 0.773 Å. For the X-ray absorption measurements two additional energies of 17.032 keV and 17.038 keV, corresponding to wavelengths of 0.728 Å and 0.727 Å, are used. For all measurement the sample-to-detector distance was set to 2m, which covers a q-range of 0.007 to 0.42 $Å^{-1}$. The data were collected by a high-sensitive fibre-optic coupled CCD detector placed in an evacuated flight tube. The protein solution was loaded in a flow-through quartz capillary.

3.5.5.2 Small angle neutron scattering

Neutron scattering techniques shows no effect of radiation damage. As mentioned above this can be related to the smaller energies of the used neutrons. The energy of the neutrons is related to their speed and connected to λ by $E = m_n v^2/2 = h/2m_n\lambda^2$ [180], where the energy is given in meV.

The contrast of neutron scattering experiments dependents compared to X-rays on the isotopes in the sample. Also compared to X-rays the SLD of the different isotopes does not follow a rule and jumps up and down by varying the isotopes. For an example the SLD for H_2O is $-0.56 \cdot 10^{-10}\,cm^{-2}$ and for D_2O is $6.33 \cdot 10^{-10}\,cm^{-2}$. This difference in the SLD is quite high and is one of the highest difference in nature between different isotopes of the same material. With this big difference it is quite easy to perform some contrast matching experiments. For experiments in solution the standard way is to varying the amount of Deuterium in the solvent to match the SLD of the sample. In case of proteins

this SLD is around $1.8 \cdot 10^{-10}\,\mathrm{cm}^{-2}$ for fully protonated proteins and $3.1 \cdot 10^{-10}\,\mathrm{cm}^{-2}$ for fully deuterated proteins. All the SLD values are taken from [180]. The experimentalist should check the stability of the sample in H_2O and D_2O before performing the contrast variation method, because in some cases the H_2O/D_2O content can change the behavior of the sample significantly.

A disadvantage of neutron scattering is, that hydrogens scatters mainly isotropically, which is the reason one finds a high background scattering in the case of H_2O, which reduces the signal to noise ratio significantly. For this reason experiments should be performed in D_2O and the sample should be partially or fully deuterated before the experiment. For samples, which change their behavior with different H_2O/D_2O ratio, this is not everytime possible. In such a case one must live with the high scattering background of hydrogens. The information about the form of the particles may be lost in this case.

SANS experiments are performed at the ILL, Grenoble, France at the beamline D11 and at the FRMII, Munich, Germany at the beamlines KWS-1 and KWS-2. At the beamline D11 a wavelength, λ, of 6 Å for a sample-to-detector distance of 1.2, 8 and 39 m and additionally a wavelength of 18 Å was used for a sample-to-detector distance of 39 m, in order to cover a broader q. The used velocity selector has a wavelength spread of $\Delta\lambda/\lambda = 9\,\%$. This leads to a smearing effect in the q-value. To detect the scattered neutrons a ^{3}He gas detector with a deadtime of 420 ns and a pixel size of 7.5 x 7.5 mm^2 was used. At the beamline KWS-1 and KWS-2 a wavelength of 4.5 Å at a sample-to-detector distance of 2 and 8 m and a λ of 10 Å,at a sample-to-detector distance of 20 m was used. The λ of 10 Å,is necessary to get an overlap in q with the KWS-3 data. A ^{6}Li-Scintillator detector with a spatial resolution of 5.25 x 5.25 mm^2 and a deadtime of 640 ns was used to record the scattering intensity. From the velocity selector the wavelength have a spread of $\Delta\lambda/\lambda = 10\,\%$ for KWS-1 and $\Delta\lambda/\lambda = 20\,\%$ for KWS-2. USANS experiments are measured at the beamline KWS-3 at the FRMII. For these measurements a wavelength of $\lambda = 12.8$ Å with a spread of $\Delta\lambda/\lambda = 0.2\,\%$ at a sample-to-detector distance of 10 m was used.

3.5.6 Light scattering

The wavelength of the incident beam is around 100 to 1000 times higher as for X-ray and neutron scattering. From Eq. 3.5 it is visible that this leads to a smaller q vector (2 to 3 magnitudes smaller) in a scattering experiment. This is the reason that light scattering is highly suitable for particle and cluster sizes in the order of several hundred nm up to some µm. In order to reach higher q-values we used an experimental setup with scattering angles above 10°. This is a wide angle scattering setup. The analysis of the time average data is discussed in the static light scattering, SLS, part, Sec. 3.5.6.1. With this setup, it is also possible to record a time dependent signal which can be also analyzed. Such an signal gives information above motions in the system. This kind of experiment is called dynamic light scattering, DLS, and is discussed in Sec. 3.5.6.3.

Another difference between light and X-ray or neutron scattering is the nature of the scattering contrast. For light scattering the scattering contrast comes from the refraction

index difference between the solvent and the sample.

3.5.6.1 Static light scattering

As the name 'static' already indicates, the 'static' data, time averaged data, is used to analyse information about the particle form and effective interactions. The time averaged scattering intensity I depends on the scattering contrast K, or b^2, the concentration c and the osmotic pressure π. I can be written as [199]:

$$I \sim b^2 k_B T \frac{c}{\left(\frac{\partial \pi}{\partial c}\right)_{T,N}} \tag{3.43}$$

where k_B is the Boltzmann constant and T the temperature. According to van't Hoff, $\partial\pi/\partial c$ can be expressed for a real solution as [199]:

$$\frac{\partial \pi}{\partial c} = k_B T \left(\frac{1}{M_W} + 2A_2 c + ... \right) \tag{3.44}$$

where M_W is the molecular weight and A_2 is the second virial coefficient which provides a quantitative measurement of the solvent-solute interactions.

As already mentioned the scattering of the incident beam dependents also on the scattering contrast which comes from a difference in the refraction index between the solvent and the sample in the case of light scattering. It is known that the refraction index also depends on the wavelength of the incident beam and on the concentration of the sample. Concerning these dependencies the contrast term can be written as [199]:

$$K = b^2 = \frac{4\pi^2}{\lambda^4 N_A} n^2_{solvent} \left(\frac{\partial n_s}{\partial c} \right)^2 \tag{3.45}$$

where N_A is the avogadro number and $n_{solvent}$, n_{sample} are the refraction index of the solvent and the sample and $\partial n_s/\partial c$ is the refraction index increment, the variation of the refraction index of the solution with varying concentration of the sample [200].

For SLS experiments, a calibration to absolute scattering intensities is helpful. In most cases, a measurement of toluene is used for the absolute calibration of the scattering data. Usually the calibration of the scattering intensity is expressed by the rayleigh ratio R_Θ [199]:

$$R_\theta = (I_s - I_{solvent}) \frac{I_{std,abs}}{I_{std}} \tag{3.46}$$

where I_s and $I_{solvent}$ are the intensities of the solution and the solvent, I_{std} is the intensity of the standard and $I_{std,abs}$ is the absolute scattering intensity of the standard.

The measured intensity depends additionally on the form factor $P(q)$ of the sample. Considering this form factor, the optical contrast K and the Rayleigh ratio R_θ Eq. 3.43 can be rewritten as [199]

$$\frac{Kc}{R_\Theta} = \frac{1}{M_W P(q)} + 2A_2 c + ... \tag{3.47}$$

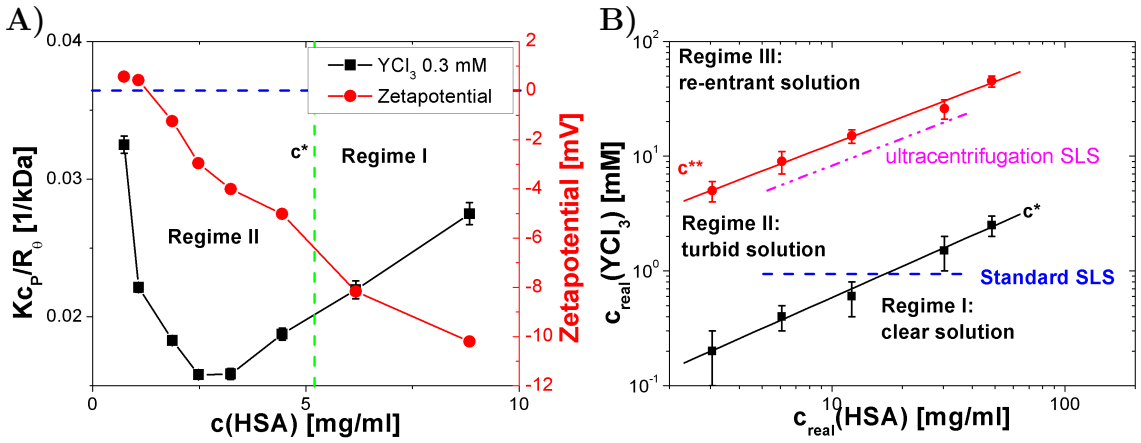

Figure 3.8: A) A typical result of a SLS experiment for samples which are prepared after the standard method is plotted. For comparison the corresponding ζ for each sample is also plotted. The dashed blue line shows a ζ of zero and the dashed green line shows the protein concentration of the c^* border for the used salt concentration. B) The reentrant HSA phase diagram is plotted. The blue dashed line highlights the samples prepared by the standard method. The dashed dotted magenta line shows an estimated line of different samples prepared after the ultracentrifuged method.

Assuming a homogeneous spherical particle, $P(q)$ can be expressed by the radius of gyration, r_G, and the equation can be written as [199]:

$$\frac{Kc}{R_\Theta} = \frac{1}{M_W}\left(1 + \frac{1}{3}\left\langle r_G^2\right\rangle q^2\right) + 2A_2c \tag{3.48}$$

where $\langle r_G^2\rangle$ is the z-average of r_G.

It should be mentioned that Kc/R_θ behaves like an inverse intensity, because $R_\theta \sim I_s - I_{solvent}$. For the case of small particles ($r < \lambda/20$) the form factor is close to 1 in the observable q-range and the scattering intensity becomes independent from the scattering angle. In this case it is enough to perform the measurement under a single angle and the Zimm equation, Eq. 3.47, changes to the Debye equation [199]:

$$\frac{Kc}{R_\theta} = \frac{1}{M_W} + 2A_2c \tag{3.49}$$

3.5.6.2 Static light scattering after ultracentrifugation

It is observed from SLS experiments in the second regime that the standard procedure for the sample preparation for SLS experiments shows a non-linear behavior. Such a non-linear behavior is shown in Fig. 3.8A). From such a curve, A_2 cannot be extracted. For the explanation of this behavior, the corresponding zeta potential ζ is plotted into this figure. From this measurement it is visible that ζ from a slightly positive value to high negative values with increasing c_p. In Fig. 3.8B) a sketch of the locations of

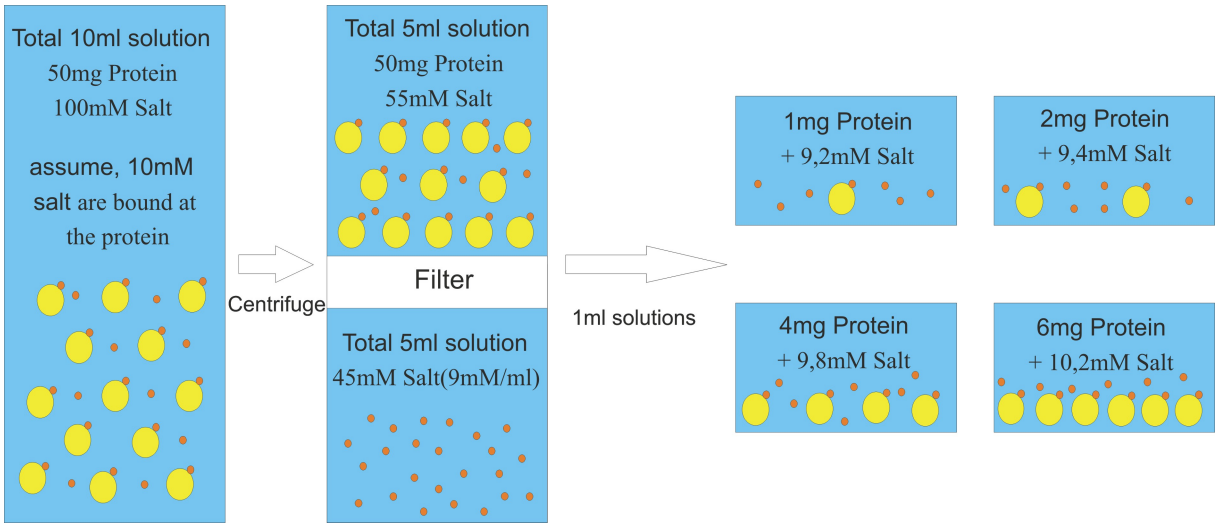

Figure 3.9: A sketch of the ultracentrifugation method for the sample preparation is shown. The original sample is separated into a protein-salt solution and a pure salt solution by ultracentrifugation. From these two solutions the samples for the SLS measurements are prepared. The protein-solution with the desired c_p is mixed with the pure salt solution to achieve the desired total volume of the sample. Figure was taken from Ref. [201]

the different samples in the RC phase diagram is plotted. The dashed blue line shows the conditions of the different samples in the phase diagram prepared by the standard method. In this case c_s is fixed and c_p is varied in different samples. From this blue line it is visible that each sample is located in a different region of the second and first regime and that a complete sample set can cross the c^* boundary. From this and the ζ-potential measurement it is visible that the Coulombic repulsion is varied with increasing c_p. This leads to a different effective interaction potential between each sample. This leads also to a variation of A_2 for each sample which is the reason that the SLS measurement shows no linear behavior in Fig. 3.8A).

An alternative way of the sample preparation is to use a method called ultracentrifugation. The procedure of the sample preparation method is sketched in Fig. 3.9. In the first step, a sample with the desired c_p and c_s is prepared. During this procedure, a part of the salt ions binds to the protein. This sample is filled into a ultracentrifugation tube with a molecular cut-off below the molecular weight of the used protein. Using centrifugation, a part of the protein free salt solution goes through the filter and is separated from the protein-salt solution. The resulting c_p of the protein-salt solution is measured by UV-Vis absorption, as described in Sec. 3.2. We assume that c_s of the protein free salt solution is the same as the unbound c_s in the protein-salt mixture. The desired amount of the protein-salt mixture is filled into a new sample tube. This new sample tube is filled up with the protein free salt solution to get the desired total volume of the sample. By filling up the protein-salt mixture with the protein-free salt solution,

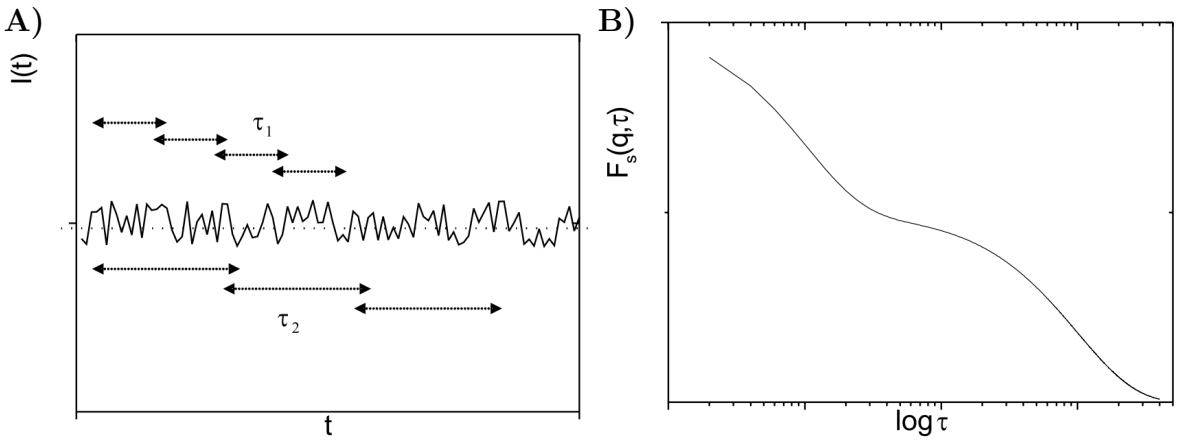

Figure 3.10: A sketch of the time dependence of the scattering intensity is plotted in A). Different pairs of scattering intensities at different time distances t and $t + \tau_i$ are compared to each other in a mathematical way, explained in the text, to the correlation function, plotted in B) for a bimodal sample. This figure is taken from Ref. [199]

the concentration of the unbound salt in the solution stays constant and the chemical potential in the solution is not changed. This is the reason that the amount of bound salt ions per protein stays constant over the hole sample set. The c_s of the complete sample increases with increasing c_p of the sample. This leads to a linear behavior of the sample location in the phase diagram, Fig. 3.8B). The location of the samples inside the phase diagram stays constant with increasing c_p, because the amount of bound salt ions per protein stays also constant. This behavior is shown by the dotted dashed magenta line.

Using this ultracentrifuge method for the sample preparation leads to a linear behavior of the second virial coefficient A_2. This is shown in Fig. 4.3. This observation shows that this method is quite useful in the used system of this study.

3.5.6.3 Dynamic light scattering

In contrast to SLS experiments, where the time average intensity is recorded, the time dependent evolution of the scattering signal is in the focus of dynamic light scattering, DLS, experiments. An example for the time dependent scattering intensity is plotted in Fig. 3.10A). The time dependent scattering intensity with a total measurement time T_M can be divided into N discrete scattering intervals Δt, with the following definition [199]:

$$\tau_d = n\Delta t \text{ with } 0 \leq n \leq N \text{ and } N\Delta t = T_M \text{ and } n \in \mathbb{N} \tag{3.50}$$

where τ_d is the delay time. The useful information from DLS experiments can be extracted from the fluctuation of the scattering intensity by constructing its time correla-

tion function defined as [183]

$$\langle I(q,0)I(q,\tau_d)\rangle = \lim_{T_M\to\infty}\frac{1}{T_M}\int_0^{T_M} I(q,t)I(q,t+\tau_d)dt. \tag{3.51}$$

This formula can be easily calculated for the two extreme cases $\tau_d = 0$ and $\tau_d = \infty$. For very short delay times, $\tau_d \to 0$, Eq. 3.51 can be reduced to [183]:

$$\lim_{\tau_d\to 0}\langle I(q,0)I(q,\tau_d)\rangle = \left\langle I(q)^2\right\rangle. \tag{3.52}$$

For delay times much greater than the typical fluctuation times, the intensity becomes uncorrelated and Eq. 3.51 can be written as [183]:

$$\lim_{\tau_d\to\infty}\langle I(q,0)I(q,\tau_d)\rangle = \langle I(q)\rangle^2. \tag{3.53}$$

The normalized intensity-time autocorrelation function is defined by Eq. 3.51 divided by the Eq. 3.53 [183, 199]:

$$g_2(q,\tau_d) = \frac{\langle I(q,0)I(q,\tau_d)\rangle}{\langle I(q)\rangle^2} \tag{3.54}$$

and the normalized field-time autocorrelation function is defined by [183, 199]:

$$g_1(q,\tau_d) = \frac{\langle E(q,0)E^*(q,\tau_d)\rangle}{\langle E(q,0)E^*(q,0)\rangle}. \tag{3.55}$$

A sketch of $g_1(q,\tau_d)$, sometimes also called $F_s(q,\tau_d)$ [199], is plotted in Fig. 3.10 for a bimodal system. Both autocorrelation functions are connected to each other by the Siegert relation [183, 199]:

$$g_2(q,\tau_d) = 1 + \beta g_1(q,\tau_d)^2 \tag{3.56}$$

where β is a setup dependent term which represent the degree of spatial coherence of the scattered light over the detector.

The main application of DLS is to extract the radius of hydration r_H from the measurement. This radius is connected to the diffusion coefficient, D_s of Brownian motion in dilute solutions by the Stokes-Einstein equation [183, 199]:

$$D_s = \frac{k_B T}{6\pi\eta r_H} \tag{3.57}$$

where η is the viscosity of the solution. The diffusion coefficient, D_s, is related to $g_1(q,\tau_d)$ by [183, 199]

$$g_1(q,\tau_d) = exp(-\Gamma\tau_d) \tag{3.58}$$

where Γ is the decay rate which is given by $\Gamma = D_s q^2$. In this simple case the experimental data can be fitted by an exponential decay.

Until know only a monodisperse sphere system was discussed. For a polydisperse sphere system, Eq. 3.58 can be extended to a superposition of single exponentials, each

corresponding to a particular particle size, weighted by the intensity scattered by the particle[183, 199]:

$$g_1(q, \tau_d) = \int_0^\infty P(D_s) exp(-D_s q^2 \tau_d) dD_s \tag{3.59}$$

where $P(D_s)$ is the normalized intensity-weighted distribution of diffusion constants, which is determined by the distribution of particle sizes. $P(D_s)$ does not only depend on the particle size because for larger particles, the scattering intensity depends also on the scattering vector q.

4 Results and discussion

The phase diagram of a protein solution in the presence of trivalent ion like Y^{3+} was added, shows several features like RC, LLPS, crystallization, condensation and gelation. Which feature is observable depends on c_p, c_s, temperature and time. A typical phase diagram with the different features, except of the gelation, is shown in Fig. 4.1. In this chapter we show the different results of this work and we discuss these results on the

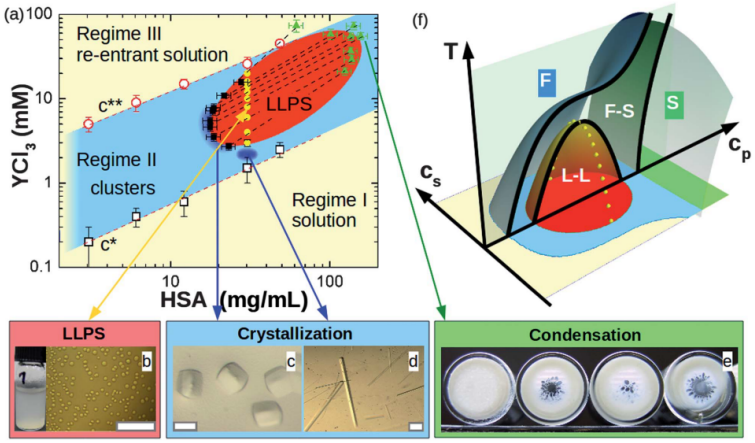

Figure 4.1: (a) Phase diagram of HSA controlled by YCl_3 in the (c_p,c_s) plane. The open symbols with error bar represent the boundary between the regimes as determined by optical transmission, while the solid symbols (red area) denote coexisting liquid phases (b) A typical optical microscopy image of a freshly prepared sample with 31.0 mg/ml HSA and 4.0 mM YCl_3 shows small droplets of protein-rich phases, which coalesce proving that a non-arrested LLPS occurs. (c+d) Crystallization with different growth mechanisms is observed in the dilute coexisting phase (c) and in the region slightly below the LLPS boundary (c_s = 2.0 mM)(d). (e) Amorphous aggregation in the protein-rich coexisting phase after storage at 20°C for two weeks indicates the general metastability of regime II to aggregation (pictures for initial HSA concentration 31.0 mg/ml with 4, 6, 10 and 15 mM YCl_3). (f) Sketch of a phase diagram with three control parameters: temperature, T, protein and salt concentration, c_p and c_s. All scale bars correspond to 0.1 mm. The figure was taken from Ref. [202].

base of our determined phase diagrams. The first (Sec. 4.1) and second section presents the phase diagrams of protein systems which undergo an LLPS by adding a trivalent salt and the effective interactions are determined. The first section is based on [160] and the second section is based on [203]. A short impression of the temperature effect onto the phase behavior and the interactions of the dilute protein phase is given in the end of the second section 4.3. The structure and the effective interactions in the dense protein phase is discussed in Sec. 4.4. The influence of the solvent dependent behavior is studied by varying the D_2O volume fraction in Sec. 4.5. The long-time stability and crystallization of both phases is investigated in Sec. 4.6. The development of a new sample holder is shown in Sec. 4.7.

4.1 Effective interactions in protein-salt solutions approaching liquid-liquid phase separation

In the following section the effective interactions in human serum albumin solutions approaching presented and is based on [160]. The effective interactions in the first, second, and third regime outside the LLPS region is monitored and compared are to the effective interaction in the LLPS region.

4.1.1 Introduction

The understanding of protein interactions in aqueous solutions is crucial for many issues in soft and biological matter. While the equilibrium phase diagram of proteins has some similarities with that of model colloidal systems, the physical mechanisms of protein crystallization with its huge importance for structural biology is far from understood, and, in most cases, remain elusive. Proteins, like colloids, in solution can be seen as big atoms that, however, interact by effective interactions resulting from the behavior of the other components in the solution, i.e. the solvent, salt, *etc.*. By changing the solvent conditions it is possible to alter the resulting protein interactions to a large degree, and thereby tune the phase behavior of protein solutions.

A particularly interesting example for phase behavior in protein solution is the metastable liquid-liquid phase separation (LLPS). LLPS in protein solution is a fundamental biophysical phenomenon and provides a mechanism for biological structure formation [2, 4–7, 67, 78, 204] such as a prerequisite for the formation of crystals in cataracts [4, 5, 7] and fibers responsible for sickle cell anemia and Alzheimer's disease [2, 204], and changes on the pathways of protein crystallization [3, 6, 124].

The physical reason of a metastable LLPS for colloids or proteins in solutions has been demonstrated both experimentally and theoretically to be due to the short-ranged nature of the attractive interactions [2, 3, 8, 14, 89, 92]. In contrast, in atomic systems, such as argon, where the attractive interaction is long-ranged compared to the molecular size, a stable gas-liquid phase separation exists [8]. Rosenbaum et al. have shown that the crystallization curves for a number of globular protein solutions are similar to those predicted by simulations for a system of hard spheres with a short-ranged

attractive Yukawa potential [92, 205]. Asherie et al. performed a combined analytical and computational study on the phase diagram of globular colloids [14]. Their study reveals that the interaction range plays a significant role in determining the structure of the phase diagram. A short-ranged attraction, i.e. the interaction range is smaller than ≈25 % of the diameter of particles, is prerequisite for the existence of the metastable LLPS in protein and colloid systems. Simulations and theoretical studies also support that a short ranged attraction leads to the metastable LLPS [3, 124, 161]. By comparing existing protein crystallization data with knowledge on a model colloid-polymer mixture, where the attraction range as well as strength between colloids can be tuned by varying the molecular weight and concentration of non-absorbing polymer, Poon suggested a hidden gas-liquid binodal inside the equilibrium fluid-crystal region of the phase diagram [89]. The critical points of LLPS can be nicely described using the thermodynamic criterion based on B_2, which has been used as a predictor in protein crystallization. George and Wilson observed that B_2 falls in a narrow range for protein crystallization [119]. Subsequent theoretical work by Vliegenthart and Lekkerkerker demonstrated that B_2 has a nearly constant value at the critical point [9, 161] and indeed can be used as a predictor for protein crystallization, i.e. the optimal conditions for crystal growth are either near the critical point where the density fluctuation enhances the nucleation rate [3], or below the critical point but near the protein-poor phase boundary where crystals grow via a two-step procedure [9].

While significant progress has been made in the understanding of the physical mechanism of the metastable LLPS, B_2 as a predictor for the critical point of LLPS has not been tested experimentally. In practice, due to the non-spherical shape and the combination of specific and non-specific interactions, it is not clear how strong the overall attraction has to be to lead to the LLPS in protein solutions.

We have shown that the interactions in protein solutions can be efficiently tuned by the variation of the ionic strength, the nature of ions and the valency of ions [10, 47, 58, 62, 154, 172, 173]. A rich phase behavior, including reentrant condensation, metastable liquid-liquid phase separation (LLPS), cluster formation, and crystallization, has been observed when trivalent salts are used [10, 47, 58, 62, 118, 155, 202, 206]. This tunable phase behavior can be used to optimize the conditions for protein crystallization [62, 118, 202, 206].

In this work, we present an experimental study combined with a theoretical discussion on the LLPS in protein solutions induced by trivalent cations. We focus on a deeper understanding of the effective protein-protein interactions in the condensed regime as a function of protein and salt concentration, which determines whether macroscopic LLPS or microscopic protein clustering occurs for a given protein solution. We present additional experimental data for the LLPS binodal. In particular, also data close to the critical point in the (c_p, c_s) plane are presented and discussed. The effective protein-protein interactions are studied using static light scattering (SLS) and small angle X-ray scattering (SAXS). The second virial coefficient is used to understand the key question: which attraction strength is needed in order to induce the LLPS. The results are further discussed within the theoretical framework established recently in colloidal systems [9, 159, 161, 207].

4.1.2 Theory: Second Virial Coefficient in Effective One-Component Systems

The theoretical part calculations are done by Roland Roth and are presented in [160].

We briefly elaborate on the phenomenon of a liquid-liquid phase separation (LLPS) in a potentially complex mixture of several components such as proteins, the solvent, added salt, etc. We provide a simple and intuitively transparent argument how LLPS relates to the second virial coefficient.

In many cases, it is natural to focus on the behavior of the largest component of the mixture, the proteins, and treating the remaining parts as a background medium. This can be done in a rigorous way by mapping the Hamiltonian of the mixture onto that of an effective one-component system [158, 159] by integrating out the degrees of freedom of the background. This mapping changes the interactions in the system from the bare interactions between all possible species combinations, i.e. protein-water, protein-ion, etc., to effective interactions between the proteins. At first we assume that the effective interaction potential $V_{eff}(r)$ is spherically symmetric.

For such a system to undergo a liquid-liquid phase separation into a low density fluid phase ("protein-gas") and a high density fluid phase ("protein-liquid"), the effective interaction has to possess a sufficiently strong attractive tail in addition to the repulsion at very short distances. The reason, independent of the precise nature of the effective interaction, is simple to understand: When a low density phase is transformed into a high density phase, the system loses entropy, which has to be compensated by the gain in interaction energy due to the attraction.

A convenient measure for the strength of the attraction is the effective second virial coefficient, which for the assumed spherically symmetric interaction potential, is defined by

$$B_2(T) = 2\pi \int_0^\infty r^2 \left[1 - \exp\left(-\beta V_{eff}(r)\right)\right] dr. \tag{4.1}$$

If B_2 is positive, the net interaction is repulsive. If it is negative, then the interaction becomes attractive . But how strong has the effective interaction to be in order to drive a phase separation? Vliegenthart and Lekkerkerker made the interesting observation that for various systems the value of the second virial coefficient B_2 at the critical point seems universal [9]:

$$\frac{B_2}{B_2^{HS}} \approx -1.5, \tag{4.2}$$

where $B_2^{HS} = 16\pi R^3/3$ is the second virial coefficient of a hard sphere of radius R. This observation was also confirmed by Noro and Frenkel [161] and was tested for hard-sphere mixtures [162] using the depletion potential [159].

The sticky hard-sphere model was introduced by Baxter [163] as an example of a system with hard-core repulsion and additional short-ranged attraction, which can undergo fluid-vapor phase separation. Some aspects of the system can be treated analytically

within certain approximate closure relations. The interaction potential is given by

$$\beta V_{eff} = \begin{cases} 1 & r < \sigma = 2R \\ -\beta u_0 = \ln\left(\frac{12\tau\Delta}{\sigma+\Delta}\right) & \sigma < r < \sigma + \Delta \\ 0 & r > \sigma + \Delta, \end{cases} \tag{4.3}$$

where usually the limit $\Delta \to 0$ is taken. In this limit the reduced second virial coefficient is given by

$$\lim_{\Delta\to 0} \frac{B_2}{B_2^{HS}} = 1 - \frac{1}{4\tau}. \tag{4.4}$$

Baxter found that within the Percus-Yevick closure relation the critical point is given by [163]

$$\tau_c = \frac{2-\sqrt{2}}{6} \approx 0.0976, \quad \text{and} \quad \eta_c = \frac{3\sqrt{2}-4}{2} \approx 0.1213, \tag{4.5}$$

so that for the reduced second virial coefficient, Eq. (4.4), at the critical point one finds

$$\frac{B_2(\tau=\tau_c)}{B_2^{HS}} = 1 - \frac{1}{4\tau_c} \approx -1.56, \tag{4.6}$$

which agrees well with the aforementioned criterion, Eq. (4.2).

In order to understand the observation by Vliegenthart and Lekkerkerker better we consider phase coexistence between a low density gas phase (density ρ_I) and a high density fluid phase (density ρ_{II}) in more detail. The two phases can coexist at the same temperature T if they are in mechanical and in chemical equilibrium, i.e.

$$P(\rho_I) = P(\rho_{II}) \quad \text{and} \quad \mu(\rho_I) = \mu(\rho_{II}) \tag{4.7}$$

where P is the pressure and μ the chemical potential of the system under consideration. For mechanical equilibrium close to the critical point to be possible, the pressure at coexistence has to be low, because the pressure of a high density liquid has to be balanced by the low pressure of the coexisting gas. Therefore, at coexistence, it is possible to expand the pressure into a virial series with only few terms with the most prominent contribution being the second virial term:

$$\beta P(\rho) \approx \rho + B_2\rho^2 + B_3\rho^3 + ... \tag{4.8}$$

Only if the attraction is sufficiently strong the pressure of a high density phase can be equally low as that of the low density phase.

The location of the critical point ρ_c and T_c, which is the onset of a fluid-fluid phase separation which is reflected by the onset of a van-der-Waals loop in the pressure, follows from

$$\left.\frac{\partial P(\rho)}{\partial \rho}\right|_{\rho=\rho_c} = 0 = \left.\frac{\partial^2 P(\rho)}{\partial \rho^2}\right|_{\rho=\rho_c}. \tag{4.9}$$

Note that the first condition in Eq. (4.9), the vanishing of the first derivative of the

pressure P w.r.t. density ρ, also expresses the condition of the vanishing of the inverse compressibility or the bulk modulus. This is important because in the limit of $q \to 0$ the structure factor $S(q)$ is proportional to the compressibility χ_T, i.e. $S(q \to 0) = k_B T \rho \chi_T$. This means that when the derivative of the pressure w.r.t. density, or the inverse compressibility, vanishes, at the critical point or at the spinodal line, the structure factor diverges for $q \to 0$. If one considers a system at a coexisting density, i.e. on the binodal line, then the state is also close to the spinodal, which implies that the compressibility and hence $S(q \to 0)$ are large, but do not diverge. The closer the system is to the critical point, the closer the binodal and spinodal lines are. Therefore close to the critical point, on the binodal (at either the low or the high coexisting density), the compressibility and $S(q \to 0)$ are large, while further away from the critical point, the distance between the binodal and spinodal increases, so that also the compressibility at a coexisting density and the structure factor $S(q \to 0)$ decrease.

By combining Eqs. (4.8) and (4.9) we obtain a set of equations which can be solved e.g. for the second and third virial coefficient at the critical point. Here only the result for B_2 is of interest. One finds that

$$\frac{B_2}{B^{HS}} \approx -\frac{1}{4\eta_c} \approx -2.06, \tag{4.10}$$

where we have inserted the value of the critical packing fraction due to Baxter [163], Eq. (4.5). While the agreement between Eqs. (4.2) and (4.10) is clearly not perfect, this simple argument helps to rationalize the origin of the B_2 criterion based solely on the idea of mechanical equilibrium. Note that the value of the second virial coefficient at the critical point based either on Eq. (4.2) or on Eq. (4.10) changes somewhat, if other estimates for the critical packing fraction η_c are employed, however, the magnitude remains of the same order of magnitude.

The conclusion is that for $\tau < \tau_c$ or $B_2/B_2^{HS} \lesssim -1.5$ the effective interaction potential is sufficiently strong to drive a phase separation into a low density and a high density phase.

In general, the effective interaction potential between proteins $V_{eff}(1,2)$ is not spherically symmetric, as assumed so far in this section, but depends on the distance r_{12} between centers of protein 1 and 2 as well as on their orientations $\hat{\Omega}_1$ and $\hat{\Omega}_2$. For such an effective interaction the second virial coefficient is given by

$$B_2(T) = \frac{1}{2V} \int\int\int\int \left[1 - \exp(-\beta V_{eff}(1,2))\right] d^3r_1 \; d\hat{\Omega}_1 \; d^3r_2 \; d\hat{\Omega}_2. \tag{4.11}$$

The second virial coefficient be calculated analytically only for special cases of $V_{eff}(1,2)$. One interesting example is the Kern-Frenkel potential [208], which accounts for short-ranged square-well attractions of depth $-\epsilon$ between isolated patches on the surface of spheres. Each sphere has n patches, which are contained within a cone, with an apex (of angle 2δ) at the center of the protein. The fraction of the surface that is covered by patches is given by $\chi = n(1 - \cos(\delta))/2$. The range of the square-well attraction is given by $\lambda\sigma$, where σ is the hard-core diameter. For this model the reduced second virial

coefficient is given by [208]

$$\frac{B_2}{B_2^{HS}} = 1 - \chi^2(\lambda^3 - 1)(\exp(\beta\epsilon) - 1), \tag{4.12}$$

which should be compared to Eq. (4.4).

If the patches cover a sufficiently large fraction of the surface, the reduced second virial coefficient at the critical point in the Kern-Frenkel model is compatible with the observation by Vliegenthart and Lekkerkerker, Eq. (4.2). However, as the fraction of the surface covered by patches, χ, decreases, the value of reduced second virial coefficient at the critical point can be significantly below –1.5 [209] so that a LLPS requires a strongly increased attraction and eventually becomes impossible.

4.1.3 Materials and Methods

4.1.3.1 Materials and sample preparation

Human serum albumin, HSA and yttrium chloride, YCl_3, were purchased from Sigma-Aldrich and used as received. All samples were prepared at room temperature (22 °C). A series of protein solutions with various salt concentrations were prepared by mixing stock solutions of dissolved protein and salt in degassed Milli-Q water. No buffer was used to avoid the effect of other co-ions. The phase diagram (reentrant condensation and LLPS) was determined by optical transmission and visual inspection. Protein concentrations (c_p) were determined by UV absorption (Cary 50 UV-Visible spectrometer from Varian Inc., California, USA.) at a wavelength of 280 nm with a coefficient of 0.51 ml/mg [164]. The protein-poor and protein-rich phase after LLPS were separated by centrifugation. c_p of the protein-poor phase was determined directly by UV absorption, and c_p of the protein-rich phase was calculated from the volume of each phase and the initial protein concentration by the lever rule. Salt partitioning was determined by X-ray absorption as described in detail in Ref. [202].

4.1.3.2 Static light scattering (SLS)

For the SLS measurements we assume the complex of the protein and the bound ions as a new "effective particle". Because of the binding of metal ions to the protein surface, conventional SLS measurements result in a nonlinear relationship between Kc_p/R_θ and c_p. This is reasonable since solutions with constant c_s and varying c_p correspond to different complexes of protein and salt and thus exhibit different interactions throughout the phase diagram, even across the phase boundary. To solve this problem, we use a method described below for our SLS measurement.

First, a series of sample solutions was prepared with a constant c_p (here, 3.1 mg/ml HSA) with various c_s ranging from 0.01 mM to 20 mM across all three regimes. Second, for each sample (2.0 ml), it was first concentrated up to ≈3 times of its initial c_p using an ultrafiltration tube (Amicon Ultra-15, Millipore Corporation, Billerica, USA, with a molecular weight cut-off of 50 kDa). The salt solution collected in the bottom of the

filter was used to dilute the concentrated solution into a series for SLS measurements. By this means, all samples were measured under comparable conditions. Measurements were carried out on a Zetasizer Nano ZS (Malvern Instrument Ltd., Worcestershire, UK) at 25 ° C with a fixed angle of 173 ° . The laser has a wavelength of 632.8 nm and a power of 4 mW. Solutions were filled in a quartz cuvette with a path length of 1 cm.

The second virial coefficient A_2 and the apparent molecular weight M_W were obtained from the Rayleigh equation [210]

$$\frac{K \cdot c_p}{R_\theta} = \frac{1}{M_W} + 2A_2 \cdot c_p, \tag{4.13}$$

where K is the universal optical constant, and R_θ is the Rayleigh ratio [210].

Since the osmotic pressure in a protein solution can be defined via either the protein concentration c_p or the protein number density ρ, the virial expansion gives two second virial coefficients A_2 and B_2, respectively [2, 119, 211]. The relation between A_2 and B_2 is given by

$$A_2 = B_2 \cdot \frac{N_A}{M_W^2}. \tag{4.14}$$

In this work, the molecular weight $M_W = 66$ kDa of a HSA monomer is used in the calculation.

4.1.3.3 Small-angle X-ray scattering (SAXS) and data analysis

The SAXS measurements were performed at the European Synchrotron Radiation Facility (ESRF) in Grenoble, France, at the beamline ID02 with two sample-to-detector distances of 2 m and 5 m. The energy of the incoming beam was 16.038 keV (wavelength 0.8 Å), with a q-range from 0.007 $Å^{-1}$ to 0.4 $Å^{-1}$. The detector was a fiber optically coupled fast-readout low-noise (FReLoN) CCD based on a Kodak KAF-4320 image sensor in an evacuated flight tube. About 0.1 ml sample was filled into a flow-through quartz capillary. The sample in the scattering volume was exchanged for every exposure. For each sample, 10 exposures of 0.1 s each were measured. The 2D intensity pattern was corrected to an absolute scale and azimuthally averaged to obtain the intensity profiles, and the solvent background was subtracted. More detailed information on data reduction and q-resolution calibration can be found in the literature [154, 212].

Data Analysis

Small-angle X-ray scattering data can be used to obtain information on the pair interaction potential [135, 184, 213]. The scattering intensity, $I(q)$, for a polydisperse or a non-spherical system, can be calculated on the basis of approximation approaches such as the "decoupling approximation" and "average structure factor" approximation [214, 215]. Both approaches assume that the particle position is not correlated with its orientation. For the case of non-spherical but monodisperse solutes at a low to intermediate concentration, such as the studied protein solutions, both assumptions give comparable results [172]. Therefore, in this work, the scattering intensity is calculated using the

average structure factor approximation, which can be expressed by

$$I(q) = N(\Delta\rho)^2 V^2 P(q)\bar{S}(q). \tag{4.15}$$

where $q = \frac{4\pi}{\lambda}\sin(2\theta/2)$ is the scattering vector, 2θ is the scattering angle, N is the number of protein molecules per unit volume in the solution, $\Delta\rho = \rho_{\mathrm{p}} - \rho_{\mathrm{s}}$ is the scattering length density difference between the solvent and the solute, and V is the volume of a single protein. $P(q)$ is the form factor of a given protein, i.e. the scattering from a single protein molecule after orientation averaging. A form factor of an oblate ellipsoid with semi-axes a and b is used to model HSA [179]. Using the average structure factor approximation $\bar{S}(q)$ is calculated from a monodisperse sphereical system, with an effective sphere diameter. In our case, the protein solution is a monodisperse but non-spherical system. The effective sphere diameter is calculated from a virtual sphere with the same second virial coefficient as the ellipsoid [173, 216]. In the following parts and for simplicity, we use $S(q)$ to denote $\bar{S}(q)$.

4.1.4 Results and discussion

4.1.4.1 Phase diagram of HSA with YCl_3 in the (c_p, c_s) plane

It has been shown in our previous work that acidic proteins such as HSA in solutions with YCl_3 exhibit a reentrant condensation phase behavior [10, 202]. Within the condensed regime, a metastable LLPS exists. Here we show additional experimental results on determining the phase boundary of LLPS, in particular the samples near the upper critical point in the (c_p, c_s) plane. Three sets of solutions with initial protein concentrations of $c_p = 31.1\,\mathrm{mg/ml}$, $47.8\,\mathrm{mg/ml}$ and $74.0\,\mathrm{mg/ml}$ were prepared at room temperature as a function of salt concentration in the condensed regime. The sample solutions were initially turbid. Upon centrifugation, a clear protein-poor phase separated from a protein-rich phase. The partitioning of both protein and salt, determined using UV-Vis and X-ray absorption method as described in the experimental section, gives the coexistence curve, the isothermal binodal.

The data are plotted in Fig. 4.2. The resulting c_p and c_s of the protein-poor phase indicate that the phase boundaries are comparable for all three sets of samples with different initial protein concentrations. The salt concentration in the protein-rich phases cannot be determined easily due to the high viscosity.

The experimental phase diagram on a log-scale shows a closed ellipsoidal area containing the LLPS. For this closed phase boundary, two critical points are expected in the (c_p, c_s) plane – one at low and one at high c_s. Although the precise location of both critical points has not been determined experimentally, possible regions are marked by orange striped areas in Fig. 4.2. The protein-poor phases for samples with initial protein concentration of $c_p = 47.8\,\mathrm{mg/ml}$ extend much closer to the upper critical point compared to the other two sets of samples. For example, the sample with the initial salt concentration $c_s = 32\,\mathrm{mM}$, gives a protein-poor phase with $c_p = 46.5\,\mathrm{mg/ml}$ which is very close to the initial concentration of $c_p = 47.8\,\mathrm{mg/ml}$, indicating proximity to the

upper critical point.

Given the closed area of the LLPS at intermediate c_p, the condensed regime of the phase diagram is divided into three regions. On the left-hand side of the LLPS, i.e. with lower protein and salt concentrations, proteins form clusters but no macroscopic LLPS can occur. On the right-hand side of the LLPS, i.e. with much higher protein and salt concentrations, although the state of the system has not been characterized, one would expect an arrested gel or a highly non-equilibrium state.

The following results on the second virial coefficient focus on the understanding of the effective protein-protein interactions in the clustering region and at the binodal of the LLPS. The questions we are interested in are the following: First, how does the interaction potential change with increasing salt concentration for a given protein concentration, such as those along the magenta dotted line in Fig. 4.2? Second, do the samples with a constant protein to salt ratio, but in different location, share the same interaction potential? For example, the samples located in the clustering region and at the binodal of LLPS. Furthermore, since we have samples located on the binodal of LLPS very close to the critical point, it would be interesting to follow the change of the interaction potential by approaching the critical point and compare it to the value predicted in theory.

We have performed both SLS and SAXS measurements to characterize the effective interactions in the cluster phase as well as at the binodal of LLPS. From that the reduced second virial coefficient has been derived. Samples for SLS and SAXS measurements are labeled by a magenta dotted line and a grey area in Fig. 4.2, respectively.

4.1.4.2 Second virial coefficient determined by static light scattering (SLS)

Using an ultracentrifugation method described in the experimental section, we have performed SLS measurements for a series of samples with a constant initial protein concentration c_p=3.1 mg/ml and varying salt concentration c_s from 0.1 to 20 mM. As shown in Fig. 4.2, these samples cover all three regimes. Typical plots of Kc_p/R_θ against c_p are shown in Fig. 4.3A. In all cases, a clear linear relationship is obtained. From the slope one can determine A_2 using Eq. (4.13). The linear extrapolation to zero protein concentration for most of the samples points to the value of 66 kDa, corresponding to the molecular weight of a HSA monomer. Therefore, the larger clusters have been effectively removed by filtration or centrifugation, and the residual protein concentration is sufficiently low not to form clusters. For samples with $c_s = 1.0$ and 7.5 mM, which are near c^* and c^{**}, the extrapolation of Kc/R_θ to $c_p = 0$ is lower, indicating the formation of protein clusters.

The values of the second virial coefficient A_2 obtained by fitting the data and the corresponding B_2/B_2^{HS} are listed in Table 4.1. For the calculation of B_2/B_2^{HS} from A_2, the excluded volume of the single particle is needed. However, precise determination of the excluded volume of a protein in aqueous solution is non-trivial due to the non-spherical shape and the hydration of proteins. As discussed in previous work [173], these two effects affect the effective excluded volume of proteins in solution. It has been shown that the effective radius determined by SAXS provides a good estimation for

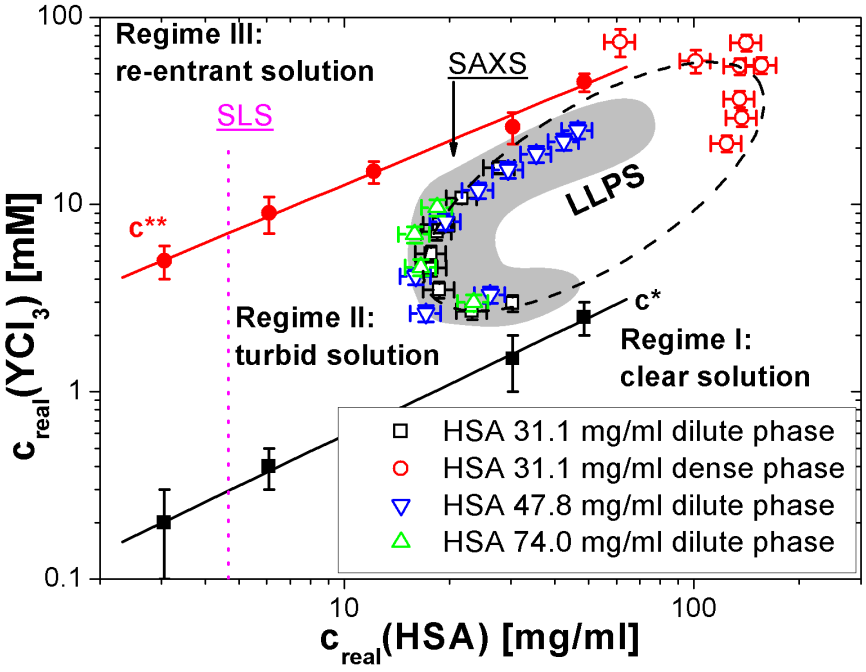

Figure 4.2: Plot of reentrant phase diagram with real protein and salt concentrations. The solid black and red symbols (square, circle) and lines correspond to the boundaries of c^* and c^{**}. Data points from the protein-poor and protein-rich phases after LLPS are presented by open symbols. The dashed ellipsoid is a guide to the eyes outlining the LLPS region. The magenta dotted line indicates the samples for SLS measurements. The gray-highlighted area around the LLPS boundary indicates the samples for SAXS. The two orange striped areas indicate the estimated regions for the lower and upper critical point.

both effects [171, 173, 217]. For HSA under physiological conditions, the effective radius determined by SAXS is $r = 33.5$ Å [173]. In the current study, in the presence of YCl_3, SAXS measurements give a value of $r = 40.4$ Å (see next section). For comparison, the radius of HSA calculated from the specific volume of the monomer $r = 26.8$ Å is also used.

The calculated reduced second virial coefficients $B_2/B_2^{HS}(r = 40.4\,\text{Å})$ are plotted in Fig. 4.3B as a function of the number of Y^{3+} per protein. The cyan area shows the theoretical limit of B_2/B_2^{HS} for LLPS ranging from –1.5 Eq. (4.2) to –2.06 Eq. (4.10). From Fig. 4.3B one can see that the values of B_2/B_2^{HS} are positive at very low salt concentrations and decreases first with increasing c_s, reaching a minimum of –5 at about 10 Y^{3+} per protein, then increases slowly and becomes positive again at very high salt concentrations. This observation is consistent with the reentrant condensation phase behavior of the protein solutions, i.e. in regime I and III, the interaction is dominated by repulsion, whereas attraction is dominated in Regime II. However, due to the systematic error in the determination of both B_2/B_2^{HS} and the values of c^* and c^{**}, it is not possible

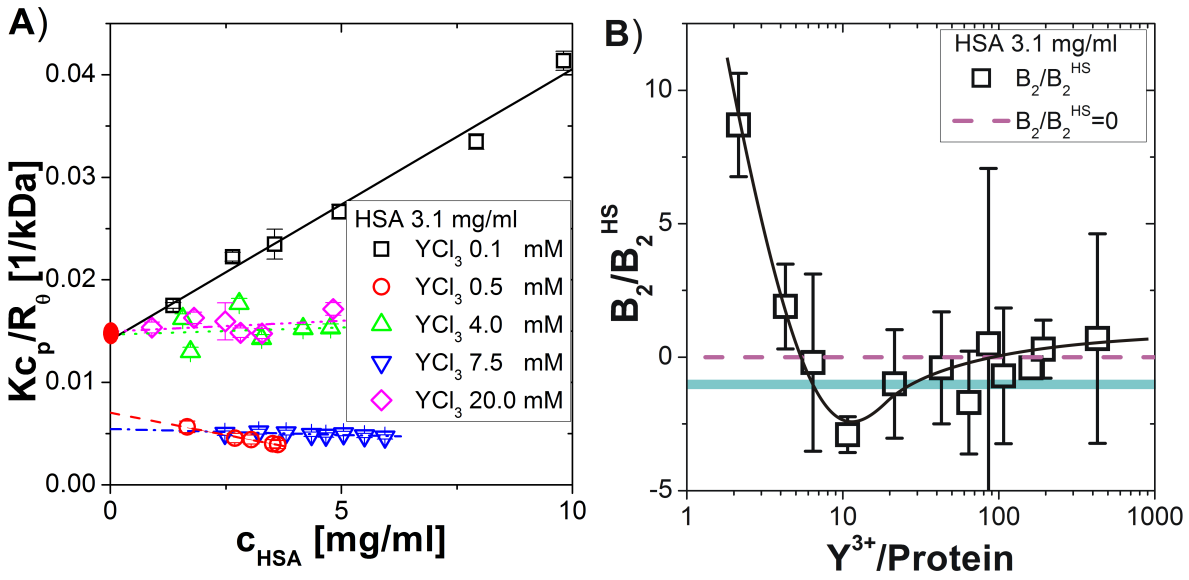

Figure 4.3: A) Typical Debye plots of Kc_p/R_θ versus c_p from SLS measurements. The red point of the y-interception corresponds to the inverse molecular weight of a HSA monomer. B) Plot of the reduced second virial coefficient B_2/B_2^{HS} determined by light scattering versus Y^{3+}/Protein ratio. The black solid line is a guide to the eyes. The cyan area shows the theoretical limit for B_2/B_2^{HS} with an isotropic interaction potential.

to deduce a precise relation between them.

4.1.4.3 Effective protein-protein interactions at the LLPS binodal determined by SAXS

The form factor of the protein solutions in the presence of multivalent metal ions has been determined using samples with c_p=1.3 and 6.0 mg/ml with various c_s. All the SAXS curves overlap in the whole q-range after normalization by c_p. Figure 4.4A shows a typical SAXS profile for a sample with c_p=1.3 mg/ml and c_s=8 mM. Optimisation of a model with an ellipsoid form factor gives the dimension of $18 \times 52 \times 52\,\text{Å}^3$ with an error of 1 Å in each dimension resulting in an effective sphere radius of $r = 40.4\,\text{Å}$ [202]. Compared to the effective radius of HSA ($r = 33.5\,\text{Å}$) under physiological conditions, the increase in size may be due to the formation of small protein clusters via cation bridging [118]. The dimension of the form factor determined here is used for the following data analysis.

A typical SAXS profile for a sample located at the LLPS binodal with a model fit is shown in Fig. 4.4B. The SAXS data were collected for a larger q-range compared to that shown in our previous work [202]. An upturn is visible in the extended low-q region, which can be explained by the protein clustering. To fit the data over the full q-range,

Table 4.1: Second virial coefficient A_2 and the corresponding B_2/B_2^{HS} determined from ultrafiltration SLS measurements for a series of samples with initial c_p=3.1 mg/ml and various c_s.

YCl_3 [mM]	Y^{3+}/ protein	$A_2 \cdot 10^4$ $[\frac{\text{mol·ml}}{g^2}]$	B_2/B_2^{HS} $r = 33.5$ Å	B_2/B_2^{HS} $r = 26.8$ Å	B_2/B_2^{HS} $r = 40.4$ Å
0.1	2.1	13.1 ± 1.7	15.3 ± 1.9	29.8 ± 1.9	8.7 ± 1.9
0.2	4.3	2.8 ± 1.4	3.3 ± 1.6	6.4 ± 1.6	1.9 ± 1.6
0.3	6.4	-0.3 ± 2.9	-0.4 ± 3.3	-0.7 ± 3.3	-0.2 ± 3.3
0.5	10.7	-4.3 ± 0.6	-5.1 ± 0.7	-9.9 ± 0.7	-2.9 ± 0.7
1.0	21.4	-1.5 ± 1.8	-1.8 ± 2.0	-3.5 ± 2.0	-1.0 ± 2.0
2.0	42.9	-0.6 ± 1.8	-0.7 ± 2.1	-1.4 ± 2.1	-0.4 ± 2.1
3.0	64.3	-2.6 ± 1.7	-3.1 ± 1.9	-6.0 ± 1.9	-1.7 ± 1.9
4.0	85.8	0.7 ± 1.6	0.8 ± 6.6	1.6 ± 6.6	0.5 ± 6.6
5.0	107.2	-1.0 ± 2.2	-1.2 ± 2.5	-2.4 ± 2.5	-0.7 ± 2.5
7.5	160.8	-0.6 ± 0.3	-0.7 ± 0.4	-1.3 ± 0.4	-0.4 ± 0.4
9.0	193.0	0.5 ± 0.9	0.5 ± 1.1	1.0 ± 1.1	0.3 ± 1.1
20.0	428.9	1.0 ± 3.4	1.2 ± 3.9	2.4 ± 3.9	0.7 ± 3.9

we use a sum of a power law and a sticky hard sphere (SHS) structure factor. The power law is used to describe the contribution from protein clusters, i.e. the upturn at low-q region. We noticed that when leaving the power as a fit parameter, the values obtained for various data are always very close to 3. We therefore fix the power to 3 for all data analysis. By fixing it we avoid artifacts in the fitting procedure for the SHS structure factor which is used to describe the short-ranged attraction between proteins. The volume fraction of the protein was fixed by the value measured by UV-Vis absorption. For the SHS model, Δ was fixed to $0.02\,\sigma$ to prevent artificial coupling with τ. This procedure gives a good fit for the complete scattering curve as shown in Fig. 4.4B.

Following the data analysis described above, we have fit all SAXS data for samples located at the LLPS binodal. We focus on the samples with an initial $c_p = 47.8$ mg/ml (Fig. 4.5A) because this series of sample cover a large region of the binodal including the data very close to the upper critical point.

We first discuss the scattering intensities at $q \to 0$, $I(0)$ (Fig. 4.5B), which provides in a model-free way the effective interactions of the system. $I(0)$ reflects the compressibility χ_T, since $S(q \to 0) = k_B T \rho\ \chi_T$ [135]. The compressibility χ_T diverges at the spinodal line. The measured samples correspond to the binodal line which approaches the spinodal line once the coexisting densities become closer. Thus, the closer the coexisting densities are, the larger is χ_T and hence $S(q \to 0)$ in the coexisting phases.

The experimental results on the microscopic interactions thus reflect the phase behavior, as can be seen by comparing the SAXS intensity normalized by c_p at $q = 0.01$ Å^{-1} (Fig. 4.5B) for samples located at the LLPS binodal. With increasing of c_s, correspond-

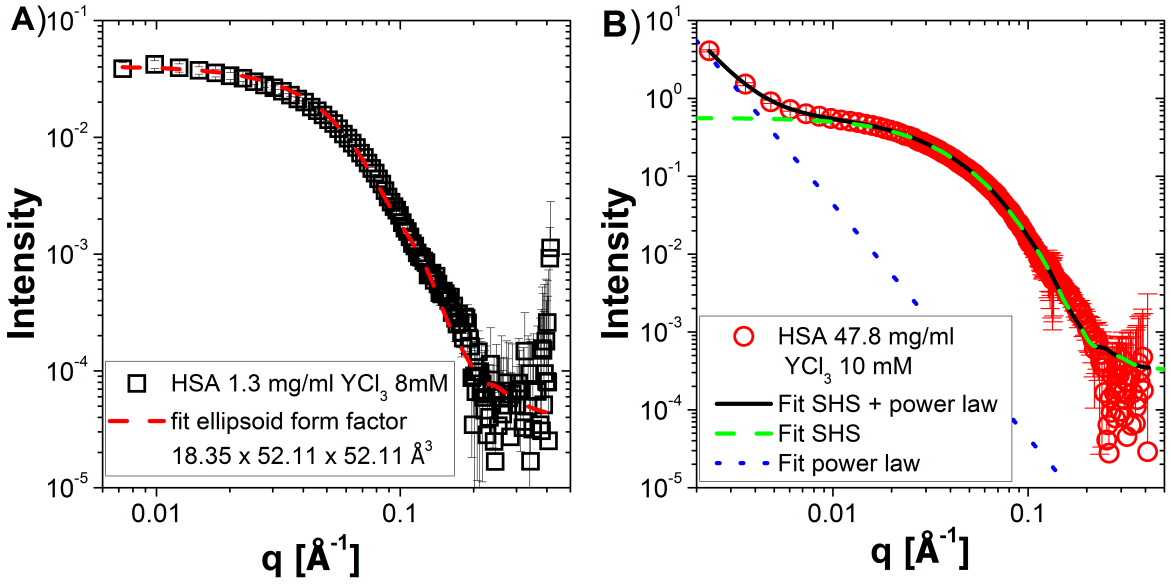

Figure 4.4: A) SAXS profile with a model fit using the form factor of an oblate ellipsoid for a dilute protein solution of 1.3 mg/ml HSA with 8 mM YCl_3. B) Typical SAXS profile of a sample located at the LLPS binodal and the corresponding model fit using a sticky hard sphere structure combined with a power law. The sample has an initial c_p=47.8 mg/ml and c_s=10 mM.

ing to an increase of the number of Y^{3+} per protein, above a critical value (around 6 Y^{3+} per protein), the system phase separates. For this c_s the system is close to c^*, which results in large values of χ_T and $S(q \to 0)$. As the c_s is increased further up to around 13 Y^{3+}/protein, the coexistence region broadens, causing χ_T and $S(q \to 0)$ to decrease. In the range between 13 to 40 Y^{3+}/protein the trend is reversed: χ_T and $S(q \to 0)$ increase again, until the solution is mixed again for Y^{3+}/protein above 40. For samples with initial c_p=47.8 mg/ml, as shown in Table 4.2, further increasing c_s above 20 mM does not change the composition of the protein-poor phase, i.e. the number of Y^{3+}/protein is nearly constant. In addition, from Fig. 4.2 we know these samples are approaching the upper critical point, therefore, the normalized scattering intensity shows a different behavior, i.e. decreases at a constant ratio of Y^{3+}/protein in Fig. 4.5B. As the system needs the minimum attraction to induce LLPS at the critical point as predicted in theory, and $S(q = 0)$ follows the similar trends of $I(q = 0)$ without the contribution of clustering, this explains the decrease of $I(0)$ approaching the critical point.

The corresponding calculated sticky hard sphere structure factors $S(q)$ are shown in Fig. 4.5C. For reasons of comparison, $S(q)$ has been replotted with a fixed protein volume fraction. As one can see, the $S(q \to 0)$ with the obtained interaction parameters consistently follows the same trend as $I(q \to 0)$ near the critical point, i.e. the overall attraction decreases approaching the critical point.

Finally, we present the effective attraction between proteins obtained from the SAXS

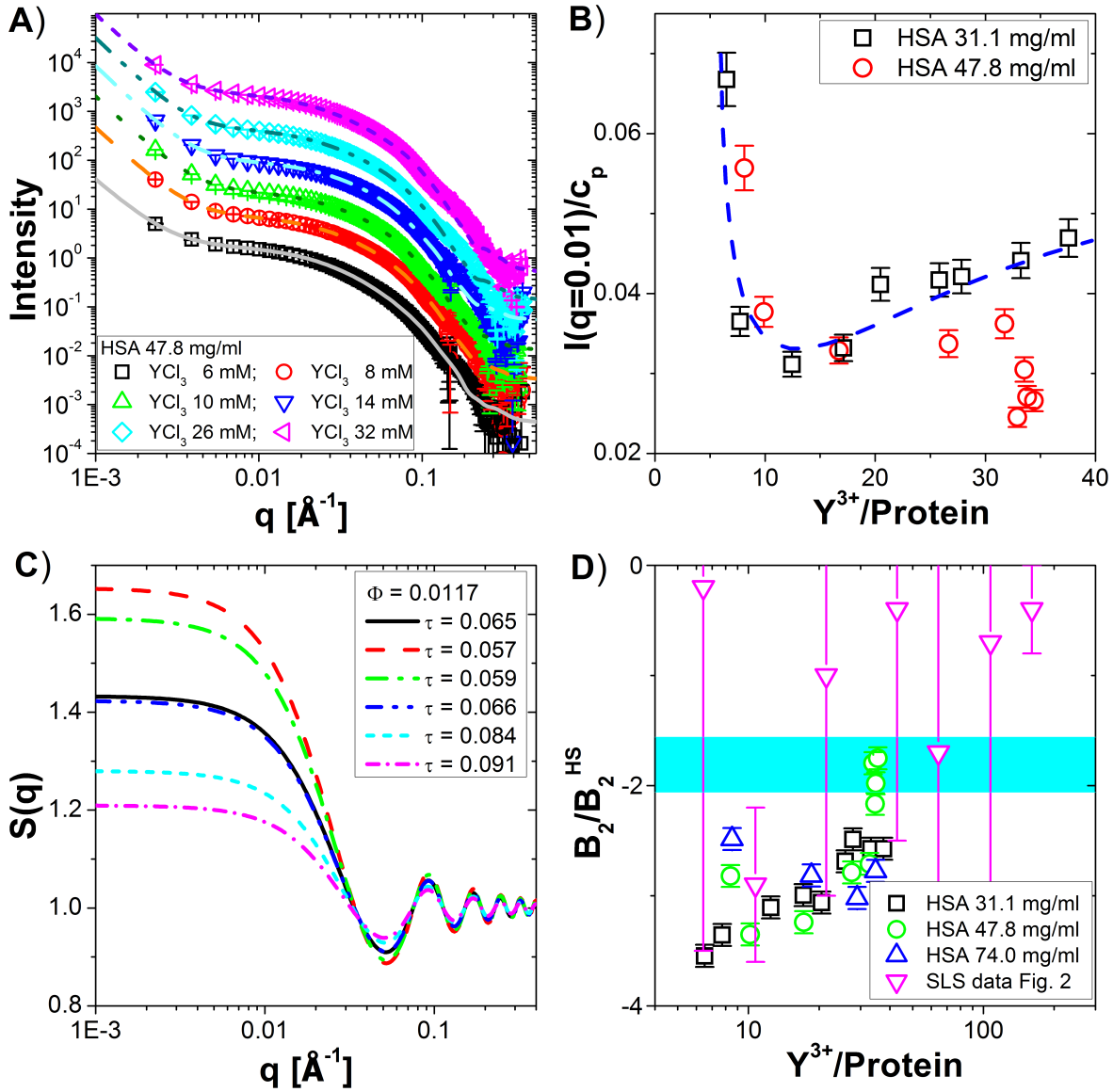

Figure 4.5: A) Typical SAXS profiles with curves generated from the model for samples of HSA 47.8 mg/ml at different c_s. The scattering curves are shifted in intensity for clarity. B) The scattering intensity at $q = 0.01$ Å^{-1} normalized by the real c_p after LLPS for samples with initial c_p of 31.1 mg/ml and 47.8 mg/ml. C) Calculated structure factors for a fixed protein volume fraction for different τ values. D) The reduced second virial coefficient B_2/B_2^{HS} as a function of the number of yttrium ions per protein for three different initial c_p of 31.1 mg/ml (black boxes), 47.8 mg/ml (red circles), 74.0 mg/ml (blue triangles). For comparison, the values from light scattering are also plotted as magenta inverted triangles.

Table 4.2: Reduced second virial coefficient B_2/B_2^{HS} determined from SAXS measurements for samples located at the LLPS binodal

c_{HSA} [mg/ml]		c_{YCl_3} [mM]		Y^{3+}/ [b]	τ	B_2/B_2^{HS} [c]	u_0
initial c_p	real c_p [a]	initial c_s	real c_s [a]	Protein			[k_BT]
47.8	26.2	6.0	3.3	8.4	0.065	-2.82	4.18
47.8	17.1	8.0	2.6	10.2	0.057	-3.35	4.31
47.8	16.0	10.0	4.1	17.2	0.059	-3.24	4.28
47.8	19.5	14.0	8.1	27.5	0.066	-2.79	4.17
47.8	24.2	18.0	11.9	32.8	0.067	-2.71	4.15
47.8	29.4	22.0	15.3	34.6	0.079	-2.17	3.99
47.8	35.4	26.0	18.5	34.8	0.084	-1.98	3.92
47.8	42.5	30.0	21.7	33.9	0.089	-1.80	3.87
47.8	46.5	32.0	24.9	35.6	0.091	-1.75	3.84

[a] real concentration in the protein-poor phase
[b] ratio between real salt and protein concentration in the protein-poor phase
[c] the error from data fitting is in general below 1 %, but we estimate the systematic absolute error to these values is about ±0.10.

data. The values of the stickiness parameter from data fitting are used to calculate the B_2/B_2^{HS} as shown in the Fig. 4.5D. The values of τ, B_2/B_2^{HS} and the depth of the potential u_0 for a complete set of sample are listed in Table 4.2. The values of τ are generally below $\tau_c = 0.0976$ Eq. (4.5) for all samples located at the binodal of LLPS. The corresponding interaction potential has a depth of $u_0 \sim -4\,k_BT$ and the value decreases when approaching the critical point. The values of B_2/B_2^{HS} for all samples at the binodal of LLPS are negative. In particular for the samples with the initial c_p of 47.8 mg/ml, the value of the B_2/B_2^{HS} increases towards the critical region predicted in theory, reflecting the vicinity to a critical point. By comparing the B_2/B_2^{HS} obtained by SLS and SAXS, one can see that despite of the large error for the SLS results, the values show a similar trend and range as those from SAXS. This finding indicates a similar interaction potential for proteins in the clustering phase and at the binodal.

4.1.5 Conclusion

From the perspective of colloid theory, a metastable liquid-liquid phase separation (LLPS) is caused by a strong attractive potential with a range much smaller than the effective hard sphere particle diameter σ [3, 14, 89]. Regardless of the precise origin of the short-ranged attraction between the proteins, its presence is essential for the LLPS: the loss of entropy in the high density phase, compared to the corresponding entropy in the low density phase, has to be compensated by the increase in internal energy due to the attraction. Mechanical equilibrium at coexistence implies that the osmotic pressure in the high density phase is equally low as in the low density phase. This can only be achieved by a sufficiently negative value of B_2. In fact it has been predicted theoretically that a reduced second virial coefficient of $B_2/B_2^{HS} < -1.5$ is required for the occurrence

of a LLPS [9, 161].

Our results from static light scattering (SLS) (Fig. 4.3B) suggest that while the experimental values for B_2/B_2^{HS} from SLS have to be corrected using the molecular volume of protein, where an effective volume accounting also for hydration and non-sphericity should be considered for the calculation, the final results agree reasonably well with those determined by SAXS. This finding means that the strength of the attractive potential, as measured by B_2/B_2^{HS}, for samples located in the clustering region is similar to the samples at the binodal of LLPS. This result is consistent with the theoretical prediction that the LLPS requires both chemical and mechanical equilibrium. While protein solutions with the constant composition share a similar chemical potential, the difference in mechanical pressure, or volume fraction, determines their different states. For most of the experimental results including our previous work [202], the B_2/B_2^{HS} values are determined for conditions near the binodal of the phase boundary. For these samples, values of B_2/B_2^{HS} below the critical value of -1.5 are expected and observed.

In addition, anisotropic interactions can vary the picture considerably. Proteins in our system behave more like patchy particles since the interaction is dominated by the bridging effect of metal ions [59, 118]. The critical value of B_2/B_2^{HS} is not constant when the interaction potential is changed from isotropic to anisotropic [209]. Even for spherically symmetric potentials there is a variation in the critical value of B_2/B_2^{HS} depending on details of the potential. If the potential is patchy then it is more than likely that the critical value of B_2/B_2^{HS} is lower than –1.5.

In this study, we have successfully studied a series of samples with an initial c_p of 47.8 mg/ml, which extend from binodal to the point very close to the upper critical point in the (c_p, c_s) plane. The evaluated B_2/B_2^{HS} from SAXS shown in Table 4.2 suggest that, approaching the critical point, the values of B_2/B_2^{HS} become less negative, indicating weaker attraction. The minimum attraction in this series gives B_2/B_2^{HS} of –1.75, slightly lower than the predicted value of –1.5. This result may suggest that either the sample is still not exactly at the critical point, or indeed the anisotropic interaction of our system leads to a lower value of B_2/B_2^{HS} at the critical point.

4.2 Liquid-liquid phase separation in protein solutions induced by multivalent cations

In the previous section the effective interactions in a HSA solution inside and outside of the LLPS region is discussed. In this section the focus is on the differences of the phase diagram and the effective interaction between an HSA and BSA solution. This section is based on [203].

4.2.1 Introduction

Many questions in soft and biological matter require the understanding of the protein interactions in aqueous solutions. The physical mechanism of protein crystallization, which is of huge importance for structural biology, is far from being understood. The practice

shows that protein crystallization is usually dominated by a short-range attraction. This effective short-range attraction is shorter than the size of the protein which leads to a metastable liquid-liquid phase separation (LLPS) [2, 3, 8, 14, 72, 89, 92, 118, 218, 219]. Such a metastable LLPS in protein solutions is of interest as a fundamental biophysical phenomenon and as a pathway of biological organization [2, 5, 6, 67, 78, 173, 204]. It has been reported that LLPS is the prerequisite for the formation of fibers that are responsible for sickle cell anemia, eye cataracts and Alzheimer's disease [4, 5, 7, 78]. Theory, simulations, and experiments have predicted that the density fluctuations near LLPS significantly reduce the energy barrier of protein condensation, e.g. crystallization [3, 14, 92, 124]. In spite of the importance of LLPS for the understanding of protein crystallization as well as the role it plays in protein condensation, this phenomenon has only been studied in a few protein systems and in those cases temperature was the main driving force [2, 204]. Without direct evidence for the interaction range and strength in protein solutions, a comprehensive understanding of LLPS is impossible.

One of the most studied proteins under various conditions is lysozyme. In the first studies the temperature was controlled to induce the LLPS [64]. Another intuitive way to control the conditions of LLPS is adding salt into the solution, which screens protein charges. The simplest and most used salt was NaCl [67]. Another possibility to tune the conditions for LLPS is varying pH which leads to a change of the effective surface charge of the protein. The effects that varying pH values and different kinds of salts have on the LLPS temperature were studied by Taratuta [65]. Using crowding agents like polyethylene glycol, LLPS can furthermore be induced by depletion forces [220]. Recently Moeller et al. demonstrated that LLPS can also be induced by varying the pressure of the system [221].

Another well studied protein system are γ-crystallins [4, 5, 7, 65, 70–74, 88]. The crystallization behavior of the studied systems has been explained by a two-step crystallization process [219]. The detail review of Vekilov [131] gives more information about the the two-step nucleation process. The work of Dorsaz [222] shows a theoretical study of the phase separation in the γ-crystallins system.

In recent years the focus also shifted towards the phase separation of monoclonal antibodies [83–87, 223]. These studies are also very interesting from a medical perspective because the monoclonal antibodies are widely used for drug delivery, and in some diseases, such as multiple myeloma, a high antibody concentration can be observed in the blood. Wang et al. have shown that it is possible to tune the critical temperature of phase separation by adding another protein such as HSA [87].

Recently, we found that negatively charged proteins in solution undergo reentrant phase behavior in the presence of multivalent counterions [10, 47], i.e. the solution becomes turbid after a critical salt concentration is reached. Further increasing salt concentration leads to a second critical salt concentration, c**, where the solution becomes clear again. Further investigations of the turbid regime of reentrant systems showed that LLPS can be induced and controlled by adding multivalent ions [160, 202]. In contrast to the protein system mentioned above the origin of the LLPS in the system studied here is the formation of patchy particles. This patchy particle formation in a protein system by adding multivalent ions was described by Roosen-Runge et al. [59].

In this work, we present the results obtained for two different serum albumins, human (HSA) and bovine (BSA). The phase diagrams for both proteins are presented. The phase diagrams reveal differences. In order to explain these differences, we measured the difference in the monomer and dimer composition between the used proteins. The effective interactions in both protein solutions are presented. For the dilute protein phase the effective interaction is below the critical value for LLPS [9]. The deviation from this behavior for the dense protein phase will be discussed. The differences in the morphologies of both dense protein phases will be shown.

4.2.2 Experimental

4.2.2.1 Materials and sample preparation

Human (HSA, A9511) and bovine (BSA, A3059) serum albumin and yttrium chloride (YCl_3, 451963) were purchased from Sigma-Aldrich Chemie GmbH, Munich, Germany, and used as received. All samples were prepared at room temperature (22 ° C). A series of protein solutions with various salt concentrations was prepared by mixing stock solutions of dissolved protein and salt in degassed Milli-Q water (18.2 MΩ). No buffer was used to avoid the effect of other co-ions.

SEC measurements were performed in order to analyse the monomer/dimer composition of the used proteins. For these measurements a Superdex 200 column (GE Healthcare Life Science , Little Chalfont, Buckinghamshire, HP7 9NA, UK), filled with a spherical composition of cross-linked agarose and dextran with an average particle size of 13 µm was used. The elution buffer contains 10 mM HEPES and 150 mM NaCl (pH=7).

4.2.2.2 Determination of the binodal of liquid-liquid phase separation

The reentrant condensation phase diagram was determined by optical transmission and visual inspection. The LLPS region inside the second regime was determined by optical microscopy. Protein concentrations (c_p) were determined by UV absorption (Cary 50 UV-Visible spectrometer from Varian Inc., California, USA) at a wavelength of 280 nm with a percentage solution extinction coefficient ($E^{1\%}_{1cm}$) of 5.1 ml/mg [164] and 6.67 mg/ml [178] for HSA and BSA. The dilute protein and dense protein phases were separated by centrifugation. c^1_p of the dilute protein phase was determined directly by UV-Vis spectroscopy, and c^2_p of the dense protein phase was calculated from the volume of each phase and the initial protein concentration by the lever rule.

Salt partitioning was determined by X-ray absorption as described in detail in Ref. [202]. These measurements were performed at the beamline ID02 at the ESRF, Grenoble, France at three different energies (E1-E3), far away (1000 eV away), slightly below (4 eV away) and directly at the K-edge. In literature an energy of the K-edge of 17038 eV is mentioned [181]. The offset from the beamline was measured and the energy of the K-edge was fixed to the measured energy. For the calibration of c_s pure salt solutions was measured. The integrated fluorescence intensity $\Delta I = I(\mathrm{E}_n) - I(\mathrm{E}_m)$ of

the salt at high-q-values leads to a linear calibration curve for the energy differences $\Delta E = \mathrm{E}_n - \mathrm{E}_m$. The averaged fluorescence intensity at high-q and for different ΔE for each dilute protein phase was determined and the real salt concentrations c_s^1 were identified by using the calibration curve which was determined by pure salt solutions with known salt concentrations. For the calculation of c_s^2 the same procedure as for c_p^2 was used.

4.2.2.3 Small angle X-ray and neutron scattering measurements

The SAXS measurements were performed at the European Synchrotron Radiation Facility (ESRF) in Grenoble, France, at the beamline ID02 with two sample-to-detector distances (SD) of 2 m and 5 m. The energy of the incoming beam was 16.038 keV (wavelength 0.8 Å), which covers a q-range from 0.007 $\mathrm{Å}^{-1}$ to 0.4 $\mathrm{Å}^{-1}$. The detector was a fiber optically coupled fast-readout low-noise (FReLoN) CCD based on a Kodak KAF-4320 image sensor in an evacuated flight tube. About 0.1 ml of sample was filled into a flow-through quartz capillary. The sample in the scattering volume was exchanged for every exposure. For each sample, 10 exposures of 0.1 s each were measured. The 2D intensity pattern was corrected to an absolute scale and azimuthally averaged to obtain the intensity profiles, and the solvent background was subtracted. More detailed information on data reduction and q-resolution calibration can be found in the literature [154, 212].

SANS measurements were performed at the instrument KWS-2 located at the FRM2, Munich, Germany. Two configurations were used with SD distances of 2 and 8 m and a collimation length of 8 m in order to cover the q-range from 0.005 to 0.35 $\mathrm{Å}^{-1}$ at a wavelength of 4.5 Å ($\Delta\lambda/\lambda = 20\,\%$). A two-dimensional array detector was used to detect neutrons scattered from sample solutions. Protein solutions were filled in rectangular quartz cells with path-length of 1 or 2 mm. Plexiglas was used as secondary standard to calibrate the absolute scattering intensity. The data correction and absolute intensity calibration were obtained using the software QtiKWS [224].

For the data fitting we used the software IGOR Pro® (version 6.1.2.1) with additional macros developed by the NIST center for neutron scattering [225]. For the fitting routine of the SAXS data we replaced the neutron contrast term by an electron density term.

4.2.2.4 Analysis of SAXS and SANS data

Small-angle X-ray and neutron scattering data can be used to obtain information on the pair interaction potential [135, 184, 213]. The scattering intensity, $I(q)$, for a polydisperse or a non-spherical system can be calculated based on approximation approaches such as the "decoupling approximation" and "average structure factor" approximation [214, 215]. Both approaches assume that the particle position is not correlated with its orientation. For the case of non-spherical but monodisperse solutes at a low to intermediate concentration, such as the studied protein solutions, both assumptions give comparable results [172]. Therefore, in this work, the scattering intensity is calculated

using the average structure factor approximation, which can be expressed by

$$I(q) = N(\Delta\rho)^2 V^2 P(q)\bar{S}(q). \tag{4.16}$$

where $q = \frac{4\pi}{\lambda}\sin(2\theta/2)$ is the scattering vector, 2θ is the scattering angle, N is the number of protein molecules per unit volume in the solution, $\Delta\rho = \rho_\mathrm{p} - \rho_\mathrm{s}$ is the scattering length density difference between the solvent and the solute, and V is the volume of a single protein. $P(q)$ is the form factor of a given protein, i.e. the scattering from a single protein molecule after orientation averaging. A form factor of an oblate ellipsoid with semi-axes a and b is used to model both proteins [172, 202]. Using the average structure factor approximation, $\bar{S}(q)$ is calculated from a monodisperse spherical system, with an effective sphere diameter. In our case, the protein solution is a non-spherical system. The effective sphere diameter is calculated from a virtual sphere with the same second virial coefficient as the ellipsoid [173, 216].

The second virial coefficient in the used sample is determined by fitting a sticky hard sphere (SHS) model, introduced by Baxter [163], to the scattering data. The interaction potential of this Baxter model is defined as:

$$U_{SHS}(r) = \begin{cases} \infty, & \text{for } 0 < r < \sigma \\ -u_0 & \text{for } \sigma < r < \sigma + \Delta \\ 0 & \text{for } \sigma + \Delta < r \end{cases} \tag{4.17}$$

where σ is the hard sphere diameter, u_0 and Δ are depth and width of the attractive well, respectively. The perturbation parameter, $\epsilon = \Delta/(\sigma + \Delta)$, must be smaller than 0.1. Within the SHS potential the strength of the attraction can be described by [191]

$$\tau = \frac{1}{12\epsilon}\exp u_o/k_B T. \tag{4.18}$$

With this equation the depth of the interaction potential, u_0, can be calculated in orders of $k_B T$:

$$u_0 = -\ln 12 \cdot \epsilon \cdot \tau, \tag{4.19}$$

and the reduced second virial coefficient, B_2/B_2^{HS} can be described by:

$$\lim_{\Delta\to 0}\frac{B_2}{B_2^{HS}} = 1 - \frac{1}{4\tau}. \tag{4.20}$$

To obtain the morphology of the dense protein phase the SANS scattering profiles with no intensity increase at low-q are fitted by a Guinier fit [184]:

$$I(q) \approx I(0)\exp -\frac{q^2 r_G^2}{3}, \tag{4.21}$$

This approximation is only valid for small q-values in the range of about $0 < q < 1/r_G$. Through this fitting routine the radius of the particles inside the sample is obtained. For scattering profiles with an increasing intensity at low-q for the dense protein phase

a Porod analysis is applied. As opposed to the Guinier analysis, the Porod analysis is only valid in the high-q-range, $q \cdot r >> 1$. The surface fractal dimension of the sample can be obtained from this analysis. The Porod law is defined by [184]:

$$I(q) = \frac{2\pi\Delta\rho^2}{q^P}\frac{S_{int}}{V} \tag{4.22}$$

where S_{int} is the sum of internal scattering surfaces and P the Porod exponent.

4.2.3 Results and discussion

4.2.3.1 Dimerization

It is known that from the protein isolating process BSA appears in a mono-/dimer composition caused by disulfide bridges between unpaired cysteines which are located at position 34 of the primary structure [11]. The results from the SEC measurements are shown in Fig. 4.6. The SEC curves do not show a dimer peak for the HSA sample. From this we can conclude that our HSA contains mainly monomers. Integrating over the monomer and dimer peak of a BSA sample yields peak areas which are proportional to the monomer and dimer concentration of the sample.

The ratio of dimer peak area to the area of both peaks correspond to a dimer fraction of 17.6 % which is a little bit below the reported literature value (21 % [226]). An average value of 17.03 % for the dimer contribution from SEC, DLS and SAXS experiments is close to another literature value of 17 % reported by Okubo et al. [227].

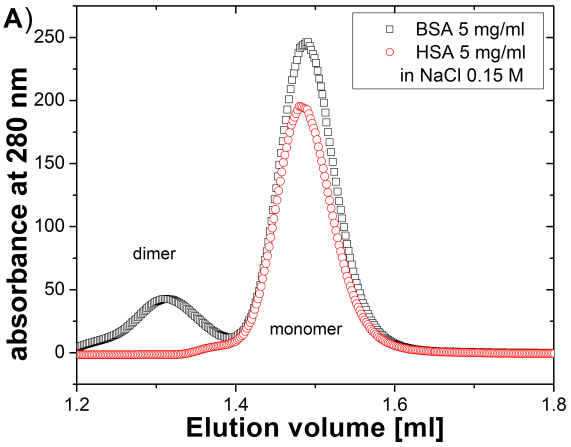

Figure 4.6: SEC measurement of a BSA 4.0 mg/ml (black squares) and HSA 3.1 mg/ml (red circles) in a 0.15 M NaCl solution.

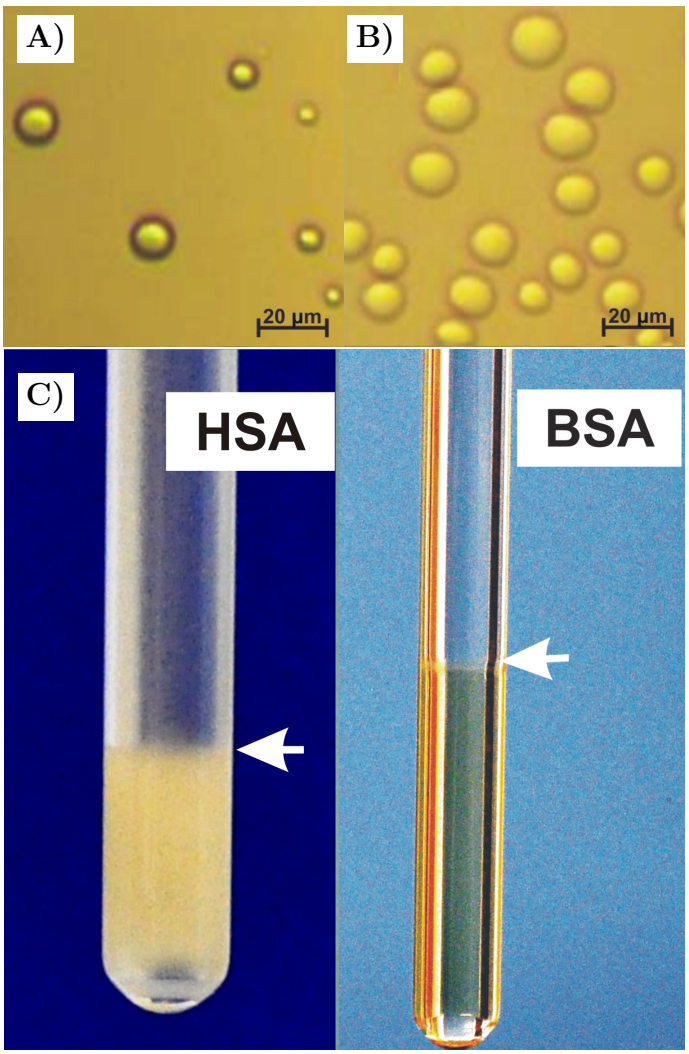

Figure 4.7: Different samples after LLPS. In an HSA sample of 31.1 mg/ml a clear solution with drops in the solution occurs. A) $c_s = 4$ mM and B) $c_s = 20$ mM. The scale bar corresponds to $20\mu m$. C) Dense phase of a HSA (left) and BSA (right) solution after phase separation at room temperature. The BSA dense phase stays clear whereas the HSA dense phase is still turbid.

4.2.3.2 Observation of LLPS in protein solutions

The presence of a LLPS is observed by a reflection confocal microscope. The LLPS region is defined by the formation of liquid droplets, with or without additional cluster formation. In Fig. 4.7 A) and B) the formation of liquid droplets is shown for samples with $c_{HSA} = 31.1$ mg/ml at different salt concentrations c_s. Outside the LLPS region, the cluster formation is observed. The formation of these liquid drops can only be observed in a narrow part of the condensed regime. First results of temperature dependent measurements indicate that the solution is more stable at low temperatures which results

in a smaller LLPS region. An example of a HSA (left) and BSA (right) sample at room temperature is shown in Fig. 4.7 C). It is clearly visible that the dense protein phase from the HSA sample is turbid against for the BSA sample the dense protein phase stays transparent. After centrifugation a sharp meniscus at the dilute-dense phase interface is visible.

4.2.3.3 Phase diagram (c_p-c_s plane)

From thermodynamics we know that a sample which is in the thermodynamic meta- or unstable region separates into two different phases [228]. The densities of these two phases are on the coexistence curve (binodal) and by measuring both protein and salt concentration (c_{p}^1, c_{p}^2, c_{s}^1 and c_{s}^2) with UV-Vis and X-ray absorption we obtain the phase boundary of the LLPS region, i.e. the coexistence curve.

LLPS and reentrant condensation

A new regime occurs in the reentrant phase diagrams of our samples by adding the phase boundaries of LLPS, determined by UV-Vis and X-ray absorption. This new regime shows where a LLPS takes place in the system and is established in the turbid regime, shown in Fig. 4.8. Each sample prepared in this region phase separates into a protein-poor and protein-rich phase with concentrations $\mathrm{c_p}$ and $\mathrm{c_s}$ corresponding to the phase boundaries. Data of the protein-poor phase shows that the phase boundaries are independent from the initial protein concentrations $c_{\mathrm{p,i}}$. This was shown for HSA (Fig. 4.8 A)) by the empty boxes, empty triangles and empty reverse triangles at $c_{p,i} = 31.1\,\mathrm{mg/ml}$, $c_{\mathrm{p,i}} = 47.8\,\mathrm{mg/ml}$ and $c_{\mathrm{p,i}} = 74.0\,\mathrm{mg/ml}$ and for BSA (Fig. 4.8 B)) by empty boxes and empty circles at $c_{\mathrm{p,i}} = 91.7\,\mathrm{mg/ml}$ and $c_{\mathrm{p,i}} = 183.3\,\mathrm{mg/ml}$. The magenta vertical bars indicate the prepared c_p before phase separation. All these data points are on the edge of a closed region where the border indicated the binodal line. As a guide to the eye the ellipsoid shape is highlighted in the phase diagrams by dashed black curves. The LLPS boundaries for the protein-rich phase are indicated by empty red circles and empty triangles for HSA and BSA. This result is consistent with the LLPS phase diagram of a colloidal system. This can be seen based on an isothermal cut through the multiparameter phase diagram [202]. A comparison between the presented phase diagrams and the phase diagram of a colloidal system [8] shows a similar phase behavior. For example a volume fraction of protein and salt in the correct region in the phase diagrams of colloidal and protein systems is necessary to cause a LLPS.

A comparison of minimal c_p for both phase diagrams shows that a roughly 1.6 times higher BSA concentration is necessary as opposed to the HSA case, which shifts the LLPS boundary for the BSA phase diagram to the right. The monomer and dimer composition of BSA solutions increases the protein and salt concentration because a higher amount of protein is necessary to reach the required amount of monomers, which is the only protein species responsible for the RC and LLPS as far as we know. The monomer/dimer composition cannot explain this high increase in the protein concentrations. Assuming a minimum HSA concentration of roughly 15 mg/ml to achieve LLPS, the BSA concentration with the same amount of monomers can be calculated by using

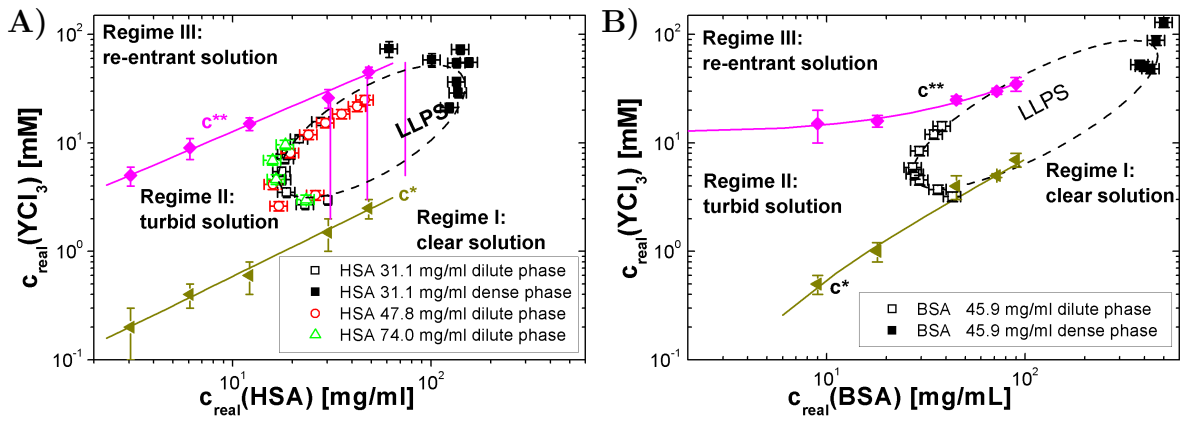

Figure 4.8: Plot of an LLPS phase diagram with real protein and yttrium concentrations determined by UV-Vis and SAXS. The solid gold and magenta lines show the phase boundaries c* and c**. Data points from the dilute protein and dense protein phases are indicated by empty and filled symbols. The dashed ellipsoids guide the eye through boundaries of the LLPS region. A) Phase diagram of HSA with different initial $c_{p,i}$ for the protein-poor phase and one $c_{p,i}$ for protein-rich phase. B) Phase diagram for a BSA sample.

the BSA dimer fraction to a value of 18.36 mg/ml. To explain the observed increase in the protein concentration, the monomer-dimer and dimer-dimer interactions have to be taken into account, too. In the case of BSA much higher protein concentrations can be achieved in the dense protein phase compared to the BSA case. This can be explained by the turbidity of the HSA dense protein phase at room temperature as shown in Fig. 4.7 C) which can be related to the formation of long range structures inside the sample. Such long-range relations can, for example, be observed in a gelation process. Due to this gelation process the c_p of the HSA dense protein phase is trapped at the gelation line and cannot reach higher protein concentrations.

Partitioning of protein and YCl_3 in the coexistent phases

The coexisting phases from one sample were connected by straight lines which are known as "tie lines" in the literature [5, 88]. We show the tie lines for different samples of HSA and BSA solutions in Fig. 4.9 A) and B). By comparing the different tie lines it is obviously that they all have positive slopes. From this we can conclude that there is an attractive interaction between the protein and the Y^{3+} cations. This can be seen by the fact that in the dense protein phases, where the protein concentration is higher as in the dilute phase, the salt concentration is also increased. This observation is consistent with observations of the crystal structure of β-lactoglobulin with YCl_3 [206], where it was shown that the salt ion binds to acidic amino acids on the protein surface. Plotting the values of the slopes against the prepared Y^{3+}/protein reveals a linear correlation between the amount of bound and prepared Y^{3+}/protein, which is presented in Fig. 4.9C). This behavior can be explained by the fact that with increasing salt concentration at constant

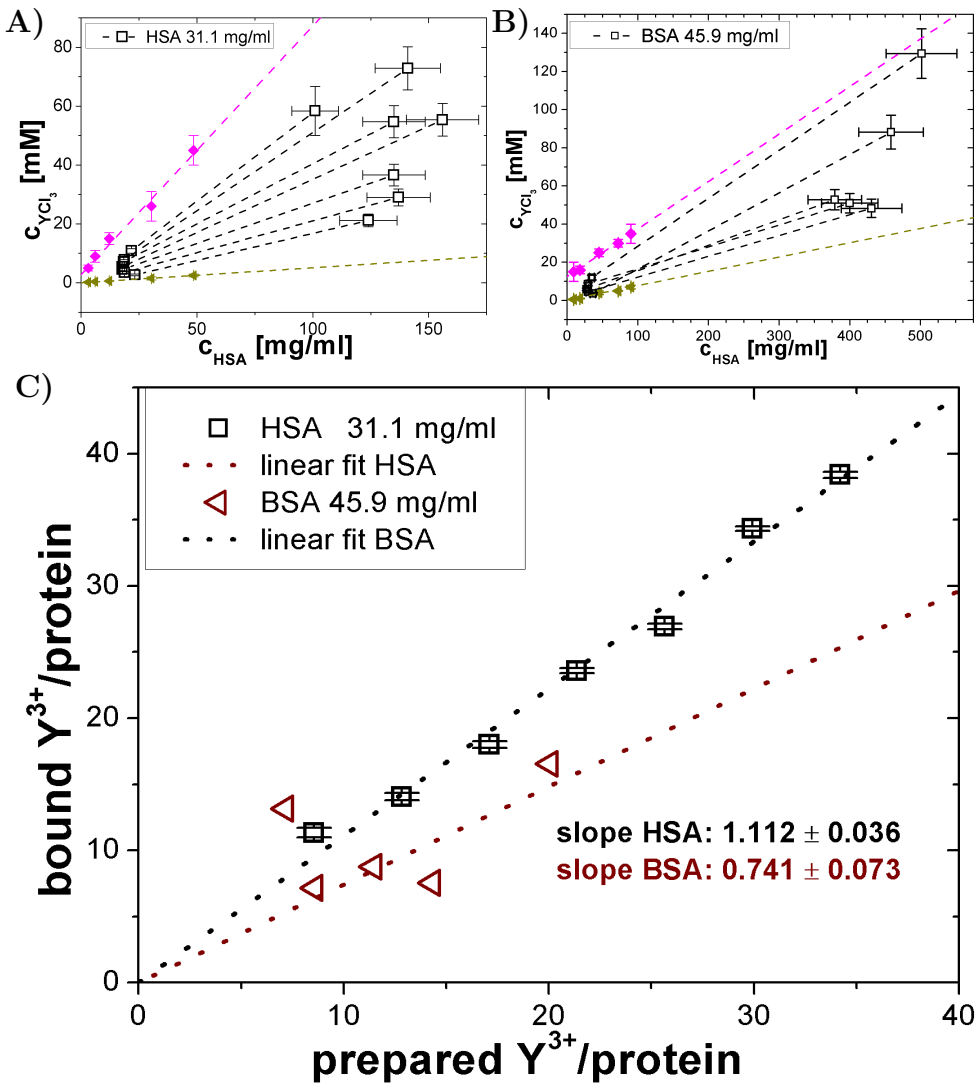

Figure 4.9: Tie lines for a sample set of HSA (A) and BSA (B). C) shows the increase of the slopes from the tie lines by increasing initial c_s.

protein concentration the number of available Y^{3+}-ions per protein will increase in the initial solution. With more available salt ions more of these ions can bind to the surface and the number of bound salt ions in the dilute and dense protein phase will also increase. Due to the negligible volume of the yttrium ion as compared to the protein a volume effect of the yttrium ion is negligible. Therefore the number of unbound yttrium in the dilute and dense phases should be similar and only the increasing number of bound yttrium to the protein will influence the slope of the tie line. The number of bound Y^{3+} ions per protein ranges between 5 – 20 for BSA and 8 – 35 for HSA. From the slopes of the liner fits in Fig. 4.9C) the increase of bound yttrium ions per protein by adding one more yttrium ion per protein in the prepared solution can be calculated. From the

slopes of the linear fits it is visible that HSA binds more yttrium ions per protein than to BSA. This effect can be explained considering that a BSA molecule has a smaller solvent-exposed surface than a HSA molecule. Therefore, less amino acids are available for the solvent and the yttrium ions. From the linear fits, shown in Fig. 4.9C), we found that adding of 1 yttrium ion per protein will increased the amount of bounded yttrium by 1.112 yttrium ions per protein, in the case of HSA. This would mean that more yttrium is bound to the protein than is contained in the solution and can be due to small pipette errors from the used pipettes. Another possible error is that the amount of yttrium in the solution is slightly overestimated by the X-ray absorption method. For the interpretation this increased value is not very important because the value is around 1, which means that we can assume that all yttrium ions are bound to the protein. This also explains why the y-interception of the tie lines is around 0. In the case of BSA the increase of yttrium ions bound to one protein molecule approximately equals 0.74. This means that the amount of bounded yttrium ions per BSA molecule is 36 % lower than in the HSA case. The value of 36 % is roughly 2 times higher than the amount of BSA dimers in the solution.

4.2.3.4 Differences in interactions in the LLPS region

In order to follow the change of the interactions in our solution we measured the samples by SAXS. Using a model fit, we extracted the reduced second virial coefficients to compare of the effective interactions for different salt concentrations and different proteins. We also apply this method to both the dilute and the dense phases after LLPS.

The reduced small angle scattering curves for a typical sample set with a c_p of 45.9 mg/ml are plotted as open symbols in Fig. 4.10A. The corresponding curves from the fitting with an ellipsoid SHS potential are shown as lines with different styles. For clarity reasons the intensities were shifted by multiplying a constant factor. The sizes of the particles were fixed in the fitting routine to the determined form factor of BSA. It is visible that our fitting routine fits the scattering curves quite well over the complete measured q-range. A small deviation is only visible for q-values between 0.1 and 0.2 $Å^{-1}$. In real space this q-range is in the order of a BSA monomer. With this we can explain the deviation from the form factor by an increasing amount of dimers or small oligomers of BSA. If the form factor is not fixed to a certain value, the fitting procedure yields a slightly increased form factor. The comparison between the increased form factor volume and the form factor volume for solutions without YCl_3, where the solutions consists of a well known mixture of monomer and dimers, yields to an increase of the form factor volume of 24.3 %. In the case of HSA this increase is 47.6 % because of the absence of dimers in yttrium free solutions. An explanation would be that by adding yttrium(III) to the protein more BSA monomers form a dimer. Measurements with a higher protein concentration would theoretically lead to an increased monomer-monomer correlation which would be visible at $q \approx 0.1$. This effect would be increased by even higher protein concentrations. This can be seen in Fig. 4.10B) by the BSA fitting curves (orange and blue). In the scattering curves this increased monomer-monomer correlation is not visible from which we can conclude that after the formation of dimers and oligomers

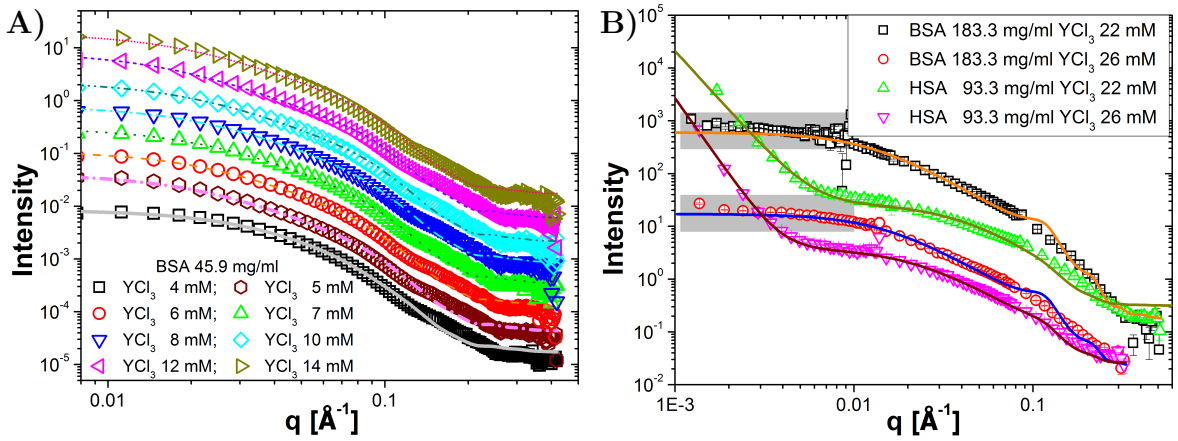

Figure 4.10: A) SAXS data and model fitting for samples with c_p of 45.9 mg/ml and different c_s from the dilute protein phase. For clarity the curves are shifted by a constant factor. B) The SANS data of the dense protein phase for two sample of BSA and HSA for two YCl_3 concentration. The corresponding fits are plotted by the solid lines. The shaded box shows the regions of the Guinier analysis. For clarity reasons the two curves for a $c_s = 22$ mM are shifted.

monomers are not distributed uniformly and the monomer-monomer correlation smears out.

From the fitting we extracted the stickiness parameter and calculated the reduced second virial coefficient B_2/B_2^{HS}. The B_2/B_2^{HS} for different sets of BSA and HSA samples is shown in Fig. 4.11. The empty symbols represent the calculated values of the dilute protein phases. The yellow area in this figure shows the theoretical limit for an LLPS [160].

All plotted curves are located more or less in the same Y^{3+}/protein region. Only for the BSA sample the maximum value of Y^{3+}/protein region is shifted slightly to lower values which also reflects also the slightly lower yttrium concentration range in the phase diagram shown in Fig. 4.8B). The trend for all curves are the same. This attractive strength of the effective attraction is weakest at the LLPS boundaries and at its maximum inside the LLPS region. For all determined samples which undergo an LLPS the B_2/B_2^{HS} is located below the theoretical limit of -1.5. Additionally, one BSA sample which is located close to the LLPS boundary was measured but does not show LLPS, for this sample the B_2/B_2^{HS} is located above the theoretical limit, which explains the absence of an LLPS. For HSA data set close to the critical point show nearly no change in the Y^{3+}/protein values but some variations in the interaction strength. From Fig. 4.11 it is also visible that the B_2/B_2^{HS} minimum for BSA is a little bit above the minima of the HSA samples which shows that the effective attraction interaction is weaker for BSA than for HSA. This can explain the decreased yttrium area of LLPS in a BSA solution.

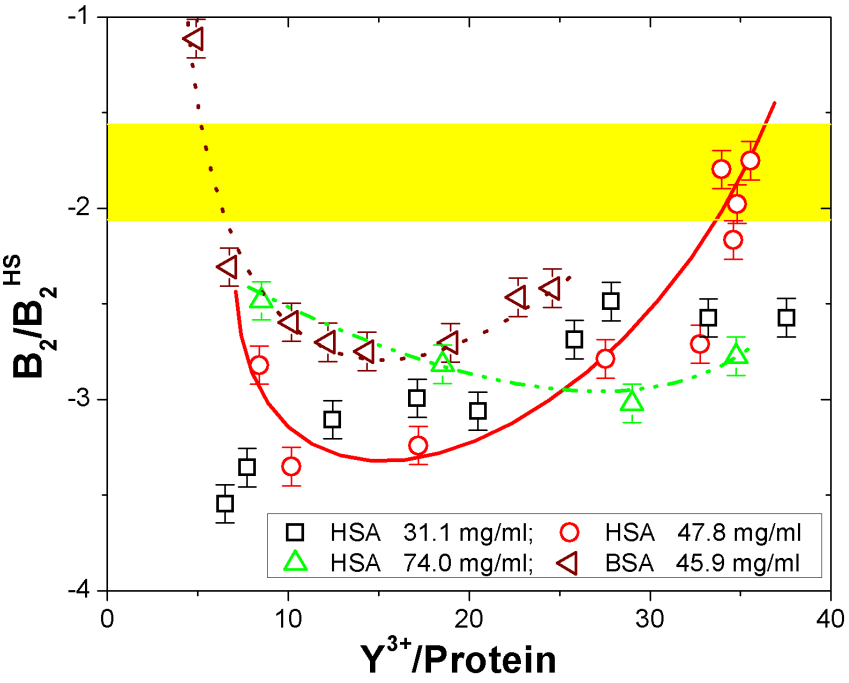

Figure 4.11: Reduced second virial coefficient B_2/B_2^{HS} of the dilute protein phase against the available number of Y^{3+} per protein. The yellow area shows the theoretical max. limit for an LLPS,[160].

Visual inspection at 20°C reveals that the dense protein phase looks transparent in the case of BSA whereas the dense phase of HSA is turbid. This turbidity comes from the formation of larger structures in the HSA sample which scatter visible light. In the SANS curves of HSA, these larger structures can be seen by an increase in scattering intensity at low-q-values (shown in Fig. 4.10B). At low-q-values the BSA samples show no increase in the scattering intensity and the BSA sample is analysed according to Guinier in order to determine the radius of gyration, r_G, of these protein particles. The q-region which is used for the Guinier analysis is shown in the figure by the light gray boxes around the scattering curve of BSA. It is found that the radius of gyration varies in the range of $73.31 \pm 1.29\,\text{Å} \leq r_G \leq 99.40 \pm 9.99\,\text{Å}$. At the lowest salt concentration of 20 mM YCl_3 the radius takes the highest value and decreases with increasing salt concentration until a minimum is reached. It then increases again at higher salt concentrations. A Guinier analysis of the HSA samples is not possible because of the reduced area of q-values with a linear behavior between the Porod region of the smaller particles and the Porod region of the larger structures. In the case of HSA the linear growth of the scattering intensity in a log-log plot at low-q-values can be observed by fitting a sum model of a power-law and SHS potential fit to the scattering curves. This power-law model yields the Porod exponent P which gives information about the fractal dimension of the larger structures. By averaging over all fitted P values a fractal dimension of 4.30 ± 0.33 is observed. This high fractal dimension, $P > 4$, can be described by a diffusive surface

of the large structure which comes from a non-homogenous density profile of the larger structures [188].

The fitting of the SHS potential shows B_2/B_2^{HS} values above the critical value of -1.5. In the case of BSA the behavior of the B_2/B_2^{HS} is reversed as compared to the behavior of the dilute protein phase. At the LLPS boundary a low value is determined and with increasing salt concentration this value increases to less negative values. In the case of HSA dense phase the B_2/B_2^{HS} values at the LLPS boundaries are higher than inside the LLPS region. However, inside the LLPS region B_2/B_2^{HS} shows no constant behavior and fluctuates. Until now we have no explanation for such a behavior.

As already shown by Zhang et al. the effect of reentrant condensation in a protein solution is not only restricted to YCl_3 and serum albumins. The authors also found RC for other negatively charged proteins at neutral pH and other trivalent ions [10, 47]. From this perspective it is also interesting if the effect of LLPS in a protein solution can also be induced by trivalent ions other than YCl_3. We tested a broad range of multivalent ions in our lab and found that ytterbium chloride ($YbCl_3$) and gadolinium chloride ($GdCl_3$) also induces LLPS in BSA solutions. LLPS can also be induced adding YCl_3 to β-Lactoglobulin (BLG) solutions. In the case of BLG the LLPS takes place several hours after the sample was prepared outside the LLPS region and the temperature was quenched below the spinodal line [118].

In this study LLPS is induced by the ion bridging effect of trivalent ions [206]. This effect describes the possibility that up to four amino acids from two different proteins can bind to the trivalent ion. In this case the trivalent ion forms a bridge between the two different proteins. In contrast to this effect another way to induce an LLPS is known in literature. It is reported that including of polyethylene glycol (PEG) can induce also the phase separation [5, 81, 88, 123, 229]. Through the volume of the PEG the available volume for the proteins is reduced which leads to an attractive force between the proteins, because the mean distance between the proteins shrinks with increasing PEG concentration. This effect is called excluded volume or depletion effect because the PEG depletes the volume between adjacent proteins. This depletion effect plays no role in our system because of the negligible size of the ions in comparison to the protein size.

4.2.3.5 Conclusions

Visual inspection of the phase diagram shows that an LLPS can be induced in a protein solution by adding multivalent salts. In a reentrant system the LLPS takes place in the turbid regime of the reentrant phase diagram where an attractive interaction exists. The positive slope of the tie lines reveals an attractive interaction between the protein and the trivalent anion. With the help of SAXS we measured the reduced second virial coefficient B_2/B_2^{HS} and we found that the value for each measured sample in the LLPS region is below the theoretical limit. We also discussed the differences between the two used proteins HSA and BSA in the phase diagram and their interactions.

4.3 Temperature effect on the effective interaction of the dilute protein phase

Between different experiments and in order to see the long time stability of our samples we stored these in the fridge to prevent bacterial growing. We did not use additional ingredients to prevent the bacterial growing because these ingredients would have also influenced the behavior of the proteins, at least by excluding volume effects. We observed that temperature changes influence the phase behavior of our samples. When heated, phase transitions occur and our solutions become turbid and when cooled down, the samples show the reversed behavior. A complete description of the temperature influence on the phase diagram and the interaction changes in a dilute protein phase is not the object of this thesis. These effects will be the subject of other diploma and master theses of our group, in particular of the theses by Michal Braun and Olga Matsarskaia. In this subsection we will give a short impression of the temperature effect on the dilute protein phase. The behavior of the dense protein phase will be shown in Sec. 4.4. To give a short impression of the temperature effect, we decided to perform two different kinds of experiments. First we prepared a sample at room temperature and separated the dilute protein phase from the dense protein phase by centrifugation. With the dilute protein phase a T dependent SANS experiment with increasing T was performed. For the second part we prepared a different BSA sample set at room temperature and at 4°C. c_p and c_s for the dilute and dense protein phases were determined and plotted in a RC phase diagram where the c* and c** boundaries are shown at room temperature. In the next step B_2/B_2^{HS} was extracted from the SAXS profiles of the dilute protein phase and the B_2/B_2^{HS} values were compared to each other.

For the first experiment the same sample was placed over the complete experimental time into the beam and T was varied between 14 °C and 30 °C. Using a X-ray beam would lead to beam damage at the sample over time which would influence our scattering curve. This is the reason why we used neutrons for this experiment. What we should note is that neutrons will not see the hydration layer around the protein and so the protein form factor will be change to smaller values. For this reason we measured also the form factor of BSA. The scattering intensity of this form factor measurement against the scattering vector q is plotted in Fig. 4.12D). For the fitting procedure, a smeared ellipsoid form factor was used, which was necessary because of the non ideal pin hole system, which is used for SANS experiments as shown in Sec. 3.5.5.2. From this experiment we found a form factor of $r_a = 12.5\,\text{Å}^{-1}$ and $r_b = 41.9\,\text{Å}^{-1}$, as suggested by Zhang et al.[173], can fit our scattering curve reasonably. This form factor yields to a protein volume of $91770 \pm 5500\,\text{Å}^3$.

The scattering intensity for the temperature dependent experiments on a dilute protein phase from a sample with $c_{i,HSA} = 31.1\,\text{mg/ml}$ with $c_{i,YCl_3} = 4\,\text{mM}$ against q are shown in Fig. 4.12A) and B). In Fig. 4.12A), we present the data for increasing intensities at low-q with increasing T. A further increase of T leads to a decreasing I, which is displayed in Fig. 4.12B). From these two figures we see that the form factor of the scattering

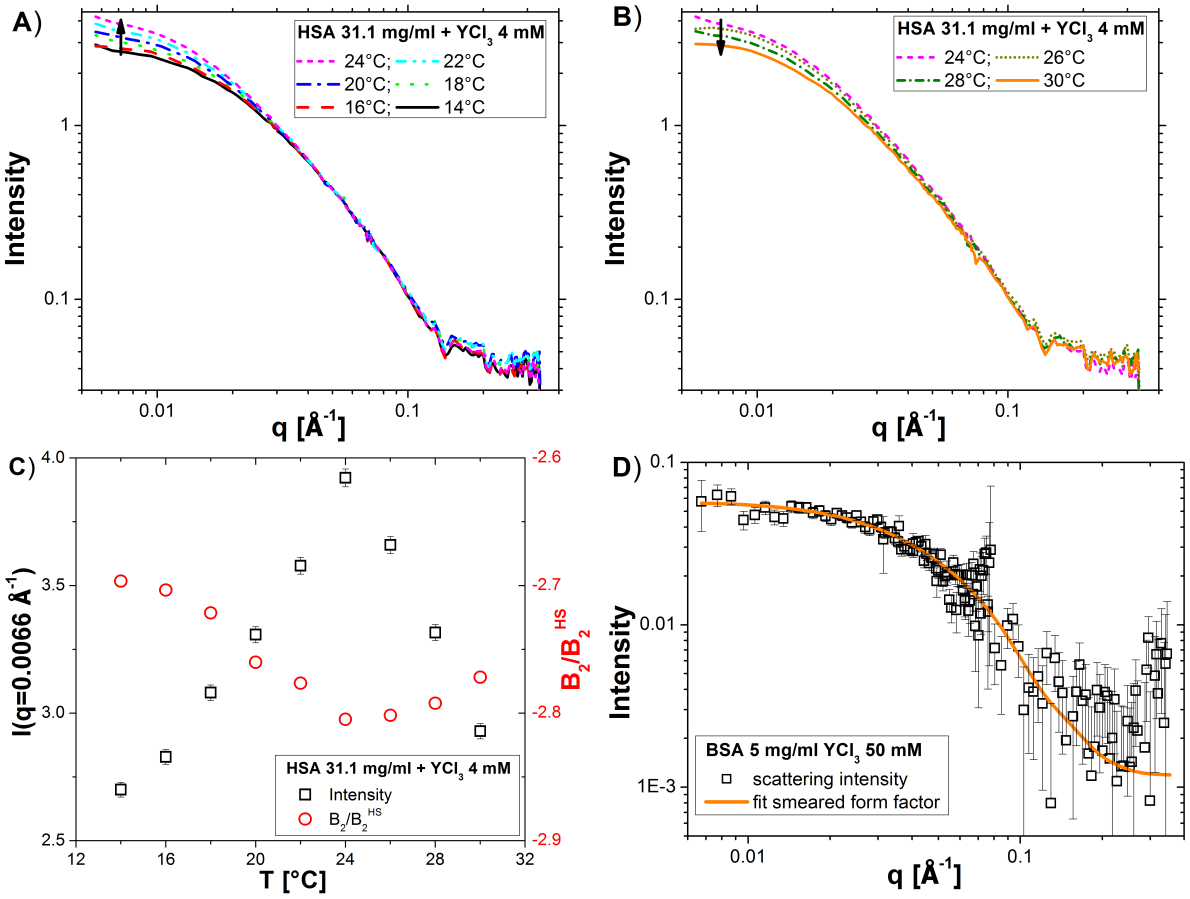

Figure 4.12: The dilute phase of a sample with a $c_{i,HSA} = 31.1\,\mathrm{mg/ml}$ and $c_{i,YCl_3} = 4\,\mathrm{mM}$ determined by SANS. In A) the increasing part of the scattering curves and in B) the decreasing part of $I(q)$ are shown with increasing temperatures. C) The scattering intensity $I(q = 0.0066\,\mathrm{Å}^{-1})$ and B_2/B_2^{HS} are plotted against T. D) The BSA form factor for SANS measurements in H_2O and the corresponding fit is shown.

curves stays constant at different temperatures and that I at low-q varies with T. This variation of I with T at $q = 0.0066\,\mathrm{Å}^{-1}$ is highlighted in Fig. 4.12C) by black squares. The scattering intensity increases first with T until it reaches a maximum at 24°C. This maximum of $I(T)$ shows the spinodal temperature of this sample. Approaching to the spinodal temperature yields to bigger intensity steps what is also shown by the diverging $S(q)$ at the spinodal line.

The B_2/B_2^{HS} at different temperature are calculated by using a smeared SHS ellipsoidal fit. For the fitting procedure the perturbation parameter ι was fixed to 0.08 and c_p to 23.2, Tab. A1, and the starting values for the scattering length density SLD to $SLD_{H_2O} = -5,6 \cdot 10^{-7}\,\mathrm{Å}^{-2}$ and $SLD_{protein} = 1.84 \cdot 10^{-6}\,\mathrm{Å}^{-2}$. Performing this fitting procedure yields to a point where τ stays constant for increasing T. This leads to a

point where τ will not decrease any longer. Decreasing τ manually leads to a breaking of the fitting. This breaking point is shifted to higher T by using a higher ι, which is the reason why we have chosen $\iota = 0.08$. Checking the resulting fitting curves for the points where τ becomes minimal it is visible that the fitted curve deviates from the scattering curves at low-q. Letting the form factor of the protein a free variable will solve this problem and also the problem with the non-decreasing τ. The problem with a variable form factor is that this will also influence the B_2/B_2^{HS} values. If the form factor becomes bigger, B_2/B_2^{HS} will increase, too, and vice versa. An increasing form factor leads to an increasing hard sphere with the same volume as the particle. This yields into a higher value for B_2^{HS}, which will decrease the value of B_2/B_2^{HS}. In our case the B_2/B_2^{HS} is negative and this leads to a less negative value with increasing form factor. From the fitting procedure, we get that the fitted form factor for a very dilute protein solution will not fit the form of the scattering curve. To fit these curves, a bigger particle form is necessary. At the lowest temperature, the volume of these bigger form factor increases to $206767 \pm 16509\,\text{Å}^3$. For the calculation of the error, the error from the fitting is taken into account. The errors from the fitting are quite small which would lead to a final error of around 1 %. In reality, we assume bigger error for the fitting and so fixed the error to $\pm 1\,\text{Å}$. The fitted volume is within the errorbars but is around 2 times higher as for the form factor which shows the formation of bigger particles like dimers or oligomers. With increasing T, the volume of the form factor also increases which leads to the assumption that the formation of oligomers takes place. This would fit to the observation made by Soraruf et al. [155]. The volume reaches maximum at the spinodal temperature and decreases again for higher T. This will influence our results in a way that the B_2/B_2^{HS} values near the spinodal T will be higher leading to a compressed curve in y-direction. The resulting B_2/B_2^{HS} are shown in Fig. 4.12C) as red dots. The B_2/B_2^{HS} curve shows the inverse behavior of the intensity curve and at high T the increase of the curve is compressed against the decrease of $I(q = 0.0066\,\text{AA}^{-1})$. In total, the B_2/B_2^{HS} curve shows the expected behavior that B_2/B_2^{HS} becomes minimal at the spinodal temperature and decreases again with higher T. For such a behavior a lower critical point in the phase diagram is expected and an LLPS takes place for higher T. Such a phase diagram shows a lower critical solution temperature (LCST) as mentioned in [230–232]. All values for this sample set are collected in Tab. A3.

For the second part of this chapter we investigated the temperature effect onto the phase diagram and the effective interactions for a different sets of BSA prepared at different initial temperatures. The first set is the already known 45.9 mg/ml set prepared at room temperature and shown in Fig. 4.8B). The BSA 45.9 mg/ml set is compared to three other sets of BSA solutions with an initial protein concentration of 91.7 mg/ml and 183.3 mg/ml. These three set were prepared in a 4°C room in order to enhance the handling of the dense protein phase. All four sample sets are shown in Fig. 4.13. The dilute protein phase of each sample are represented by the empty data points whereas the solid black and red data points shows the dense protein phase. The LLPS region at an initial temperature of 22°C are highlighted by the dashed black ellipsoid and the light orange area. In contrast to this the dashed blue line and the light cyan area represents the LLPS region at a preparation temperature of 4°. It can be easily seen that the LLPS

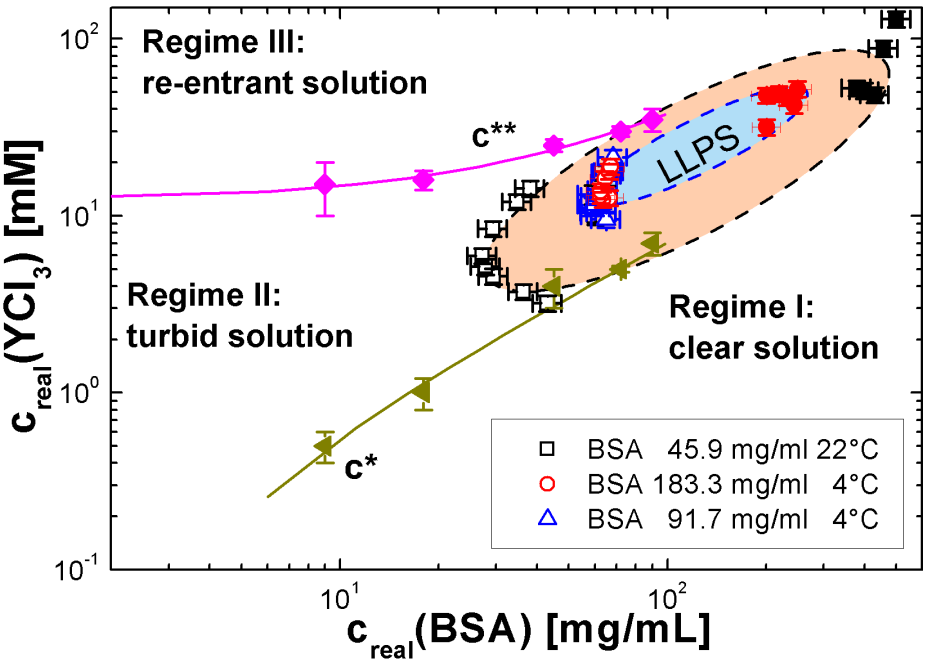

Figure 4.13: RC phase diagram with LLPS is plotted for 4 different BSA sample sets prepared at 2 different preparation temperatures. The empty data points represents the dilute protein phase where the solid black and red data points indicates the dense protein phase. As a guide to the eye the dashed black, 22°C, and blue lines, 4°C, shows the LLPS boundaries. The light orange and light cyan area represents the LLPS area for both used temperatures.

region at 4° is shrinked compared to the 22° ones in c_p and c_s direction. This shrinked LLPS region can be explained by the diploma thesis of Michal Braun from our group, which shows that the so called lower critical solution temperature effect of our system can be explained by hydration effects [233]. For low temperature the yttrium ions are surrounded by bounded water molecules. The temperature in the system is to low to break up the the bindings and the yttrium ions can not bound to the proteins. With increasing temperature more and more water bounds breaks and the yttrium ion can work as a bridging agent between the proteins an the LLPS region increases.

SAXS experiments were performed for the dilute protein phases shown in Fig. 4.13. The scattering curves were fitted by a SHS potential and the B_2/B_2^{HS} for each sample was calculated. The calculated value for the dilute protein phases are plotted in Fig. 4.14 against the available number of Y^{3+} ions per protein. This plot clearly shows that a much broader LLPS region can be achieved at higher sample temperature in the preparation process. With increasing T also the attraction strength increases. The minima in the B_2/B_2^{HS} curve, prepared at low T, is quite close to the critical value. At low T a small deviation in c_s from the minima is enough to reach the critical B_2/B_2^{HS} value for an LLPS. This effect explains also the smaller LLPS region at low T.

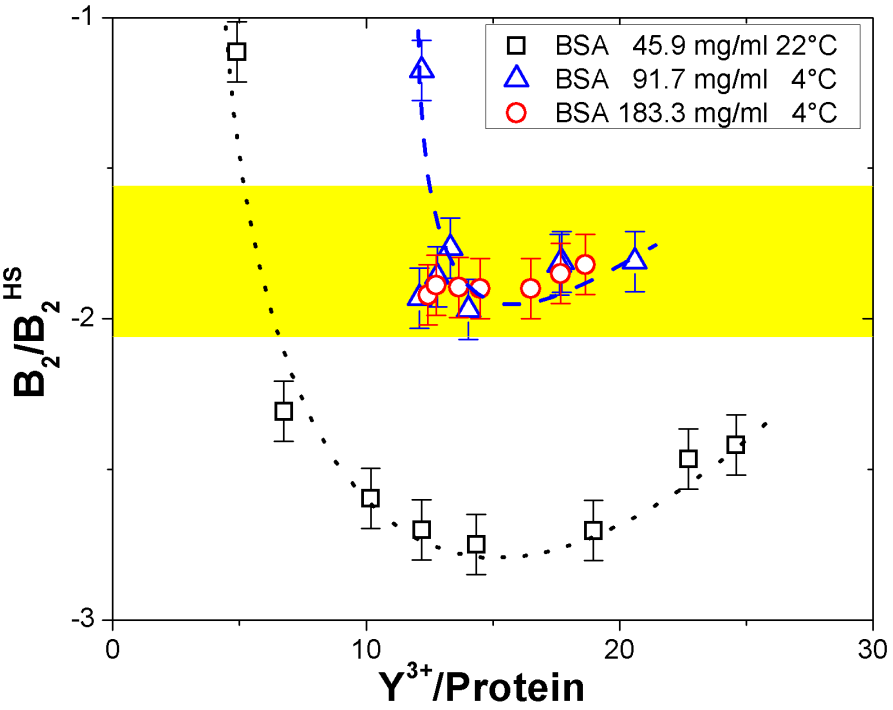

Figure 4.14: Reduced second virial coefficient B_2/B_2^{HS} of the dilute protein phase against the available number of Y^{3+} per protein for different temperatures. The yellow area shows the theoretical max. limit for an LLPS,[160].

In this section and the section before, we have characterized our proteins in solutions and we have seen that in a BSA solution an amount of dimers exists. By adding YCl_3 to the solution a RC behavior takes place and LLPS occurs in a closed area of the second regime. An LLPS is identified by microscopy and the dilute and dense protein phase are separated by centrifugation. The protein and salt concentrations of the dilute protein phase are determined and from these values the concentrations in the dense protein phase are calculated. This leads to the LLPS region in the RC phase diagram (Fig. 4.8). Connecting the corresponding dilute and dense phase from each sample leads to the so called tie-lines and from the positive slope of the tie-lines an attractive interaction between protein and salt are concluded. The strength of the interactions are extracted from SAXS data and for all samples inside the LLPS region, B_2/B_2^{HS} is below the critical value for the LLPS. The behavior of the scattering intensity in the LLPS region follows the compressibility which diverges at the spinodal line. Inside the LLPS region, I will be higher as outside of the LLPS region which can be explained by the fact that the LLPS boundary corresponds to the binodal line which is close to the spinodal line, especially at the critical point. An impression of the temperature effect onto the interaction potential is shown in the last part of this section. However this last part is only an impression and will be discussed in further diploma and master theses.

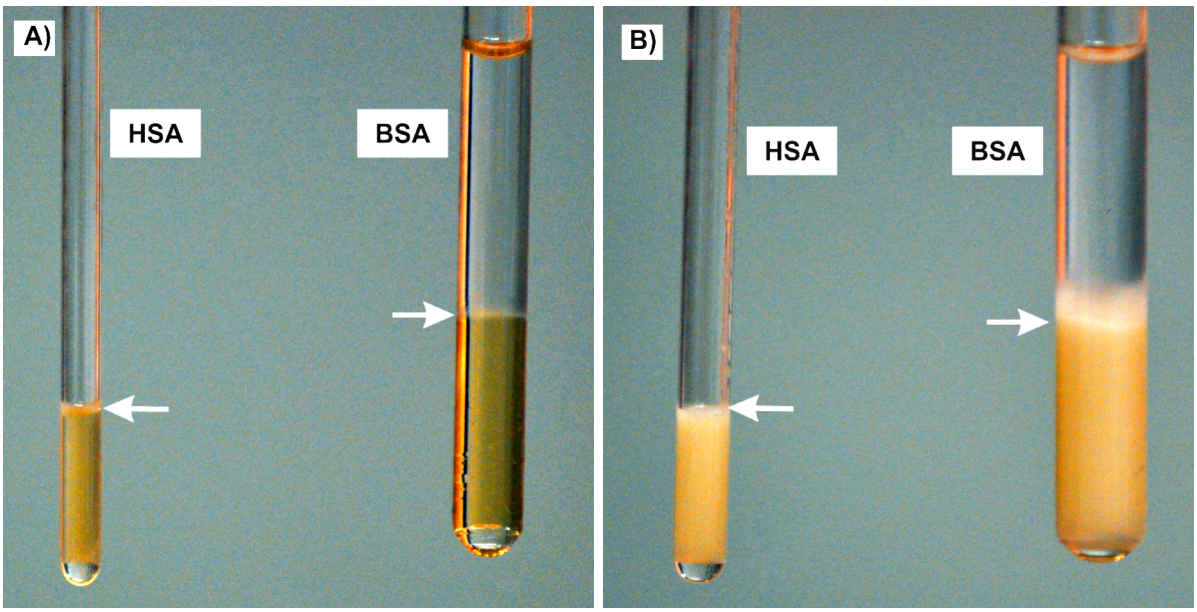

Figure 4.15: The temperature behavior of dense protein phases are shown. A) For samples at low temperature (5°C) and B) for a higher temperature (30°C).

4.4 Morphology and temperature dependant behavior of the dense protein phase

In the previous sections (Sec. 4.1 and Sec. 4.2) we showed how we come to an LLPS phase diagram and how it behaves. The effective interactions for the dilute protein phases are measured and the development with c_p, c_s and T are mapped. In this section, we will focus on the behavior of the dense protein phase. Differences between the two used proteins, observed by eye and by microscopy, are highlighted in Sec. 4.4.1. Differences in the hierarchical structure on microscopic lengthscales by varying T are observed by small angle techniques, shown in Sec. 4.4.2, and the interactions in different phases are calculated in Sec. 4.4.3.

4.4.1 Morphology of the dense protein phase determined by eye and microscopy.

As we have shown in Fig. 4.7C), a dense protein phase can be separated from the dilute protein phase by centrifugation. Storage of the dense phases in a fridge revels also their temperature dependent behavior. At low T, these dense phases are optically transparent in the case of BSA or less turbid for HSA samples (Fig. 4.15A)). Heating up these phases yields to a highly turbid solution as presented in Fig. 4.15B). Here we will discuss the influence of the temperature followed by microscopy.

A small amount of the dense protein phase is added between two cover slides and

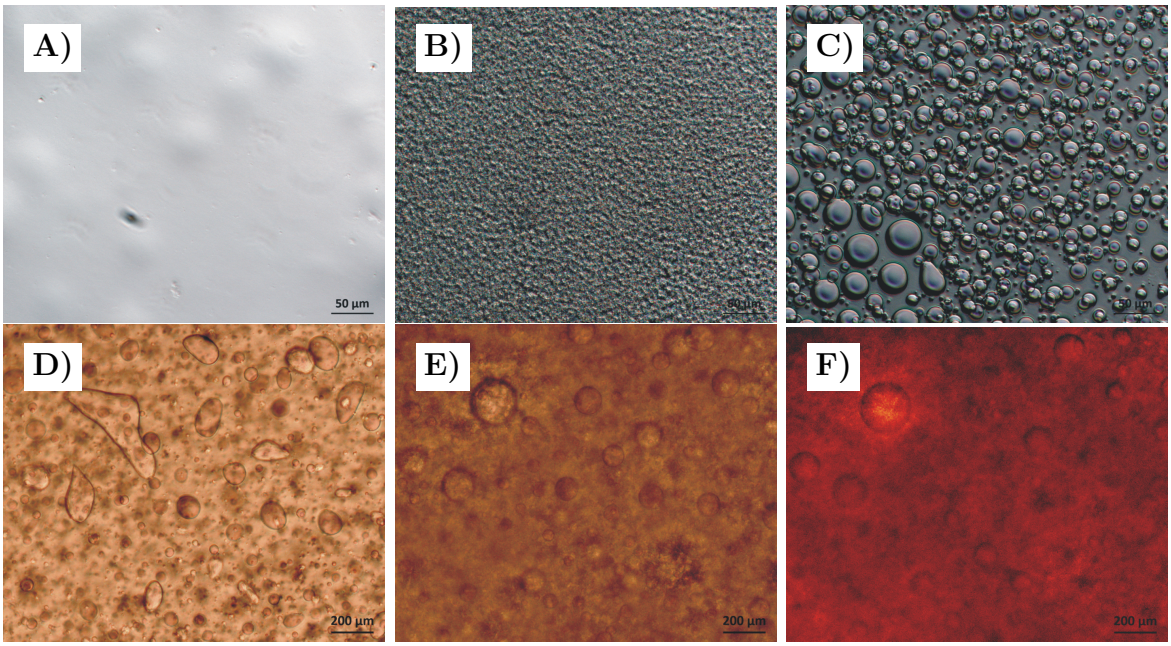

Figure 4.16: Microscope pictures from the dense BSA phase, A)-C), and the dense HSA phase, D)-F). A) and D) show the starting point of the temperature ramp, $T_{BSA} = 10\,°C$ and $T_{HSA} = 5\,°C$. At this temperature, a clear phase for BSA and a non clear phase for HSA can be observed. B) and E) show an example for the point when the dense protein phase becomes turbid. C) and F) presented examples for the highest T where the samples are highly turbid .

pressed to a thickness of around 100 µm. To protect the dense phase from evaporation, the two cover slides are sealed with silicon gel. With this small thickness, it is possible to follow the changes of the high turbid dense phase by varying T. The sealed two cover slides are placed into a Linkam temperature stage and a temperature ramp from low temperature (transparent or low turbidity) to high temperature (high turbidity) are applied. The temperature stage is placed under a microscope and a time series of pictures is recorded. Equal time steps between the recording of each picture are chosen to achieve a constant increase of T. An example for such a series is shown in Fig. 4.16. The pictures from the starting points of the temperature ramp are shown in Fig. 4.16A) and D). For BSA (4.16A)), a clear phase without features is visible. From Fig. 4.16D), the existence of droplets can be seen. These droplets are the reason for the turbidity of the HSA dense phase at low temperatures. From our experiments, we did not get rid of these droplets by further cooling down the dense phase before the sample freezes. Increasing T above a critical temperature conserves these droplets. The rest of the solution becomes turbid in the case of HSA. This is shown in Fig. 4.16E). An undefined structure forms by crossing the critical T in a BSA solution, which we presented in Fig. 4.16B). A further increase of T leads to the formation of bigger droplets in the case

of BSA. The droplets are also visible in the HSA solutions but the surrounding liquid phase becomes highly turbid. The end state of these experiments is shown in Fig. 4.16C) and F). For HSA, no variations of the bigger droplets are visible compared to the point where the background becomes turbid. Therefore it can be assumed that the HSA dense phase forms an arrested state. For the BSA sample, the formation of the bigger droplets can be followed by time. From C) it looks like the sample undergoes a further phase separation which cannot be observed by storing the sample in the mixing tube for several days. One possible explanation for the missing of a phase separation in the mixing tubes is that the surface of the used cover slides influences the sample and forced it to a phase separation. Another possibility would be that a local phase separation takes place but the overall density is to high to get a complete phase separation of the sample. First rheological experiments, performed by an other PhD student, Stefano Da Vela, on the BSA system gives some hints that the dense phase becomes at a gel above the critical T. We also assume gel formation in the HSA systems, with the difference to BSA that the gel is formed at all used temperatures.

What we should mention is that the resolution limit of the microscope pictures is around 1.2 µm for the BSA sample and 4.2 µm, for the HSA sample, which we owing to the magnification of the used objective lens. This low resolution is caused by the use of long working distance objectives which yields to a low numerical aperture. With the knowledge of the resolution limit of the microscope we can conclude that microscopy is an easy way to investigate the structure of our samples above a length scale of 1.2 µm. For the structure at shorter length scales another method is necessary. To determine the structure of the sample below this limit, we used SANS and USANS experiments. With the help of the USANS experiment connected to a very high resolution detector it is possible to get structure information of the sample up to a length scale of around 2 µm. So it should be possible to identify the undefined BSA structure in Fig. 4.16B) and also the structure of the turbid background in Fig. 4.16E) in the HSA case. These results are presented in the following section.

4.4.2 Phase behavior of the dense protein phase determined by small angle scattering

In the previous section visible light is used to characterize the dense protein phase. To observe changes at smaller length scales, we must switch to smaller wavelengths of the incoming beam. In this section, we used neutron radiation in a small angle scattering setup to characterize our samples. In the first part (Sec. 4.4.2.1), the influence from the different methods of loading the sample onto the scattering results is explored. Afterwards the structure of the dense protein phase is discussed on the base of the scattering profile (Sec. 4.4.2.2). The results from the fitting of the scattering curves are shown in Sec. 4.4.3. In the last part of this section, the long time stability of the dense protein phase is investigated.

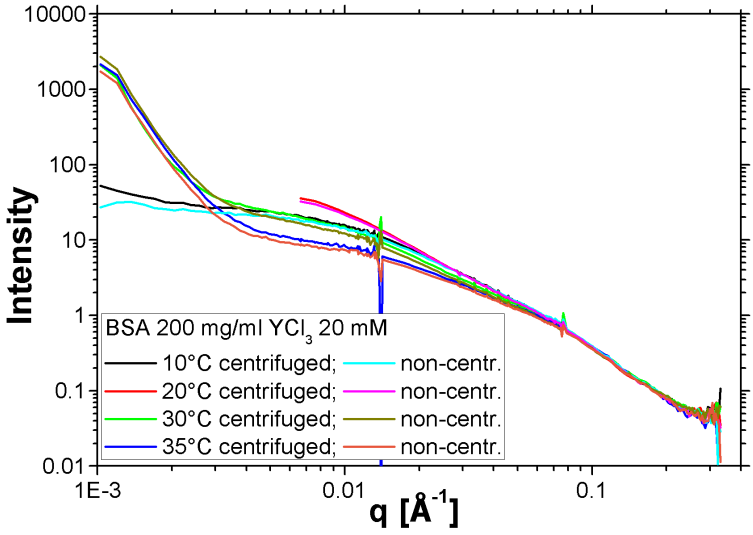

Figure 4.17: Comparison between preparation with and without centrifugation, as mentioned in the text at different T.

4.4.2.1 Scattering intensity dependent on the method of sample loading

The high viscosity of the dense protein phase prevents filling it easily into the sample cell (quarz glass cuvette). In addition, the thickness of the used cuvette hinders us to load the dense protein phase small spoon or similar tools. In this section, it is shown that the way to load the sample into the sample cells for SAS measurements does not influence the scattering curves. In the beginning, some sandwich cells with a teflon spacer inside to control the sample thickness are tried. By screwing the windows onto the cell, the samples were sealed. This method has the disadvantage that pressure and a shear force are applied to the sample. This leads to scattering curves which cannot be reproduced. To solve the problem of reproducibility, the sample is mixed directly in the cuvette. To separate the dilute from the dense protein phase, two different methods are possible. The first one is very simple but takes a long time. For this the gravity phase separates the sample with time, which takes several hours. Another disadvantage of this method is that the thickness of the cuvettes should not be smaller than 1 mm because otherwise, even after a waiting time of 1 day the phases are still not separated for smaller sample thicknesses as experimentally observed. The second method is to use centrifuge to separate the two phases from each other is used. For this purpose, special adapters were developed for the cuvettes that were built into the centrifuge. Using a moderate speed of 4000 RPM for 10 min is enough to separate both phases.

In order to get enough of the dense protein phase into the cuvette to perform the scattering experiment, the dilute phase is removed after the separation and on top of the dense phase a fresh sample was prepared and centrifuged. This is repeated for several times. The second method was chosen because of the low cost in time. In the case of the second method we need only 1 to 2 hours for the preparation of one sample,

where at least 24 hours is needed with the first method. To compare both methods with each other we prepared the same protein-yttrium composition from the same stock solutions and performed SANS measurements on both samples. The result from these measurements is shown in Fig. 4.17. It is visible that the scattering curve shapes of all non-centrifuged samples compared to centrifuged samples are similar. A small shift to lower intensities can be observed, in the case of non-centrifuged samples. This can be explained by pipetting errors at the sample preparation. At this point, we will not go into the details of the scattering curves. This will be part of the next section. From this experiment, we can conclude that a method, with first mixing and then centrifuging the sample, for loading the cuvette is found, which delivers reproducible scattering results.

4.4.2.2 Variation of the scattering profile by varying temperature

After showing, that the scattering data can be reproduced, the variation of the scattering profile by varying temperature will be investigated. The structure of the dense protein phase is discussed on the base of the T dependance of the scattering profiles. For this reason SANS experiments at the beamlines KWS-1 and KWS-2 at the FRM2, Garching, Germany and at D11 at the ILL, Grenoble, France, are performed. In addition to the SANS experiments USANS experiments at the beamline KWS-3 at the FRM2, Garching, Germany, are used to cover longer length scales. First the different contributions to the scattering profile are presented and afterwards the variation of the scattering profile with varying T is shown.

To discuss the scattering profile for HSA and BSA we will have a look Fig. 4.18. Only the lowest and highest T scattering profiles are shown, because all important features of the profiles are included at these temperatures. The first thing which is visible in Fig. 4.18A) and B) is the strong decrease of the scattering intensity at low-q and high T. Compared to this at low T no or a slight decrease in the case of BSA and an even smaller decrease occurs in the case of HSA. At medium q the low T scattering curves show a lower scattering intensity than the high T ones. At high-q the low and high T scattering curves are similar. A possible explanation for this is that particles with medium sizes are consumed and particles with bigger sizes form by heating up. Heating does not lead to a structural change of the protein, because no change of the high-q region occurs. This high-q region shows the form factor of a single protein.

To get knowledge about the structure of our samples we perform different kinds of fits to characterize the different length scales in the sample. First, the form factor of the protein is measured, which constitute the building blocks of the structures in our samples. To calculate the form factor, normally a dilute samples is needed, which is not available for the dense phase. The problem is that the dense protein phase cannot be diluted and if it would be possible to dilute the dense protein phase it would lead to a dilute protein phase. The assumption that the measured form factor from a dilute phase corresponds to the form factor of the dense phase is possibly not correct. The shape of a single protein molecule in the dense phase might differ from the shape it has in the dilute phase. To solve this problem, a form factor is searched, which can describe in both cases, with and without interaction potential, the high-q part of the scattering

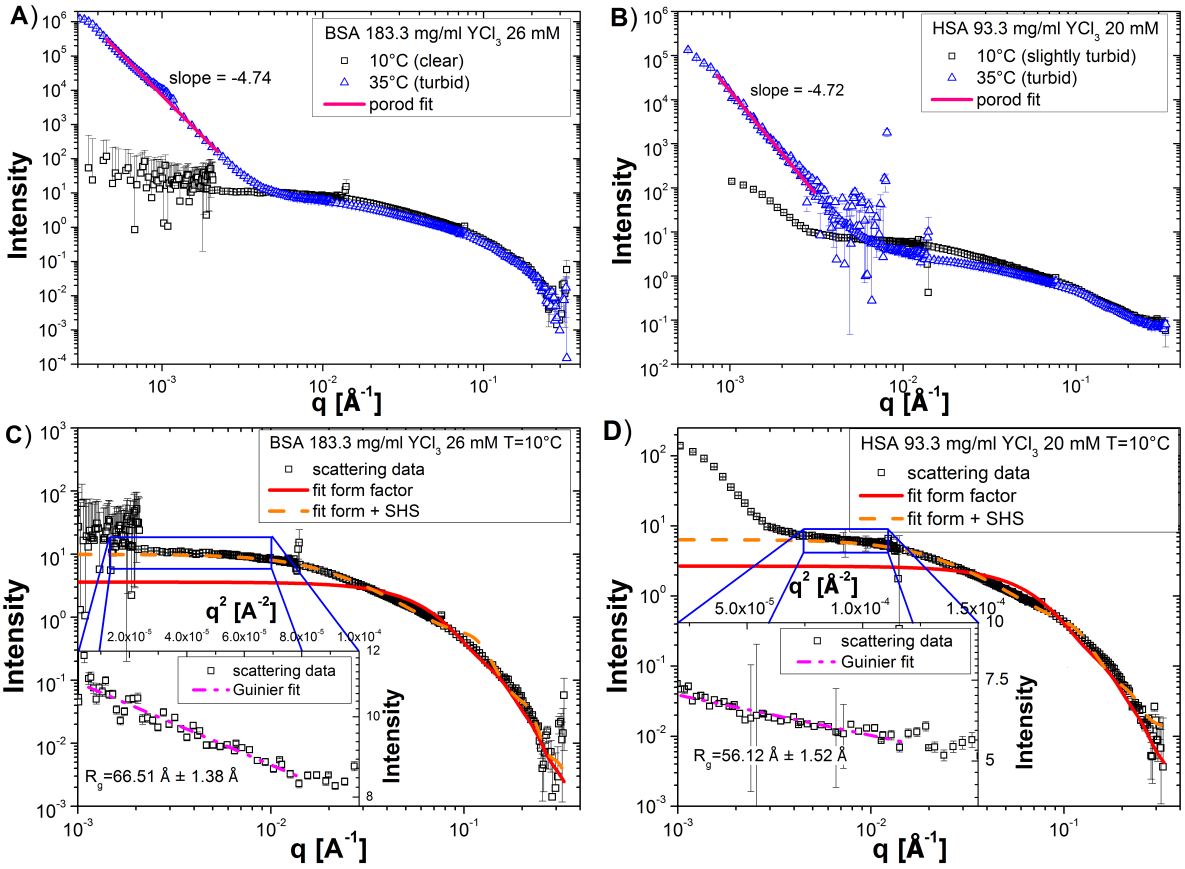

Figure 4.18: Scattering profiles at the lowest and highest T for an example of BSA, A), and HSA, B), dense phases are shown. In C) and D) the corresponding fits of the form factor and the form factor + SHS potential are presented. In the insets we plotted a Guinier plot of the low T curves with the corresponding Guinier fit at medium q.

curve. By using this fitting routine we found for both proteins an ellipsoid form factor which can describe the high-q region of the scattering curves. At $q < 0.1\,\text{Å}^{-1}$ a deviation of the form factor from the scattering curve is visible, when the interactions between the proteins are neglected. This influence hinders us to extract a correct form factor which is the reason why we call the fitted one an effective form factor. From the fitting we get an effective form factor of 12 * 42 * 42 Å^{-3} in the case of BSA and of 10.5 * 38.3 * 38.3 Å^{-3} in the case of HSA samples. This form factors correspond to a volume of 88668 Å^{-3} for BSA and 64517 Å^{-3} in the case of HSA. The fitted form factor curves with and without a SHS potential are plotted in Fig. 4.18C) and D).The fitted form factor for BSA matches to the determined form factor for dilute samples under physiological conditions as mentioned in [173]. From this we can assume that the extracted form factor fits to the real form factor of the protein. In the case of HSA the fitted form factor yields to a reduced protein volume which is around 25 % below the dry volume of the protein.

From the measurements on the protein stock solutions we know that in the case of BSA some dimers will be inside the sample which would lead to an increased volume of the form factor. This can explain the increased volume of the effective BSA form factor of around 10 % against the dry volume of the protein. The value of the increased volume is below the dimer fraction value presented in Sec. 4.2. There are two possible reasons for this lower value. The first could be a decreasing BSA dimer fraction in the dense protein phase. The other explanation would be that the interactions between the proteins will influence the fitting of the effective form factors. With this reason it would also be possible to explain the decreased volume of the effective HSA form factor.

The BSA sample at low T shows no additional feature at low-q, so that a Guinier fit can be used to determine the radius of gyration r_G of the particles. The low T HSA sample also shows a linear behavior within a q^2-range of $0.7 \cdot 10^{-4}\,\text{Å}^{-2} \leq q^2 \leq 1.2 \cdot 10^{-4}\,\text{Å}^{-2}$ in a Guinier plot. This is the reason why we also perform this analysis in the HSA case. It should be mentioned, that in an HSA sample at low T an increase of the scattering intensity at small q-values occurs. This would mean that a Guinier fit is not suitable in a strict sense, but if the particle is small against the bigger particle, which are responsible for the scattering intensity increase at low-q, an uninfluenced linear part can be observed in a Guinier plot. As long as the condition $q_{max} \cdot r_G < 1$ holds it should also be possible to extract r_G for the smaller particle from the scattering curve. At low T our HSA sample fulfills these conditions. With increasing T the length of the linear part in a I vs. q^2 plot shrinks and is shifted to higher q. The point of inflexion of the scattering curves is shifted into the linear part, which influences the linear part of the curves. This is the reason why, for HSA, the Guinier fit is performed only at small T. For the BSA samples we performed the fitting for low and high Tas long as no intensity increase occurs at low-q. Both the fitting routines and the corresponding parts of the scattering curve are shown as a Guinier plot in the insets of Fig. 4.18C) and D). For BSA we get a r_G of 66.51 Å ± 1.38 Å which corresponds to a volume of 1,232,393 Å^{-3}. Dividing this volume by the form factor volume leads to the amount of monomers in such a particle, which gives a value of 13.9 in the BSA case . From this we can assume that about 14 monomers form a bigger particle, in this case a oligomer. The calculated radius of $r_G = 56.12\,\text{Å} \pm 1.52\,\text{Å}$ for the HSA sample leads to a volume of 740,358 Å^{-3} which corresponds to 11.5 monomers per particle, using the fitted form factor of the dense protein phase. Using the dry volume of an HSA monomer leads to 9.1 monomers per particle. We assume that a value of about 9 monomers per particle is closer to reality than the other value because the measured volume of an HSA monomer is below the calculated dry volume, which is already a lower limit for the monomer volume. By dividing the volume from the Guinier fit by the form factor volume of BSA leads to a more realistic value. A more realistic value we will get This is possible because of the highly similar shape of HSA and BSA, obtained by crystal structures, as shown in [11, 12]. All values of r_G and the corresponding numbers of monomers per particle are listed in Tab. A4. From these results it is visible that at low T the r_G start with a high value at the border of the LLPS region and with increasing salt concentration first drop down. Inside the LLPS region a minimum is reached and a further increase of salt

concentration leads to an increase in particle size. From the BSA samples at $T = 20°$ it can be observed that the particle radius is also increased with increasing T. Furthermore the BSA particle sizes are bigger than the HSA ones. This increased particle size in the BSA case shows that this protein can form bigger particles more easily compared to HSA.

To learn more about the long scale structures we used two kinds of fit methods, the Porod and the Beaucage fits [187]. The Beaucage fit is a combination of a Guinier and a Porod fit which is the reason why both methods deliver knowledge about the surface fractal dimension of the long scale particles from the porod exponent. In literature different values for the exponent P are known [187, 234]. With a porod exponent of $P = 1$ a stiff rod or thin cylinder can be described. For a 'fully swollen' chain (in a good solvent) P changes to 5/3. Gaussian polymer chains and two-dimensional structures like lamellas or platelets deliver an exponent of $P = 2$. An exponent of 3 is reached by 'collapsed' polymer chains (bad solvent) and very rough surfaces. $P = 4$ points to particles with smooth surfaces. Generally, $P < 3$ applies for mass fractals, $3 < P < 4$ for surface fractals and $P > 4$ for diffuse interfaces [187, 235, 236]. All values obtained from the Porod and Beaucage fit are shown in Tab. A4. From the single Porod fit, shown in Fig. 4.18A) and B), we get an average $\bar{P}_{BSA} = 4.57 \pm 0.29$ and $\bar{P}_{HSA} = 4.61 \pm 0.38$ for $T = 30°$C and $T = 35°$C respectively. Using only a single Porod fit has the advantage that we can perform it also with a limited number of data points from the increasing part of scattering curve at low-q. Using only a limited number of data points for this fit leads already to a reliable result, although the errors of the fits, which use only a limited number of data points, should be increased. With this advantage it is possible to perform the single Porod fit on simple SANS data without using a special USANS beamline. This is the reason why we can use this fitting method also at lower temperatures as long as an increase at low-q can be observed, which is the case for the HSA samples only. The fitting procedure yields a $\bar{P}(T = 20°C) = -4.30 \pm 0.33$ and $\bar{P}(T = 10°C) = -3.46 \pm 0.38$. From these values it looks as if at low T in the HSA case the surface of the long scale particles is between completely rough and completely smooth. With increasing T the surface becomes first completely smooth before it changes to a diffusive one. In the BSA case at low T there is no increase of the scattering curve at low-q. At medium T we have only one value of -4.2 from the Porod fit. For BSA it is difficult to give a general answer concerning the surface of the bigger particles but we assume that the particles also start from a smooth surface before they get a diffuse surface.

The Beaucage fit comes with the advantage that additional to the Porod exponent P the radius of gyration r_G for the long scale structures can also be extracted. The disadvantage of this fit is that enough data points are necessary to obtain reliable values, especially at low-q. These data points are needed to do the Guinier analysis of the fitting method. To this, neutron scattering in a USANS set up is performed, at the beamline KWS-3, FRMII, Garching, Germany. For this experiment a longer experimental time is necessary to get a good scattering statistics. This is also the reason why we performed these measurements at the highest T because the scattering in forward direction is maximized at this T. An example for such a fit is presented in Fig. 4.19. The values for r_G and P are written in Tab. A4.

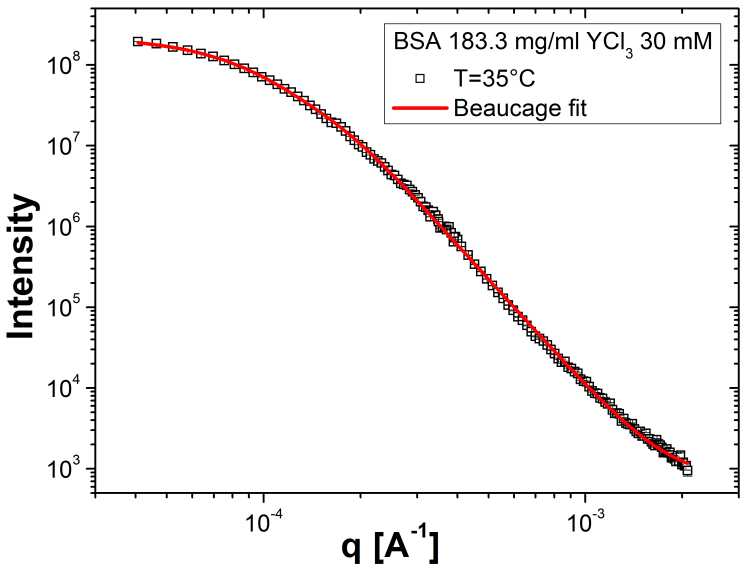

Figure 4.19: Scattering profile and the corresponding Beaucage fit.

From their averaged Porod exponents of $\bar{P}_{BSA}(T = 35°C) = -4.14 \pm 0.10$ and $\bar{P}_{HSA}(T = 30°C) = -4.11 \pm 0.09$ are found. In total the $\bar{P}$ values of the single Porod and the Beaucage fits within the experimental errorbars. The Beaucage fit shows also that at high T the long scale structure has a diffuse surface. For the size of the long scale structure the fitting leads to an average radius of $r_{G,BSA} = 1.81 \pm 0.19\,\mu$m and $r_{G,HSA} = 1.70 \pm 0.23\,\mu$m. Thus the long scale particle radii of both proteins are comparable. The polydispersity, PDI, index is calculated from the Beaucage fit to $PDI_{BSA} = 3.33 \pm 1.21$ and $PDI_{HSA} = 8.70 \pm 6.29$. The existence of the diffusive surface can be explained by the polydispersity of the bigger lengthscale in the systems. This polydispersity is reflected in the polydispersity index, which is greater than 1.62, as shown in [188, 190]. The error for the PDI in the case of HSA is quite high, which comes from the big difference in a single value. Compared to the case of BSA the polydispersity is higher in the HSA system.

In the next step we want to discuss how the different parts of the scattering profiles change with varying T and how we can connect these variations with the already mentioned length scales. For this purpose we divided the different scattering curves at the different temperatures by the scattering curve with the lowest temperature. The undivided scattering curves are shown in Fig. 4.20A) and C) and the corresponding divided scattering curves for both proteins in Fig. 4.20B) and D). For both proteins we can see that at all measured T the high-q part of the scattering curves does not change with varying T. This shows that the form factors of the monomers do not change, as already mentioned above. Variations in the scattering curves are visible at lower q and can be divided into two q-ranges. The first at medium q-values and the second at low-q-values. For BSA we see that the scattering intensity first increases at medium q without the

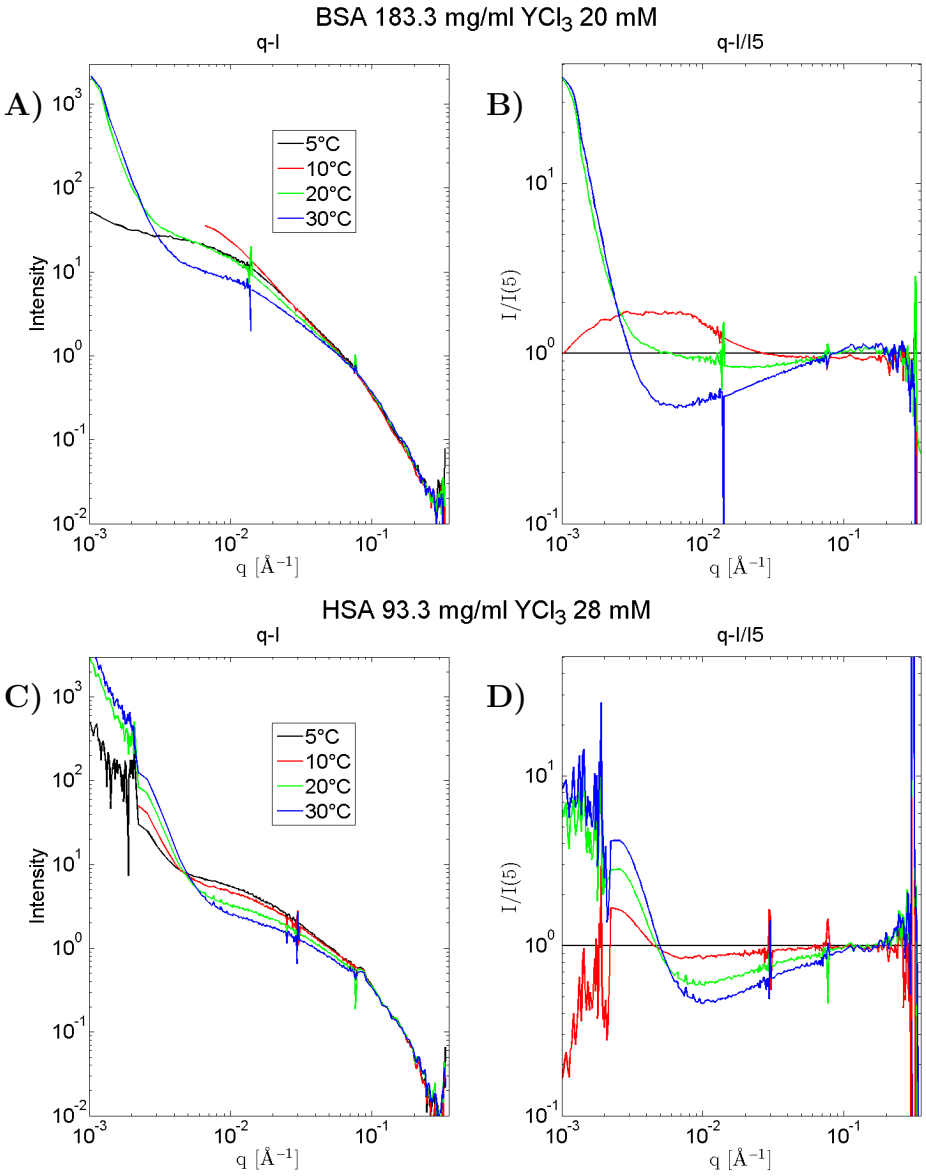

Figure 4.20: The variation of the scattering profiles with varying T is presented. In A) and C) the different scattering curves at different T for both proteins are plotted. These curves are divided by the curve with the lowest T of the corresponding protein, plotted in B) and D).

appearance of an additional peak at low-q. The guinier fit for these curves at 20 °C shows an increased r_G from which we can conclude that the medium particles size will grow slightly by increasing T from 10 to 20 °C. Further increase of T leads to the appearance of an additional peak at low-q, which can be explained by the formation of bigger particles. These bigger particles are formed by consuming the medium length scale particles, as can -be deduced from the decreasing scattering intensity at medium

q. The low-q scattering profile at the highest T [°C] does not show big changes. At medium q, compared to the 30°C curve a further decrease of I occurs. This decrease shows that even more bigger particles are formed. The profile at low-q does not change. Therefore the size of the bigger particles is the same as at 30°C. In Fig. 4.20 the lowest q-value only corresponds to a point on the flank of the scattering profile from the bigger particles. This flank characterizes the surface of the particles as explained above (Porod fit). At lower q the scattering intensity for the 35°C curve should be above the intensity for the 30°C curve, if more bigger particles are present. However this increase is outside of the measured q-range. The non changing r_G at the highest T shows also that the long scale structure of the system is fixed to a size of around 1.9 µm, as shown by the Beaucage fit. In the HSA case a similar behavior can be observed. The differences for HSA are that at low-q the additional peak for the long scale structure is visible at all investigated T and that the scattering intensity decreases in the medium q-range when T increases. This helps us to determine the variation of the long scale structure surface from a rough surface to a diffusive surface. Interestingly the sizes of these structures are the same in the BSA and HSA case from which we conclude that this size is unique for a serum albumin system.

In this section we have presented how the dense protein phase is build up. We found that the monomer form factor, determined by Zhang et al. [173] and already mentioned for the dilute protein phase in Sec. 4.3, can describe the scattering curve in the high-q-range, neglecting the interactions. Using the same form factor to fit an elliptical SHS potential shows deviations between the used form factor and the high-q part of the scattering curve. These deviations originate from the high protein volume fraction in our solutions, which leads to some special features of an ellipsoid scattering curve. This special features cannot be reproduced by the Serum Albumins, because they are not completely spherical. But the ellipsoid form is the -best fitting geometrical form to describe the proteins. We conclude that we can use the monomer form factor to describe the scattering curve. For BSA no increase in the low-q part of the scattering curve occurs at low T, which shows that no bigger particles are formed at these temperatures. At low T only a medium sized particle can be observed and the size is described by a Guinier fit. With increasing T the size of the medium size particle increases. After crossing a critical temperature the formation of a low-q peak occurs, which can be described by the formation of longer scale structures. When this low-q peak arises a decrease of the medium size structure can be observed. This shows that the longer scale structures consume the medium size structures. The same applies to the HSA scattering curves at different T. The only difference is that the low-q peak can be observed at all investigated temperatures and that the amount of medium size particles is decreasing continuously by increasing T. So far we made only a qualitative description of the system. A more quantitative description will be given in the next section where we will describe the effective interactions in the system.

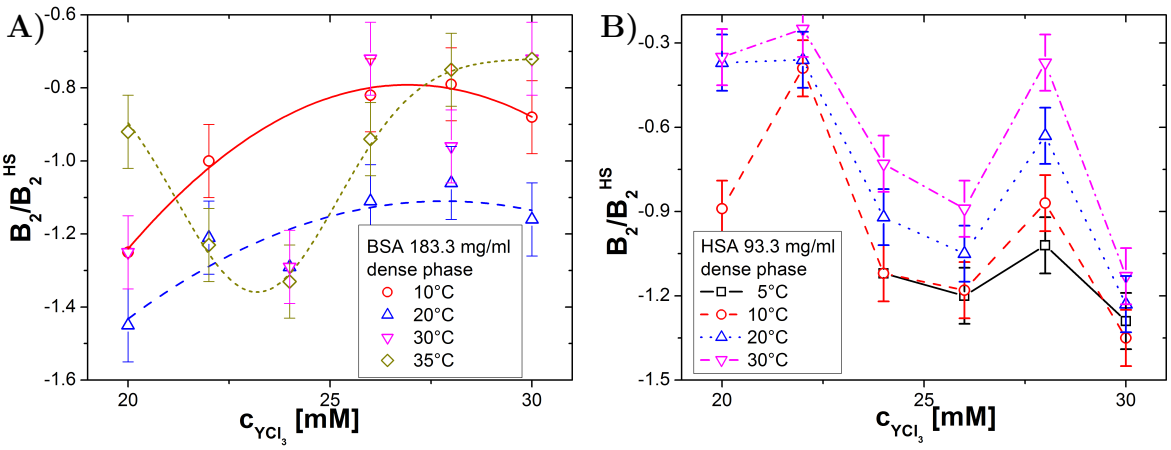

Figure 4.21: The c_s dependence of B_2/B_2^{HS} is plotted for different T for both used proteins, BSA, A), and HSA, B).

4.4.3 Effective interactions in a dense protein phase studied by small angle scattering

Whereas in the previous section we described the interactions of the dense protein phase in a qualitative way, this section shall deal with a more quantitative description. To this end we used a SHS potential to calculate the B_2/B_2^{HS} as already done for the dilute protein phase in Sec. 4.1 and Sec. 4.2. The resulting B_2/B_2^{HS} values and the corresponding potential depth, u_0, are shown in Tab. A5 for the BSA system and in Tab. A6 for the HSA case.

The c_s dependence of B_2/B_2^{HS} for different T values is visualized for BSA in Fig. 4.21A) and for HSA in Fig. 4.21B). As a guide to the eye we plotted a parabolic fit for the two lowest temperatures and a manually drawn line for the highest T curve in Fig. 4.21A). For HSA we plotted the data as symbols connected by lines because there is no clear relationship between B_2/B_2^{HS} values for the different salt concentrations. For BSA we found that for $T \leq 20°C$ the B_2/B_2^{HS} values at the edge of the LLPS region are lower than in the LLPS region, which shows that the attraction is higher at the edges. This is in contrast to the findings for the dilute protein phase where the attraction is higher inside the LLPS region. Although initially counterintuitive, there is still a reasonable explanation for this phenomenon. From the theoretical side the second virial expansion is only valid for small protein volume fractions. In the case of the dense protein phase the volume fraction is high. With such a high volume fraction additional interactions, which are neglected at low concentrations, influence the second virial coefficient. If this influence leads to an increase or a decrease of B_2 can not be easily answered. From the experiments it seems that B_2/B_2^{HS} increases and an effective weaker attraction is observed. This does not mean that it is impossible for the system to undergo an LLPS with the observed values, because the critical value for an LLPS will also be shifted. Increasing T from 10°C to 20°C leads to an increase in attraction which is visible at lower values of B_2/B_2^{HS}. The B_2/B_2^{HS} values do not change with increasing

salt concentration. This also explains the results obtained from the Guinier fits shown in Tab. A4. The Guinier plots show that the size of the medium sized particles increases when T is increased to 20°C. We see here that the increasing interaction between the proteins leads to the formation of particles with a larger size. As long as no gelation takes place the dependence of B_2/B_2^{HS} on c_s looks straight forward. Above 20°C the start of a gelation process is observed in the dense protein phase. This leads to a more complex behavior of B_2/B_2^{HS}. For $T = 30$°C no straightforward behavior can be observed and the B_2/B_2^{HS} values vary strongly with increasing c_s. The behavior is opposed to the one observed at $T = 35$°C. Therefore, it seems that the highest attraction takes place inside the LLPS region. For higher T values we found a second LLPS in the dilute protein phases, shown in Sec. 4.3, and by following the same argumentation as above it can be explained that the interaction decreases nearly all samples. Until now we have no explanation for this behavior. This behavior was not expected because of the LCST behavior of the system. For such a system showing LCST behavior, we assumed an increased interaction between the proteins in the dilute protein phase at higher T values. Below the critical point of such an LCST system the interaction is not strong enough for an LLPS. Increasing T above this critical temperature leads to an increased attraction, and the system undergoes an LLPS. A stronger interaction in the dilute protein phase would lead to a decreased interaction in the dense protein phase. For the HSA system (Fig. 4.21), where gelation takes place for all T values, we could not observe effects of c_s variations on B_2/B_2^{HS} either. In this system, the attraction between the proteins clearly decreases with increasing temperature. This system's behaviour corresponds to our expectations. It is important to mention that for both systems all calculated B_2/B_2^{HS} values for the dense protein phase are located above the critical B_2/B_2^{HS} value of -1.5 for LLPS. This can be related to the high protein concentration of the dense phase. When the attractive interaction is strong enough gelation takes place, which changes the B_2/B_2^{HS} behavior. Until now we cannot describe the changes in B_2/B_2^{HS}. Concerning the fitting routine it has to be stressed that by using the power-law potential to describe the visible part of the upcoming low-q peak only a small part of the scattering curve, between the low and medium q region, is used to calculate the interactions in the system. With increasing T this part shortens because the low-q peaks start at higher q-values. This means that it is possible that the fitted value for the interaction can be slightly influenced which can lead to the jumping behavior of the B_2/B_2^{HS} values. For low T values in the BSA system this problem does not occur because there is no low-q peak. This could lead to the observed dependence of B_2/B_2^{HS} on the salt concentration.

In this section we used different experimental techniques to cover a large region of length scales between some Å up to several µm. With this huge length scale range we qualitatively and quantitatively described the structure of the dense protein phase as a function of T. We found that the form of the SANS curves can be described by an ellipsoid form factor with the volume of a protein monomer. These monomers form the basis of particles with a medium length scale between 10 and 20 nm in diameter in the case of BSA and between 6 and 12 nm in diameter in the HSA case. This size would correspond to a number of 10 to 50 monomers in one particle in the BSA system and between 2 and 10 monomers per particle in the HSA system. For the BSA solutions

we found that for $T > 20°C$ a peak appears at longer length scales. In contrast to the BSA system this low-q peak is visible for all investigated T values in the HSA system. From rheological measurements on the BSA system, performed by another PhD student, Stefano da Vela, we know that at higher T a gelation takes place in the dense phase of the sample. Therefore we can connect the low-q peaks in the SANS curves to the gelation process. A Beaucage fit leads to a size of approximately 1.75 µm for the longer length scale structure. This size corresponds to the medium size of cages which will be formed during the gelation process and in which the medium sized particles and monomers are trapped. With increasing T we also found that the intensity of the low-q peak increases whereas in the q-range of the medium sized particles the intensity decreases. This shows that at higher T the amount of gel cages increases, the gel density increases and that these gel cages are built up by the medium sized particles, observed by rheology experiments. According to the Beaucage and Porod fit parameters, the surface of the gel has a diffusive surface. Using an SHS and a power-law potential for the fitting yields the B_2/B_2^{HS} values. It becomes clear that in the BSA system at low T the effective interaction increases first with increasing T. After the gelation process has started the effective interaction decreases with increasing T. For the HSA system the interaction strength decreases with T. This is illustrated by the gelation peak in the SANS curves at all investigated temperatures. Concerning the effective interactions it is interesting that for all samples the B_2/B_2^{HS} value is above the critical value for an LLPS but still negative. We conclude that an attractive interaction is necessary for the systems to form a gel but the interaction must not be too strong, since strong interactions lead to LLPS as an alternative phase transition. In the next section we will investigate how the phase diagrams and interactions are influenced by varying the content of water and heavy water in the solvent. The composition of the solvent will be changed stepwise from a 100 % water to a 100 % heavy water solution.

4.5 Influence of heavy water on liquid-liquid phase separation

For neutron experiments it is an advantage to prepare the samples in heavy water, D_2O, because of the high isotropic scattering of normal water, H_2O. The high isotropic scattering of normal water is caused by the hydrogens bound to oxygen in normal water. This isotropic scattering increases the background of the experimental results which will increase the needed scattering time at high-q to get a good statistic. This high background also leads to a loss of shape information of the single particles which makes it difficult to determine the form factor of small particles in H_2O. In this section we will discuss the influence of D_2O onto the phase behavior of the used protein-salt mixtures. Changes in the phase behavior that appear upon changing the solvent from H_2O to D_2O can be explained by the difference in hydrophobicity of the two solvents, with D_2O being more hydrophobic. In the first part, Sec. 4.5.1, microscopy data is used to show how LLPS is influenced by changing from . In the following two sections observed qualitative,

Sec. 4.5.2, and quantitative, Sec. 4.5.3 observed by SAS techniques are discussed.

4.5.1 Optical observations of the solvent effects on LLPS

In this section we investigate how the phase diagram varies by adding D_2O. For this reason we focused on optical observations by eye and by microscopy. The first step to describe the influence of this different solvent on a system is to investigate the phase behavior of this new mixture. If the phase behavior stays constant it can be assumed that the solvent plays no role for the used system. However, even small amounts of D_2O inside the solutions lead to differences in the behavior. Big cluster which are visible by eye can be observed in the sample tubes by using some D_2O inside the second regime. A shift of the c^{**} boundary can also be observed between a pure water and a pure heavy water system. For the c^* boundary no big variation can be observed. To locate the LLPS for the different Φ_{D_2O} a microscope was used to identify LLPS, as shown in Sec. 4.2. For example, a series of BSA microscope pictures are shown in Fig. 4.22 where Φ_{D_2O} was

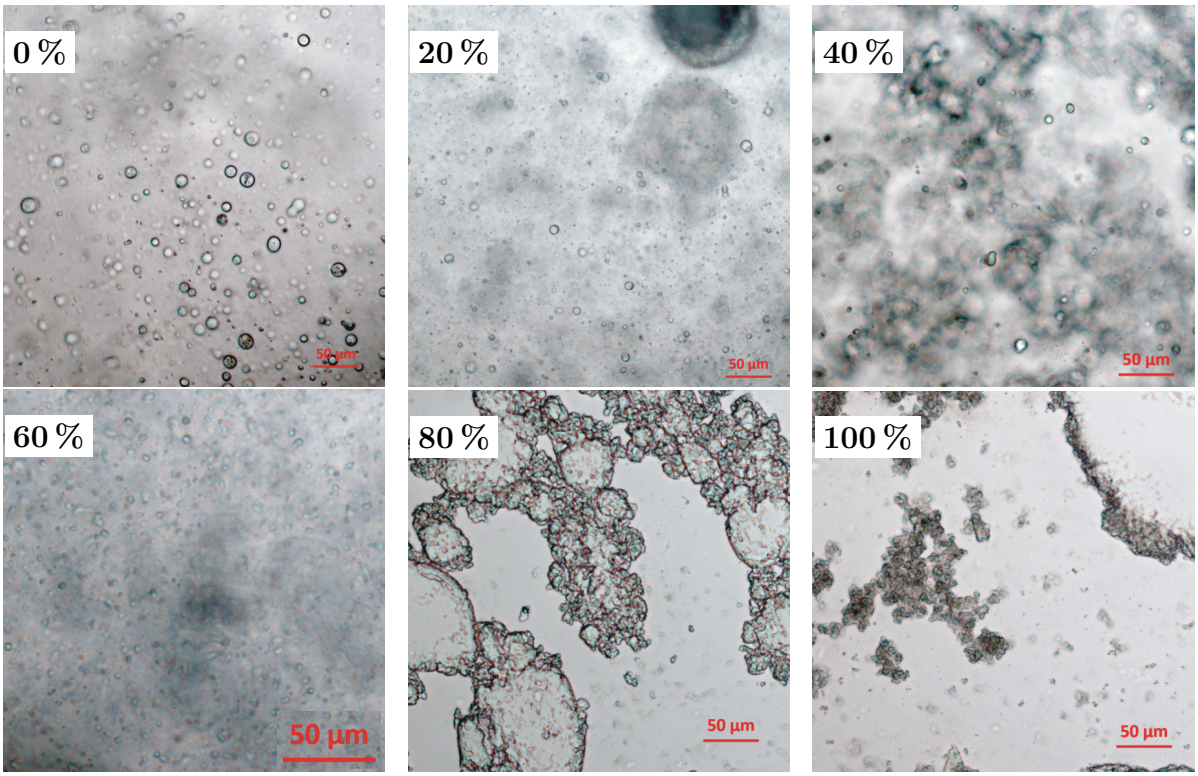

Figure 4.22: The increasing cluster formation with increasing Φ_{D_2O} is shown as an example at 6 different BSA 91.7 mg/ml + YCl_3 solutions with varying Φ_{D_2O}. Six different Φ_{D_2O} are shown: A) 0 %, B) 20 %, C) 40 %, 60 %, 80 % and 100 %. For a Φ_{D_2O} of $\geq$ 80 % and Φ_{D_2O} the turbidy becomes very strong and the sample was covered by a cover slide to decrease the thickness. No LLPS can be observed for these D_2O volume fractions.

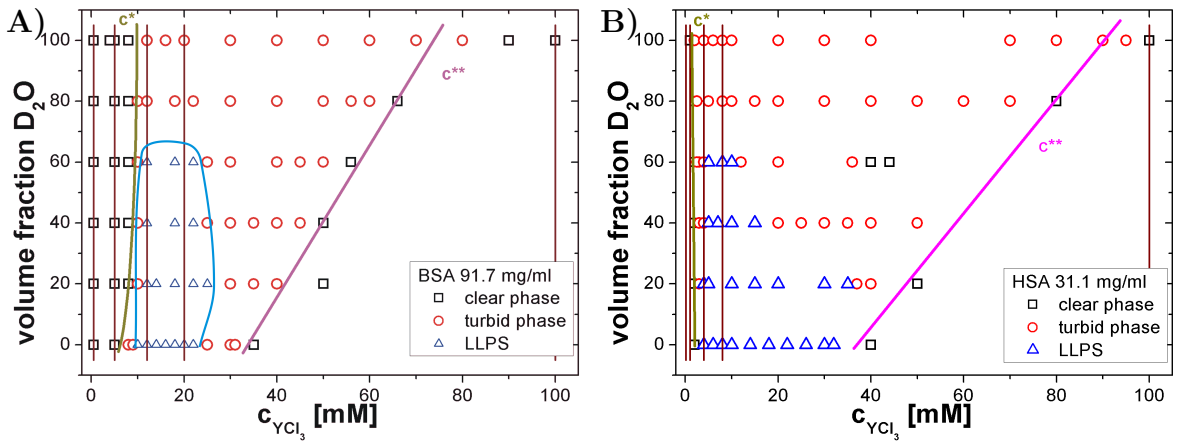

Figure 4.23: Dependance of the phase behavior on volume fraction of heavy water (Φ_{D_2O}) and salt concentration for fixed protein concentrations. The resulting phase diagram in the (c_s, Φ_{D_2O}) is shown for BSA, A), and HSA, B). The chosen salt concentrations for the SAXS experiments are marked by the brown lines in both phase diagram.

increased from 0 %, in steps up to a Φ_{D_2O} of 100 %. It is visible that with increasing Φ_{D_2O} an increased cluster formation can be observed. At low Φ_{D_2O} both LLPS and cluster formation takes place. With increasing Φ_{D_2O} the amount of liquid droplets inside the solution decreases while the cluster volume fraction increases.

With the knowledge of the phase boundaries we produced a new phase diagram in the (c_s, Φ_{D_2O}) plane. These new phase diagrams are plotted in Fig. 4.23A) for BSA and in B) for HSA. As a guide to the eye we plotted the golden and magenta line to indicate the c^* and c^{**} boundaries and the blue line to show the LLPS boundary. For the c^* of the HSA system nearly no change is visible and in the BSA case a slight shift to higher salt concentrations for a medium Φ_{D_2O} can be observed. From this small variation of the c^* boundary we can conclude that the first part of the charge inversion, from a negatively charged protein to an uncharged protein, is nearly not influenced by changing the solvent from H_2O to D_2O. The c^{**} boundary in both systems shifts to higher salt concentrations with increasing Φ_{D_2O} where the maximum c_s is reached at a $\Phi_{D_2O} = 100\,\%$. For the LLPS region a quite interesting behavior can be observed. The low c_s boundary stays constant with increasing Φ_{D_2O} as long an LLPS can be observed. The high c_s boundary of the LLPS region varies with varying Φ_{D_2O}. For a low Φ_{D_2O} of 20 % the LLPS is larger. A further increase of Φ_{D_2O} leads to a shrinking LLPS region before the LLPS region vanishes at a Φ_{D_2O} of 80 %. The difference in the salt concentration between the higher LLPS boundaries and the c^{**} slightly increase in a log scale by changing the solvent from pure H_2O to a solvent with a Φ_{D_2O} of 20 %. A further increase of Φ_{D_2O} leads to an increased distance between these two boundaries. To investigate the reason for the changes in the phase diagram we used SAXS and SANS experiments. The results from these experiments are shown in the next section.

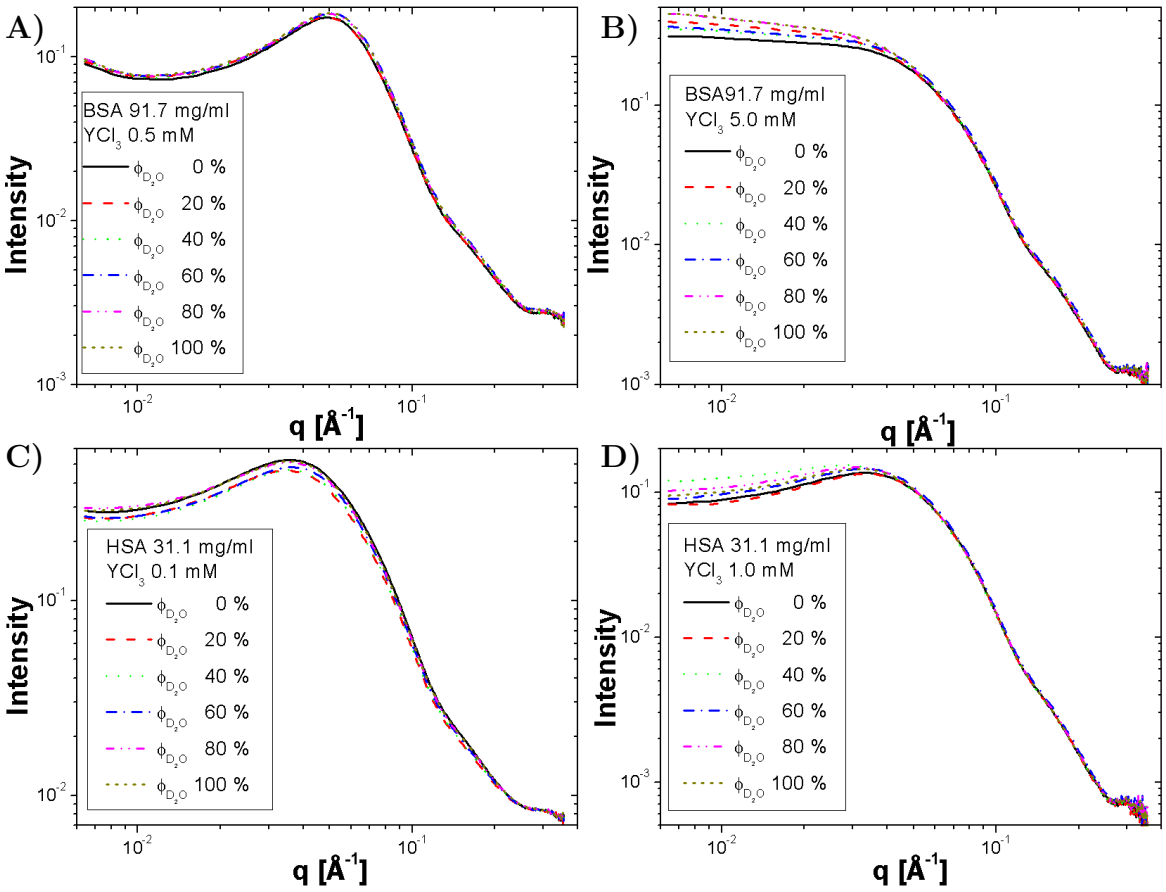

Figure 4.24: The SAXS scattering intensities for samples in the first regime are plotted against q. For both proteins, (top: BSA, bottom: HSA), a point far away (A and C) and close (B and D) to the c^* boundaries is shown.

4.5.2 Variations of the protein-salt mixtures observed by SAS

In the previous section, the influence of the solvent on the LLPS is investigated by using optical microscopy. In this section, the influence of the solvent on the phase diagram would be investigated on smaller length scales. For this purpose, SAXS is applied to the sample and the scattering curves are recorded. The recorded scattering curves are separated into three figures, depending of the regime in the phase diagram. The sample compositions corresponding to the different SAXS curves are shown as magenta lines in Fig. 4.23. The samples from the first regime are plotted in Fig. 4.24. The samples from the LLPS region in the second regime are shown in Fig. 4.25 and the reentrant regime is plotted in Fig. 4.26.

In Fig. 4.24 the scattering curves from different samples located in the first regime are plotted. A) and B) show samples for the BSA system and C) and D) for the case of HSA. For both samples, A) and C), which are located far away of the c^* boundary, a clear peak around $q = 0.05\,\text{Å}$ is visible. This peak can be ascribed to Coulombic repulsion

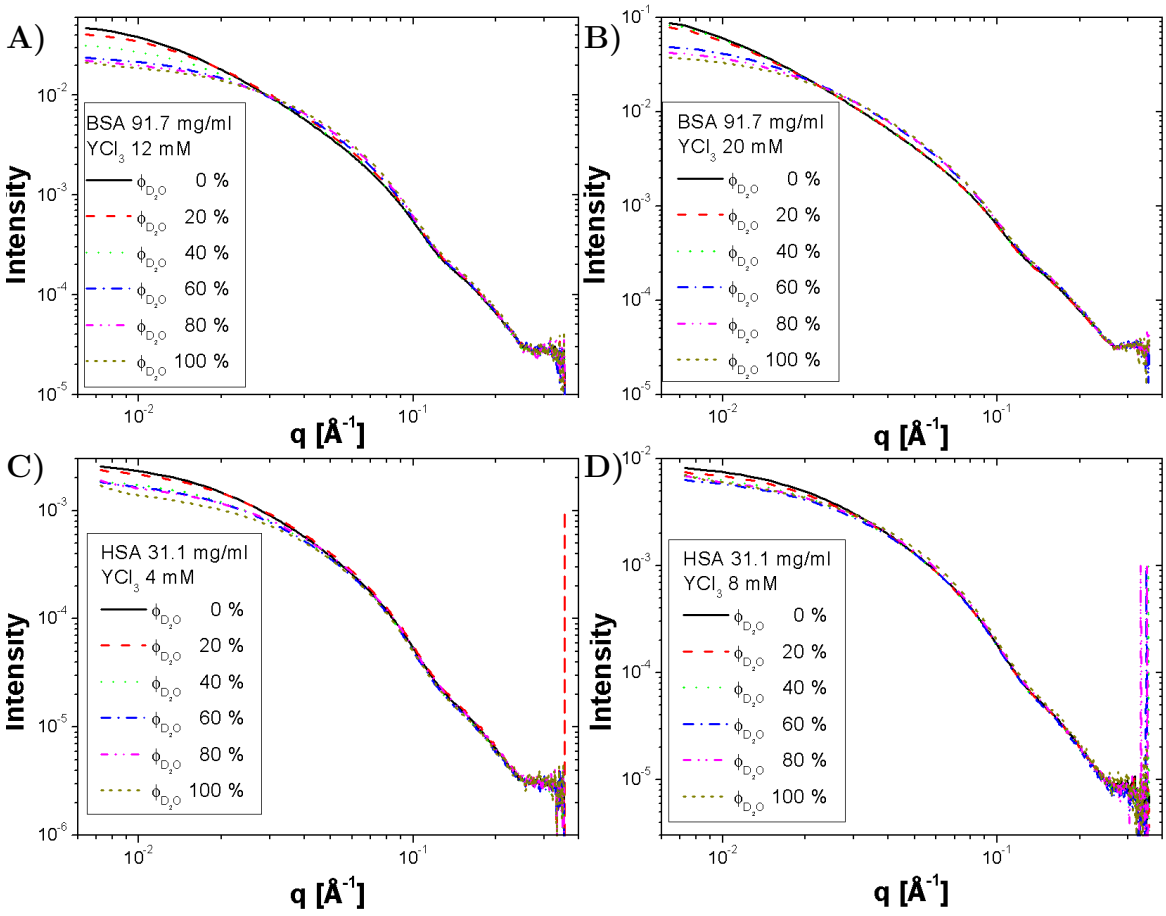

Figure 4.25: The SAXS scattering intensities for samples in the second regime. For both proteins a point close to the lower and upper LLPS boundary, A) and C) in the case of BSA and B) and D) for the HSA system, is shown. The salt concentrations were chosen from the phase diagram of a pure H_2O system.

because at this position of the phase diagram the proteins are highly negatively charged. Increasing salt concentration to a point near the c^* boundary leads to a shrinking peak until this peak vanishes completely. Adding more YCl_3 leads to more free Y^{3+} ions in the solution which can bind to the protein which, in turn, yields into a less negatively charged protein until the protein surface charge get close to 0 at the c^* boundary. For the variations in the scattering curves with varying Φ_{D_2O} no systematic behavior is observed. A possible configuration for these variations can be small variations of the salt concentration by pipetting errors. This would also explain the bigger variations for the samples close to the c^{**} boundary, because the influence on the protein surface charge is bigger for proteins near to neutral surface charge than for a highly charged protein.

To investigate the interactions for different areas of the second (condensed) regime, two different salt concentrations for both proteins are chosen. These 4 c_s are chosen

because they show a LLPS in a pure H_2O system and at a $\Phi_{D_2O} = 60\,\%$. The different scattering curves are shown in Fig. 4.25. A) and B) represent the case of BSA while C) and D) show the case of HSA. The c_s, which is close to the lower LLPS boundary, is presented in A) and C). The samples which are located close to the upper LLPS boundary are shown in B) and D). The macroscopic LLPS, which can be observed under an optical microscope, vanished upon further increase of the D_2O concentration up to $\Phi_{D_2O} = 80\,\%$. For such a high and higher Φ_{D_2O} only cluster formation is visible under the microscope. This visible change in the phase behavior is also visible in a change of interactions by increasing Φ_{D_2O}. For the samples in the second regime a clear trend is visible. At medium q in Fig. 4.25A), B) and D) the scattering intensity increases slightly while the scattering intensities in the low-q-range decrease with increasing Φ_{D_2O}. This behavior is related to a decrease of the attractive interaction potential between the proteins. From microscopy we know that an increased Φ_{D_2O} leads to an increased cluster formation in the sample. This increased cluster formation is not directly visible from the scattering curves. To make the cluster formation visible lower q-values are needed. Only for HSA, Fig. 4.25C) and D), samples show a slight upturn in the scattering curve at low-q. An increased cluster formation leads to a decrease in the amount of smaller particles, which is reflected in a decrease of the scattering curves in the low-q-range of Fig. 4.25. A decrease in the amount of medium size particles corresponds to a decrease of the attractive interaction potential on this length scale. In Fig. 4.24 it is shown that for highly negatively charged proteins the repulsive interaction is increased as compared to proteins with a charge close to zero. This increased repulsive interaction is shown in Fig. 4.24 by the increased peak at medium q. For samples with a decreased interaction, which corresponds to an increased repulsive part of the interaction potential, scattering intensity increases at medium q. A possible explanation for the vanished macroscopic LLPS is that the effective attractive interaction, which can be expressed by B_2/B_2^{HS}, decrease below the critical value of LLPS. This will be investigated in the next section, Sec. 4.5.3.

From the phase diagram the interactions in the reentrant regime can be estimated. With increased Φ_{D_2O} the samples with a fixed c_s are located closer to the c^{**} boundary. Therefore the repulsive interaction in the reentrant regime should decrease with increasing Φ_{D_2O}. For the pure D_2O system an increasingly repulsive interaction is expected, because the c^{**} boundary shifts to lower c_s. The scattering curves obtained from these samples located in the reentrant regime are plotted in Fig. 4.26A) for BSA and in B) for HSA. In the case of BSA the expected behavior is found. With increasing Φ_{D_2O} the scattering intensity at low-q increases, which reflects the increase of attraction in the system. Interestingly the pure D_2O system shows the highest scattering intensity at low-q. This cannot be explained by the phase diagram. Until now no explanation for this behavior exists. For the HSA system the scattering curves show an unusual behavior which is shown in Fig: 4.26B). The deviation of the scattering intensity in the high-q region is usually related to a change in the form factor of the protein. A change of the protein form factor with increasing Φ_{D_2O} is quite uncommon, because the change of hydrogen to deuterium stabilizes the protein [237]. If this stabilization leads to a different form factor of the protein, this should also be visible in the other regions of the phase diagram,

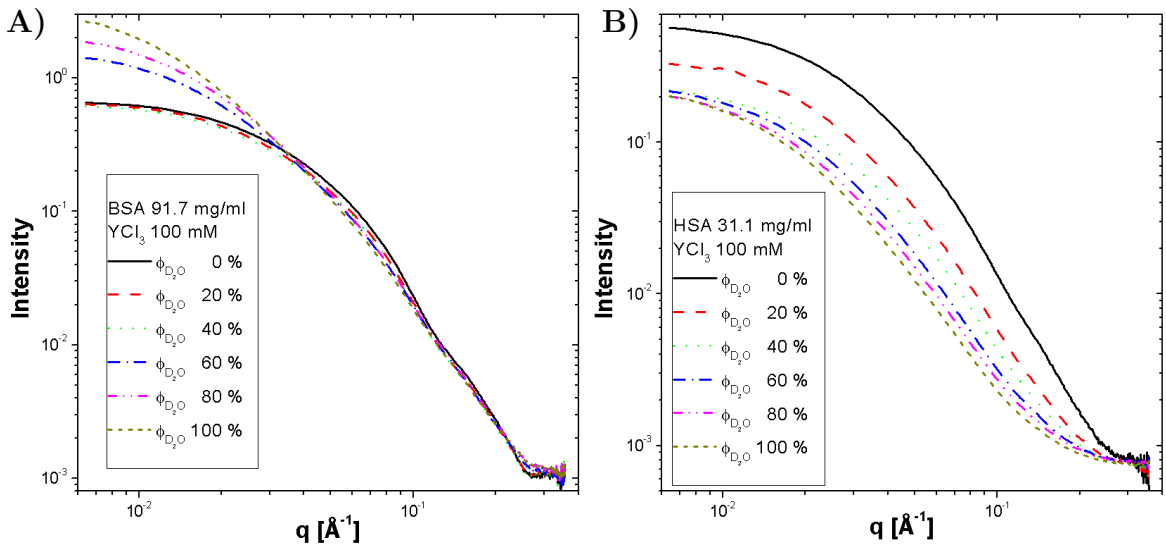

Figure 4.26: The SAXS scattering intensities for samples in the third regime. The BSA system is shown in A) and the HSA case in B).

which is not the case. We cannot explain this behavior of the scattering curves. This samples will be measured again at a following beamtime to verify the reproducibility of this observed behaviour.

4.5.3 Variation of the reduced second virial coefficient with varying D_2O volume fractions

To quantify the variation of the scattering curves with varying Φ_{D_2O} in the condensed regime, the effective structure factor $S(q)_{eff}$ is calculated by dividing the scattering curves by the form factor, determined in Fig. 4.4A). In order to divide the scattering curves by the form factor, the scattering intensity of the form factor was shifted to match the scattering intensities of the scattering curves at high-q. This leads to an effective structure factor for high-q of around 1. Dividing the scattering curves by the effective form factor can lead to a difference to $S(q)_{eff}$, which is multiplied by a constant. For this reason the resulting curve is referred to effective structure factor. The $S(q)_{eff}$ of the BSA system is plotted against q in Fig. 4.27A) and B), while the case of HSA is shown in Fig. 4.27C) and D). In $S(q)_{eff}$ a peak around $q = 0.1\,\text{Å}^{-1}$ is visible. This q-value corresponds to a length scale of 63 Å. This length scale is approximately two times higher than BSA's radius of gyration of 30.5 nm [168]. The monomer-monomer distance can be deduced from this length scale, which is the distance between two monomers connected by ion bridges, as described by [206]. The appearance of the peak compared to the form factor can be explained by the increased protein concentration in the solution. This increased c_p leads to more free monomers in the solution, which can form oligomers or clusters by the ion bridging effect. In general the dimerization is enhanced with increasing Φ_{D_2O}, which is visible by the increase of the peak intensities around $q =$

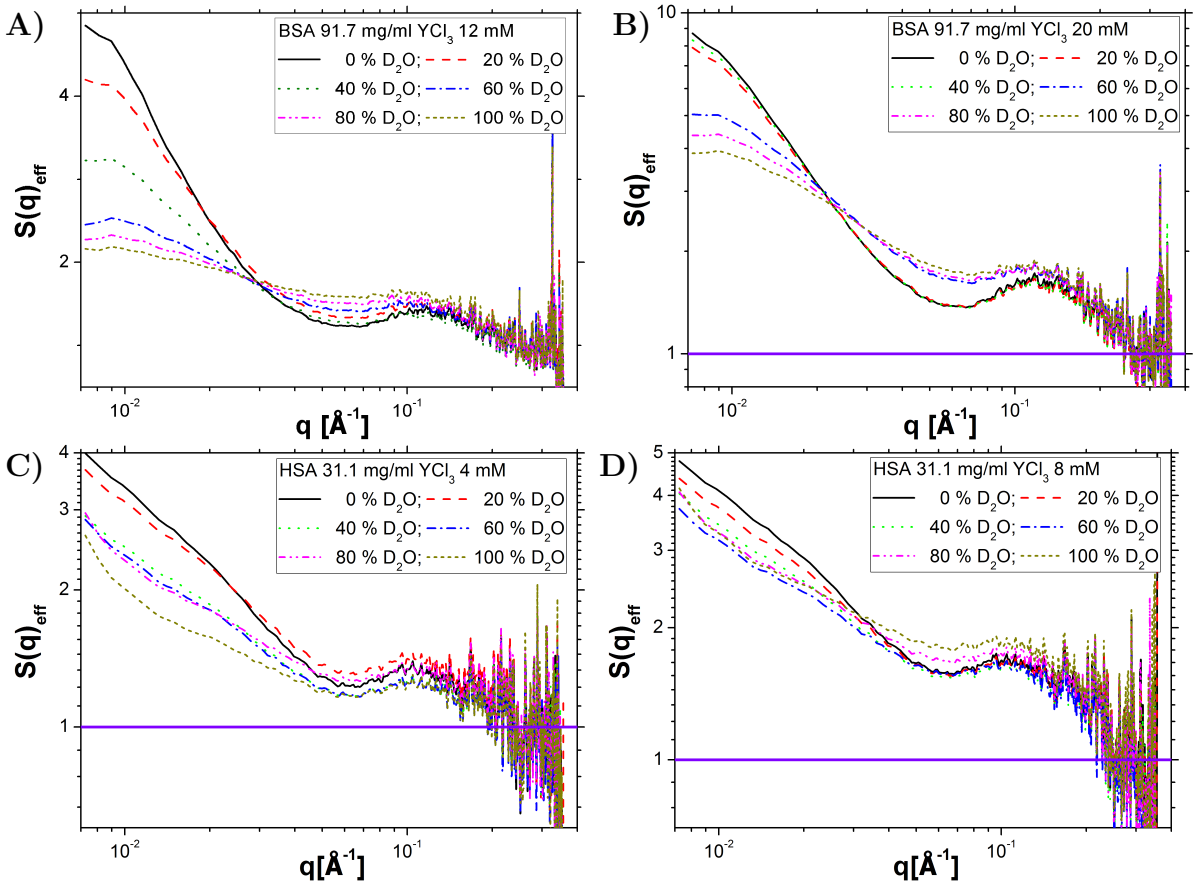

Figure 4.27: The variations of the effective structure factor, $S(q)_{eff}$, with increasing Φ_{D_2O} are monitored by dividing all scattering curves in the turbid regime by the scattering curve of the form factor.

$0.1\,\text{Å}^{-1}$. This trend is not observed in Fig. 4.27C) as opposed to all other figures. For this case no trend can be determined. For $\lim_{q\to 0}$ the structure factor shows the strength of interaction between the proteins. For $S(q) > 1$ the interactions are attractive and for $S(q) < 1$ repulsive. The values of $S(q)_{eff}$ in the low-q regions of Fig. 4.27 are above 1. Therefore it can be concluded that an attractive interaction in the second regime also exists in a pure D_2O system. The strength of the attraction decreases with increasing Φ_{D_2O} until the weakest interaction is reached in the pure D_2O system. A comparison of the interaction strengths close to the lower and the upper LLPS boundaries shows, that the attractive interactions are stronger at the upper LLPS boundary. In a pure H_2O system the stronger attraction of the samples which are closer to the upper LLPS boundary, can be explained by the location of these samples in the phase diagram. In this case the samples are located in the middle of the LLPS region, where the highest attraction can be observed. With increasing Φ_{D_2O} the samples are located closer to the upper LLPS boundary and the attraction is reduced. In the pure D_2O system the attraction is also stronger compared to the samples located at the lower LLPS boundary.

For this system only the formation of clusters can be observed. This stronger attraction can be explained with the help of Fig. 4.3B). From this figure it is visible that outside of the LLPS region the attraction is also maximized between the c^* and the c^{**} boundaries. The samples at the lower LLPS boundary are also located close to the c^* boundary, which explains the weaker attraction for these samples at higher Φ_{D_2O}.

In this part the qualitative analysis of the interactions between the proteins with varying Φ_{D_2O} is presented. Compared to the form factor from a dilute system the formation of dimers by ion bridging is visible. With increasing Φ_{D_2O} the amount of the dimers increases and also some oligomers form. This can be explained by the increased amount of proteins in a non-dilute sample. In contrast to this the interaction between the proteins decreases with increasing Φ_{D_2O}, which are reflected in the decreasing scattering intensities and the decreasing value of $S(q)_{eff}$ in the low-q region. The quantitative analysis of this behavior is investigated in the following section.

In this part we will discuss how the qualitative variations of the system with increasing Φ_{D_2O} can be explained in a more quantitative way. In order to do so the already mentioned SHS potential, [163] is used to fit the data. With the help of this fitting routine the stickiness parameter, τ, can be extracted and B_2/B_2^{HS} as well as the depth of the interaction potential u_0 can be calculated. For the fitting routine we fixed the volume fraction and the size of the form factor to obtain values which are not influenced by volume and size changes. The corresponding values are listed in Tab. A7.

This table shows that the B_2/B_2^{HS} values increase with increasing Φ_{D_2O}. This fits to the qualitative observations. In most cases the reduced second virial coefficient is below the critical value of the LLPS. Only the BSA sample set with 12 mM YCl_3 is above this value before the LLPS vanishes. For a sample with $\Phi_{D_2O} \geq 60\,\%$ of this sample set the B_2/B_2^{HS} value is above the critical value and a macroscopic LLPS is observable under the microscope. A possible explanation for the observable LLPS in this sample is that the LLPS is formed in the mixing procedure before the sample was completely homogenized and the interactions leading to LLPS dissolving are not strong enough to eliminate the already formed LLPS. For the other sample sets the B_2/B_2^{HS} is below the critical value for all Φ_{D_2O}, which would mean that the attraction between the proteins is in principle strong enough to form a macroscopic LLPS. The reason for the absence of the LLPS is that the c_p in the resulting dilute phase is too low to form a macroscopic LLPS. For example, the HSA sample with 4 mM YCl_3 in pure D_2O has a protein concentration of $c_p = 11.88\,\mathrm{mg/ml}$, which is located outside the LLPS region. The decrease in the protein concentration can be explained by increased cluster formation with increasing Φ_{D_2O}. The proteins, which are located in the clusters cannot contribute to the macroscopic LLPS formation, which is the reason why no LLPS can be observed for samples with a high Φ_{D_2O}.

In this section we have demonstrated how the variation of the solvent influences the phase behavior of the used protein system. The resulting phase diagram is shown and explained in the first part. Qualitative and quantitative analyses of the resulting SAXS curves are discussed, especially for the samples located in the second regime. It was observed that with increasing Φ_{D_2O} the protein concentration and the interaction strength between the protein decrease. The effective structure factor $S(q)_{eff}$ shows that in a

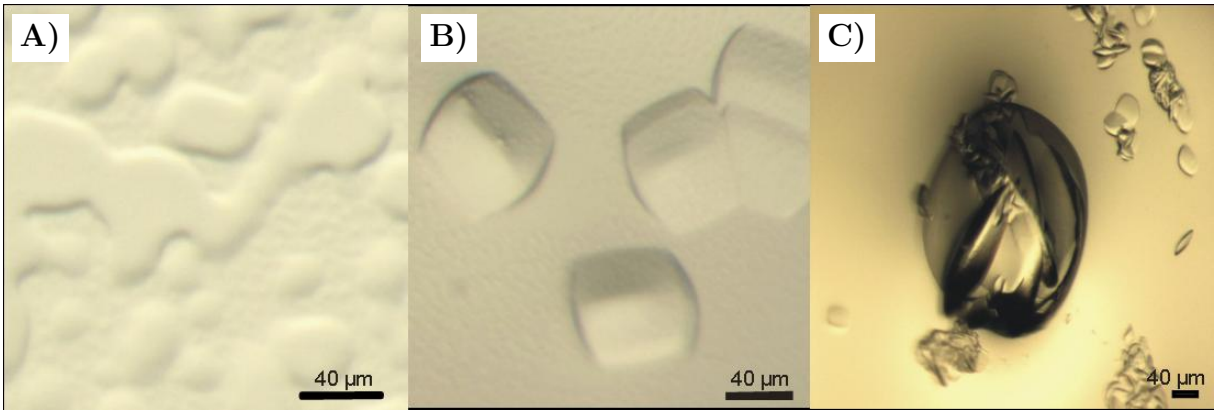

Figure 4.28: Different steps in the crystallization process of the dilute HSA phase are observed. Formation of a dense phase, A), crystallization without any precursor, B), and crystallization from the dense phase, C), by using optical microscopy. The two different pathways of crystallization, without and with the formation of a dense protein phase before crystallization, are called one- and two-step crystallization process.

non-dilute sample the formation of dimers is increased as compared to the form factor measurement in a dilute sample. This increased dimer formation can be explained by yttrium bridges between the proteins. After the behavior of the dilute and dense protein phase and the variation of the dilute protein phase changing the solvent the focus of the next section, the long time stability of the dilute and dense protein phase, is discussed.

4.6 Long time stability of the dilute and dense protein phases

The variation of the dilute and dense protein phase by varying c_s, T and the solvent is discussed in the previous sections. In this section the focus is on the long time stability of both protein phases. If the protein solutions with LLPS are not stable over time, dissolving of the dense liquid droplets, crystallization or the formation of an arrested state, such as gelation or glass, takes place.

Using optical microscopy it is found that the dilute protein phase can undergo a crystallization process for small salt concentrations, 3 mM to 8 mM within 3 to 4 days. Time dependent microscope pictures show the formation of a dense protein phase on the walls of the glass bottles, Fig. 4.28A), before crystallization takes place. In this crystallization process, first the formation of round plates can be observed before an additional structure occurs on the round plates, Fig. 4.28C). Such a process is named a two-step crystallization process in this thesis. In some cases the formation of rectangular crystals is observed. In this case no phase separation or another precursor can be observed, Fig. 4.28C) which can be understand as a classical one-step crystallization process.

In the following optical observations of the two-step crystallization process are presented. For the observation of the crystallization process a type 120 quartz glass cuvette from Hellma GmbH, Müllheim, Germany, with a pathlength of 2 mm was used. The sample is prepared in a separate tube. After mixing the sample is filled into the quartz cuvette which is sealed by a connector and paraffin film. The morphology of the solution at a fixed point inside the cuvette is monitored by an optical microscope. The obtain pictures for a HSA sample with an initial protein concentration $c_p = 31.1$ mg/ml with an initial salt concentration of $c_s = 6$ mM are presented in Fig. 4.29 for different time steps. The formation of dense droplets at the glass solution interfaces of the cuvette can be obtained after 37 min after sample preparation in Fig. 4.29A). For longer waiting times structures of dense liquid forms at the glass/solution interfaces. After 71.45 h the formation of big dense liquid structures additional to the normal dense liquid structure can be obtained in B). In Fig. 4.29E) the bigger dense liquid structure is presented in a higher magnification and a Oswald rippening zone [238] can be observed around this big structure. After around 144 h the first crystal structures are visible at the surface of this bigger structure Fig. 4.29F). An increased crystallization in the bigger structure (Fig. 4.29G) and the formation of samller crystals on the other side of the cuvette can be observed 24 hours later Fig. 4.29C) and H). The formation of the smaller crystals can also be described by a two-step process where first round plates are formed from which the crystals starts to grow. This is also presented in Fig. 4.29H) where the round plates and the crystal formation from these plates are visible. A few days later (311.38 h) the hole glass/solution surface of the cuvette is covert by crystals (Fig. 4.29D)).

To quantify the crystal structure of the observed crystals, several crystals are grown. After the crystals are grown they are collected and filled into a quartz capillary for SAXS measurements. For each type of crystals one separate capillary is prepared. The results from both crystal types are similar and an examplary scattering curve with the corresponding 2D detector image is plotted in Fig. 4.30. The 2D detector image show rings around the center of the beam. In the rings some spots with higher intensities can be observed. The origin of the rings can be explained in the following way: single spots on the 2D image appear if only a single crystal is investigated by the X-ray beam. For this system several crystals in a solution are placed into the X-ray beam. Because of the increased degrees of freedom in the solution the different crystals are orientated differently with respect to each other. Each different orientation of two crystals to each other produces an additional spot, which is located on a ring due to the constant q-value. An average over all possible orientations smears out the several spots to a complete ring in the detector image. The observation of several spots in the rings is related to an inhomogeneous orientation of the different crystals in the beam. Radial averaging of the 2D detector image yields sharp Bragg peaks which are seen in the plotted scattering curves, Fig. 4.30. Through the crystallization process several preferred distances occurs which are defined by the crystal structure. These preferred distances are shown by the Bragg peaks in the scattering curve. For an HSA sample with YCl_3, prepared slightly outside of the LLPS region, an unpublished crystal structure exists, measured from an HSA crystal, grown in a c_p of 31.1 mg/ml with 2 mM YCl_3 solution, by X-ray diffraction. This crystal structure shows an orthorhombic crystal system with space

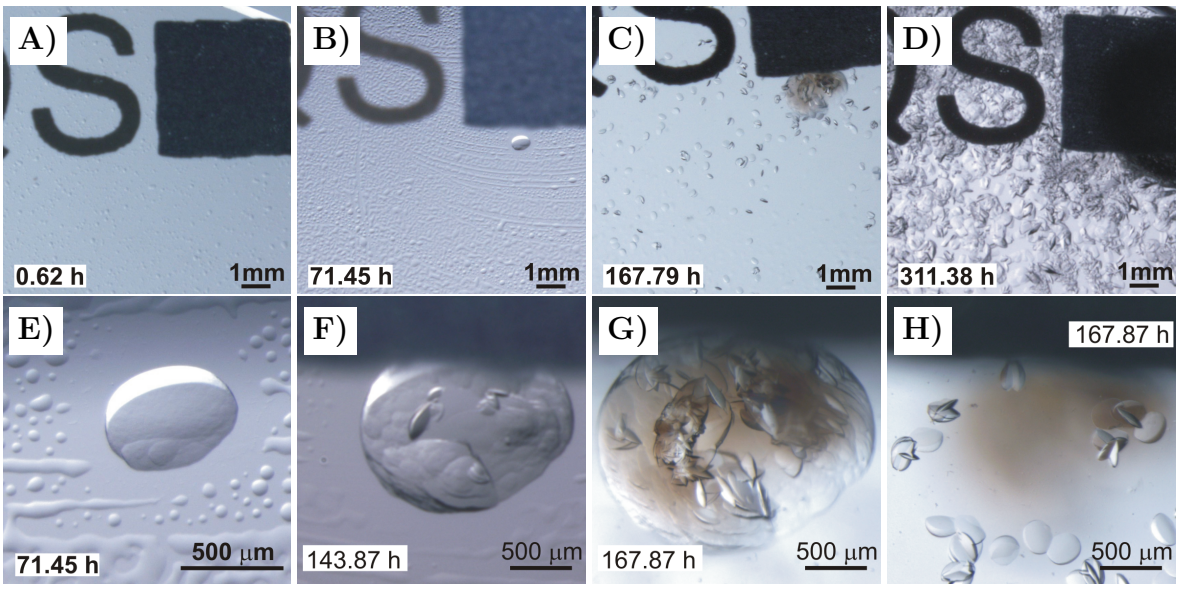

Figure 4.29: Microscopic observations of a time dependent two-step crystallization process. Figures A) - D) shown an overview from a part of the cuvette. After the first big structures occurs a zoomed in observation is presented in E) - H). G) and H) shown are obtained to the same time but on different glass/solution surfaces.

group 19 ($P2_12_12_1$). The unit cell has a size of $A = 55.68 * B = 71.84 * C = 180.58\,\text{Å}^3$. Comparing the Miller indices calculated from the unpublished crystal structure with the positions of the Bragg peaks in the scattering curve shows a good agreement between the observed scattering curve and the already known crystal structure. Out of the first nine Bragg peaks, eight can be explained by this crystal structure. The corresponding Miller indexes for each Bragg peaks are also shown in Fig. 4.30. From this nice agreement it can be concluded that the different morphology of the crystals plays no role for the crystal structure.

In order to determine the long time stability of the dense protein phase, one sample was stored after a SANS experiment for 44 days in the fridge. After this time another SANS experiment was performed for this sample. The measured scattering curves from both experiments are shown in Fig. 4.31A). A reduction of the scattering intensity I in the 44 days old sample against the freshly prepared sample at medium and low-q occurs. The reduction of the scattering intensity can be explained by the reduction of the available protein concentration in the sample. A part of the proteins are consumed by crystal formation. This is visible by the spots in the 2D detector image, shown in the inset, and by the Bragg peak in the scattering curve at $q = 0.069\,\text{Å}^{-1}$. The contribution of these proteins to the scattering intensity is only visible in the region of the form factor and at the corresponding q-values of the preferred protein distances in the crystal, the Bragg peaks. In the other parts of the scattering curve these proteins are not visible and the scattering intensity decreases.

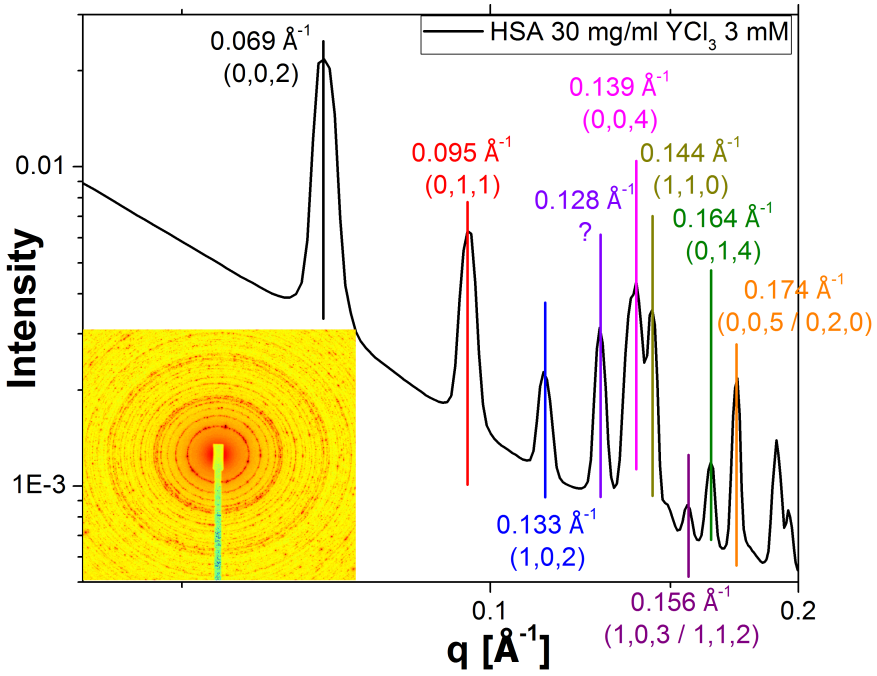

Figure 4.30: The scattering profile of HSA crystals observed by SAXS are plotted. The Bragg-peaks are number by the corresponding Miller index (hkl). The Miller indices are determined by an unpublished HSA crystal structure. In the inset the corresponding 2D SAXS image is presented. The samples are prepared by Marco Grimaldo.

To follow the time dependent variation of the scattering intensity three samples with the same c_p and c_s, as used for the long time stability measurement of the dense phase, are prepared in advance before another beamtime. Additionally a fourth sample is prepared directly before the first measurement of this sample. The oldest sample is prepared 27 days before the beamtime. An earlier preparation of the sample was not possible because of the scheduling of the beamtime, which took place 28 days before the beamtime. In Fig. 4.31B) the scattering curve of the freshly prepared sample is plotted as the dotted blue line. For clarity reasons the blue line is shifted upwards by a constant factor of 5. For comparison the already shown scattering curves from Fig. 4.28A) are also plotted into the graph. It is visible, that both freshly prepared samples have the same scattering curve. Over time the development of a Bragg peak is not visible. Only small variations of the scattering intensity at small q can be observed. This variation is plotted in the inset. From this inset it is visible that I slightly increases within the first 10 hours after the sample preparation. After 10 hours I increases much faster over time until a maximum is reached after around 200 hours. After the maximum is reached, I decays within the next 200 hours quite fast. The last 3 data points are measured from separately prepared samples, which can leads to variations of I between the different sample. For this reason, one can question the decrease of I, which takes place after 200

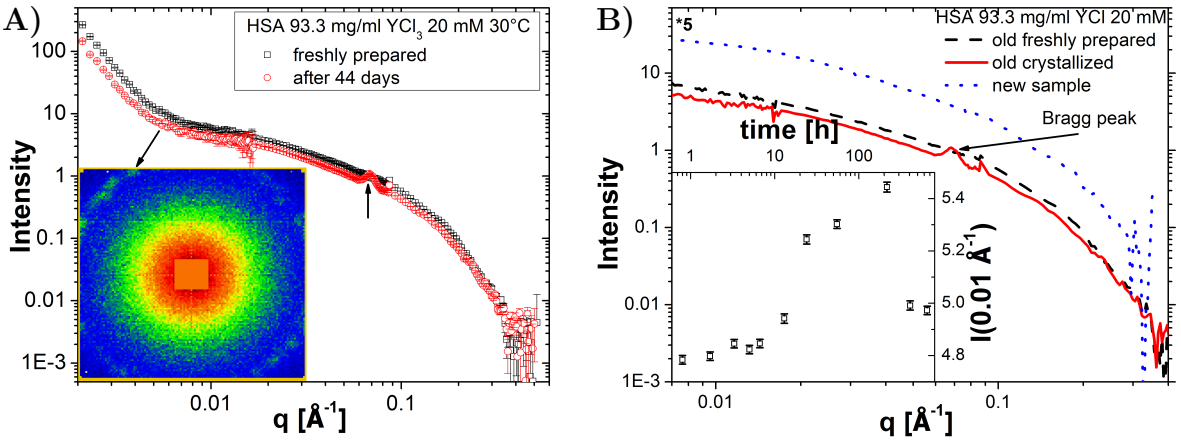

Figure 4.31: The time dependent scattering intensity I of the dense protein phase is plotted against the scattering vector q. The formation of protein crystals is visible in A). The sample is stored for 44 days after the first measurement in the fridge before the second scattering experiment is performed. The inset shows the 2D detector image, of the second run, which shows several spots, located on a ring, which can be related to Bragg peak in the scattering curve of the 44 days old sample. To investigate the time dependent behavior of the scattering curve the experiment is repeated and the scattering profiles are determined at different time steps, B). The inset shows the variation of the scattering intensity at $q = 0.01\,\text{Å}^{-1}$ over time.

hours. The increase of I is not questionable because the same sample is measured at different times at the same T. The increase of I in the first 200 hours must be related to structural changes inside the sample. From the knowledge of the early performed measurement, where crystallization takes place, the decrease of I can be explained by a crystallization process. Our interpretation of the time dependent scattering intensity is, that in the first 200 hours, some precursor of crystallization are formed, which leads to an increase of I at low-q. After the precursors are formed crystallization takes place and I decreases with time. That no Bragg peaks is visible can be explained by the big uncertainty of the wavelength from the incident neutron beam. This uncertainty leads to a smearing effect and small peaks are smeared out and are no longer visible in the scattering curve. With time the Bragg peaks increases and the smearing effect is no longer strong enough and a broad Bragg peak appears in the scattering curve. Such a peak is visible in Fig. 4.28A). It looks like the measured time slot was not long enough to observe the formation of a Bragg peak in the scattering curve. The observed way of the crystallization fits to an two-step crystallization process as described by Sauter et al. [239].

The formation of crystals in the dense protein phase is also observed by using optical microscopy. The observed crystals are shown in Fig. 4.32. In Fig. 4.32A) the protein crystal, from an HSA 93.3 mg/ml with YCl_3 20 mM sample, stored in a fridge for several weeks, is observed by a confocal reflection microscope. The observed crystals are located

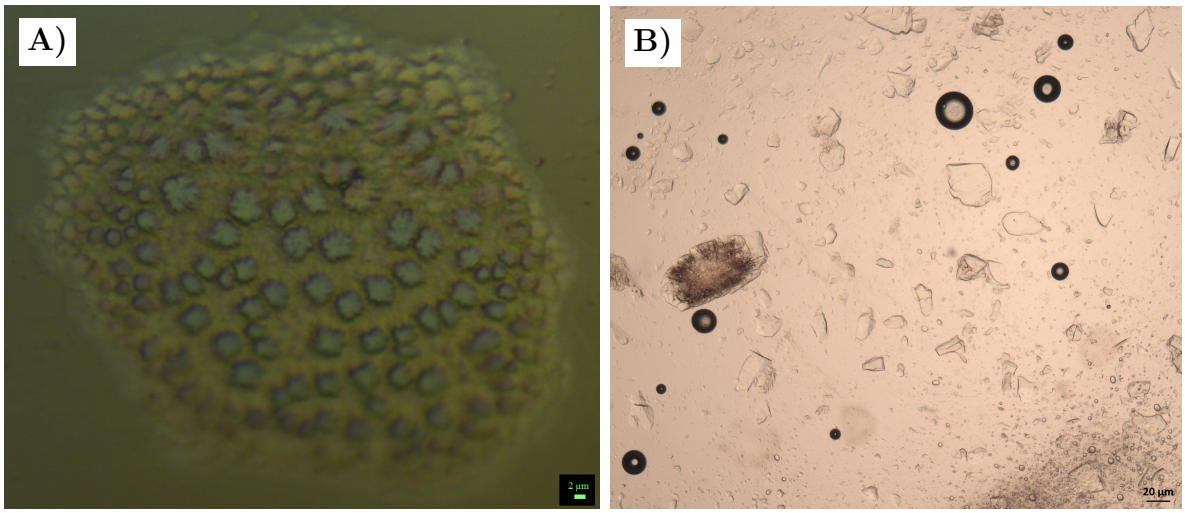

Figure 4.32: In both pictures crystals from the dense protein phase of an HSA 93.3 mg/ml with YCl_3 20 mM are shown. In A) the crystals are observed by a confocal reflection microscope and in B) by a normal light transmission microscope. For B) the crystals are taken out of the sample tube which is the reason that only destroyed crystals are observed.

at the glass wall of a quartz capillary. Several small rectangular crystals can be observed in the shown crystal spot. The length of the small crystals are between 2 µm and 6 µm. In Fig. 4.32B) crystals from the dense protein phase with the same sample composition, which is prepared at another time and stored for several month at room temperature, are shown. In this case much bigger crystals can be observed. All the crystals in the Fig. 4.32B) looks damaged. This may come from the fact that the crystallization takes place only at the interface of the sample tube. The sample is taken out by a spoon and placed under the microscope. By this procedure the crystals are broken from the tube-sample interface and only damaged crystals can be observed.

As far as known the dense protein phase is in an arrested state, such as a gel. Why can crystallization take place in such a gel-like state? One reason is that the volume fraction in the HSA dense phase is quite small, so the possible gel is maybe some kind of equilibrium gel. In such a gel the single proteins would have enough space to move and reorient at a longer time scale. Another reason is that the interface maybe plays a role in the crystallization process. Until now only crystallization at the interface is observed which shows that the protein-interface interaction plays an important role in the crystallization process. And the last possible reason for the crystallization in a gel is that the gel forms a network. Inside this network a diluted protein phase can be trapped. In this dilute phase crystallization can takes place and with time the crystals can grow into other cells of the gel network. This fact would explain why rectangular crystals with a length of 2 µm, 4 µm and 6 µm can be observed in Fig. 4.32. From the observation the last two reason are most likely included in the observed crystallization process.

In this section the long time stability of the dilute and dense protein phase is investigated. It is shown that both phases can undergo a crystallization process over time. This shows that both phases are a metastable phase with respect to the crystal phase. The focus of the last section in the result chapter is on a complete different story. In this section we describe the development of a new sample holder, which combine inelastic neutron experiments with light absorption and spectroscopy experiments.

4.7 Development of a sample holder for simultaneous light and neutron experiments

In the previous part of this section the behavior of a serum albumin solution in the presence of YCl_3 is discussed, especially in the case of a LLPS. The focus of this section is on the development of a new sample holder to combine inelastic neutron and light absorption and spectroscopy measurements. This is a combined work with our collaborators from the ILL, Grenoble, France, Tilo Seydel and Marco Grimaldo, and from the University of Oxford, UK, Robert Jacobs.

The idea of this project is to combine inelastic neutron experiments, such as time-of-flight, backscattering and spin-echo, with different light scattering techniques, such as DLS and absorption, UV-Vis and raman spectroscopy. This combination of these different techniques should be available under several sample conditions, especially under a broad temperature range. To achieve such a broad temperature range it is necessary to place the sample into a cryostat by mounting the sample holder on a sample stick. In order to place the sample and the different optical parts into the sample holder the available standard stick of the ILL must be modified and a new design, based on the standard sample holder design, is necessary.

I joined the development of this new sample holder after the first version of the sample holder was tested. The sample stick and the first version of the new holder are shown in Fig. A1 and Fig. A2. The sample stick is designed to place the sample into a cryostat for the neutron experiment. To avoid water condensation in the cryostat, a vacuum pump or a purge gas can be connected to the outside of the sample stick. The idee behind this sample holder in the first version is to measure light absorbance in a liquid sample. For this purpose a laser beam is coupled into an optical fiber outside of the cryostat. The optical fiber can be pulled through the inner tube of the sample stick. The sample holder is mounted at the bottom of the sample stick and the optical fiber is connected to the lens holder. The lens holder is mounted on top of the sample holder, as shown in Fig. A2. The optical lens has the purpose to get a parallel beam. The parallel light beam runs through the sample solution and a part of the beam is absorbed. At the mirror, the beam is reflected back to the lens and the optical fiber. The optical pathway is doubled and less solution is necessary to achieve the same absorption as without the mirror. Using an optical fiber with a y-shape construction, which means that at one side of the fibre two connections exists. At one connection the laser beam is coupled into the fibre. At the other end of the fibre the laser beam is emitted from the fibre and

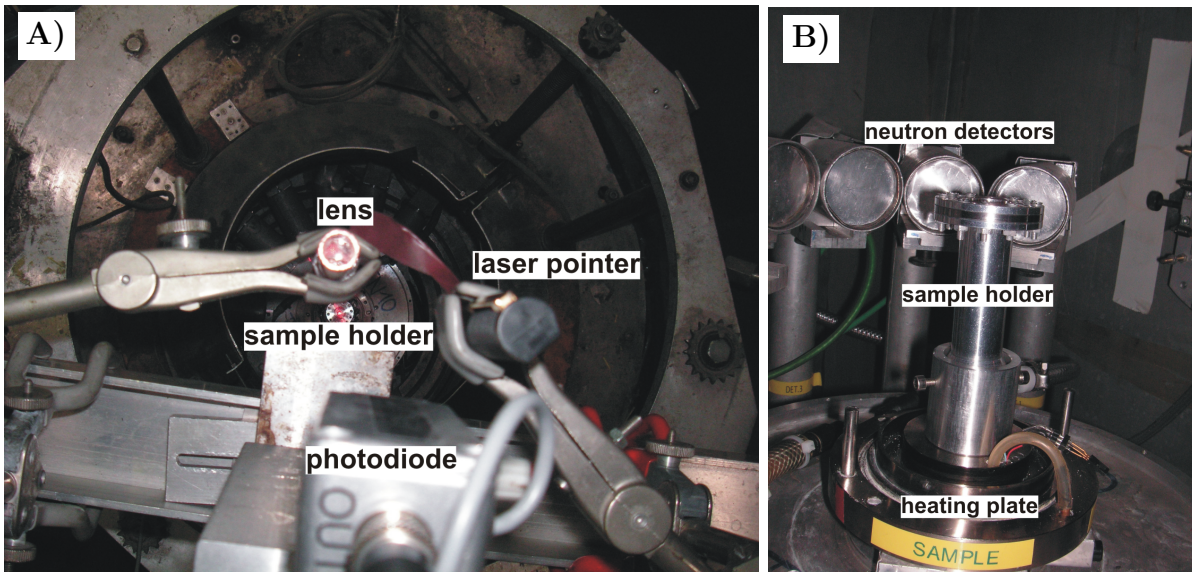

Figure 4.33: The setup of the second experiment in the first version is shown. The upper part of the setup, A), The parts which are the laser pointer, sample holder, lens and photo diode are shown in A). The sample holder, which is placed on a heating plate inside the neutron spectrometer is shown in B).

reflected back from the sample to the fibre. The reflected beam is splitted up into two parts, one goes back to the laser and the second goes to the second connection to the fibre, where the intensity of the reflected beam can be analysed at the second end with the help of an optical detector. Measuring the intensity of the reflected beam onetime with, I, and without solution, I_0, the absorbance of the solution can be determined, as shown in Sec. 3.2. For the neutron signal a small thickness of the protein solution in a cylindrical cell is necessary. For this purpose an inner cylinder is placed into the sample holder. This leads to a gap of 150 µm thickness between the inner and outer cylinder waals. The optical parts of the sample holder are placed outside of the neutron part to avoid a contamination of the neutron signal by the optical components. Only the connection of the optical fiber to the sample holder is placed above the neutron part. The first test of the sample holder showed problems in the detection of a signal.

To determine the source of this problem, we decided to reduce a number of the components in the system. For this reason the sample stick, optical fiber and the optical lens was not included in the setup of the second experiment. For this experiment, we used a laser pointer, the sample holder, another optical lens and a photodiode. To measure the intensity of the laser pointer the laser beam is directed in a non-perpendicular way onto the mirror. The optical lens is placed in the reflected laser beam to focus the laser beam. The photodiode is placed into the focus of the laser beam. The sample holder is placed on a heating plate to control the temperature at the sample. The setup is shown in Fig. 4.33. Within this experiment, a stable signal was recorded for more than 10 hours at a constant sample temperature. This shows that the principal idea behind the setup

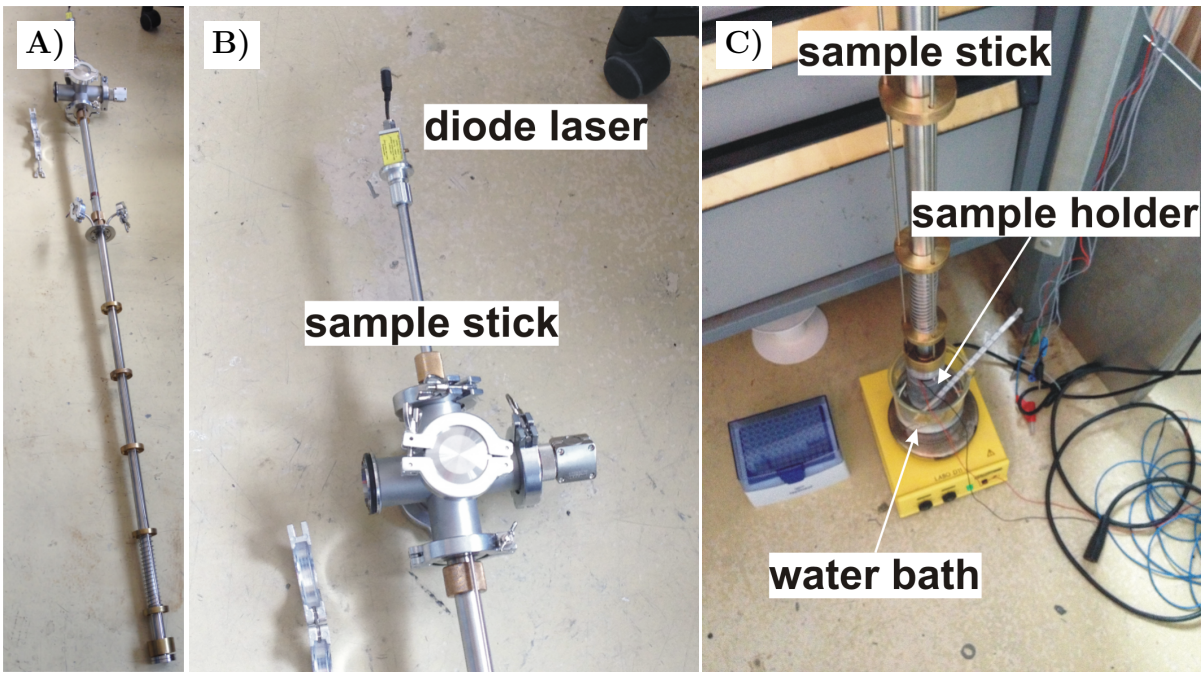

Figure 4.34: The sample holder, in the second version, is mounted onto the sample stick. The laser is connected at the top of the sample stick. A) The hole sample stick with the connected diode laser, B) the upper part of the sample stick with the mounted diode laser is shown. C) The sample holder is connected to the sample stick and placed in a water bath. The sample holder is placed in a cylindrical cover to protect the sample holder.

will work. The problems of the first experimental setup be located in the coupling of the laser within the optical fiber, in both directions, or at the connection of the optical fiber with the optical setup. A new problem occurs when we varying the temperature of the sample is varied. With varying T, the position of the focused laser beam spot changes. This leads to an unstable intensity measurement by varying temperature. The reason for this problem is maybe the fact that with increasing T the metal of the sample holder expands. If the expansion becomes to large the available space between the different parts of the sample holder are filled and to expand further the metal deform. This would lead that a declination of the mirror to the laser beam changes and the laser beam will be reflected to another point.

In order to solve the instability problem at varying temperatures, the mirror in the bottom of the sample holder is replaced by a normal glass slide. Below this glass slide, the photodiode is mounted. This setup has the advantage that the distance between the top of the glass slide and the photodiode is very small. The deformation of the glass slide or other parts of the holder would also lead to a deviation of the transmitted beam. With respect to the small glass slide - photodiode distance the deviation is quite small and the influence to the observed signal can be neglected. Under lab conditions, where the laser beam is focused onto the photodiode and the sample holder is placed in

a water bath for controlling temperature, the stability and reversibility of the system is demonstrated. After the first successfully performed measurements of this sample holder under lab conditions, the sample holder is mounted to the sample stick. In this case the laser is mounted at the top of the sample stick. The temperature of the sample holder is controlled by placing the sample holder into a water bath. The setup of this experiments is shown Fig. 4.34. Within this experiment, it is found that the intensity signal is stable over long time for a fixed temperature. With varying temperature, the intensity changes. Checking the laser beam at the bottom of the sample stick after demounting the sample holder shows an elliptical shape of the laser spot. The position and the shape of the spot varies by adding small forces at the bottom of the sample stick, in order to deform the sample stick slightly. This shows that the laser beam does not pass the sample stick unreflected. With varying T, the metal of the sample sticks changes also the length, by contraction or stretching, which influences the point where the laser beam is reflected.

In order to get rid of the problem with the reflection of the laser beam inside the sample stick, the position of the diode laser is shifted to the bottom of the sample stick. To reduce the distance between the laser diode and the sample, the construction of the sample holder is inverted so that the sample is located in the upper part of the sample holder. In this version, the photo diode is placed into the sample liquid. To protect the photo diode and the electrical connections, the lower part of the photo diode and the electrical connections are sealed by rosin. The blue print for this version of the sample holder is presented in Fig. A3. This version of the sample holder is still under construction.

In parallel to the third version of the absorption/transmission sample holder, another kind of sample holder is developed. With this sample holder optical signals from reflection or backscattering process should be analysed, such as raman spectroscopy. In the special case of raman spectroscopy, a commercially available raman probe and spectrometer from ocean optics, Dunedin, Florida, USA, is connected to the top of the sample holder. This raman probe is connected to the laser source via an optical fiber. The backscattered raman signal is detected by the raman probe and can be analysed. To achieve a good signal the light path inside the signal should be between 1 cm and 2 cm. For this reason, a gap of 1 cm is chosen for the gap between the raman probe and the inner part of the sample holder. The blueprint of this raman sample holder is shown in Fig. A4. The tests of this sample holder will be performed by our collaborators from the ILL, Grenoble, France, where such a raman probe is available.

In this section, the different steps of the development of a new sample holder to combine light absorption, transmission and spectroscopy measurements with neutron experiments are shown. Up to now, the setup could not be used successfully for measurements. Measurements in a reduced setup are successful, which shows that the principal idea behind this concept is working. The next version of the sample holder should show reproducible results from absorption measurements. If this was achieved, the next step would be to connect an optical fiber to the sample holder to have the advantage of placing the laser outside of the hole system. In this way, the laser beam will not be influenced by varying temperatures.

In this chapter, the results from this PhD thesis are presented. In the first two

sections (Sec. 4.1 and Sec. 4.2) the phase diagram and the behavior of the dilute proteins phase is discussed. It is shown how an LLPS is defined in this study, by the formation of macroscopic liquid droplets in the solution. Different methods, UV-Vis and X-ray absorption, for the determination of protein and salt concentrations at the binodal line of the LLPS are used. The hole phase diagram with the corresponding LLPS regions for both used proteins are presented, Sec. 4.2, and the protein and Y^{3+} partitioning is discussed. It is visible that the system shows attractive interactions between the proteins inside the LLPS region. The interactions in the system are quantified by using SLS and SAXS experiments. It is found that attractive interactions can be observed in the second regime. In a closed region of the second regime, the interactions are strong enough that the system can undergo an LLPS, which takes place under the correct protein concentration. At constant T the strength of the interaction depends on the available amount of Y^{3+} per protein in the case of HSA. In the case of BSA, no clear dependence is observed. The interaction strength can also be influenced by varying T. This comes from the fact that a further phase separation of the dilute phase takes place by heating up. The dense protein phase is in the focus of the second section, Sec. 4.4. The structure of the dense protein phase is determined, Sec. 4.4.1. From this determination three different sizes in the dense protein phase are identified. The smallest one is the monomer of the protein which forms oligomers in the case of HSA and small clusters in the case of BSA. In all HSA samples and for the BSA samples above 20°C, the formation of a bigger structure with a diffuse surface and a size of around 2 µm occurs. First rheology measurements show some indications that the samples form a gel in these cases. If this is really true, the bigger structure can be related to network formation inside the gelation process. The effective interaction of the dense protein phase shows an increased value, Sec. 4.4.3, which is located above the critical value of the LLPS. In this method, the volume fraction of the protein is quite high. At this high volume fractions, the second virial coefficient is influenced by additional interactions. It is quite difficult to give a general rule how the B_2 changes here. From the fact that the sample is separated from an LLPS the effective interaction should be stronger, and so B_2/B_2^{HS} smaller, as observed in the experiments. The influence of the solvent onto the phase diagram is investigated in Sec. 4.5, by varying the H_2O/D_2O content of the solvent. A shift of the c^{**} boundary to high salt concentration can be observed with increasing D_2O volume fractions. At high D_2O fractions, no LLPS appears, Sec. 4.5.1. The effective attraction in the system decreases with increasing D_2O volume fraction, Sec. 4.5.2. In one case, it has been observed that the attraction decreases below the critical strength for an LLPS, but in the most cases this is not observed. This can be explained by a reduction of the available c_p in the dilute protein phase with increasing Φ_{D_2O} by the formation of clusters. In this case, the position of the sample is shifted to the left in the phase diagram and at high Φ_{D_2O} outside of the LLPS region. The long-time stability and crystallization of the observed systems is presented in Sec. 4.6. It has been observed that over time both protein phases can undergo a crystallization process. The structure of the observed crystals fits to a crystal structure from a sample, which is located slightly outside of the LLPS region. The development of a new sample holder to combine inelastic neutron experiments with light spectroscopy is shown in Sec.

4.7. In the next chapter, Cha. 5 a short conclusion of this study is given.

5 Conclusions

In this study it is shown that an LLPS in a serum albumin solution (BSA and HSA) can be induced by multivalent ions (YCl_3) inside the turbid regime of a reentrant condensation phase diagram. The LLPS region for both proteins is identified by optical microscopy and the position is defined by the protein and salt concentration of the poor and dense protein phase, determined by UV-Vis and X-ray absorption [160, 202, 203]. The protein-yttrium interaction is estimated from the tie-lines and an attractive interaction is found. The protein-protein interaction for low protein concentrations in different regions of the phase diagram is determined by SLS (Sec. 4.1). This experiments show a sufficiently strong effective attractive interaction in the second regime to form an LLPS. The absence of the LLPS comes from the low protein concentration of the samples. The effective interaction inside the LLPS region is measured by SAXS (Sec. 4.1 and Sec. 4.2). The resulting effective attractive interactions inside this region are sufficiently strong, below the limit of Eq. 2.8, for the formation of dense liquid droplets. At the binodal lines the lowest effective interactions are found which increase by varying the sample composition to locations inside the LLPS region. A master curve behavior for B_2/B_2^{HS} compared to the salt concentration, plotted in Fig. 4.11, is found in the HSA case[160]. In general we can conclude that the effective protein-protein interactions are stronger in an HSA solution compared to a BSA solution. Increasing the temperature of a dilute protein solution, which is separated after an LLPS, leads to an increase of the effective attraction strength until the solution undergoes a second LLPS. A further increase of T results into a decrease of the effective attraction strength. This feature is related to the mentioned LCST behavior of serum albumin-yttrium mixture.

The optical behavior of the dense protein phase reveals also differences between HSA and BSA (Sec. 4.4.1). At low T the dense protein phase of a BSA solution is transparent, which is in contrast to the slightly turbid HSA solution at the same temperature (Fig. 4.15). Heating the system above a critical temperature both protein solutions becomes highly turbid. The temperature dependant phase behavior at smaller length scales is determined by SANS experiments (Sec. 4.4.2.2). For low temperatures no increase of the scattering intensity at low-q can be observed. Compared to the BSA solution an increase of the scattering intensity at low-q occurs in HSA solutions, which can be related to the formation of larger structures. For both proteins the formation of oligomers and small clusters can be observed. With increasing temperature an increase in the scattering intensity in the low-q-range compared to the low T scattering profiles for both proteins is observed. The radius of the large scale structures at higher T is measured by USANS experiments, which reveals a radius of around $r \approx 1.75 \pm 0.2\,\mu m$ for both proteins. From the fitted Porod exponent the formation of a diffusive interface, with an increased polydispersity in the HSA case, between the large scale structures and the

solution is visible. First rheologic measurements on the BSA dense protein phase reveals the transition from a liquid state to a gel state with increasing T. From this we conclude that in both protein cases a gel state is formed. For HSA this gel state is already reached for low T where higher temperatures are necessary for the gel formation in a BSA solution. The formation of the large scale structure with increasing T can be related to the formation of the gel network which is increased at higher T, which will explain the increased turbidity in both protein cases. Comparing the scattering curves for different temperatures shows that the smaller particles will be consumed by the formation of the gel network (Fig. 4.20). The effective interactions of the dense protein phase reveals differences compared to the dilute dense phase (Sec. 4.4.3). The interpretation of these differences is quite difficult because of the high protein concentration in the dense protein phase. The virial expansion, from which B_2/B_2^{HS} can be calculated, is only valid for dilute systems which means that in the dense protein phase also multibody interactions must be considered. In general it can be concluded that the effective interaction is below the critical value of an LLPS and decreases with increasing temperature.

Optical observations by eye and microscopy reveal an increased cluster formation with increasing D_2O volume fraction. The phase diagram for constant initial protein concentration with varying salt concentration and D_2O volume fraction is determined, Fig. 4.23. An LLPS region can be observed for $\Phi_{D_2O} < 80\,\%$. Small variations of the c^* line but a stronger variations of the c^{**} line with varying Φ_{D_2O} are visible from the recorded phase diagram. UV-Vis experiments reveal a decrease of the protein concentration in the dilute protein phase with increasing D_2O volume fractions. Comparing the variations of the scattering curves, measured by SAXS, for different Φ_{D_2O} reveals the structural changes in the samples of the second regime. In the observed q-range an increased formation of small oligomers instead of medium size clusters can be observed. Comparing with optical observation (Fig. 4.22) we can conclude that these small oligomers are build into big clusters, which are not visible in the observed q-range. From the SAXS measurements the effective interaction is calculated. From these calculations it is visible that the effective attraction reduces with increasing Φ_{D_2O}. The effective interaction decreases with increasing Φ_{D_2O} and stays in the most cases below the critical LLPS value. Therefore LLPS should be visible in principle but from the fact of the decreasing protein concentration of the dilute protein phase after LLPS with increasing Φ_{D_2O} we conclude that for $\Phi_{D_2O} > 80\,\%$ not enough unclustered proteins are left in the solution to form liquid droplets.

From the theoretical side LLPS results in metastable state and we investigated the stability of the dilute and dense protein phase in this study. In the case of HSA, the dilute phase can crystallize within in several days for salt concentrations close to c^*. Optical microscopy reveals that the crystals form in a two-step crystallization process. Waiting for longer times shows also one-step crystallization without visible precursors. The crystals are collected and the structure is determined by SAXS. The determined Bragg peaks are compared to an already measured and unpublished HSA crystal structure which shows a nice agreement. Time dependent SANS experiments for the HSA dense protein phase show the formation of a Bragg peak within 44 days. This single Bragg peak can be related to the (0,0,2) Bragg peak of the already measured crystal structure. From

SANS experiments an increase in the scattering intensity at the lowest q-values with time is observed until a maximum is reached and the scattering intensity starts to drop down. We relate the increase of the scattering intensity to the formation of bigger structures inside the dense protein phase. From the measurements we conclude that the bigger structures are consumed by the formation and the growth of crystals. This observed behavior from the scattering curves can be explained by a two-step crystallization process afs described by Sauter et al. [239].

A new type of sample holder to combine light spectroscopy with neutron experiments is developed in several steps. Test measurements of the stand alone sample holder demonstrate that in principal it is possible to measure the turbidity of a sample. Yet, when the sample holder is mounted onto a sample stick and placed into a cryostat no signal could be recorded anymore. Because of this result we redesigned the sample holder to bring the light source closer to the detector in order to reduce possible disturbances of the light beam. Until now the new sample holder is still under construction. The first test measurements of the new sample holder are planned for the near future.

6 Outlook

We investigated several features of the LLPS in a serum albumin solution induced by the multivalent Y^{3+} ion. As already mentioned, further work of our group also reveals a liquid-liquid phase separation for other salts like $YbCl_3$, $GdCl_3$ and $LaCl_3$. From this observation it seems that the LLPS in serum albumin solution is a salt independent behavior as long the salt is trivalent. An interesting point of further work would be to investigate the effective interactions for the LLPS in other salt solution than yttrium chloride. Can we also find a master curve behavior in the HSA case? Is the interaction with other trivalent metal ions stronger or weaker?

For some salts an increased LLPS region is observed where the low protein concentration boundary is shifted to lower protein concentrations. The lowest observed protein concentration is located below the protein concentrations observed in pure D_2O solution with YCl_3. Maybe it is possible to induce a LLPS also in pure D_2O solutions. If this is possible it would be quite interesting how the effective potential varies in pure D_2O solutions with varying type of salt.

A big issue for further work will be the studies of the LCST behavior of the LLPS in serum albumin solutions. Recording the 3D phase diagram (temperature, protein and salt concentration) leads to the possibility to calculate thermodynamic quantities by determining the LLPS surface, as demonstrated by Annunziata [5, 88]. The influence of the cation on these thermodynamic properties should also be determined to get a full overview of the serum albumin system.

In other studies of our group the anions of the salt are varied and it was found that they have also influences on the reentrant behavior of the system. An interesting point in this direction would be if also an LLPS occurs by varying the anion. If an LLPS occurs by varying the anion, the whole thermodynamic and effective interaction analysis procedure can be applied in order to complete this story.

The gelation of the dense phase with increasing T was determined only for one BSA sample until now. In order to confirm the assumption that the gelation takes also place in the HSA case further rheology experiments must be performed. As already mentioned for the dilute protein phase the influence of varying the cation and anion on the dense phase would also be quite interesting.

Until now the crystallization process was not completely monitored. This comes from the problem that the crystallization needs several days in the dilute protein phase and up to more than a month in the dense protein phase. Information about the crystallization process would be quite helpful to understand the crystallization procedure. Until now only one HSA crystal structure from slightly below the LLPS boundary exists. It would be interesting to get more high quality structures. From these high quality structures it would be possible to deduce the amount of bound yttrium ions per protein. This is a

crucial value for theoretical predictions and for simulations of the system. The crystal structure from the dense protein phase would reveal if the crystal structure is the same as in the dilute protein phase as we assume from the single observed Bragg-peak observed by SANS.

The tests of the redesigned sample holder must be performed in the future. If they are successful the change of the light source position by using optical fibers must be discussed to increase the flexibility of the system.

7 Appendix

7.1 Tables of the reduced second virial coefficient for HSA and BSA determined by SAXS

Table A1: Values for the initial and the real c_p and c_s in the dilute phase, the available number of yttrium ions per protein Y^{3+}/protein, the stickiness parameter τ and the reduced second virial coefficient B_2/B_2^{HS} for different sets of HSA samples.

c_{HSA} [mg/ml]		c_{YCl_3} [mM]		$Y^{3+}/$ [b]	τ	B_2/B_2^{HS} [c]	u_0
initial c_p	real c_p [a]	initial c_s	real c_s [a]	Protein			$[k_BT]$
31.1	30.3	3.0	3.0	6.5	0.055	-3.55	4.35
31.1	23.2	4.0	2.7	7.7	0.058	-3.36	4.29
31.1	18.7	8.0	3.5	12.4	0.061	-3.11	4.24
31.1	17.8	10.0	4.6	17.1	0.063	-2.99	4.21
31.1	17.7	14.0	5.5	20.5	0.062	-3.06	4.23
31.1	18.4	16.0	7.1	25.8	0.068	-2.69	4.14
31.1	18.7	18.0	7.8	27.8	0.072	-2.49	4.08
31.1	21.7	20.0	10.8	33.2	0.070	-2.57	4.11
31.1	27.8	25.0	15.7	37.5	0.070	-2.57	4.11
47.8	26.2	6.0	3.3	8.4	0.065	-2.82	4.18
47.8	17.1	8.0	2.6	10.2	0.057	-3.35	4.31
47.8	16.0	10.0	4.1	17.2	0.059	-3.24	4.28
47.8	19.5	14.0	8.1	27.5	0.066	-2.79	4.17
47.8	24.2	18.0	11.9	32.8	0.067	-2.71	4.15
47.8	29.4	22.0	15.3	34.6	0.079	-2.17	3.99
47.8	35.4	26.0	18.5	34.8	0.084	-1.98	3.92
47.8	42.5	30.0	21.7	33.9	0.089	-1.80	3.87
47.8	46.5	32.0	24.9	35.6	0.091	-1.75	3.84
74.0	23.4	10.0	3.0	8.5	0.072	-2.49	4.06
74.0	16.6	12.5	4.6	18.5	0.066	-2.82	4.15
74.0	15.9	14.5	6.9	29.0	0.062	-3.02	4.21
74.0	18.4	15.0	9.6	34.8	0.066	-2.78	4.14

[a] real concentration in the protein-poor phase

[b] ratio between real salt and protein concentration in the protein-poor phase

[c] the error from data fitting is in general below 1 %, but we estimate the systematic absolute error to these values is about ±0.10.

Table A2: Values for the initial and the real c_p and c_s in the dilute phase, the available number of yttrium ions per protein Y^{3+}/protein, the stickiness parameter τ, the reduced second virial coefficient B_2/B_2^{HS} for different sets of BSA samples and the corresponding room temperature for the preparation.

c_{BSA} [mg/ml]		c_{YCl_3} [mM]		Y^{3+}/ [b]	τ	B_2/B_2^{HS} [c]	u_0	T
initial c_p	real c_p [a]	initial c_s	real c_s [a]	Protein			$[k_BT]$	[°C]
45.9	43.0	4	3.2	4.9	0.118	-1.11	3.56	22
45.9	36.4	5	3.7	6.8	0.076	-2.31	4.00	22
45.9	29.4	6	4.6	10.2	0.070	-2.60	4.09	22
45.9	27.9	7	5.2	12.2	0.068	-2.70	4.12	22
45.9	27.2	8	5.9	14.3	0.067	-2.75	4.13	22
45.9	29.4	10	8.5	19.0	0.068	-2.70	4.12	22
45.9	38.1	12	14.3	24.6	0.073	-2.42	4.04	22
45.9	34.8	14	12.0	22.7	0.072	-2.46	4.06	22
91.7	63.1	8	11.7	12.2	0.115	-1.17	3.59	4
91.7	60.6	10	12.9	14.0	0.084	-1.97	3.90	4
91.7	60.3	12	11.1	12.1	0.085	-1.93	3.89	4
91.7	59.1	14	11.5	12.8	0.087	-1.86	3.87	4
91.7	63.8	16	12.9	13.3	0.090	-1.77	3.84	4
91.7	65.4	18	17.6	17.7	0.089	-1.81	3.85	4
91.7	66.5	20	17.8	17.6	0.089	-1.82	3.85	4
91.7	68.3	22	21.4	20.6	0.089	-1.81	3.85	4
183.3	66.7	18	12.6	12.4	0.086	-1.92	3.89	4
183.3	63.6	20	12.3	12.8	0.087	-1.89	3.87	4
183.3	62.6	22	13.0	13.7	0.086	-1.90	3.88	4
183.3	62.6	24	13.8	14.5	0.086	-1.90	3.88	4
183.3	64.4	26	16.2	16.5	0.086	-1.90	3.87	4
183.3	66.5	28	17.9	17.7	0.088	-1.85	3.86	4
183.3	67.1	30	19.0	18.6	0.089	-1.82	3.88	4

[a] real concentration in the protein-poor phase

[b] ratio between real salt and protein concentration in the protein-poor phase

[c] the error from data fitting is in general below 1 %, but we estimate the systematic absolute error to these values is about ±0.10.

Table A3: Stickiness parameter τ and the reduced second virial coefficient B_2/B_2^{HS} for an HSA sample with varying T and the corresponding size of the fitted ellipsoid.

$c_{i,HSA}$ [mg/ml]	c_{YCl_3} [mM]	T [°C]	r_a [Å]	r_b [Å]	V_{Sphere} [Å^3]	τ	B_2/B_2^{HS} [a]	u_0 [k_BT]
31.1	4.0	14.0	16.2	55.2	206767	0.0676	-2.70	-4.12
31.1	4.0	16.0	16.0	57.0	217750	0.0675	-2.70	-4.12
31.1	4.0	18.0	15.9	58.8	230271	0.0672	-2.72	-4.13
31.1	4.0	20.0	15.9	59.8	238171	0.0665	-2.76	-4.14
31.1	4.0	22.0	15.9	61.8	254368	0.0662	-2.78	-4.14
31.1	4.0	24.0	16.0	63.0	266004	0.0657	-2.80	-4.15
31.1	4.0	26.0	15.2	62.8	251103	0.0658	-2.80	-4.15
31.1	4.0	28.0	14.6	61.0	227563	0.0659	-2.79	-4.15
31.1	4.0	30.0	14.0	59.4	206914	0.0663	-2.77	-4.14

[a] the error from data fitting is in general below 1 %, but we estimate the systematic absolute error to these values is about ±0.10.

7.2 Tables for the fitting results on the dense protein phase

Table A4: Values from the Guinier, Porod and Beaucage fits for the dense protein phases with an initial $c_{p,BSA} = 183.3\,\mathrm{mg/ml}$ and $c_{p,HSA} = 93.3\,\mathrm{mg/ml}$.

		Guinier fit			Porod fit		Beaucage fit			
Protein	c_{YCl_3} [mM]	T [°C]	r_G [Å]	# monomers/ [a] particle	T [°C]	slope [d]	T [°C]	r_G [µm]	slope [c]	PDI [d]
BSA	20	10	90.95 ± 0.94	35.5 ± 1.1	35	-4.7	35	1.9	-4.1	5.64
BSA	22	21	99.40 ± 9.99	46.4 ± 14.0	35	-4.0 [b]	35	2.0	-4.0	2.56
BSA	24	21	98.06 ± 1.09	44.5 ± 1.5	25	-4.2				
BSA	24				33	-4.5				
BSA	26	10	66.51 ± 1.38	13.9 ± 0.9	35	-4.7				
BSA	26	20	84.74 ± 1.15	28.7 ± 1.2			35	2.0	-4.1	1.98
BSA	28	10	54.05 ± 1.65	7.5 ± 0.7	35	-4.7 [b]	35	1.9	-4.2	3.99
BSA	28	20	76.31 ± 1.29	21.0 ± 1.1						
BSA	30	10	61.43 ± 1.33	11.0 ± 0.7	35	-4.8	35	1.5	-4.3	3.28
BSA	35						35	1.7	-4.2	3.29
BSA	40						35	1.7	-4.1	2.54
HSA	20	10	56.12 ± 1.52	8.3 ± 0.7	30	-4.7	35	1.5	-4.1	5.19
HSA	20				35	-4.7				
HSA	22	10	223.56 ± 8.11	527.8 ± 57.4	10	-3.1 [b]				
HSA	22	10			21	-3.9 [b]				
HSA	22				33	-4.7	35	1.5	-4.1	6.81
HSA	24				5	-3.1				
HSA	24				20	-4.6				
HSA	24				33	-4.5	35	1.7	-4.1	5.19
HSA	26	10	36.25 ± 0.72	2.3 ± 0.1	5	-3.9				
HSA	26				20	-4.6				
HSA	26				30	-5.2				
HSA	28	10	39.66 ± 0.75	2.9 ± 0.2	5	-3.4				
HSA	28				20	-4.0				
HSA	28				30	-3.9	35	1.7	-4.1	5.29
HSA	30	5	60.40 ± 1.36	10.4 ± 0.7	5	-3.8				
HSA	30				20	-4.4				
HSA	30				30	-4.6	35	2.1	-4.3	22.7
HSA	35						35	1.5	-4.1	7.58
HSA	40						35	1.9	-4.0	8.11

[a] calculated volume divided by the BSA monomer volume
[b] limited number of data points
[c] the estimate systematic absolute error to these values is about ±0.10
[d] the estimate systematic absolute error to these values is about ±0.20.

Table A5: Values from SHS potential fits for the dense protein phases with an initial $c_{p,BSA}$ = 183.3 mg/ml.

T [°C]	10		20		30		35	
c_{YCl_3} [mM]	B_2/B_2^{HS} [d]	u_0 [k_bT]	B_2/B_2^{HS} [d]	u_0 [k_bT]	B_2/B_2^{HS} [d]	u_0 [k_bT]	B_2/B_2^{HS} [d]	u_0 [k_bT]
20	-1.25	-3.63	-1.45	-3.71	-1.25	-3.63	-0.92	-3.47
22	-1	-3.5	-1.21 [a]	-3.61 [a]			-1.23	-3.62
24			-1.29 [a]	-3.64 [a]	-1.29 [b]	-3.64 [b]	-1.33 [c]	-3.66 [c]
26	-0.82	-3.41	-1.11	-3.56	-0.72	-3.47	-0.94	-3.36
28	-0.79	-3.4	-1.06	-3.54	-0.96	-3.49	-0.75	-3.37
30	-0.88	-3.44	-1.16	-3.59	-0.72	-3.36	-0.72	-3.36

[a] measured at $T = 21$°C
[b] measured at $T = 29$°C
[c] measured at $T = 33$°C
[d] the error from data fitting is in general below 1 %, but we estimate the systematic absolute error to these values is about ±0.10.

Table A6: Values from SHS potential fits for the dense protein phases with an initial $c_{p,HSA}$ = 93.3 mg/ml.

T [°C]	5		10		20		30	
c_{YCl_3} [mM]	B_2/B_2^{HS} [c]	u_0 [k_bT]	B_2/B_2^{HS} [c]	u_0 [k_bT]	B_2/B_2^{HS} [c]	u_0 [k_bT]	B_2/B_2^{HS} [c]	u_0 [k_bT]
20			-0.89	-3.45	-0.37	-3.13	-0.35	-3.11
22			-0.39	-3.14	-0.36 [a]	-3.12 [a]	-0.25 [b]	-3.04 [b]
24	-1.12	-3.56	-1.12	-3.56	-0.92	-3.47	-0.73	-3.36
26	-1.2	-3.6	-1.18	-3.59	-1.05	-3.52	-0.89	-3.45
28	-1.02	-3.51	-0.87	-3.44	-0.63	-3.3	-0.37	-3.13
30	-1.29	-3.64	-1.35	-3.67	-1.23	-3.62	-1.13	-3.57

[a] measured at $T = 21$°C
[b] measured at $T = 33$°C
[c] the error from data fitting is in general below 1 %, but we estimate the systematic absolute error to these values is about ±0.10.

7.3 Table for the fitting results of the interaction changes by varying the D_2O volume fraction

Table A7: Values for the initial c_p and c_s in the dilute phase, the stickiness parameter τ and the reduced second virial coefficient B_2/B_2^{HS} for varying Φ_{D_2O} in the case of HSA and BSA are shown.

Φ_{D_2O} [%]	c_{HSA} [mg/ml]	c_{YCl_3} [mM]	τ	B_2/B_2^{HS} [a]	u_0 $[k_BT]$	c_{YCl_3} [mM]	τ	B_2/B_2^{HS} [a]	u_0 $[k_BT]$
0	31.1	4.0	0.061	-3.09	4.22	8.0	0.056	-3.44	3.44
20	31.1	4.0	0.062	-3.05	4.21	8.0	0.056	-3.44	3.44
40	31.1	4.0	0.063	-2.94	4.19	8.0	0.057	-3.42	3.42
60	31.1	4.0	0.064	-2.89	4.17	8.0	0.058	-3.34	3.34
80	31.1	4.0	0.068	-2.70	4.12	8.0	0.058	-3.31	3.31
100	31.1	4.0	0.071	-2.52	4.07	8.0	0.060	-3.17	3.17

Φ_{D_2O} [%]	c_{BSA} [mg/ml]	c_{YCl_3} [mM]	τ	B_2/B_2^{HS} [a]	u_0 $[k_BT]$	c_{YCl_3} [mM]	τ	B_2/B_2^{HS} [a]	u_0 $[k_BT]$
0	91.7	12.0	0.084	-1.96	3.90	20.0	0.086	-1.92	3.88
20	91.7	12.0	0.086	-1.89	3.88	20.0	0.086	-1.91	3.88
40	91.7	12.0	0.090	-1.78	3.84	20.0	0.086	-1.92	3.88
60	91.7	12.0	0.104	-1.39	3.69	20.0	0.090	-1.78	3.84
80	91.7	12.0	0.116	-1.16	3.58	20.0	0.093	-1.69	3.80
100	91.7	12.0	0.129	-0.93	3.48	20.0	0.098	-1.56	3.75

[a] the error from data fitting is in general below 1 %, but we estimate the systematic absolute error to these values is about ±0.10.

7.4 Blueprints for the development of a new sample holder

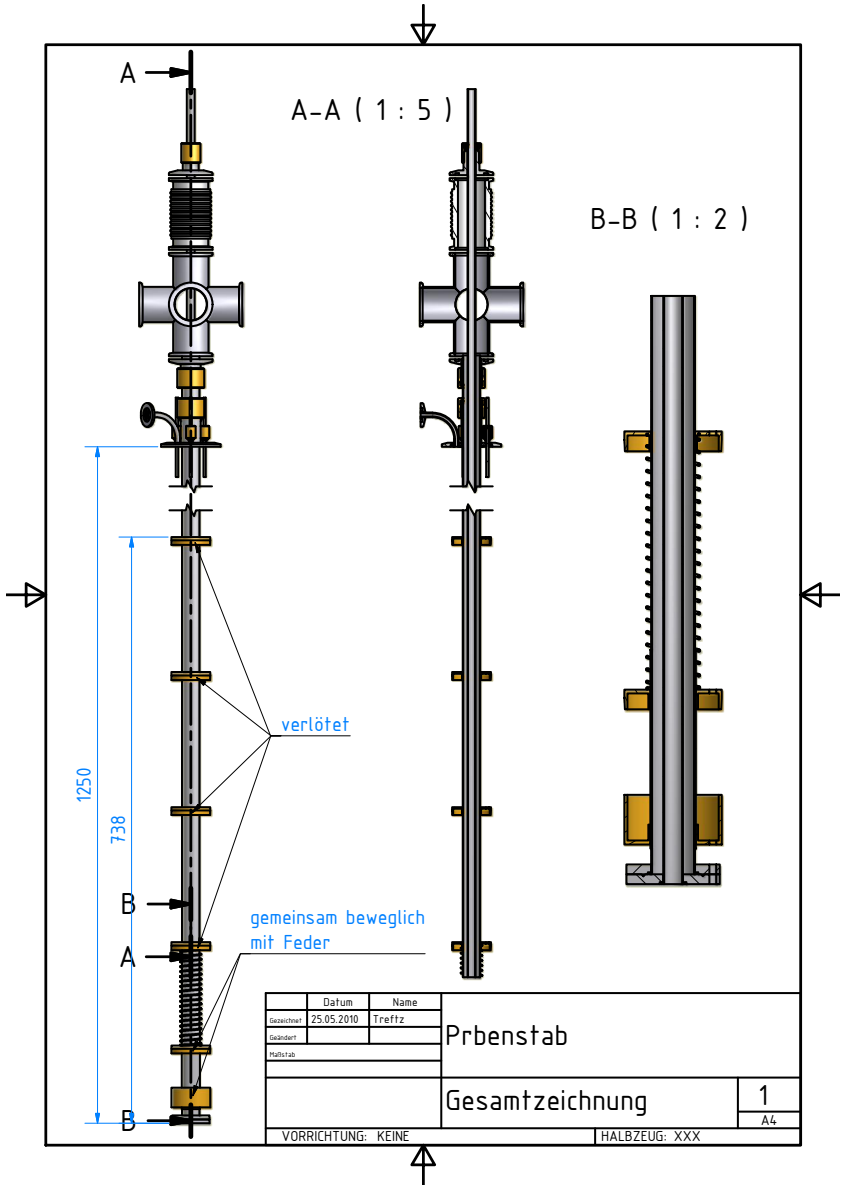

Figure A1: Blueprint for the sample stick at which the new sample holder should be mounted. The sample stick is designed in the purpose to instal the new sample holder into a cryostat. On the left side an overview of the hole sample stick is shown. In the middle an overview over the upper part of the sample stick is presented. It is visible that a tube is placed in the center of the stick, which goes through the complete stick. On the right sight the lower part of the stick is plotted. The length of the sample stick can be adjusted by a spring, which is shown on the figures on the left and right side.

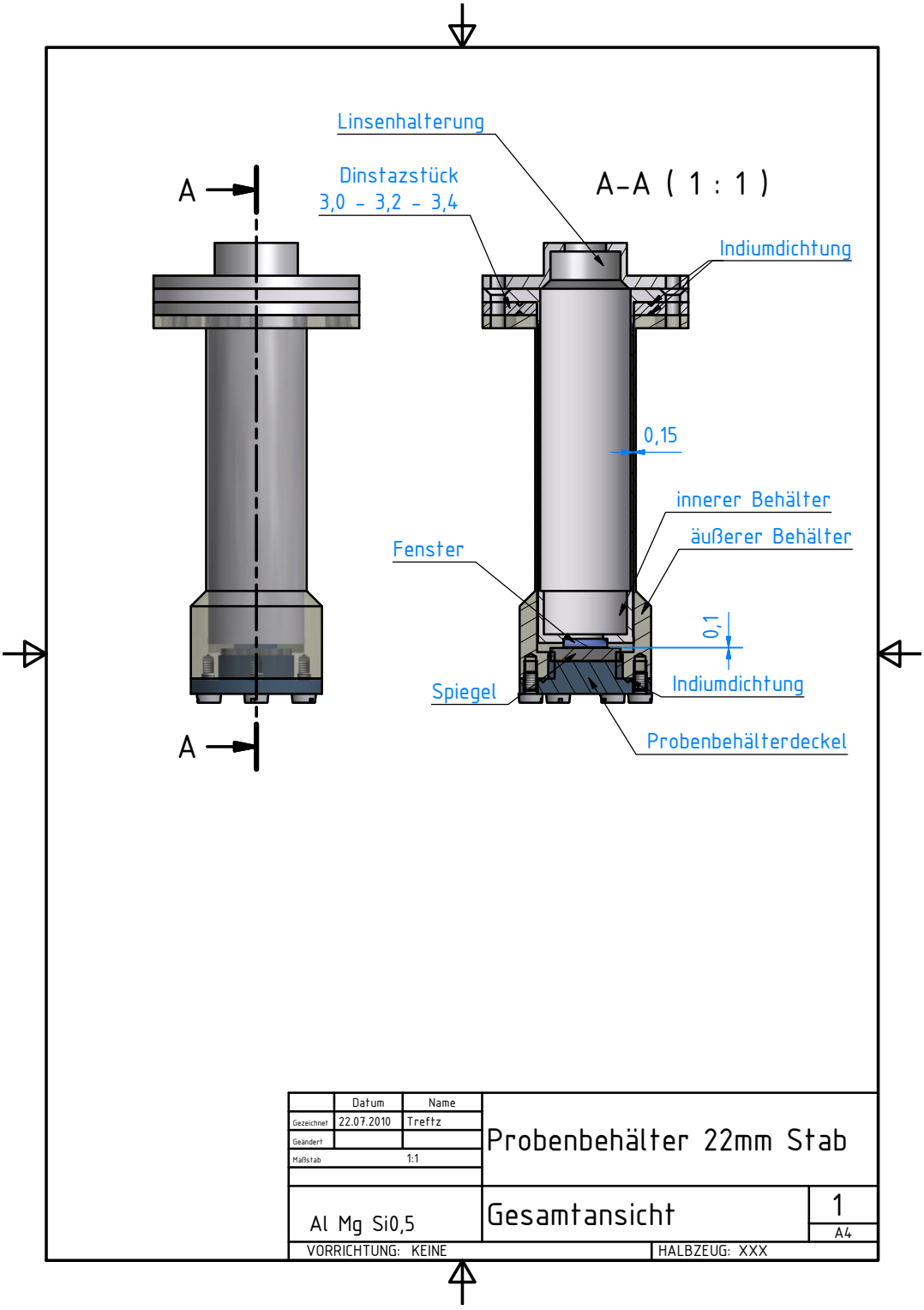

Figure A2: The blueprint of the sample holder, in the first version is plotted. At the top of this sample holder a holder for an optical lens and the connections to a optical fiber is placed. Over a mirror, located at the button of the sample holder the laser beam, which comes through the optical fiber is reflected back to the fiber.

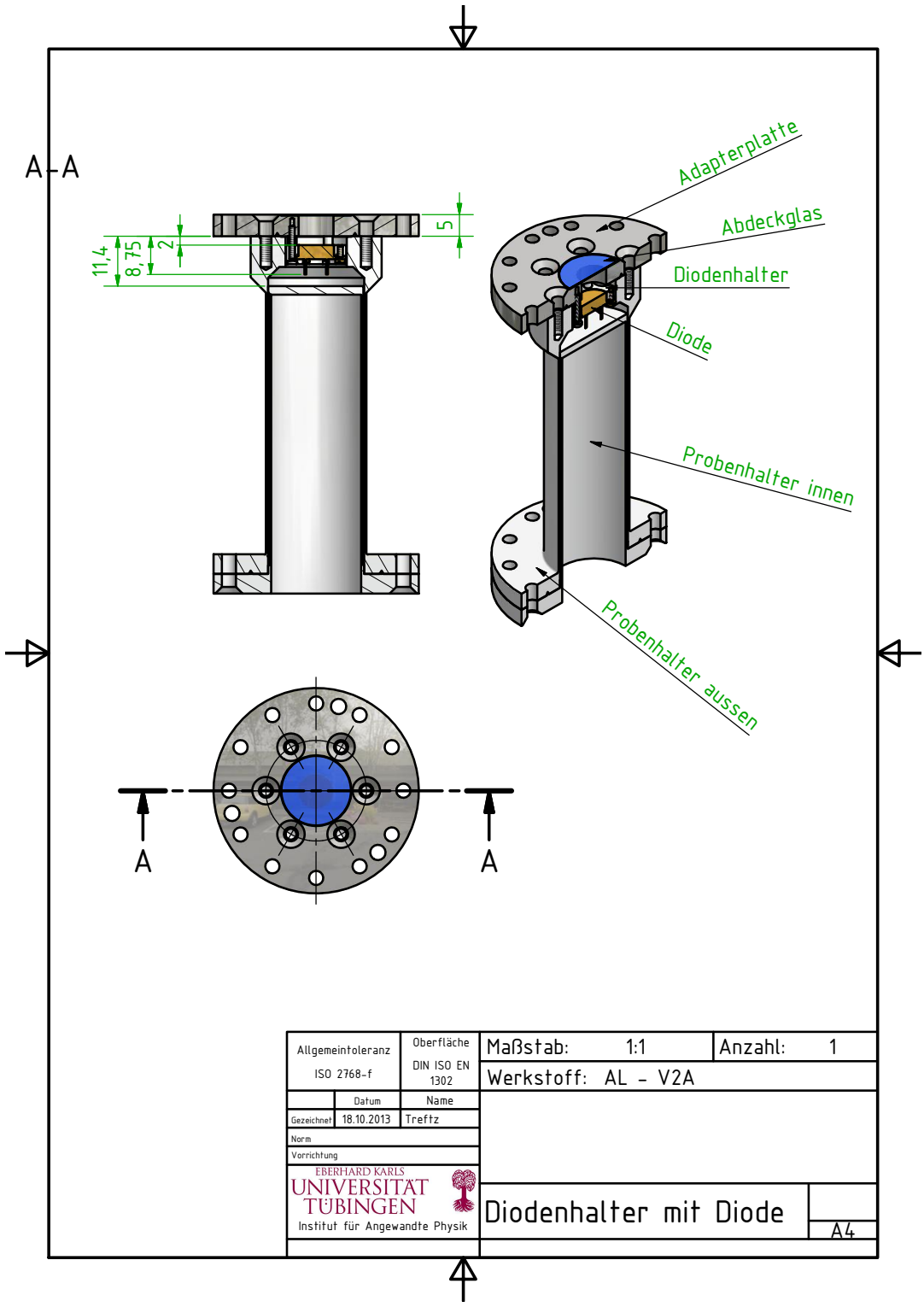

Figure A3: The blueprint of the sample holder, in the third version is plotted. The optical part is placed above the neutron part of the sample holder in order to reduced the laser - photo diode distance. The photo diode is placed into the liquid and the bottom of the diode and the electrical connections are sealed by rosin. The photo diode can be read out via electrical connections through the cover plate and the sample stick.

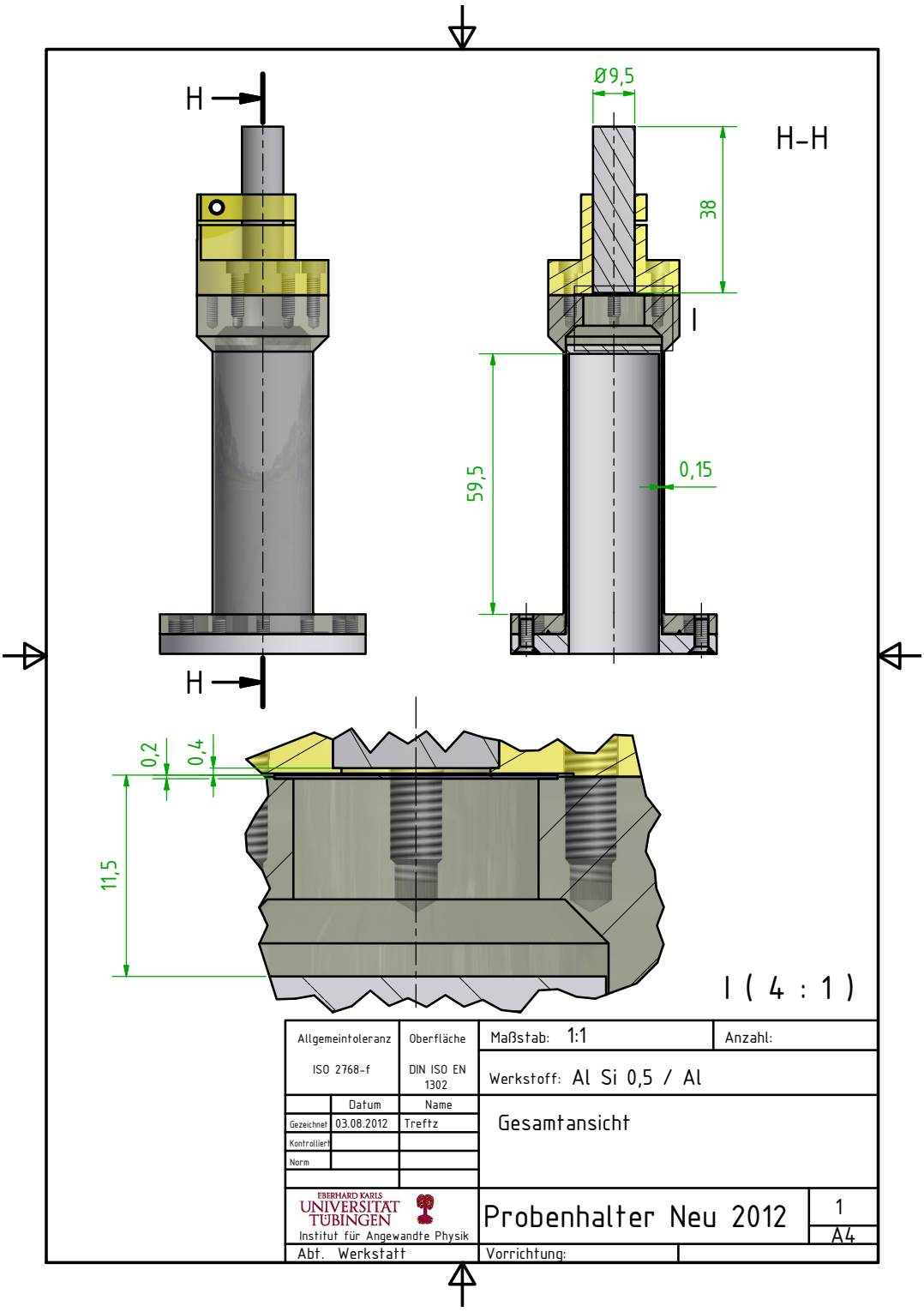

Figure A4: The blueprint of the raman sample holder is shown. The optical part is placed above the neutron part of the sample holder. To place the raman probe above the sample holder a special holder is designed.

Bibliography

[1] Alberts, B., Johnson, A., Lewis, J., Rafi, M., Roberts, K., and Walter, P. *Molecular Biology of the Cell*. Garland Science, Taylor & Francis Group, New York, 5th revised edition, (2008).

[2] Gunton, J., Shiryayev, A., and Pagan, D. *Protein Condensation: Kinetic Pathways to Crystallization and Disease*. Cambridge University Press, (2007).

[3] Wolde, P. R. t. and Frenkel, D. *Science* **277**(5334), 1975–1978 (1997).

[4] Pande, A., Pande, J., Asherie, N., Lomakin, A., Ogun, O., King, J., and Benedek, G. B. *Proc. Natl. Acad. Sci. USA* **98**(11), 6116–6120 (2001).

[5] Annunziata, O., Ogun, O., and Benedek, G. B. *Proc. Natl. Acad. Sci. USA* **100**(3), 970–974 (2003).

[6] Vekilov, P. G. *Cryst. Growth Des.* **4**(4), 671–685 (2004).

[7] Wang, Y., Lomakin, A., McManus, J. J., Ogun, O., and Benedek, G. B. *Proc. Natl. Acad. Sci. USA* **107**(30), 13282–13287 (2010).

[8] Anderson, V. J. and Lekkerkerker, H. N. W. *Nature* **416**(6883), 811–815 (2002).

[9] Vliegenthart, G. A. and Lekkerkerker, H. N. W. *J. Chem. Phys.* **112**(12), 5364–5369 (2000).

[10] Zhang, F., Skoda, M. W. A., Jacobs, R. M. J., Zorn, S., Martin, R. A., Martin, C. M., Clark, G. F., Weggler, S., Hildebrandt, A., Kohlbacher, O., and Schreiber, F. *Phys. Rev. Lett.* **101**(14), 148101 (2008).

[11] Bujacz, A. *Acta Crystallogr., Sect. D* **68**(10), 1278–1289 (2012).

[12] Majorek, K. A., Porebski, P. J., Dayal, A., Zimmerman, M. D., Jablonska, K., Stewart, A. J., Chruszcz, M., and Minor, W. *Mol. Immunol.* **52**(34), 174 – 182 (2012).

[13] Benedek, G. B. *Invest. Ophth. Vis. Sci.* **38**(10), 1911–1921 (1997).

[14] Asherie, N. R., Lomakin, A., and Benedek, G. B. *Phys. Rev. Lett.* **77**(23), 4832–4835 (1996).

[15] Glenner, G. G. and Wong, C. W. *Biochem. Biophys. Res. Commun.* **120**, 885–890 (1984).

[16] Sipe, J. D. and Cohen, A. S. *J. Struct. Biol.* **130**(23), 88 – 98 (2000).

[17] Hardy, J. and Selkoe, D. J. *Science* **297**(5580), 353–356 (2002).

[18] Chiti, F. and Dobson, C. M. *Annu. Rev. Biochem.* **75**, 333–366 (2006).

[19] Gouy, M. *J. Phys. Theor. Appl.* **9**(1), 457–468 (1910).

[20] Chapman, D. L. *Phil. Mag.* **25**(148), 475–481 (1913).

[21] Messina, R. *J. Phys.: Condens. Matter* **21**(11), 113102 (2009).

[22] Debye, P. and Hückel, E. *Phys. Z.* **24**(9), 185–206 (1923).

[23] Derjaguin, B. V. and Landau, L. *Acta Physicochim. USSR* **14**, 633–662 (1941).

[24] Verwey, E. and Overbeek, J. *Theory of the Stability of Lyophobic Colloids*. Elsevier, Amsterdam, (1948).

[25] Boström, M., Williams, D. R. M., and Ninham, B. W. *Phys. Rev. Lett.* **87**(16), 168103 (2001).

[26] Petsev, D. N. and Vekilov, P. G. *Phys. Rev. Lett.* **84**(6), 1339–1342 (2000).

[27] Hofmeister, F. *N-S Arch. Pharmacol.* **24**, 247–260 (1888).

[28] Arakawa, T. and Timasheff, S. N. *Biochemistry* **23**(25), 5912–5923 (1984).

[29] Collins, K. D. and Washabaugh, M. W. *Q. Rev. Biophys.* **18**, 323–422 (1985).

[30] Baldwin, R. *Biophys. J.* **71**(4), 2056 – 2063 (1996).

[31] Collins, K. *Biophys. J.* **72**(1), 65 – 76 (1997).

[32] Collins, K. D. *Methods* **34**(3), 300 – 311 (2004).

[33] Jungwirth, P. and Winter, B. *Annu. Rev. Phys. Chem.* **59**(1), 343–366 (2008).

[34] Levin, Y. *Phys. Rev. Lett.* **102**, 147803 (2009).

[35] Dahirel, V. and Jardat, M. *Curr. Opin. Colloid Interface Sci.* **15**(12), 2 – 7 (2010).

[36] Ninham, B. W. and Nostro, P. L. *Molecular Forces and Self Assembly: In Colloid, Nano Sciences and Biology*. Cambridge University Press Cambridge, (2010).

[37] Schwierz, N., Horinek, D., and Netz, R. R. *Langmuir* **26**(10), 7370–7379 (2010).

[38] Heyda, J., Hrobárik, T., and Jungwirth, P. *J. Phys. Chem. A* **113**(10), 1969–1975 (2009).

[39] Manning, G. S. *J. Chem. Phys.* **51**(3), 924–933 (1969).

[40] Moreira, A. G. and Netz, R. R. *Europhys. Lett.* **52**(6), 705 (2000).

[41] Deserno, M., Holm, C., and May, S. *Macromolecules* **33**(1), 199–206 (2000).

[42] Grosberg, A. Y., Nguyen, T. T., and Shklovskii, B. I. *Rev. Mod. Phys.* **74**(2), 329–345 (2002).

[43] Terao, T. *Colloid Surface A* **273**(1-3), 141 – 146 (2006).

[44] Shklovskii, B. I. *Phys. Rev. E* **60**(5), 5802–5811 (1999).

[45] Besteman, K., Zevenbergen, M. A. G., Heering, H. A., and Lemay, S. G. *Phys. Rev. Lett.* **93**(17), 170802 (2004).

[46] Besteman, K., Van Eijk, K., and Lemay, S. G. *Nat. Phys.* **3**(9), 641–644 (2007).

[47] Zhang, F., Weggler, S., Ziller, M. J., Ianeselli, L., Heck, B. S., Hildebrandt, A., Kohlbacher, O., Skoda, M. W. A., Jacobs, R. M. J., and Schreiber, F. *Proteins* **78**(16), 3450–3457 (2010).

[48] Tanford, C., Swanson, S. A., and Shore, W. S. *J. Am. Chem. Soc.* **77**(24), 6414–6421 (1955).

[49] Tanford, C. and Kirkwood, J. G. *J. Am. Chem. Soc.* **79**(20), 5333–5339 (1957).

[50] Permyakov, E. Y. *Metalloproteomics*. John Wiley & Sons, Hoboken, New Jersey, (2009).

[51] Williams, P. and Peacocke, A. *Biochem. J.* **105**(3), 1177–85 (1967).

[52] Aasa, R., Malmström, B. G., Saltman, P., and Vänngård, T. *Biochim. Biophys. Acta* **75**(0), 203 – 222 (1963).

[53] Trapp, G. A. *Life Sci.* **33**(4), 311 – 316 (1983).

[54] Martin, R. B. *Clin. Chem.* **32**(10), 1797–806 (1986).

[55] Tainer, J. A., Roberts, V. A., and Getzoff, E. D. *Curr. Opin. Biotechnol.* **2**(4), 582 – 591 (1991).

[56] Berthon, G. *Pure Appl. Chem.* **67**, 1117–1240 (1995).

[57] Yamashita, M. M., Wesson, L., Eisenman, G., and Eisenberg, D. *Proc. Natl. Acad. Sci. USA* **87**(15), 5648–5652 (1990).

[58] Roosen-Runge, F., Heck, B. S., Zhang, F., Kohlbacher, O., and Schreiber, F. *J. Phys. Chem. B* **117**(18), 5777–5787 (2013).

[59] Roosen-Runge, F., Zhang, F., Schreiber, F., and Roth, R. *submitted and under review* (2013).

[60] Gibaud, T. and Schurtenberger, P. *J. Phys.: Condens. Matter* **21**(32), 322201 (2009).

[61] Gibaud, T., Mahmoudi, N., Oberdisse, J., Lindner, P., Pedersen, J. S., Oliveira, C. L. P., Stradner, A., and Schurtenberger, P. *Faraday Discuss.* **158**, 267 (2012).

[62] Zhang, F., Roosen-Runge, F., Sauter, A., Wolf, M., Jacobs, R. M. J., and Schreiber, F. *Pure Appl. Chem.* **86**, 191–202 (2014).

[63] Tanaka, T. and Benedek, G. B. *Invest. Ophth. Vis. Sci.* **14**(6), 449–56 (1975).

[64] Tanaka, T., Ishimoto, C., and Chylack, L. *Science* **197**(4307), 1010–1012 (1977).

[65] Taratuta, V. G., Holschbach, A., Thurston, G. M., Blankschtein, D., and Benedek, G. B. *J. Phys. Chem.* **94**(5), 2140–2144 (1990).

[66] Broide, M. L., Tominc, T. M., and Saxowsky, M. D. *Phys. Rev. E* **53**(6), 6325–6335 (1996).

[67] Muschol, M. and Rosenberger, F. *J. Chem. Phys.* **107**(6), 1953–1962 (1997).

[68] Galkin, O. and Vekilov, P. G. *Proc. Natl. Acad. Sci. USA* **97**(12), 6277–6281 (2000).

[69] Petsev, D. N., Wu, X., Galkin, O., and Vekilov, P. G. *J. Phys. Chem. B* **107**(16), 3921–3926 (2003).

[70] Siezen, R. J., Fisch, M. R., Slingsby, C., and Benedek, G. B. *Proc. Natl. Acad. Sci. USA* **82**(6), 1701–1705 (1985).

[71] Thomson, J. A., Schurtenberger, P., Thurston, G. M., and Benedek, G. B. *Proc. Natl. Acad. Sci. USA* **84**(20), 7079–7083 (1987).

[72] Schurtenberger, P., Chamberlin, R. A., Thurston, G. M., Thomson, J. A., and Benedek, G. B. *Phys. Rev. Lett.* **63**(19), 2064–2067 (1989).

[73] Broide, M. L., Berland, C. R., Pande, J., Ogun, O. O., and Benedek, G. B. *Proc. Natl. Acad. Sci. USA* **88**(13), 5660–5664 (1991).

[74] Berland, C. R., Thurston, G. M., Kondo, M., Broide, M. L., Pande, J., Ogun, O., and Benedek, G. B. *Proc. Natl. Acad. Sci. USA* **89**(4), 1214–1218 (1992).

[75] Annunziata, O., Pande, A., Ogun, O., Lubsen, N. H., and Benedek, G. B. *Biochemistry* **44**, 1316–1328 (2005).

[76] Liu, C., Asherie, N. R., Lomakin, A., Pande, J., Ogun, O., and Benedek, G. B. *PNAS* **93**, 377–382 (1996).

[77] San Bagio, P. L. and Palma, M. U. *Biophys. J.* **60**, 508–512 (1991).

[78] Galkin, O., Chen, K., Nagel, R. L., Hirsch, R. E., and Vekilov, P. G. *Proc. Natl. Acad. Sci. USA* **99**(13), 8479–8483 (2002).

[79] Chen, Q., Vekilov, P. G., Nagel, R. L., and Hirsch, R. E. *Biophys. J.* **86**(3), 1702 – 1712 (2004).

[80] Grouazel, S., Perez, J., Astier, J.-P., Bonneté, F., and Veesler, S. *Acta Crystallogr., Sect. D* **58**(10 Part 1), 1560–1563 (2002).

[81] Vivarès, D. and Bonneté, F. *J Phys. Chem. B* **108**, 6498–6507 (2004).

[82] Vivarès, D., Kaler, E. W., and Lenhoff, A. M. *Acta Crystallogr., Sect. D* **61**(6), 819–825 (2005).

[83] Mason, B. D., van Enk, J. Z., Zhang, L., Remmele, Jr., R. L., and Zhang, J. *Biophys. J.* **99**(11), 3792 – 3800 (2010).

[84] Nishi, H., Miyajima, M., Nakagami, H., Noda, M., Uchiyama, S., and Fukui, K. *Pharm. Res.* **27**(7), 1348–1360 (2010).

[85] Lewus, R. A., Darcy, P. A., Lenhoff, A. M., and Sandler, S. I. *Biotechnol. Prog.* **27**(1), 280–289 (2011).

[86] Trilisky, E., Gillespie, R., Osslund, T. D., and Vunnum, S. *Biotechnol. Prog.* **27**(4), 1054–1067 (2011).

[87] Wang, Y., Lomakin, A., Latypov, R. F., and Benedek, G. B. *Proc. Natl. Acad. Sci. USA* **108**(40), 16606–16611 (2011).

[88] Annunziata, O., Asherie, N., Lomakin, A., Pande, J., Ogun, O., and Benedek, G. B. *Proc. Natl. Acad. Sci. USA* **99**(22), 14165–14170 (2002).

[89] Poon, W. *J. Phys.: Condens. Matter* **14**, R859–R880 (2002).

[90] Kulkarni, A. M., Chatterjee, A. P., Schweizer, K. S., and Zukoski, C. F. *Phys. Rev. Lett.* **83**(22), 4554–4557 (1999).

[91] Kuznetsov, Y., Malkin, A. J., and McPherson, A. *J. Cryst. Growth* **232**, 30–39 (2001).

[92] Rosenbaum, D., Zamora, P., and Zukoski, C. *Phys. Rev. Lett.* **76**(1), 150–153 (1996).

[93] Jackson, G., Chapman, W. G., and Gubbins, K. E. *Mol. Phys.* **65**(1), 1–31 (1988).

[94] Bianchi, E., Largo, J., Tartaglia, P., Zaccarelli, E., and Sciortino, F. *Phys. Rev. Lett.* **97**, 168301 (2006).

[95] Ruzicka, B., Zaccarelli, E., Zulian, L., Angelini, R., Sztucki, M., Moussaïd, A., Narayanan, T., and Sciortino, F. *Nat. Mater.* **10**, 56–60 (2011).

[96] Sciortino, F. and Zaccarelli, E. *Curr. Opin. Solid. St. M* **15**(6), 246 – 253 (2011).

[97] Groenewold, J. and Kegel, W. K. *J. Phys. Chem. B* **105**(47), 11702–11709 (2001).

[98] Sciortino, F., Mossa, S., Zaccarelli, E., and Tartaglia, P. *Phys. Rev. Lett.* **93**, 055701 (2004).

[99] Spohr, E., Hribar, B., and Vlachy, V. *J. Phys. Chem. B* **106**(9), 2343–2348 (2002).

[100] Mossa, S., Sciortino, F., Tartaglia, P., and Zaccarelli, E. *Langmuir* **20**(24), 10756–10763 (2004).

[101] Jiang, T. and Wu, J. *Phys. Rev. E* **80**, 021401 (2009).

[102] Kowalczyk, P., Ciach, A., Gauden, P., and Terzyk, A. *J. Colloid Interface Sci.* **363**(2), 579 – 584 (2011).

[103] Fierro, A., Abete, T., Coniglio, A., and de Candia, A. *J. Phys. Chem. B* **115**(22), 7281–7287 (2011).

[104] Stradner, A., Sedgwick, H., Cardinaux, F., Poon, W. C. K., Egelhaaf, S. U., and Schurtenberger, P. *Nature* **432**, 492–495 (2004).

[105] Stradner, A., Cardinaux, F., and Schurtenberger, P. *J. Phys. Chem. B* **110**(42), 21222–31 (2006).

[106] Shukla, A., Mylonas, E., Di Cola, E., Finet, S., Timmins, P., Narayanan, T., and Svergun, D. I. *Proc. Natl. Acad. Sci. USA* **105**(13), 5075–5080 (2008).

[107] Barhoum, S. and Yethiraj, A. *J. Phys. Chem. B* **114**, 17062–17067 (2010).

[108] Porcar, L., Falus, P., Chen, W.-R., Faraone, A., Fratini, E., Hong, K., Baglioni, P., and Liu, Y. *J. Phys. Chem. Lett.* **1**(1), 126–129 (2010).

[109] Cardinaux, F., Zaccarelli, E., Stradner, A., Bucciarelli, S., Farago, B., Egelhaaf, S. U., Sciortino, F., and Schurtenberger, P. *J. Phys. Chem. B* **115**(22), 7227–7237 (2011).

[110] Li, Y., Lubchenko, V., and Vekilov, P. G. *Rev. Sci. Instrum.* **82**(5), 053106 (2011).

[111] Liu, Y., Porcar, L., Chen, J., Chen, W.-R., Falus, P., Faraone, A., Fratini, E., Hong, K., and Baglioni, P. *J. Phys. Chem. B* **115**(22), 7238–7247 (2011).

[112] Piazza, R. and Iacopini, S. *Eur. Phys. J. E* **7**(1), 45–48 (2002).

[113] Gliko, O., Neumaier, N., Pan, W., Haase, I., Fischer, M., Bacher, A., Weinkauf, S., and Vekilov, P. G. *J. Am. Chem. Soc.* **127**(10), 3433–3438 (2005).

[114] Gliko, O., Pan, W., Katsonis, P., Neumaier, N., Galkin, O., Weinkauf, S., and Vekilov, P. G. *J. Phys. Chem. B* **111**(12), 3106–3114 (2007).

[115] Pan, W., Galkin, O., Filobelo, L., Nagel, R. L., and Vekilov, P. G. *Biophys. J.* **92**(1), 267 – 277 (2007).

[116] Pan, W., Vekilov, P. G., and Lubchenko, V. *J. Phys. Chem. B* **114**(22), 7620–30 (2010).

[117] Johnston, K. P., Maynard, J. A., Truskett, T. M., Borwankar, A. U., Miller, M. A., Wilson, B. K., Dinin, A. K., Khan, T. A., and Kaczorowski, K. J. *ACS Nano* **6**(2), 1357–1369 (2012).

[118] Zhang, F., Roosen-Runge, F., Sauter, A., Roth, R., Skoda, M. W. A., Jacobs, R., Sztucki, M., and Schreiber, F. *Faraday Discuss.* **159**, 313–325 (2012).

[119] George, A. and Wilson, W. W. *Acta Crystallogr., Sect. D* **50**(4), 361–365 (1994).

[120] Haas, C. and Drenth, J. *J. Cryst. Growth* **196**(24), 388 – 394 (1999).

[121] Vekilov, P. G. *Cryst. Growth Des.* **10**(12), 5007–5019 (2010).

[122] Galkin, O. and Vekilov, P. G. *J. Am. Chem. Soc.* **122**(1), 156–163 (2000).

[123] Jion, A. I., Goh, L.-T., and Oh, S. K. *Biotechnol. Bioeng.* **95**(5), 911–918 (2006).

[124] Lutsko, J. F. and Nicolis, G. *Phys. Rev. Lett.* **96**, 046102 (2006).

[125] Auer, S. and Frenkel, D. *Nature* **409**, 1020–1023 (2001).

[126] Gasser, U., Weeks, E. R., Schofield, A., Pusey, P. N., and Weitz, D. A. *Science* **292**, 258–262 (2001).

[127] Erdemir, D., Lee, A. Y., and Myerson, A. S. *Acc. Chem. Res.* **42**(5), 621–629 (2009).

[128] Hutchens, S. B. and Wang, Z.-G. *J. Chem. Phys.* **127**(8), 084912 (2007).

[129] Bonnett, P. E., Carpenter, K. J., Dawson, S., and Davey, R. J. *Chem. Commun.* **0**, 698–699 (2003).

[130] Navrotsky, A. *Proc. Natl. Acad. Sci. USA* **101**(33), 12096–12101 (2004).

[131] Vekilov, P. G. *Soft Matter* **6**(21), 5254–5272 (2010).

[132] Segrè, P. N., Prasad, V., Schofield, A. B., and Weitz, D. A. *Phys. Rev. Lett.* **86**, 6042–6045 (2001).

[133] Sztucki, M., Narayanan, T., Belina, G., Moussaïd, A., Pignon, F., and Hoekstra, H. *Phys. Rev. E* **74**(5), 051504 (2006).

[134] Jones, R. A. L. *Soft Condensed Matter*. Oxford University Press, USA, (2002).

[135] Hansen, J.-P. and McDonald, I. R. *Theory of simple liquids*. Academic press, 3rd edition, (2006).

[136] Baglioni, P., Fratini, E., Lonetti, B., and Chen, S. H. *J. Phys.: Condens. Matter* **16**(42), S5003 (2004).

[137] Gibaud, T., Cardinaux, F., Bergenholtz, J., Stradner, A., and Schurtenberger, P. *Soft Matter* **7**, 857–860 (2011).

[138] Poon, W. C. K. *Phys. Rev. E* **55**, 3762–3764 (1997).

[139] Narayanan, T. and Kumar, A. *Physics Reports* **249**, 135–218 (1994).

[140] Olvera de la Cruz, M., Belloni, L., Delsanti, M., Dalbiez, J. P., Spalla, O., and Drifford, M. *J. Chem. Phys.* **103**, 5781–5791 (1995).

[141] Bloomfield, V. A. *Curr. Opin. Struct. Biol.* **6**, 334 (1996).

[142] Saminathan, M., Antony, T., Shirahata, A., Sigal, L. H., Thomas, T., and Thomas, T. J. *Biochemistry* **38**(12), 3821–3830 (1999).

[143] Shklovskii, B. I. *Phys. Rev. Lett.* **82**(16), 3268 (1999).

[144] Gelbart, W. M., Bruinsma, R. F., Pincus, P. A., and Parsegian, V. A. *Phys. Today* **53**(9), 38 (2000).

[145] Nguyen, T. T., Rouzina, I., and Shklovskii, B. I. *J. Chem. Phys.* **112**(5), 2562–2568 (2000).

[146] Solis, F. J. and Olvera de la Cruz, M. *J. Chem. Phys.* **112**, 2030–2035 (2000).

[147] Burak, Y., Ariel, G., and Andelman, D. *Biophys. J.* **85**, 2100–2110 (2003).

[148] Butler, J. C., Angelini, T., Tang, J. X., and Wong, G. C. L. *Phys. Rev: Lett.* **91**(2), 028301 (2003).

[149] Murayama, Y., Sakamaki, Y., and Sano, M. *Phys. Rev. Lett.* **90**(1), 018102 (2003).

[150] Burak, Y., Ariel, G., and Andelman, D. *Curr. Opin. Colloid Interface Sci.* **9**(12), 53 – 58 (2004).

[151] Yang, J. and Rau, D. C. *Biophys. J.* **89**, 1932–1940 (2005).

[152] Hsiao, P.-Y. *J. Chem. Phys.* **124**, 044904 (2006).

[153] Kornyshev, A. A., Lee, D. J., Sergey, L., and Wynveen, A. *Rev. Mod. Phys.* **79**, 943–996 (2007).

[154] Ianeselli, L., Zhang, F., Skoda, M. W. A., Jacobs, R. M. J., Martin, R. A., Callow, S., Prévost, S., and Schreiber, F. *J. Phys. Chem. B* **114**(11), 3776–3783 (2010).

[155] Soraruf, D., Roosen-Runge, F., Grimaldo, M., Zanini, F., Schweins, R., Seydel, T., Zhang, F., Roth, R., Oettel, M., and Schreiber, F. *Soft Matter* **10**, 894–902 (2014).

[156] Cheng, S. Z. D. *Phase transitions in polymers : the role of metastable states*. Elsevier North-Holland, 1st ed. edition, (2008).

[157] Dao, V. N., Morris, P. H., and Dux, P. F. *Cement and Concrete Research* **38**, 1302–1305 (2008).

[158] McMillan, Jr., W. G. and Mayer, J. E. *J. Chem. Phys.* **13**(7), 276–305 (1945).

[159] Roth, R., Evans, R., and Louis, A. A. *Phys. Rev. E* **64**(5), 051202 (2001).

[160] Wolf, M., Roosen-Runge, F., Zhang, F., Roth, R., Skoda, M. W. A., Jacobs, R. M. J., Sztucki, M., and Schreiber, F. *J. Mol. Liq.* , in press (2014).

[161] Noro, M. G. and Frenkel, D. *J. Chem. Phys.* **113**(8), 2941–2944 (2000).

[162] Dijkstra, M., van Roij, R., and Evans, R. *Phys. Rev. E* **59**, 5744–5771 (1999).

[163] Baxter, R. J. *J. Chem. Phys.* **49**(6), 2770–2774 (1968).

[164] Carter, D. C. and Ho, J. X. *Adv. Protein Chem.* **45**, 153–203 (1994).

[165] Barbosa, L. R., Ortore, M. G., Spinozzi, F., Mariani, P., Bernstorff, S., and Itri, R. *Biophys. J.* **98**(1), 147 – 157 (2010).

[166] Nossal, R., Glinka, C. J., and Chen, S.-H. *Biopolymers* **25**(6), 1157–1175 (1986).

[167] Kotlarchyk, M. and Chen, S.-H. *J. Chem. Phys.* **79**(5), 2461–2469 (1983).

[168] Bendedouch, D. and Chen, S.-H. *J. Chem. Phys.* **87**(9), 1473–1477 (1983).

[169] Bendedouch, D., Chen, S. H., and Koehler, W. C. *J. Phys. Chem.* **87**(14), 2621–2628 (1983).

[170] Roosen-Runge, F., Hennig, M., Seydel, T., Zhang, F., Skoda, M. W., Zorn, S., Jacobs, R. M., Maccarini, M., Fouquet, P., and Schreiber, F. *BBA-Proteins Proteom* **1804**(1), 68 – 75 (2010).

[171] Roosen-Runge, F., Hennig, M., Zhang, F., Jacobs, R. M. J., Sztucki, M., Schober, H., Seydel, T., and Schreiber, F. *Proc. Natl. Acad. Sci. USA* **108**(29), 11815–11820 (2011).

[172] Zhang, F., Skoda, M. W. A., Jacobs, R. M. J., Martin, R. A., Martin, C. M., and Schreiber, F. *J. Phys. Chem. B* **111**(1), 251–259 (2007).

[173] Zhang, F., Roosen-Runge, F., Skoda, M. W. A., Jacobs, R. M. J., Wolf, M., Callow, P., Frielinghaus, H., Pipich, V., Prevost, S., and Schreiber, F. *Phys. Chem. Chem. Phys.* **14**, 2483–2493 (2012).

[174] Sugio, S., Kashima, A., Mochizuki, S., Noda, M., and Kobayashi, K. *Protein Eng.* **12**, 439–446 (1999).

[175] Jordan, E., Roosen-Runge, F., Leibfarth, S., Zhang, F., Sztucki, M., Kohlbacher, O., Hildebrandt, A., and Schreiber, F. *submitted and under review* (2013).

[176] Swinehart, D. F. *Journal of Chemical Education* **39**, 333–335 (1962).

[177] Pace, C. N., Vajdos, F., Fee, L., Grimsley, G., and Gray, T. *Protein Sci.* **4**, 2411–2423 (1995).

[178] Sober, H. A. *CRC Handbook of Biochemistry: Selected data for molecular biology.* CRC, (1970).

[179] Feigin, L. A. and Svergun, D. I. *Structure Analysis by Small-Angle X-Ray and Neutron Scattering.* Plenum Press, New York, (1987).

[180] Svergun, D. I., Koch, M. H. J., Timmins, P. A., and May, R. P. *Small Angle X-ray and Neutron Scattering from Solutions of Biological Macromolecules.* Ox, (2013).

[181] Goerigk, G. and Mattern, N. *Acta Mater.* **57**(12), 3652 – 3661 (2009).

[182] Lehninger, A. L., Nelson, D. L., and Cox, M. M. *Lehninger Pricniples of Biochemistry.* W. H. Freeman, (2005).

[183] Lindner, P. and Zemb, T. *Neutrons, X-rays, and Light: Scattering Methods Applied to Soft Condensed Matter.* Elsevier North-Holland, (2002).

[184] Glatter, O. and Kratky, O. *Small angle X-ray scattering.* Academic Press, (1982).

[185] Hayter, J. B. and Penfold, J. *Colloid Polym. Sci.* **261**, 1022–1030 (1983).

[186] Als-Nielsen, J. and McMorrow, D. *Elements of Modern X-ray Physics.* john Wiley & Sons, West Sussex, United Kingdom, (2011).

[187] Beaucage, G. *J. Appl. Cryst.* **29**(2), 134–146 (1996).

[188] Tomchuk, O. V., Bulavin, L. A., Aksenov, V. L., Garamus, V. M., Ivankov, O. I., Vul, A. Y., Dideikin, A. T., and Avdeev, M. V. *J. Appl. Cryst.* **47**, 642–653 (2014).

[189] Ferrer, M. L., Duchowicz, R., Carrasco, B., de la Torre, J. G., and Acuna, A. U. *Biophys. J.* **80**(5), 2422 – 2430 (2001).

[190] Beaucage, G., Kammler, H. K., and Pratsinis, S. E. *J. Appl. Cryst.* **37**, 523–535 (2004).

[191] Menon, S. V. G., Manohar, C., and Rao, K. S. *J. Chem. Phys.* **95**(12), 9186–9190 (1991).

[192] Jacrot, B. and Zaccai, G. *Biopolymers* **20**(11), 2413–2426 (1981).

[193] Kratky, O., Pilz, I., and Schmitz, P. J. *J. Colloid Interf. Sci.* **21**, 24–34 (1966).

[194] Sztucki, M., Gorini, J., Vassalli, L.-P., Goirand, L., van Vaerenbergh, P., and Narayanan, T. *J. Synchrotron Rad.* **15**, 341–349 (2008).

[195] Hainbuchner, M., Villa, M., Kroupa, G., Bruckner, G., Baron, M., Amenitsch, H., Seidl, E., and Rauch, H. *J. Appl. Cryst.* **33**, 851–854 (2000).

[196] Alefeld, B., Schwahn, D., and Springer, T. *Nucl. Instrum. Meth.* **A274**, 210–216 (1989).

[197] Goerigk, G. and Varga, Z. *J. Appl. Cryst.* **44**, 337–342 (2011).

[198] Garrison, W. M. *Chem. Rev.* **87**, 381–398 (1987).

[199] Schärtl, W. *Light scattering from polymer solutions and nanoparticle dispersions*. Springer, (2007).

[200] Hecht, E. *Optics*. Addison WeslAd, San Francisco, (2002).

[201] Wolf, M. Master's thesis, Eberhard Karls University Tuebingen, (2010).

[202] Zhang, F., Roth, R., Wolf, M., Roosen-Runge, F., Skoda, M. W. A., Jacobs, R. M. J., Sztucki, M., and Schreiber, F. *Soft Matter* **8**, 1313–1316 (2012).

[203] Wolf, M., Zhang, F., Roosen-Runge, F., Roth, R., Skoda, M. W. A., Jacobs, R. M. J., Sztucki, M., and Schreiber, F. *J. Mol. Liq.* **200**, 20–27 (2014).

[204] Asherie, N. R. *Methods* **34**(3), 266–272 (2004).

[205] Hagen, M. H. J. and Frenkel, D. *J. Chem. Phys.* **101**(5), 4093–4097 (1994).

[206] Zhang, F., Zocher, G., Sauter, A., Stehle, T., and Schreiber, F. *J. Appl. Cryst.* **44**(4), 755–762 (2011).

[207] Ashton, D. J., Wilding, N. B., Roth, R., and Evans, R. *Phys. Rev. E* **84**, 061136 (2011).

[208] Kern, N. and Frenkel, D. *J. Chem. Phys.* **118**(21), 9882–9889 (2003).

[209] Foffi, G. and Sciortino, F. *J. Phys. Chem. B* **111**(33), 9702–9705 (2007).

[210] Brown, W. *Light Scattering: Principles and Development*. Monographs on the Physics and Chemistry of Materials. Clarendon Press, (1996).

[211] Bajaj, H., Sharma, V. K., and Kalonia, D. S. *Biophysical Journal* **87**(6), 4048 – 4055 (2004).

[212] Narayanan, T. *Soft Matter Characterization*, chapter Synchroton small-angle X-ray Scattering, 899ff. Springer (2008).

[213] Svergun, D. I. and Koch, M. H. J. *Rep. Prog. Phys.* **66**(10), 1735–1782 (2003).

[214] Pedersen, J. S. *Adv. Colloid Interface Sci.* **70**(0), 171 – 210 (1997).

[215] Chen, S.-H. *Annu. Rev. Phys. Chem.* **37**(1), 351–399 (1986).

[216] Isihara, A. *J. Chem. Phys.* **18**(11), 1446–1449 (1950).

[217] Heinen, M., Zanini, F., Roosen-Runge, F., Fedunova, D., Zhang, F., Hennig, M., Seydel, T., Schweins, R., Sztucki, M., Antalik, M., Schreiber, F., and Nägele, G. *Soft Matter* **8**, 1404–1419 (2012).

[218] Piazza, R. *J. Cryst. Growth* **196**(2-4), 415 – 423 (1999).

[219] Lomakin, A., Asherie, N. R., and Benedek, G. B. *PNAS* **100**(18), 10254–10257 (2003).

[220] Wang, Y. and Annunziata, O. *Langmuir* **24**(6), 2799–2807 (2008).

[221] Möller, J., Grobelny, S., Schulze, J., Bieder, S., Steffen, A., Erlkamp, M., Michael, P., Tolan, M., and Winter, R. *Phys. Rev. Lett.* **112**, 028101 (2014).

[222] Dorsaz, N., Thurston, G. M., Stradner, A., Schurtenberger, P., and Foffi, G. *Soft Matter* **7**(5), 1763–1776 (2011).

[223] Chen, S., Lau, H., Brodsky, Y., Kleemann, G. R., and Latypov, R. F. *Protein Sci.* **19**(6), 1191–1204 (2010).

[224] Pipich, V. http://www.qtikws.de, (2012).

[225] Kline, S. R. *J. Appl. Cryst.* **39**(6), 895–900 (2006).

[226] Squire, P. G., Moser, P., and O'Konski, C. T. *Biochemistry* **7**(12), 4261–4272 (1968).

[227] Okubo, M., Azume, I., and Yamamoto, Y. *Colloid P* **268**, 598–603 (1990).

[228] Cahn, J. W. and Hilliard, J. E. *The Journal of Chemical Physics* **31**(3), 688–699 (1959).

[229] Wang, Y. and Annunziata, O. *J. Phys. Chem. B* **111**, 1222–1230 (2007).

[230] Dormidontova, E. E. *Macromol.* **35**, 987–1001 (2002).

[231] Moelbert, S. and De Los Rios, P. *Macromolecules* **36**(15), 5845–5853 (2003).

[232] Lee, H.-N. and Lodge, T. P. *J. Phys. Chem. Lett.* , 1962–1966 (2010).

[233] Braun, M., Matsarskaia, O., Wolf, M., Zhang, F., Roosen-Runge, F., Roth, R., and Schreiber, F. *in preparation* .

[234] Hammouda, B. *J. Appl. Cryst.* **43**, 1474–1478 (2010).

[235] Schmidt, P. W. *J. Appl. Cryst.* **15**, 567–569 (1982).

[236] Koberstein, J. T., M. B. and Stein, R. S. *J. Appl. Cryst.* **13**, 34–45 (1980).

[237] Efimova, Y. M., Haemers, S., Wierczinski, B., Norde, W., and Well, A. A. V. *Biopolymers* **85**(3), 264–273 (2006).

[238] Streets, A. M. and Quake, S. R. *Phys. Rev. Lett.* **104**(17), 1–4 (2010).

[239] Sauter, A., Roosen-Runge, F., Zhang, F., Lotze, G., Jacobs, R. M. J., and Schreiber, F. *J. Am. Chem. Soc., accepted* **137**, 1485–1491 (2015).

Acknowledgements

Numerous people have contributed to the scientific work included in this thesis. This thesis was only possible due to their inspiring lives and work environment. I am pleased to acknowledge the helpful support.

First of all, I would like to thank my first supervisor Frank Schreiber for giving me the opportunity to work in this interesting scientific area. Discussions on the interpretations of experimental data, general aspects of soft condensed matter, academic life and scientific writing are very helpful.

Special thanks go to Fajun Zhang for his support durin this thesis. His scientific inspirations and the innumerable discussions build the basic concepts of this work. His experience how to tackle scientific problem was a great help. It was a pleasure to work in Fajun's subgroup because of his ingenuity.

I express my gratitude to my second supervisor Thilo Stehle from the Interfaculty Institute of Biochemistry for allowing us to use equipment which was not available in our work group. Furthermore discussions with the members of his group helped understand the behavior of proteins.

My thanks also goes to Roland Roth for the very constructive and pleasant collaboration. He was greatly helped me deepen my understanding statistical physic of soft condensed matter. He always remained calm even when our experimental results conflicted with his theories.

Another important and smart person for this work was Felix Roosen-Runge. I would like to thank him for the nice discussions and his help as regards for the theoretical understanding of the system.

I am grateful to all coworkers of the protein subgroup that accompanied my research. I thank them for the smooth team work during several beamtimes at the FRM II as well as for our good cooperation in our connected research projects. I would like to thank Andrea Sauter and Felix Roosen-Runge.

Special thanks goes to the "legendary" room P19. It was a great pleasure to work with my roommates Andrea Sauter, Michal Braun and Olga Matsarskaia. It was amazing to see the good mood and the efficiency of our discussions. All of them are great colleagues and we also had a lot of fun with external activities outside of the work.

I would like to thank Tilo Seydel, Marco Grimaldo and Robert Jacobs for the discussions and the nice time at the beamtimes during the tests of the new sample holder.

I would also acknowledge the discussions with Fabio Zanini and Daniel Sorauf on the topic of light scattering. They helped me to see special problems in light scattering and with the discussion of the resulting data.

Within this thesis I participated in numerous experiments at large-scale facilities. I would like to thank the coworkers – Robert Jacobs, Maximilian Skoda and all mem-

bers of the subgroup who joined us for these experiments – as well as the scientific staff of the beamlines – in particular Theyencheri Narayanan, Michael Sztucki, Gudrun Lotze, Aurel Radulescu, Noemi Szekeley, Vitaly Pipich, Zhendong Fu, Zhenyu Di, Ralf Schweins, Guiseppe Zaccai and Vasyl Haramus – for their help, their good humor and their knowledge on scattering techniques and data analysis.

I am also grateful for discussions with Georg Zocher and Christoph Schall from the Interfaculty institute of biochemistry as well as for their support with many experiments and the helpful discussions for interpreting the received results.

Many thanks goes to present and former group members of the work group in Tübingen for the nice atmosphere and enjoyable discussions also beyond scientific problems. To spend my time with all of the group members at the annual excursions to Oberjoch and the travel to conferences was a notable experience. I admire the excellent organization of the group by Alexander Gerlach.

I would like to thank Alexander Gerlach, Andrea Sauter, Johannes Dieterle, Yulia Fulmes, Daniel Sorauf and Fabian Hecht for the good team work during the practical physics courses for medical students.

I am happy to acknowledge the prompt and very helpful proofreading by Michal Braun, Olga Matsarskaia, Andrea Sauter, Stefano da Vela, Felix Roosen-Runge and Marco Grimaldo.

Finally I will also acknowledge several influences from outside of the academic life. First their is my work at the German Red Cross which helps me to get clear my mind. And special thanks to all my friends and my family who supported and enabled this thesis in a way that a few lines would not to justice. I am very thankful for the time spent together, and I am looking forward to more.